The University Of Sheffield.

The use of $M_{n+1}AX_n$ phases in Accident Tolerant Fuel cladding

Thesis submitted in fulfilment of the requirements for the degree of Doctor of Philosophy

Thomas Galvin

140218783

September 2018

Department of Materials Science and Engineering

University of Sheffield

Contents

Acknowledgements

Funding for this project from EPSRC and National Nuclear Laboratory under the Industrial CASE scheme (grant no. 1614290) is gratefully acknowledged. I would like to thank my primary academic supervisor Professor Ian Reaney, for all of his guidance, help and encouragement over the course of this project, which I don't think I could have completed without his supervision. I would also like to extend my thanks to my other academic supervisors Professors Mark Rainforth and Neil Hyatt, for their help and advice. My thanks also go to my industrial supervisor at NNL, Daniel Shepherd, for his excellent supervision and for his thorough and insightful comments on my thesis.

I would also like to extend my thanks to all the academics, technicians and students who have assisted me during this project, in particular: Andrew Mould, Martin Stennett, Lisa Hollands, Dean Haylock, Chris Holland, Christopher Smith, Everth Hernandez-Nava and Amit Rana. Further to this I thank all of my colleagues in the Immobilisation Science Laboratory for their advice and support.

I have struggled, both mentally and emotionally throughout this project. Therefore I would like to thank my parents for their support throughout the project and my life in general, my wonderful partner Ellie for always being there to help, and my good friend Dan for his emotional support and willingness to watch terrible cooking shows with me.

Abstract

Following the discovery of the unique set of properties exhibited by a group of layered ternary carbides and nitrides known as MAX phases, they have been proposed as a candidate for use in nuclear engineering. Specifically, they have been proposed as an Accident Tolerant Fuel (ATF) coating or cladding material, to provide extra protection from the high temperature oxidation conditions during a Loss of Coolant Accident (LOCA), conditions which current zirconium-based cladding has limited resistance to as seen at Fukushima in 2011. Following a survey of the literature on the properties, synthesis techniques and methods of application of MAX phases, the body of experimental work falls into three sections, which contain a series of proof-of-concept experiments relating to the use of MAX phases in ATF cladding.

The first is concerned with methods of synthesis of MAX phases. Spark Plasma Sintering (SPS) was used to synthesise Ti_3SiC_2, while Molten Salt Synthesis (MSS) was used to synthesise Ti_3SiC_2, Ti_3AlC_2 and Ti_2AlC, the latter of which was found to be 88wt.% pure, with a synthesis temperature approximately 100°C lower than by other methods reported in the literature. Both SPS and MSS were used to conduct a series of experiments attempting to form reactor suitable hybrid MAX phases that may have been suitable as an ATF material. These attempts were sadly unsuccessful, though promising such phases have now been synthesised by hot pressing in the literature and potentially with this additional guidance on stable phases now available, future SPS or MSS synthesis may prove more fruitful.

The following section covers experiments to create a method of coating existing fuel rods with a protective MAX phase layer. Depositions were carried out of MAX phases onto flat and tubular geometry using Electrophoretic Deposition (EPD), a room temperature deposition technique that can be performed in water. Deposition was carried out onto copper, titanium, graphite and ZIRLO® (zirconium alloy) substrates. Commercially available Ti_3SiC_2 powder was used as a placeholder MAX phase due to its availability over other more suitable phases. Unsintered depositions of 1.89±0.26 mg/cm^2 were achieved on titanium substrates in 10 minutes. These powder coatings were then rapidly densified using a Selective Laser Melting (SLM) 3D printer, and a study of laser power and focus was carried out. Dense coatings of up to 30µm thick were achieved on titanium that did not amorphise, but with a thin surface phase of TiC_{1-x} present. Varying the laser focus parameter resulted in bands of coating, moving towards fuller coverage with a widening focus. Laser sintered samples on ZIRLO® substrates did not densify, however it is believed this is due to an unavoidable change in the SLM 3D printer used, and not an underlying issue.

The final experimental section explores the possibility of creating MAX phase cladding, by using the well-established technique slip casting to produce short lengths of tube. Ti_3SiC_2 slips of varying composition were analysed for their rheological properties and used to cast tubes in plaster moulds. An investigation of sintering conditions was carried out, and the resulting densified tubes were found to be ~89% of maximum density. The tubes were carefully drilled out and polished, and then subjected to destructive hoop stress tests. The highest hoop stress per unit wall thickness value for a tube was calculated at 9.1±2.2 MPa/mm.

A discussion section then considers the results found in this project and examines them in the larger context of other techniques, and their feasibility for use in the nuclear industry. The proof of concept experiments performed were moderately successful, in that a synthesis method for MAX phases was found to be effective for certain phases, a method for coating and densifying MAX phases onto substrates was found, and MAX phase tubes were cast. Work done in this project can serve as a starting point for further investigations into methods of applying MAX phases to the nuclear industry.

Glossary of acronyms

ATF – Accident Tolerant Fuel

EPD – Electrophoretic Deposition

LOCA – Loss of Coolant Accident

MSS – Molten Salt Synthesis

SLM – Selective Laser Melting

SPS – Spark Plasma Sintering

1 – Introduction and Aims

During both the 1986 Chernobyl and 2011 Fukushima nuclear incidents, large explosions occurred inside the core leading to the release of fission products into the environment [1]. These explosions were the result of the ignition of hydrogen within the reactor cores; liberated from the coolant water and steam by the oxidation of zirconium alloy cladding, and to a lesser extent the radiolysis of water and oxidation of the control rods [2]. Unfortunately despite its suitability for use as cladding in many aspects, zirconium alloys perform poorly in the event of Loss of Coolant Accidents (LOCAs), also including the 1979 Three Mile Island (TMI) incident where fission products were not released. After 1 hour at 1000 °C, zirconium alloys can undergo a phenomenon called breakaway oxidation, where the rate of oxidation increases severely, and is accompanied by an increase in hydrogen embrittlement (the diffusion of hydrogen into the cladding and subsequent hydriding), leading to more cracking and exposure of more cladding to oxidise [3] .

Finding a suitable Accident Tolerant Fuel (ATF) cladding replacement for zirconium alloys presents a problem, as a material would need to fulfil several criteria for normal operation, namely oxidation resistance at operating temperature, resistance to hydrogen embrittlement and resistant to radiation induced damage, while still being neutronically 'transparent' enough to not interfere with reactor operation. The material also needs good mechanical properties to resist external pressure from the coolant and internal pressure from the accumulation of fission gas as well as any damage during transport, fuel insertion and removal, and end of cycle storage. Finally it must act as a barrier between fuel pellets and coolant; stopping any migration of fission products from within the rod. To surpass the performance of zirconium alloys, the material would also have to retain its oxidation resistance under high temperature steam, and resist hydrogen uptake, as well as having sufficient mechanical strength and toughness. In a LOCA event, ATF cladding would seek to significantly extend the time before any environmental release occurs giving operators more time to restore coolant flow and bringing the reactor back under control.

One possibility for an ATF cladding is to use a unique family of carbides and nitrides known collectively as $M_{n+1}AX_n$ (MAX) phases. Although they were discovered in the 1960s [4], they have recently gained attention due to their combination of ceramic and metallic properties. Excellent conductors of electricity and heat, they also exhibit high stiffness and fracture toughness [5]. Certain phases have superior oxidation resistance [6], while some have been shown to exhibit some resistance to heavy ion and neutron based radiation [7] [8]. As such they are being considered for in-core applications in both current and future reactor designs [9] [10].

Although there are several candidates, no existing phase has been shown to be ideally suited for a core application, however in addition to the ~60 MAX phases that have been discovered there is potential to create a much larger number of different 'hybrid' MAX phases, one or more of which may exhibit the desired properties. Therefore, research needs to be undertaken on practical methods of applying MAX phases to an ATF scenario.

The overall hypothesis of this project is that ***"MAX phases are a suitable candidate for ATF cladding solutions: a) from a synthesis and manufacturing standpoint, b) as a coating on existing zirconium alloy cladding, c) as a partial or complete replacement for zirconium alloy."***

The aims for this project are as follows:

- Determine an appropriate synthesis route for suitable MAX phases.
- Determine a method to apply dense coatings of MAX phase to zirconium alloy cladding without overheating the substrate.
- Explore the feasibility of the manufacture and testing of MAX phase cladding.

This project serves as a starting point for practical use of MAX phases for this purpose. Synthesis methods were explored with industrial scalability in mind, using reactive Spark Plasma Sintering (SPS) and the Molten Salt Synthesis (MSS). The synthesis of aforementioned hybrid MAX phases was attempted. The feasibilities were explored of both a MAX phase coating on zirconium alloys through the use of Electrophoretic Deposition (EPD) coupled with rapid laser sintering, and a full MAX phase replacement of zirconium alloys via slip casting of cladding tubes.

Arguably, nuclear safety is the biggest issue in nuclear power; from both an operational and legal licensing standpoint but also in the public eye. Previous reactor incidents and an association with nuclear weapons mean that trust will have to be increased with the general public if nuclear power is to continue to reduce our dependence on fossil fuels, and any advancements made in reactor safety can only help to build that trust.

References

[1] G. Steinhauser, A. Brandl, and T. E. Johnson, "Comparison of the Chernobyl and Fukushima nuclear accidents: A review of the environmental impacts," Sci. Total Environ., vol. 470–471, pp. 800–817, 2014.

[2] J. Yanez, M. Kuznetsov, and A. Souto-Iglesias, “An analysis of the hydrogen explosion in the Fukushima-Daiichi accident,” Int. J. Hydrogen Energy, vol. 40, no. 25, pp. 8261–8280, 2015.

[3] M. Yamato, F. Nagase, and M. Amaya, “Reduction in the onset time of breakaway oxidation on Zircaloy cladding ruptured under simulated LOCA conditions,” J. Nucl. Mater., vol. 445, no. 1–3, pp. 78–83, 2014.

[4] W. Jeitschko, H. Nowotny, and F. Benesovsky, “Kohlenstoffhaltige ternaire Verbindungen (H-Phase),” Monatshefte für Chemie, vol. 332, pp. 2–6, 1963.

[5] M. W. Barsoum, “MAX Phases: Properties of Machinable Ternary Carbides and Nitrides,” in Wiley-VCH, vol. 1, Wiley-, 2013.

[6] X. H. Wang and Y. C. Zhou, “High-temperature oxidation behavior of Ti2AlC in air,” Oxid. Met., vol. 59, no. 3–4, pp. 303–320, 2003.

[7] Q. Huang, R. Liu, G. Lei, H. Huang, J. Li, S. He, D. Li, L. Yan, and J. Zhou, “Irradiation resistance of MAX phases Ti3SiC2 and Ti3AlC2: Characterization and comparison,” J. Nucl. Mater., vol. 465, pp. 640–647, 2015.

[8] D. J. Tallman, E. N. Hoffman, E. N. Caspi, B. L. Garcia-Diaz, G. Kohse, R. L. Sindelar, and M. W. Barsoum, “Effect of neutron irradiation on select MAX phases,” Acta Mater., vol. 85, pp. 132–143, 2015.

[9] E. N. Hoffman, D. W. Vinson, R. L. Sindelar, D. J. Tallman, G. Kohse, and M. W. Barsoum, “MAX phase carbides and nitrides: Properties for future nuclear power plant in-core applications and neutron transmutation analysis,” Nucl. Eng. Des., vol. 244, pp. 17–24, 2012.

[10] K. Lambrinou, T. Lapauw, A. Jianu, A. Weisenburger, J. Ejenstam, P. Szak´los, J. Wallenius, E. Ström, K. Vanmeensel, and J. Vleugels, “Corrosion-Resistant Ternary Carbides For Use in Heavy Liquid Metal Coolants,” in The American Ceramic Society, 2015, pp. 19–34.

2 – Literature Review

2.1 – Overview of current fuel cladding technology

2.1.1 Introduction

Since the 1950s nuclear power has been a viable alternative energy source to reduce our reliance on fossil fuels. In light of global climate change and rising energy demands, changes need to be made in the way we generate power, and nuclear fission in tandem with renewable energy sources can fill the gap left by decreasing reliance on fossil fuels [1] [2] [3] [4] [5].

2.1.2 Brief history of nuclear power

What follows is an abridged timeline for important events in the history of Nuclear energy [6] [7] [8]:

1911 – Ernest Rutherford discovers the atomic nucleus.

1932 – James Chadwick discovers the neutron.

1934 – Enrico Fermi and his research team split uranium atoms with neutrons.

1938 – Nuclear fission named and confirmed as phenomenon.

1942 – Chicago Pile 1, a 200W test reactor, and the world's first brought online.

1943 – Oak Ridge 1MW test reactor brought online.

1950 – Windscale Piles 1 and 2, UK based plutonium breeder reactors brought online.

1956 – Calder Hall 50MWe (Magnox gas cooled reactor) brought online in the UK, and the world's first reactor to generate large-scale electricity for a national grid.

1957 – Windscale fire in Pile 1: The UK's worst nuclear incident.

1957-60 – First US reactors connected to the grid (boiling and pressurised water reactors).

1959 – First French nuclear power station connected to the grid (gas cooled reactor similar to Magnox).

1964 – First USSR large-scale electricity generating reactors brought online.

1970s-1980s – Widespread international commercial growth of nuclear power.

1979 – Three Mile Island nuclear incident.

1986 – Chernobyl nuclear incident.

2011 – Fukushima nuclear incident.

2.1.3 Operation of a nuclear reactor

Nuclear reactors rely on the fission of heavy elements (typically uranium or plutonium isotopes) by neutron absorption to generate heat, which is then removed from the core via a coolant system and used to drive turbines. In the case of uranium-235 the following fission reaction occurs:

$$^{1}n + {}^{235}U \rightarrow A + B + x\ {}^{1}n \quad (2.1.1)$$

Where A and B represent two fission product nuclei (usually unequal in mass) and x represents a number of emitted neutrons [6]. These neutrons go on to cause more fissions creating a self-sustaining chain reaction. By absorption of excess neutrons by control rods, the reaction can be limited such that an equal number of fissions occur in a given time (or neutron count remains constant), a state known as 'critical'. When a reactor hits criticality, it is self-sustaining at a manageable rate.

Naturally occurring uranium occurs largely in two isotopes: U-238 makes up over 99%, while U-235 is approximately 0.71% [9]. Only U-235 is fissile (capable of self-sustaining a reaction) and so for most reactors the fraction of 235 to 238 must be increased, a process known as enrichment. Enrichment involves reacting the uranium with fluorine to form uranium hexafluoride (UF_6) gas. The gas is then centrifuged in large rotating columns, and due to their slight variation in molecular weights (the mass difference of the two uranium isotopes) the different isotopes can be partially fractioned. For most reactors (CANDU and Magnox reactors have used natural uranium as fuel, for example) enrichment brings the U-235 content up to 3–5%[10]. The UF_6 is then converted to uranium oxide (UO_2) to make fuel pellets.

Another important step in achieving criticality in a 'thermal' reactor is to moderate the energy spectrum of the emitted neutrons. When expelled from a fission reaction, the neutrons are typically emitted with a range of energies with a peak around 1 MeV [6]. To ensure a higher probability of causing more fissions, the neutrons need to be made less energetic, and this is achieved by the use of a moderator. Typically graphite or water (normal or heavy) is used, and reduces the neutron energy spectrum through repeated collisions between neutron and moderator nuclei. This energy transfer causes the moderator to heat up: another reason that sufficient coolant flow and hence heat transfer is required.

2.1.4 Reactor types

The ~450 civil reactors currently operational worldwide can be categorised in several fashions, but broadly speaking the overwhelming majority are cooled by some form of water [8]. In these cases, nuclear fission of uranium heats water to steam which drives electric turbines. Of the water-cooled

reactors, the Pressurised Water Reactor (PWR) and the Boiling Water Reactor (BWR) are the most common, known collectively as Light Water Reactors (LWR). Pressurised Heavy Water Reactors (PHWR) such as the CANDU reactors originating in Canada use heavy water (containing deuterium) as a coolant but in essence they operate similarly to PWRs. The now least common water-cooled reactor design is the Light Water-cooled Graphite-moderated Reactors (LWGR or RBMK – the Russian abbreviation) built by the Soviet Union, of which 15 are still operational (Chernobyl was of this type). In a BWR, the coolant water is allowed to boil and provides steam for the turbines, whereas PWR and PHWR coolant is under pressure such that it doesn't boil under normal operation. A secondary water coolant loop is isolated from the core coolant by a heat exchanger, and it is this water that generates steam to drive the turbines. Fig. 2.1.1 shows schematics for both PWR and BWR.

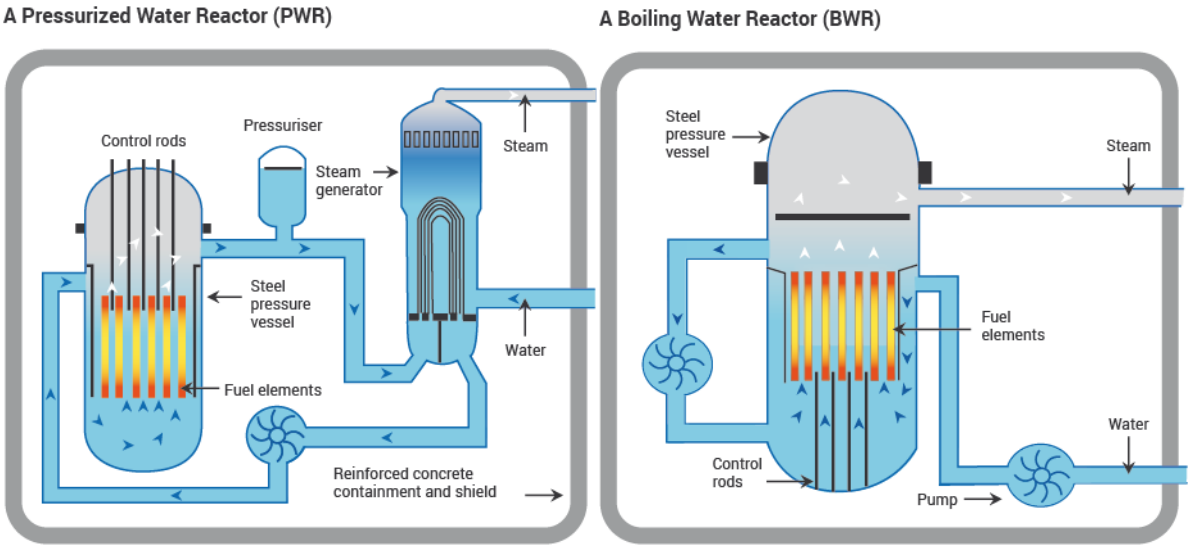

Fig. 2.1.1 – Schematic diagrams of PWR and BWR cores and coolant systems [11]

Far less common are the reactors that do not use water as a coolant. Of the reactors currently operating, there are 3 Fast Breeder Reactors (FBR) and 14 Gas Cooled Reactors (GCR). Fast breeder reactors rely on 'fast neutrons' emitted directly from fission to sustain the chain reaction without being slowed down, and so do not require a moderator. As the name suggests, they are able to breed more fissile plutonium from U-238 than the fissile material they consume in operation, thereby offering the potential for significantly more sustainable fuel cycles that utilise much more than the 1% of available energy in uranium that is typically released for usage in current cycles [12]. As U-238 is not capable of self-sustaining fission in these reactors, the fuel must contain a higher percentage of initial fissile plutonium, or in some cases U-235, than for other reactor types to compensate. FBR are typically cooled with liquid sodium (Sodium-cooled Fast Reactors) and are currently challenging to operate economically, hence the limited uptake, though adoption is predicted to increase significantly in the long term as demand for mined uranium increases. GCRs make up the remainder of the world's

nuclear power generation, and as their name implies use a gaseous coolant, such as CO_2 in the primary coolant loop. In the case of the Advanced Gas-cooled Reactor (AGR) which makes up the bulk of the UK's nuclear power generation, the cladding used is stainless steel [13].

2.1.5 Zirconium alloys and fuel cladding

To isolate fuel from the cooling water and to facilitate easy refuelling of the reactor, the fuel is encased within sealed tubes, known as cladding to make fuel rods. These rods are bundled between spacer grids to form fuel assemblies. For a typical PWR, assemblies consist of a matrix of 17x17 rods (with some spaces for control rod insertion) and the core will contain approximately 157 assemblies [14]. In water-cooled reactors that operate on fission from 'thermal neutrons' (neutrons in thermal equilibrium with the core), zirconium alloys are used for the cladding and most of the assembly materials, due to zirconium having a low thermal neutron capture cross section. This low cross section means that fewer neutrons that could otherwise have caused fissions are absorbed by the cladding, allowing the reactor to run more efficiently. Proprietary zirconium alloys for the nuclear industry (e.g. the Zircaloy series, ZIRLO, M5) contain some trace elements to improve mechanical properties and oxidation resistance. Fortunately zirconium has good oxidation resistance within normal operating reactor temperatures, as it forms a thin passivation layer of zirconium oxide [15].

2.1.6 Problems with zirconium alloys

Unfortunately, use of zirconium as fuel cladding is not without issues: their performance under Loss of Coolant Accidents (LOCA) is poor, and they also suffer attack by hydrogen over their operational lifetime. These issues are covered in further detail below.

Oxidation under Loss of Coolant Accident (LOCA) conditions

In the event that nuclear reactor operation starts to become out of control, the reactor can be shut down by fully inserting the control rods (sometimes known as SCRAM), halting the fission by absorbing enough of the neutrons to make the reactor sub-critical. However some of the shorter lived fission products still emit a significant amount of decay heat, and so the core still requires cooling [16]. In the event of a LOCA, the core temperature starts to rise. At higher temperatures where the coolant water becomes superheated steam, zirconium is less able to resist oxidation, and strips oxygen from water molecules causing both breakaway oxidation and the dangerous release of hydrogen gas [17]. Breakaway oxidation has been shown to occur by Yamato *et al*. after 1 hour at 1000 °C in a steam atmosphere, and in as little as 25 minutes if the cladding has ruptured (due to increased surface area)

[18]. Billone *et al.* carried out extensive testing on zirconium alloy cladding under LOCA conditions, and found that a rougher surface finish has a detrimental effect on the ability to resist breakaway oxidation [19] and that breakaway oxidation time was minimised at around 1000 °C.

Some of the hydrogen gas can lead to further cladding embrittlement (see below), but combined with oxygen liberated from water by radiolysis can lead to catastrophic explosions, which were seen at Chernobyl, and more recently at Fukushima [20] [21]. Explosions in the core, combined with severely weakened cladding or even molten cladding and fuel in a core meltdown scenario can lead to structural damage and a loss of containment, followed by the release of radioactive material into the environment. As the overwhelming majority of currently operating reactors used water-cooling and zirconium alloy cladding and with alternative reactors still being some decades from widespread deployment, other safety measures need to be explored.

Hydrogen Embrittlement

During operation, small amounts of hydrogen dissolved in the water or liberated from oxidation by water can diffuse into the cladding, forming zirconium hydrides. These disrupt the metal matrix and can lead to blisters on the surface of the cladding and cause cracks to propagate, a phenomenon known as hydrogen embrittlement [22] [23]. This process is exacerbated at LOCA temperatures above ~860 °C, as the zirconium undergoes a phase change from hexagonal close packed (hcp) to the more open body centred cubic (bcc), which allows more diffusion of hydrogen into the cladding [24] as well as causing the zirconium alloy to lose strength, start to balloon and eventually burst due to internal pressure from fission gases. Another issue is known as Delayed Hydride Cracking (DHC), whereby cracks can occur in the cladding and the end cap joints after the assembly has been removed from the reactor, typically in storage [25]. Brittle zirconium hydrides form and crack, exposing more zirconium and leading to crack propagation. This presents a major problem during long term storage before disposal.

Despite zirconium alloys being excellent materials for nuclear reactor cladding in some respects, their flaws are serious under certain conditions and so replacement or improvement of existing fuel cladding technology is a priority in the nuclear industry. Accident Tolerant Fuel (ATF) cladding is key to the long term success and safety of both current and future generations of reactors, and one such candidate being investigated is a family of materials known as MAX phases.

2.2– MAX Phases

2.2.1 Overview

$M_{n+1}AX_n$ phases (also known as MAX phases) are a family of nanolaminate carbides and nitrides, comprised of a transition metal (M), an 'A' group element (A) and carbon or nitrogen (X). The name $M_{n+1}AX_n$ phase also serves as a chemical formula for half the unit cell, and as such MAX phases can be split into '211', '312' '413' phases for n=1, 2, 3 and so on [26]. The first MAX phases were discovered by Hans Nowotny in the 1960s [27]; their structures and compositions were recorded under the designation of Hägg-phases (interstitial compounds) and were then largely ignored. In 1993, Pietzka and Schuster were also successful at synthesising Ti_2AlC and Ti_3AlC_2, the latter as a new discovery [28]. Then in 1996, Prof. Michel Barsoum and his research group at Drexel University synthesised bulk samples of Ti_3SiC_2 and discovered the unique combination of properties, and since then research has exploded [29], with well over 60 stable pure phases discovered. Other ternary and quaternary carbides and nitrides have been discovered which do share some similarities but do not conform the same formulae and structure as the 'true' MAX phases [30]; these are not covered in this project.

MAX phases seem to straddle the boundary between metals and ceramics, combining good high temperature performance, oxidation resistance, high stiffness and toughness with more metallic properties, such as electrical and thermal conduction, and a relatively high toughness which allows easy machining. The properties will be further discussed in a later section.

Due to these properties, MAX phases have found a number of commercial applications in the form of furnace tubes, burner nozzles and other refractory components through to formers for latex gloves and a potential non-stick cookware coating [26]. Alongside these applications, some phases have been proposed as 'reactor applicable' materials; favourable neutronics and radiation damage tolerance combined with their high temperature performance mean that components of a reactor core could feasibly be constructed from select MAX phases and retain its integrity. Currently suggested nuclear applications involve fuel cladding and in liquid metal cooled reactors, specifically the pump impeller for Lead-cooled Fast Reactors (LFR, a proposed alternative to sodium) [31] [32]. The following sections deal with the structure and properties of some well researched MAX phases, and finally cover synthesis, deposition and densification.

2.2.2 Structure and composition

The unit cells of the three simplest MAX phase types are shown in Fig. 2.2.1. They are in the space group $P6_3/mmc$ [33], and layers of the 'A' element separate layers of binary 'MX' carbide or nitride. The thickness of the binary layer determines which order the max phase is, with thicker layers resulting in higher orders. The orientation of the 'MX' layer alternates between 'A' layers, giving rise to a characteristic herringbone pattern on high resolution Transmission Electron Microscopy (TEM) images taken perpendicular to the c-axis [34] (fig. 2.2.2).

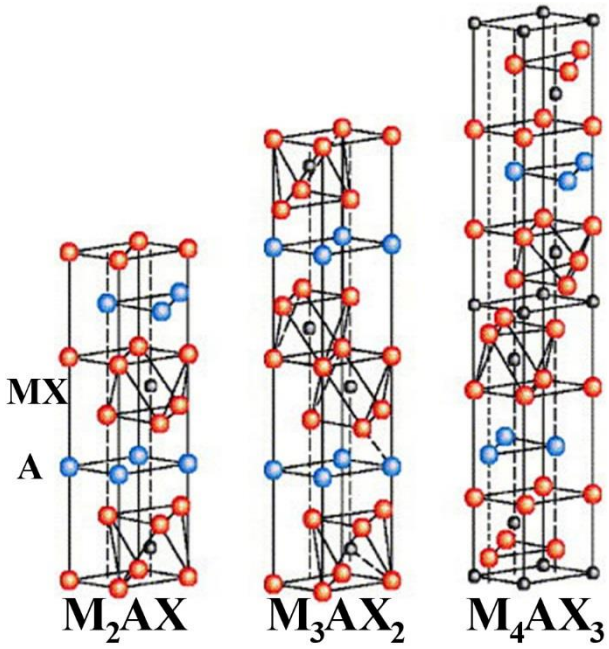

Fig. 2.2.1 – Unit cells for the three lowest order MAX phases [35].

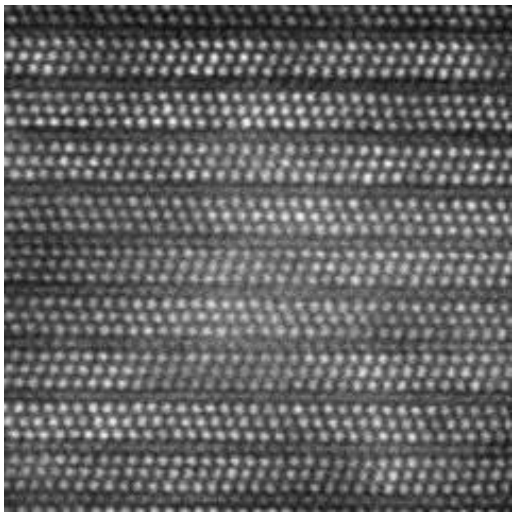

Fig. 2.2.2 – TEM image of Ti_3SiC_2 showing the herringbone pattern when viewed perpendicular to the c-axis [36].

Some ‘hybrid’ phases consisting of a unit cell made from two different formula cells have been reported [34] [37], as well as double ‘A’ layer MAX phases. These will not be covered in the literature review; due to their relative rarity they remain largely unexplored. Partial substitution (alloying) of the M, A and/or X sublattices is also possible, either as a stabiliser or to improve the properties [38]. These will be covered further in the properties and the synthesis section.

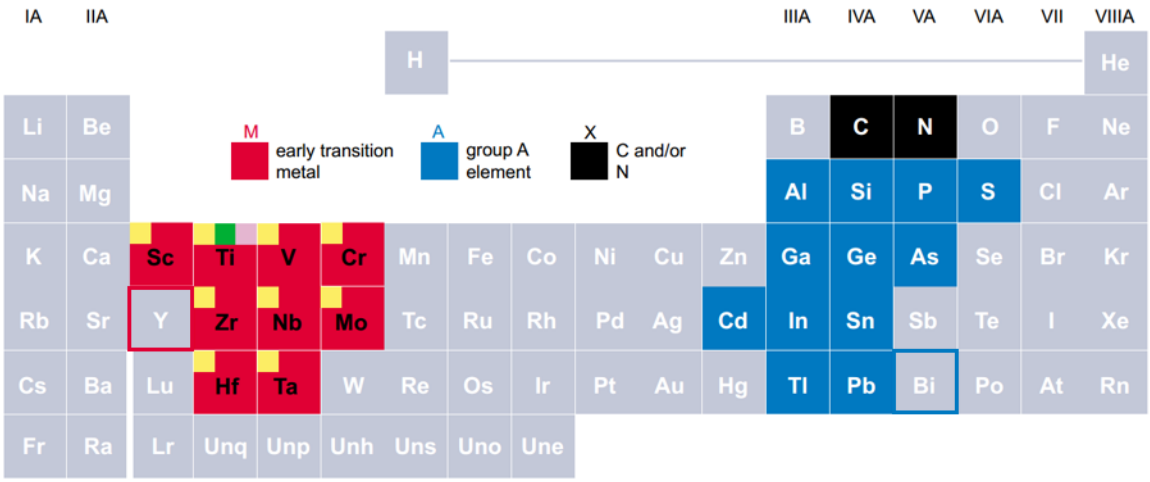

Fig. 2.2.3 – Periodic table highlighting elements commonly found in MAX phases (outline indicates synthesis only reported as part of a hybrid) [26].

Fig. 2.2.3 shows some elements commonly present in MAX phases. The ‘M’ element is usually an earlier transition metal, and the ‘A’ element is typically from group IIIA or IVA in the periodic table. Nitrides will not feature largely in the literature survey, due to the higher neutron capture cross section of nitrogen-14, which also forms radioactive carbon-14 under irradiation, making them largely unsuitable for a reactor material (it is possible to enrich nitrogen in the rarer N-15 isotope which does not suffer from these issues but obtaining high purity is expensive and supply is still limited) [39]. From here on, ‘X’ will refer to carbon and ‘MAX phases’ to carbides unless otherwise stated. The possibility of boron-containing MAX phases on either A or X sites has been postulated but not yet demonstrated in either experiment or simulation. The MX layers are strongly bonded, while the M-A bonds are typically weaker. This allows layers to slide over one another, delaminate and kink. It is through this mechanism that MAX phases get their physical damage tolerance; the deformation of layers allows the material to dent rather than shatter, with kinks and delaminated layers locking, preventing damage propagation and causing local hardening at the damage site [40].

2.2.3 Thermal and electrical properties

Barsoum *et al.* studied the thermal properties of Ti_3SiC_2 up to 1200°C using high temperature X-ray and neutron diffraction [41]. Bulk thermal expansion, heat capacity and thermal conductivity measurements were also performed on polycrystalline hot pressed samples of Ti_3SiC_2. The thermal expansion was found to be $9.12x10^{-6}K^{-1}$ and the molar heat capacity ranges from $110Jmol^{-1}K^{-1}$ at room temperature up to $155Jmol^{-1}K^{-1}$ at 1200°C. The thermal conductivity was found to drop from $37Wm^{-1}K^{-1}$ at room temperature to $32Wm^{-1}K^{-1}$ at 1200°C. From Rietveld refinement of the neutron diffraction data, Barsoum *et al.* found that the Ti atoms thermal vibrations are more apparent along the c-axis than the a-axis, while the silicon atoms were largely isotropic in their vibrations, and had much higher amplitudes. Here Si is referred to as a 'rattler', and it is common for the A elements due to their weaker bonding [26].

The thermal and electrical properties of Ti_2AlC, Nb_2AlC and the solid solution $(Ti,Nb)_2AlC$ were researched by Barsoum *et al.* [42]. The Hot Isostatic Pressed (HIP) samples were measured for their electrical resistances, thermal expansion coefficients and heat capacity. The room temperature electrical resistances were all found to be low: 0.29μΩm for Ti_2AlC, 0.38μΩm for Nb_2AlC and 0.78μΩm for the solid solution, which Barsoum *et al.* posit is higher due to defects from partial substitution of the M element. Thermal expansion coefficients were found to be $8.7x10^{-6}K^{-1}$ for the two pure phases and $8.9x10^{-6}K^{-1}$ for the solid solution. Heat capacities were found to vary between ~25 and ~1025°C as follows: Ti_2AlC ranged from 46–$36Jmol^{-1}K^{-1}$, Nb_2AlC increased from $23Jmol^{-1}K^{-1}$ to $27Jmol^{-1}K^{-1}$ and the solid solution also increased from 16.6–$24Jmol^{-1}K^{-1}$. The much larger heat capacities for Ti_2AlC can be attributed to a larger effect from phonons.

Another studied MAX phase is Cr_2AlC. W B Tian *et al.* tested and measured the thermal and electrical properties of bulk Cr_2AlC synthesised through hot pressing [43]. The four probe method was used to measure the electrical conductivity, while Differential Scanning Calorimetry (DSC) was used to determine the heat capacity, and thermal conductivity was derived from the temperature conductivity coefficient, measured using laser-flash technique. Thermal expansion was measured in the range of 30–1200°C. Electrical conductivity was found to decrease with increasing temperature; a room temperature value was given as approximately $1.4x10^{6}\Omega^{-1}m^{-1}$. Heat capacity at 25°C was reported as $560Jkg^{-1}K^{-1}$ while thermal conductivity at 200°C was given as $17.5Wm^{-1}K^{-1}$. The coefficient of thermal expansion was found to be $1.33x10^{-5}K^{-1}$ (for 30—1200°C).

2.2.4 Mechanical properties

MAX phase mechanical properties vary greatly with composition, grain size and density. A brief overview of general properties, with some specific examples are given below (see also the Synthesis section). Their Vickers hardness is typically lower than their binary carbide equivalent, ranging from 2—8GPa, with hardness increasing with decreasing grain size, while their fracture toughness falls between 5—20 $MPa.m^{1/2}$ [26] [40] [44]. They are stiff yet have relatively low density; Ti_3SiC_2 for example is approximately 3 times stiffer than titanium metal [44]. El-Raghy *et al.* first reported on the damage tolerance and physical properties of Ti_3SiC_2 after Barsoum *et al.* (including El-Raghy) first synthesised polycrystalline bulk samples of the material [45]. Samples were indented with a micro-hardness tester in the range of 0.5—10N, and with a Vickers hardness tester at 100N, and up to 300N. Notched samples were also tested for their fracture toughness at room temperature. The Ti_3SiC_2 had grain sizes of approximately 100 µm. The hardness was found to be 8 GPa at the lowest load and approaching 4 GPa at 100N. The fracture toughness at room temperature was determined to be 6 $MPa.m^{1/2}$, which El-Raghy *et al.* noted is high for a material "prone to delamination". Scanning Electron Microscopy (SEM) inspection of the indentations showed no cracking even with loads as high as 300N, but instead a curious aggregation of displaced material around the indentation edges. It was determined that Ti_3SiC_2 exhibits room temperature micro-plasticity through a combination of kinks, grain pull-outs and push-outs, and delamination. This was the first report on the unusual damage tolerance of MAX phases, which through kink bands and delamination, can deform slightly before breaking [46].

Ti_3SiC_2 has also been found resistant to fatigue induced from thermal cycling between room temperature and 1200°C [47]. Chen *et al.* reported that the crack growth from heat cycling was more contained in both a fine and coarse grained sample of Ti_3SiC_2 than in comparable refractory ceramics. The difference between the room temperature fracture toughness and the value at 1100°C was found to be very small: ~$6MPa.m^{1/2}$ and $7MPa.m^{1/2}$ at room temperature for fine and coarse respectively with an 8% and 13% reduction at temperature. At 1200°C however, the fracture toughness reduced greatly to $2.3MPa.m^{1/2}$ and $4.5MPa.m^{1/2}$.

The 'machinability' of dense Ti_3SiC_2 was investigated by Hwang *et al.* and compared small grained (average grain size 3.58µm) and large grained (average grain size 11.49µm) MAX phase samples alongside SM45C steel [48]. The samples were cut on a CNC lathe with a WC-Co composite tool to a depth of 0.1mm, with a feed rate of 0.1mm/rev and speed of 800rpm, and the resistance to cutting was measured on the tool head. Oil-based cutting lubricant was used to reduce friction and heating,

and facilitate the removal of material. Large-grained Ti_3SiC_2 offered a resistance of 7N, while small-grained Ti_3SiC_2 and steel gave values of 9.6N and 9N respectively. The Vickers hardness of the two was found to be 2.7GPa for the large-grained material and 4.5GPa for the small-grained material. Examining the tool head by SEM, some wear was apparent from the steel, but the tool used to cut the smaller grained MAX phase exhibited a lot of damage (due to its higher hardness) including small Ti_3SiC_2 pull-out grains embedded in the tool surface. Hwang *et al.* suggest the use of compressed air as a lubricant and chip-removal fluid as the cutting oil was ineffective at preventing aggregated material around the cut. However, they showed that bulk Ti_3SiC_2 can be easily machined with WC based tools with only slightly increased wear when compared with steel.

2.2.5 Oxidation resistance

Resistance to oxidation is a crucial property for any reactor cladding. In PWRs, during normal operation the cladding will be exposed to water at approximately 300°C at high pressure, and in the event of a LOCA the steam temperature can exceed 1000°C [49] [50] . Therefore resistance to oxidation and water based corrosion via a passivation layer or otherwise is key when considering materials selection.

Lee *et al.* studied the oxidation resistance of Cr_2AlC in high temperature air [51]. A bulk polycrystalline sample was hot pressed from $CrC_{0.5}$ and Al powder, and then cut into 10x5x5mm samples. These samples were polished with 2000 grit grinding paper and then oxidised in furnaces held at 1300°C for varying lengths of time. After 15 hours in the furnace, Al_2O_3 had formed on the surface, along with a Cr_7C_3 layer underneath; the preferential oxidation of aluminium being common in Al-containing MAX phases [52]. Examining cross sections of the samples, small voids were observed in the Cr_7C_3 layer due to the loss of aluminium. The samples were held for up to 336 hours in the furnace, during the course of which the Al_2O_3 layer and Cr_7C_3 underlayer grew, as well as growth of the previously observed voids which eventually led to flaking off of the Cr_7C_3 layer.

Ti_2AlC is widely reported to have excellent oxidation resistance, through the growth of a protective predominantly-Al_2O_3 scale [52] [53]. The scale is well-adhered and parts can be heat-cycled repeatedly without spalling of the oxide layer [54]. Cui *et al.* studied the evolution of the oxide layer in bulk Ti_2AlC [55]. Small cubes of hot pressed Ti_2AlC were heated in furnaces between 900—1400 °C for an hour, and also subjected to Thermogravimetric Analysis (TGA) up to 1200°C with heating/cooling rates of 10°C.min^{-1} and 20°C.min^{-1}. At 900°C TiO_2 is detected alongside Al_2O_3, which correspond with a sharp mass gain on the TGA graph. However the TiO_2 phase stays largely constant at higher temperatures with preferential formation of Al_2O_3. At 1400°C the oxide layer starts to show Al_2TiO_5, at the expense of TiO_2.

The oxidation of Ti_2AlC coatings on stainless steel in air and water was investigated by Feng *et al.* [56]. Ti_2AlC was magnetron sputtered onto 316L stainless steel, and then heated in a furnace at 750°C for 200 hours in both air and water vapour. Before oxidising, the coating was found to contain some Ti_3AlC, as well as an Al-rich diffusion layer. There was also some surface cracking. After being heated in air, Feng *et al.* found that the surface scale was composed of titanium and aluminium oxides on the surface, with aluminium-chromium oxide below (from the steel), and iron and titanium oxide layer below this and an innermost layer of alumina. They also observed that the cracks were filled with titanium oxide, but observed no loss of coating. In water the scale was found to contain TiO_2, Al_2TiO_5, alongside Ti_2AlC and Ti_3AlC. Compared to uncoated stainless steel (which they show undergoes breakaway oxidation during the steam test), the coated samples resisted bulk damage to the underlying steel. However Feng *et al.* note that likely due to the surface cracks, the oxidation resistance of the coatings are not as good as bulk Ti_2AlC.

Sun *et al.* investigated the oxidation of Ti_3SiC_2 in air up to 1300°C [57]. Hot pressed samples were heated in a TGA and held between 900—1300°C for 20 hours. Another sample was also heat-cycled in a furnace: up to 1100°C for 1 hour and then down to room temperature. At 900°C the mass gain was low, and the oxide was found to be mainly TiO_2, with some SiO_2 as well as detectable Ti_3SiC_2 from under thin scale. At 1000°C Ti_3SiC_2 was no longer visible in the XRD patterns due to the thickness of the oxide layer. Above 1100°C only TiO_2 was detectable in the scale, and the mass gain increased significantly. Without the protective alumina scale found in aluminium-containing phases, the M element is free to oxidise without self-limiting. During heat cycle testing, Sun *et al.* found that the oxide was well-adhered, and so detected only mass gain through each heat cycle.

A study of the corrosion resistance of select MAX phases in simulated PWR coolant water was undertaken by Ward *et al.* [49]. Small samples of Ti_2AlC, Ti_3AlC_2, Ti_3SiC_2 and Cr_2AlC were subjected to 28 days in an autoclave at 300°C. The flowing water was adjusted with trace amounts of hydrogen, oxygen and lithium to simulate coolant water. Of the four phases tested, only Cr_2AlC exhibited little change, suggesting that the formation of a chromia passivation layer is more important that alumina when water based corrosion is the primary oxidation route. The Ti containing phases were preferentially stripped of their 'A' layer elements, which caused delamination and no passivation layer, ultimately resulting in titanium oxides forming.

Table 2.2.1 summarises the literature on oxidation resistance. Despite poor performance in air at 1300°C, Tallman *et al.* conclude in a review of MAX phase oxidation, Cr_2AlC is excellent up to 1000°C and good up to 1100°C and it oxidises slower than Ti_2AlC at temperatures below 1200°C [58], but the formation of a Cr_7C_3 underlayer is problematic if the surface oxide is ever removed. However, Cr_2AlC

exhibits excellent corrosion resistance in water via the formation of a chromia layer rather than an alumina layer. Anodising of Cr_2AlC to form this scale before testing/use may further improve its resistance.

MAX phase	Environment	Temp (°C)	Exposure time	Oxidation products	Comments	Authors
Cr_2AlC	Air	1000–1300	various	Al_2O_3, Cr_7C_3 underlayer	Excellent resistance in air up to 1000°C, good at 1100°C, intermediate at 1200°C, and poor at 1300°C where void formation in underlayer causes cracking.	Tallman *et al.*[58] Lee *et al.* [59] Lin *et al.*[60]
Cr_2AlC	Air	1300	336 hours	Al_2O_3, Cr_7C_3 underlayer	Void formation in underlayer caused flaking.	Lee *et al.* [51]
Cr_2AlC	Water (simulated coolant)	300	28 days	Cr_2O_3	Formed passivation layer, very little corrosion	Ward *et al.* [49]
Ti_2AlC	Air	900–1400	1 hour	TiO_2, Al_2O_3. Al_2TiO_5 at 1400 °C	After initial TiO_2 formation, quantity remains relatively constant	Cui *et al.* [55]
Ti_2AlC (coating)	Air and water vapour	750	200 hours	TiO_2, Al_2O_3, Al_2TiO_5 (in water), Other oxides from substrate	Cracks in the coating led to increased oxidation and corrosion compared to bulk Ti_2AlC.	Feng *et al.* [56]
Ti_3SiC_2	Air	900–1300	20 hours	TiO_2	Slow to oxidise at 900°C but proceeds rapidly above 1000°C	Sun *et al.* [57]

Table 2.2.1 – Summary of some MAX phase oxidation experiments.

2.2.6 The effects of irradiation

Any potential cladding material must be able to survive the high levels of radiation induced damage present in the core. Fast neutrons are emitted from fission reactions with an average energy of 2MeV in PWRs, which is then 'thermalised' by the moderator and reduced to around 25meV [61]. Cladding in a PWR can be subjected to up to 2 displacements per atom (dpa) per year from collisions with neutrons; for fast reactors the value can be up to 15dpa/year [62].

Several irradiation studies of Ti_3SiC_2, Ti_3AlC_2 and other MAX phases have been undertaken, typically using helium ions to simulate gas evolved by alpha decay or heavy nuclei to simulate fission products, the parameters of which have been summarised in Table 2.2.2. However, only one neutron irradiation

was found to have been performed to date [63] [64]. Therefore further neutron irradiations are required of some of the more novel and potentially more reactor applicable MAX phases (see synthesis section below). Recently, work has been done using proton (hydrogen ion) irradiation to provide a better simulation of neutron irradiation than heavy ions; protons have been shown to effectively mimic neutron damage in the near surface region of the material while reducing the level of activation in the irradiated samples [65]. Thus proton irradiation is a cost effective means of performing screening studies, however neutron irradiation of promising candidates is still required to progress reactor qualification. The following section covers some of the irradiation studies from the literature, however it should be borne in mind that the MAX phases shown below are unlikely to be suitable from a neutronics perspective [66].

MAX phase	**Ions used**	**Fluences (cm^{-2}), Temperature in parentheses**	**Calculated DPA**	**Author**
Ti_3AlC_2	50 keV He	$5x10^{16}$—$6x10^{17}$ (RT)	<31 (SRIM 2008)	Yang *et al.* [67]
	500 keV He	$5x10^{16}$—$1x10^{18}$ (RT, 300°C, 500°C)	<52 (SRIM 2008)	Song *et al.* [68]
	50 keV He	$8x10^{16}$—$1x10^{18}$ (RT)	<52 (SRIM 2010)	Wang *et al.* [69]
	200 keV He	<$2x10^{17}$ (500°C)	<5.5 (SRIM 2008)	Patel *et al.*[70]
Ti_3SiC_2	700 keV C	$8.9x10^{15}$—$1.78x10^{17}$ (120–580°C)	<58	Qi *et al.* [71]
	400 keV Ag^{2+}, 2 MeV Au^{2+}, 1 Mev Cs^{13+}	$2.8x10^{14}$ (600 °C) (Ar) $1x10^{14}$ (-43–600°C) (Au) $5.7x10^{14}$ (400°C) (Cs)	110 (Ar) (SRIM03) 60 (Au) (SRIM03) 240 (Cs) (SRIM03)	Jiang *et al.* [72]
	4 MeV Au, 90 MeV Xe	$1x10^{12}$—$1x10^{15}$ (RT)	None given	Nappé *et al.* [73]
Ti_3SiC_2, Ti_3AlC_2	1 MeV Kr^{2+}, 1 MeV Xe^{2+}	$6.25x10^{15}$(-223°C, 27°C) (Kr) (27°C) (Xe)	25-30 (SRIM 2008)	Whittle *et al.* [74]
	7 MeV Xe^{26+}	$4x10^{14}$–$4x10^{15}$ (RT) , $6x10^{15}$ (600)	<10 (SRIM 2008)	Huang *et al.* [75]
	1.5 MeV H^+	$1.438x10^{14}$ (350°C)	<0.1 (SRIM)	Ward *et al.* [65]
Cr_2AlC, V_2AlC	1 MeV Au^+	$1x10^{14}$–$1x10^{16}$ (RT)	<100 (SRIM 2010)	Wang *et al.* [76]
Ti_3AlC_2 Ti_3SiC_2 Ti_2AlC Ti_2AlN	Neutrons (energy spectrum simulating LWR)	$3.4x10^{20}$ (360°C) $4.8x10^{20}$(695°C)	<0.1	Tallman *et al.*[63] [64]

Table 2.2.2 – Summary of some irradiation studies carried out in the literature

Before any detailed microstructural damage is considered, it is also important to determine the level of neutron absorption activation in the MAX phase that would occur during time spent in the core. The former is the most important as it degrades the economics of the reactor if it is too high and the latter has ramifications for post-reactor storage disposal in the case that the fuel is separated from the clad and reprocessing (if direct disposal of clad spent fuel is performed then activation of the clad is dwarfed by the radioactivity of the irradiated fuel within).

Grove *et al.* conducted some first principles research into potential reactor applicable MAX phases in terms of their neutronics [66]. They simulated the neutron absorption and activation from both thermal and fast neutrons on 23 common MAX phase constituent elements, and bismuth, which has recently been included in Zr_2AlC on the A sites as a stabiliser [38]. The elements were modelled individually due to the lack of data on MAX phase densities, to give a starting point for further testing of specific phases. The models also differentiated between beginning and end of cycle (BoC and EoC) by simulating core neutron fluxes from fresh and burnt-up fuel. For thermal and fast reactors, the optimum phase for neutron transparency is shown to be $Zr_{x+1}PbC_x$ with possible inclusion of Bi on the A site. It should be noted that the high absorption combinations could still have potential applications as MAX phase based control rods. Table 2.2.3 recreates the element ranking by Grove *et al.* for suitability by neutron absorption in potential thermal neutron cladding. The rankings by activation are similar but not identical.

After initial simulations, 5 MAX phases were modelled including structure and density estimates to give a better idea of their neutron absorption. Of these, Zr_2PbC is shown to have the lowest thermal neutron capture cross section, lower than Zircaloy-4 for the same thickness of clad. Bi may also be included but is initially activated to form dangerous Po-210, however Grove *et al.* identify that a cooling time of 2 years after use is long enough to mitigate this.

Hoffman *et al.* also simulated neutron activation from both fast and thermal neutron spectra on Ti_3SiC_2, Ti_3AlC_2 and Ti_2AlC for 10, 30 and 60 years 'in the reactor' and compared the activity with SiC and Inconel Alloy 617 [77] [78]. It was concluded that for the timescales simulated for both neutron spectra, the level of activation of the three MAX phases was comparable to that of SiC, while the specific activity of the Inconel 617 was approximately 1000x higher.

Rank	M	A	X
1	Zr	Bi	C
2	Cr	Pb	N
3	Nb	Si	
4	V	Al	
5	Mo	P	
6	Ti	Sn	
7	Sc	S	
8	Hf	Ge	
9	Ta	Ga	
10		Tl	
11		As	
12		In	
13		Cd	

Table 2.2.3 - Elements found in MAX phases ranked by their suitability for thermal neutron cladding from work done by Grove et al. [66]

Under He ion irradiation at 500°C, Patel *et al.* posit that the Ti_3C_2 planes in Ti_3AlC_2 largely retain their structure while the Al layers become disorganised. A contraction and expansion in the *a* and *c* axes respectively was also observed, along with the presence of He bubbles <1nm in diameter [70]. Yang *et al.* note no amorphisation at all after room temperature He irradiation, but at low displacements per atom (dpa) the material undergoes a phase change to β-Ti_3AlC_2 (A polymorph that can occur in 312 phases, where the A layer is offset within the unit cell with respect to the M_3X_2 layers) along with Ti-Al anti-site defects. At higher dpa levels there is formation of nanosized Ti_3AlC_2 grains [67]. Song *et al.* also note no amorphisation occurs, and that the structure of Ti_3AlC_2 starts to recover at temperatures of 300—500°C [68]. Wang *et al.* focused on the He implantation and bubble growth at room temperature, and found no bubbles at lower fluences. Spherical nanometre sized bubbles appeared with increasing dose, which eventually grew together and formed large defects. They also noted the formation of irregular shaped bubbles at grain boundaries. The irradiated surface was analysed using Atomic Force Microscopy (AFM) and found have blisters, with a radius of 2.21μm and a height of 313nm at the highest fluence [69].

Huang *et al.* used Xe ions to simulate fission product damage in Ti_3AlC_2 [75]. They noted that although also undergoing a phase transition to β-Ti_3AlC_2, there was some recovery in the XRD peak intensity when the irradiation was carried out at 600°C.

Ti_3SiC_2 is an unlikely candidate itself for a reactor core, due to its poor oxidation resistance compared to Ti_2AlC (see Table 2.2.1). Studies that have compared the ion radiation tolerance of Ti_3AlC_2 and Ti_3SiC_2 have observed that Ti_3SiC_2 is less resistant than its aluminium-containing counterpart [74] [75]. However Qi *et al.* report that after its decomposition into TiC induced by C irradiation, the original structure recovers at temperatures at low as 270°C, and above 350°C recovers to slightly damaged Ti_3SiC_2 [71].

Wang *et al.* studied ion induced damage in Cr_2AlC and V_2AlC using 1 MeV gold ions at room temperature [76]. They note that while the structure of V_2AlC becomes a face centred cubic after irradiation, Cr_2AlC totally amorphises, which is not promising for use in the nuclear industry.

A potential problem with MAX phases as fuel cladding was investigated by Jiang *et al.* [72] who compared the diffusion of implanted Ag, Au and Cs ions through Ti_3SiC_2, 3C-SiC (β-SiC) and a composite material of both. Using Ag, Au and Cs ions, the samples were irradiated and annealed at various temperatures and then analysed using Rutherford Backscattering Spectroscopy. It was found that while 3C-SiC trapped the nuclei largely where they embedded, Ti_3SiC_2 tended to accumulate the heavy nuclei on the surface at temperatures between 500—700 °C. This would potentially render these MAX phases unsuitable for high temperature reactor applications due to permeability at high temperatures, but more work needs to be done at PWR/BWR temperatures, and with a wider variety of MAX phases.

Tallman *et al.* have conducted neutron irradiation experiments on Ti_3SiC_2, Ti_3AlC_2, Ti_2AlC and Ti_2AlN [63]. The samples were irradiated under a He-Ne atmosphere at the MIT 6MW research reactor with fluences of $3.4x10^{20}cm^{-2}$ at 360°C and $4.8x10^{20}cm^{-2}$ at 695°C, which corresponds to ~0.1dpa (extrapolated from Monte Carlo simulations on SiC). After irradiation all the carbon-containing phases increased in TiC content, and Ti_2AlN exhibited the formation of Ti_4AlN_3. The room temperature resistivity of the samples increased after irradiation at 360°C, the largest increase of which was for Ti_3AlC_2 (0.262μΩm up to 2.84μΩm), but at 695°C the increase was greatly reduced, again suggesting good high temperature dynamic recovery of MAX phases. Tallman *et al.* suggest that the two 312 phases were the best candidates to resist neutron irradiation.

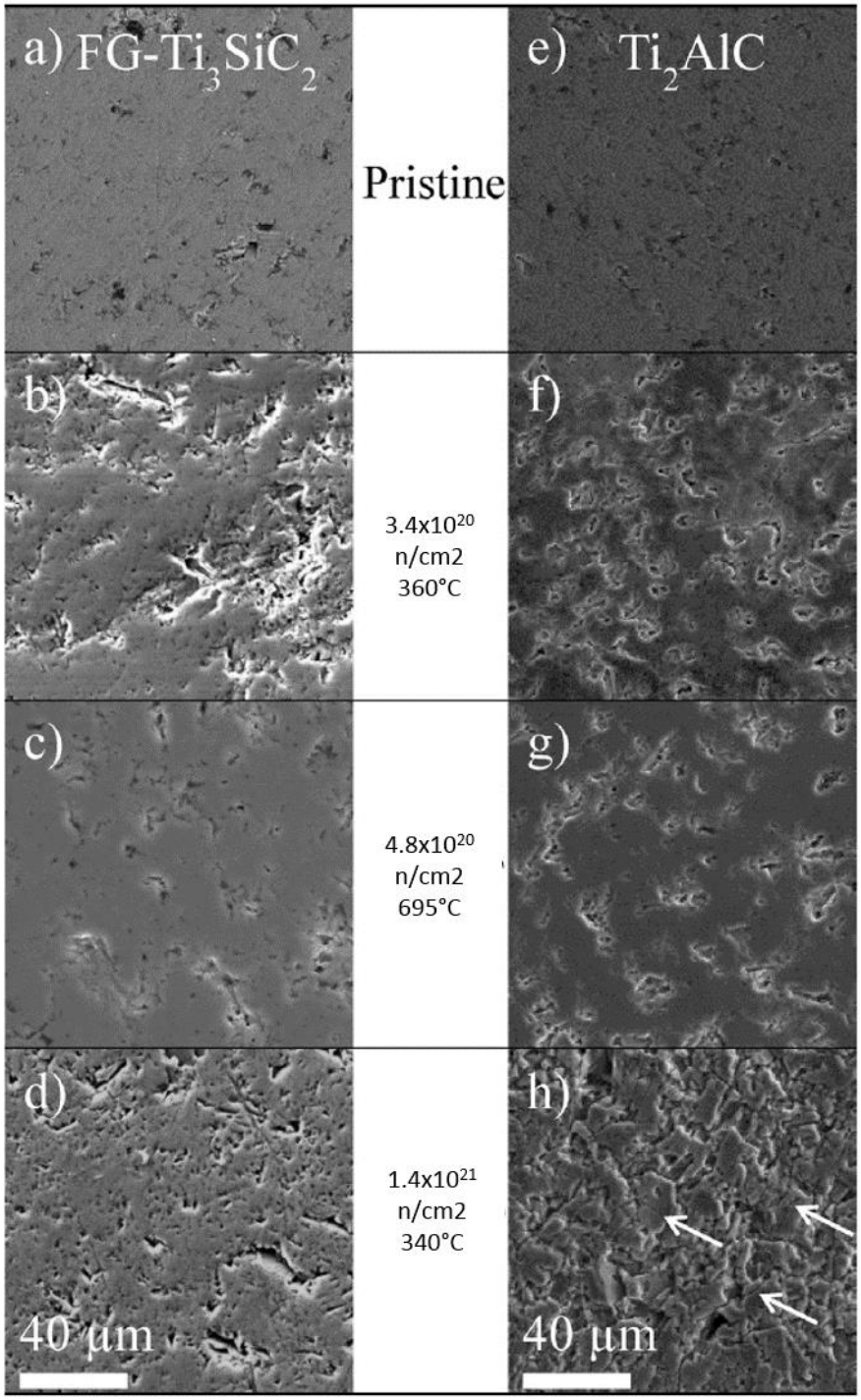

Fig.2.2.4- SEM images of surface damage due to irradiation on fine-grain Ti_3SiC_2 and Ti_2AlC [64]. *Arrows indicate microcracks.*

Following up on this work, Tallman *et al.* report on defects formed in Ti_3SiC_2 and Ti_2AlC as a result of the neutron irradiation covered previously [64]. They found that the density of dislocation loops formed in Ti_3SiC_2 ($3x10^{21}$ loops/m^3) were much lower than in Ti_2AlC ($1x10^{23}$ loops/m^3). Microcracks were also observed on the surface of Ti_2AlC that were present to a lesser degree on the Ti_3SiC_2 samples

(see Fig.2.2.4). They also note that the damage to the ancillary phases Al_2O_3 and TiC was far greater than that in the MAX phases, which Tallman *et al.* attribute to the A-layer absorbing more damage.

The first use of protons to irradiate MAX phases was carried out by Ward *et al.* [65]. They note that irradiated Ti_3SiC_2 and Ti_3AlC_2 breaks down into TiC, alongside initial changes to the unit cell and the formation of antisite defects. They conclude that proton irradiation is an acceptable surrogate for neutron irradiation, and that the damage is higher in Ti_3AlC_2 than Ti_3SiC_2 for a given irradiation period.

Zapata-Solvas *et al.* performed Density Functional Theory (DFT) calculation to simulate radiation damage (specifically Frenkel defect formation) in Zr_3AlC_2, Zr_3SiC_2, Ti_3AlC_2 and Ti_3SiC_2 [79]. They calculated that the energy to form defects is higher in the Al-containing phases, and conclude that these phases are more radiation tolerant than their Si-containing counterparts.

Overall, the prevailing consensus is that while a number MAX phases perform well at fast reactor irradiation temperatures (>500°C), finding ones that perform well at LWR irradiation temperatures (~300°C) is proving much more challenging, though studies are ongoing.

2.2.7 Synthesis

MAX phases can be synthesised through a number of different processes. Jeitschko, Nowotny and Benesovsky initially used vapour deposition yielding thin films [27], but since then many techniques have arisen to give film, bulk or powder samples of varying purity. Pietzka and Schuster first used pressureless sintering to make Ti_2AlC and their new discovery Ti_3AlC_2 [28]. Barsoum and his group originally used reactive hot pressing to synthesise their first bulk samples of Ti_3SiC_2 [80]. Barsoum and El-Raghy also synthesised the phase through the use of Hot Isostatic Pressing (HIP), which resulted in a purer phase. As noted previously, it was Barsoum and El-Raghy's paper that also shed light on some of the remarkable properties of Ti_3SiC_2, including its resistance to thermal shock, its high degree of machinability and its combined high thermal and electrical conductivity. The following section will cover the most common methods for MAX phase synthesis, along with some more novel approaches such as Spark Plasma Sintering (SPS). It should be noted that in addition to synthesis, methods such as hot pressing, HIP and SPS are also able to densify MAX phases into small components of simple geometry. This aspect is not discussed further in detail in the Shape Forming section as they are not foreseen to be capable of producing the required geometry for a long cladding tube.

Hot Pressing (uniaxial) and HIP

Hot pressing is a common technique for densification of ceramic pellets: powder is compressed uniaxially within a die and then heated under compression by a surrounding furnace. HIP by comparison sees powder loaded into sealed canisters, compressed by a high pressure gas and heated. Both typically yield high density samples which can then be used in experiments to measure the material properties.

As mentioned briefly above, Barsoum and El-Raghy first used hot pressing and HIP to manufacture polycrystalline samples of Ti_3SiC_2 [80]. Using a stoichiometric mix of Ti, SiC and C powders, the pellets were cold-pressed at 180MPa and then hot pressed at 1600°C at 40MPa for 4 hours. The resulting pellet was shown to contain <2% vol. ancillary phases (SiC and TiC_x) and was almost completely dense. The impurities were reduced when the powder was HIPed to below 1%; Barsoum and El-Raghy attribute this to excess carbon transferring from the graphite hot press dies. Access to a bulk sample allowed Barsoum and El-Raghy to measure some of the unusual properties of the material (covered above) and sparked scientific interest in the material.

Ti_3SiC_2 was also synthesised via hot pressing by Hwang *et al.* who tested the 'machinability' of dense MAX phase as compared to SM45C steel [48]. Substoichiometric TiC_x (x=0.67) was first synthesised and then combined with Si. The powder was hot pressed under 25MPa and flowing argon for 90 minutes at 1360°C and 1420°C. At the lower temperature, some TiC remained, but the pellet was single phase at 1420°C. The average grain sizes were 3.58µm (dubbed SG for small grain) and 11.49µm (BG for big grain) respectively.

Ti_2AlC has also been successfully synthesised via hot pressing by Wang *et al.* from starting powders of TiC, Ti, Al and activated carbon [81]. A stoichiometric mixture was hot pressed at 1300—1500°C and held for 60 minutes under 30MPa and flowing argon. From XRD analysis, at 1300°C Ti_2AlC is the main phase (alongside TiC and Ti-Al compounds), which becomes the single phase at 1400—1450°C. At 1500°C the formation of Ti_3AlC_2 starts to be favoured. The 1400°C sample was analysed under SEM, which showed the average grain size was 15µm. Wang *et al.* postulate the reaction pathway via hot pressing to be the initial formation of TiC and Ti-Al intermetallic compounds, which then react to form the product Ti_2AlC.

The synthesis of Cr_2AlC through hot pressing was investigated by Tian *et al.* [43]. Starting with stoichiometric elemental powders, the samples were hot pressed at 1400°C for 60 minutes under 20MPa in flowing argon. After XRD analysis it was determined that Cr_2AlC was the main phase, alongside some Cr_7C_3 and a very small quantity of unidentified phase. The properties they measured are covered in a previous section. Further to this Tian *et al.* synthesised Cr_2AlC via hot pressing (using

the previous parameters) as a comparison for Cr_2AlC synthesised via spark plasma sintering (see below) [82].

The novel phase Zr_3AlC_2 was achieved using hot pressing by Lapauw *et al.* [83] Zr-containing MAX phases are sought after due to the low thermal neutron capture cross section of zirconium atoms. Lapauw *et al.* attempted to synthesis a 413 MAX phase; although Zr_3AlC_2 had been predicted by DFT calculations [84], attempts to synthesise it had previously been unsuccessful. ZrH_2, Al and C powders were mixed in the ratio 4:1.25:2.6 respectively and hot pressed at 1500°C for 30 minutes at 20MPa. The resulting pellet was found to contain roughly 60% Zr_3AlC_2 alongside ZrC and $ZrAl_2$. Lapauw *et al.* were also successful in synthesising the 211 phase as well [85], hot pressing at a temperature of 1525°C for 30 minutes with an altered stoichiometry. ZrC is also formed alongside the product phase.

Solid solution MAX phases have also been investigated and synthesised with hot pressing. Lapauw *et al.* determined that Zr could be substituted into Nb_4AlC_3 on the M sites [86]. $NbH_{0.89}$ was synthesised and then combined with ZrH_2, Al and graphite in the ratio of 4:1.25:2.6 for the total M, A and X components. The ratio of Nb to Zr was varied from 100:0 to 50:50. Powders were pressed in graphite crucibles and hot pressed at 1700°C for 30 minutes under 20MPa in a vacuum. The resulting pellets were analysed with XRD and EPMA and the solid solution phase $(Nb_xZr_{1-x})_4AlC_3$ was stable up to x=0.8, which agreed with DFT calculations that put the maximum solubility of Zr into the Nb sites was 18.5%. The mechanical properties of $(Nb_xZr_{1-x})_4AlC_3$ where x=0.85 were tested and compared to pure Nb_4AlC_3: the Vickers hardness, Young's modulus and 4-point bend tests yielded very similar results, but the solid solution had a higher fracture toughness than the pure material (10.1MPa.$m^{-1/2}$ and 6.1MPa.$m^{-1/2}$) which Lapauw *et al.* partially attribute to the larger grain size.

Liu *et al.* investigated the solid solutions with the Ti-Cr-Al-C system [87], by hot pressing combinations of elemental powders at 1500°C for 60 minutes under 30MPa and flowing argon. The stoichiometry was changed to attempt synthesising both a 312 phase and a 413 phase. Of the myriad combinations, Liu *et al.* determined that both the phases $(Cr_{2/3}Ti_{1/3})_3AlC_2$ and $(Cr_{5/8}Ti_{3/8})_4AlC_3$ are viable solid solutions.

Zapata-Solvas *et al.* utilised hot pressing to synthesise $(Zr_{1-x},Ti_x)_3AlC_2$ at 1450°C [88], using a dwell time of 1 hour and uniaxial pressure of 30 MPa. Several ratios of Zr to Ti were targeted, and using a reactant ratio of 5:1 for Zr and Ti yielded a sample that was 94wt.% $(Zr_{1-x},Ti_x)_3AlC_2$, x=0.15, with TiC as the only ancillary phase. Density functional theory was used to calculate the lattice parameters, and they were found to conform to Vegard's law. Zapata-Solvas *et al.* also reported on the synthesis of $Zr_3(Al_{1-x}Si_x)C_2$ by hot pressing samples a 1500°C for 1 hour under argon atmosphere [88]. They found that for a value of x<0.1 the samples contained up to 59wt.% of the quaternary MAX phase. They also performed simulations on its radiation tolerance (see section 2.2.6).

Recently a pure hybrid MAX phase with substitutions on both the M and the A sites was synthesised via hot pressing by Lapauw *et al.*, namely $(Zr_{0.8}, Nb_{0.2})_2(Al_{0.5}, Sn_{0.5})C$ [89]. The samples were hot pressed under 30MPa with a 60 minute dwell time, at temperatures of 1250–1600°C and show no ancillary phases. The addition of Nb and Sn were shown to reduce distortion that occurs in Zr_2AlC leading to a more complete synthesis. This research is particularly promising for MAX phases in the nuclear industry, not only because $(Zr_{0.8}, Nb_{0.2})_2(Al_{0.5}, Sn_{0.5})C$ is high in zirconium (and so may be appropriate for a cladding material) but also as a potential method for stabilising and synthesising new potential cladding candidates.

The recent discovery of hybrid MAX phases exhibiting order with respect to the hybrid elements both in-plane and out of plane, dubbed i-MAX and o-MAX phases respectively was reported on by Dahlqvist *et al.* [90], who report on the ordering in $(V_{2/3}Zr_{1/3})_2AlC$ and $(Mo_{2/3}Y_{1/3})_2AlC$. This also represents the first yttrium containing MAX phase, and opens the door for the inclusion of new elements and increasing the potential for a suitable MAX phases. Chen *et al.* also explore i-MAX phases, with the synthesis via. hot pressing [91] of $(Cr_{2/3}Zr_{1/3})_2AlC$ (~85% pure). This latter is particularly interesting since compared to Cr_2AlC, a third of the chromium is displaced by zirconium, which would potentially reduce neutron absorption and the ordering could act to resist irradiation amorphisation (see Section 2.2.6), while the phase likely still containing enough chromium to give high corrosion resistance (see Section 2.2.5). These hypotheses however have yet to be tested and higher purity is likely to be required if they are to be proved valid.

Spark Plasma Sintering (SPS)

A popular method of MAX phase synthesis is through the use of a Spark Plasma Sintering (SPS) furnace. SPS, sometimes referred to as Pulsed Electric Current Sintering (PECS) or Pulsed Discharge Sintering (PDS) or Field Assisted Sintering Technique (FAST) is a process of densification in which powder is loaded into a graphite die with punches (Fig. 2.2.5) These dies are placed in a chamber that is evacuated or filled with argon and placed under a uniaxial load, while a pulsed high current is passed through the die and powders (if they are conductive) or through the die (if the powder is insulating). Through a combination of Joule heating and micro-arcs/welds [92] between the powder particles, a high density single phase pellet can be produced. Heating rates are typically high (~100°C/min) and typical dwell times are around 10 minutes [93].

Most of the work done on SPS synthesis of MAX phases has been on Ti_3SiC_2 or the two Ti-Al-C phases (211 and 312). One of the first papers on the subject was published in 2002 by *Gao et al.* [94]. They started with a stoichiometric mixture of Ti, Si and TiC powders, which were mixed and sintered at

temperatures of 1125—1400°C and uniaxial pressures of 20—60MPa under vacuum. High purity dense samples were obtained, which it was theorised was due to a Ti-Si liquid phase forming during the process, aiding diffusion and the formation of plasma in the voids and spaces between particles. However, it has been shown that SPS generates neither sparks nor plasma, which has led to the adoption of PECS, PDS or FAST to describe the process.

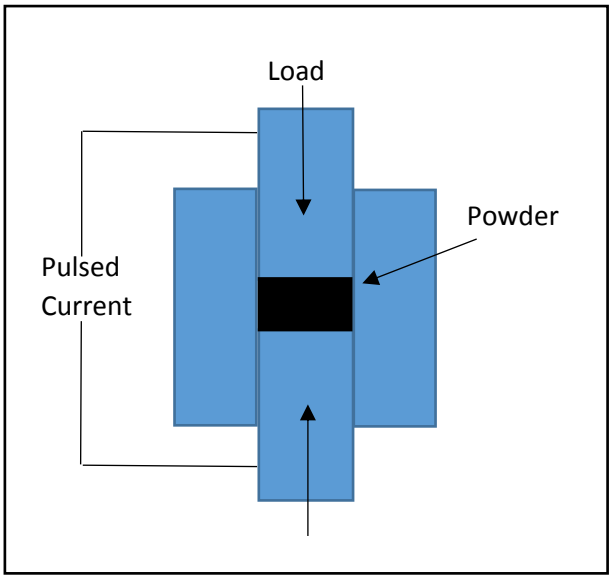

Fig. 2.2.5 – Schematic of Spark Plasma Sintering furnace

SPS synthesis of Ti_3AlC_2 was first achieved by Zhou *et al.* [95]. The phase having been originally discovered by Pietzka and Schuster [28] through pressureless sintering. Zhou *et al.* had also previously synthesised the phase using Self-propagating High-temperature Synthesis (SHS, see section below). This SHS product was crushed and sintered using SPS, and compared to a reactive SPS from elemental powders. A sample made in a hot press was used for comparison. It was found that both reactive SPS and SPS of SHS powder gave dense high purity samples. However the reactive SPS resulted in a textured sample, where the long plate like grains of Ti_3AlC_2 were aligned perpendicular to the applied current and load. Zhou *et al.* hypothesised this occurred as small crystallites of MAX phase were formed early in the synthesis reaction. These small crystallites align easily and act as nucleation points, growing into larger oriented grains. However in their SHS-SPS process, the large crystals of Ti_3AlC_2 were already formed, and so could not reorient easily.

The effect of aluminium on the formation of Ti_3SiC_2 by SPS was investigated by Zhu *et al.* They sintered several samples: a stoichiometric sample, one with excess silicon, and one with added aluminium [96]. The excess silicon was added due to its tendency to evaporate leading to formation of TiC [97]. A spike in the pressure of the chamber was noted in the aluminium-containing sample. This indicated a gas

release at this point due to the aluminium catalyst. TiC was formed in the stoichiometric sample, but this was reduced in the sample with excess silicon. Zhu *et al.* reported no impurities to their aluminium-containing sample. However, as Ti_3SiC_2 and Ti_3AlC_2 are isostructural, it is possible that their sample was a mix of the two, and that XRD used to characterise the samples was unable to differentiate between them.

Zhu *et al.* confirmed the previous results, and investigated the effect of silicon catalysis in the formation of Ti_3AlC_2 [98]. They followed the previous work by using the samestoichiometry and procedure. Zhu *et al.* reported pure Ti_3SiC_2 in samples sintered at 1250—1300°C, and pure Ti_3AlC_2 at 1200—1250°C, however TiC was present in the sample sintered at 1300°C, possibly due to thermal decomposition of the product. The pellet density was measured and found to be approximately 99% of the theoretical density, indicating that SPS can be a successful method of densification.

Liang *et al.* studied the effect of a prior mechanical alloying step before SPS, and also tested the addition of aluminium powder to their Ti_3SiC_2 synthesis [99]. Mechanical alloying uses a high energy ball mill for a long period of time to repeatedly crush reactants together which then partially combine chemically. Liang *et al.* used a stoichiometric ratio of elemental powders, along with small additions of aluminium (Ti:Si:C:Al 3:1:2:x where x is 0, 0.1, 0.2 or 0.3), which were milled at 300rpm for 10 hours under argon gas. Following the mechanical alloying step, XRD revealed the most abundant phase was TiC, although some Ti_3SiC_2 and $TiSi_2$ had also formed. After SPS at 1100°C for 10 minutes at 30MPa, the sample containing no aluminium was largely still TiC, while aluminium produced high purity Ti_3SiC_2. Liang *et al.* hypothesise that a small amount of Al helps retard the formation of TiC during the mechanical alloying stage, as the relative abundance of the Ti_3SiC_2 was higher with x=0.1 aluminium. Higher levels of aluminium resulted in less product formation. Abderrazak *et al.* also studied the effects of mechanical alloying as a pre-step to SPS [100], but from Ti, SiC and C powders. However, they did not use aluminium as a sintering aid, and found that the unalloyed sample that was sintered at 1300°C for 20 minutes at 64MPa had a much higher abundance of Ti_3SiC_2 than the sample which underwent mechanical alloying.

Other MAX phases have also been synthesized through SPS. Tian *et al.* synthesised Cr_2AlC from elemental powders [82]. They also compared the reaction between coarse and fine starting powders. Samples were sintered with a 5 minute dwell time, and compared to samples made in a hot press at 1400°C for 1 hour. XRD of samples revealed Cr_2AlC to be the main phase in the coarse powdered samples sintered between 1250—1400°C, along with small impurity phases of Cr_3C_7 and Cr-Al alloy. The fine powder samples resulted in a similar composition, with marked decreases in the impurity

phases and fewer surface pores. Samples were largely identical in composition to those synthesised in the hot press.

Tian *et al.* also looked at Cr_2AlC synthesis starting with Al_4C_3 to compare results with their previous studies. Starting with the same molar ratio as before, Tian *et al.* sintered Cr, Al_4C_3 and graphite powders with SPS for 15 minutes between 850—1350°C [101]. Below 1000°C the samples did not react, but within the temperature region of 1150—1350°C Cr_2AlC was the main product formed, along with some small amounts of Cr_7C_3. Previous work with elemental powder synthesis had revealed that most of the reaction took place between 850—1050°C, which was not the case with this study. Tian *et al.* hypothesise that the previous lower temperature reactions involved aluminium melting and mixing with chromium, giving a liquid medium for the reaction to take place. Using aluminium carbide removed this liquid phase.

Synthesis of gallium containing MAX phases has also been achieved through SPS. Sun *et al.* synthesised both Ti_2GaC and Cr_2GaC from stoichiometric ratios of elemental powders [93]. Both compositions were heated in crucibles under vacuum to 1000°C, the sintered bodies were then crushed and milled and loaded into an SPS furnace. They were sintered at 1200°C with a soak time of 20 minutes resulting in two predominantly single phase samples, close to the theoretical density. Vickers hardness was measured, and Cr_2GaC was found to have H_V of 1.4GPa, which is soft, even for MAX phases. However the usefulness of these phases in nuclear reactors is doubtful, due to spontaneous ejection of gallium from Cr_2GaC. Under SEM gallium whiskers can be seen self-extruding from the basal planes of grains. This points to gallium (possibly due to its very low melting temperature) forming only metastable phases.

Textured samples can be achieved through SPS. Mizuno *et al.* first synthesised Ti_3AlC_2 from a reactive SPS procedure from elemental powders, which were sintered at temperatures between 1300—1500°C [102]. The pellets were then crushed, milled, and sieved to give a powder of plate-like grains. This was then sintered by SPS and the textured pellets anisotropic properties were measured. One side of the pellet was polished flat in addition to the two faces to allow accurate measurement. XRD of the two surfaces showed an orientation, which was quantified using the Lotgering orientation factor, based on XRD peak heights. The factor was found to be 0.69 for the sample, where 0 is unoriented and 1 is fully oriented. Vickers hardness measurements show an anisotropy between top and side, being 5.9 and 7GPa respectively. These values of Vickers hardness are higher than other previously reported values for hardness for Ti_3AlC_2 [26], which is theorised to be due to the high orientation of the sample.

Grain orientation through SPS was reported by Hu *et al.* [103] starting with commercially available Ti_3SiC_2, which was milled and mixed in a slurry of 20%wt. powder in distilled water with

polyethyleneimine (PEI) as a dispersant (1.5%) [104]. This mixture was then slip-cast into glass tubes standing on plaster and a fine filter paper. This allowed a 20mm dia. green body to develop on the filter paper, ready for SPS. During the slip-casting, a 12T magnetic field was applied across the tubes to align the grains with the c-axis of their unit cells perpendicular to the field. After drying, the green bodies were cold isostatic pressed (CIP) and placed in an SPS furnace at 1100°C with a 10 minute soak time. This resulted in a textured pellet of ceramic, with a Lotgering orientation factor of 0.95 on the side parallel to the applied field, and 0.31 on the perpendicular face. This method has also been used to cast and sinter textured pellets of Nb_4AlC_3 [105]and Ti_3AlC_2 [104] with similar results.

Self-propagating High-temperature Synthesis

Another method of synthesis is 'Self propagating High temperature Synthesis' (SHS). A reaction is initiated in the mixture of powdered reactants, which is exothermic such that it sustains itself and propagates through the sample. The synthesis is typically over in several seconds, and results in a porous product which must then be crushed and sintered. The product often contains impurity phases such as TiC in the formation of Ti_3SiC_2 and Ti_3AlC_2 [106]. Hendaoui *et al.* worked on reducing impurities by facilitating fast cooling of the samples after the reaction. Starting with a stoichiometric composition of Ti, Al and C powders, which were milled and pressed, these pellets were installed in steel sample holders in such a way that enough heat could escape the sample to halt the reaction. This 'quenching' resulted in one end being untouched by the SHS process while the SHS went to completion at the other end, and there was a middle region where the reaction had started but did not propagate. XRD showed large quantities of $TiAl_3$ near the outer regions of the pellet (where it was in contact with the holders) which is then replaced with Ti_3Al and Ti_3AlC_2 along the pellet. Hendaoui *et al.* suggest that SHS is therefore a reaction between $TiAl_3$ (formed as an intermediate), Ti, and C. They also posit that rapid cooling and therefore smaller samples are the key to attaining high purity, though of course smaller batches are less suitable for industrial scale-up – hence in common with production of many materials there is likely to be a trade-off between purity and batch size.

Khoptiar and Gotman attempted to remove the need for sintering after SHS by reaction under pressure [107]. A stoichiometric mix of elemental powders was separated into several experiments. The first was compacted into an Inconel 718 (a Ni-Cr-Mo based alloy [108]) and topped with TiO_2-Al-Mg powder to act as an initiating source. Another sample was cold pressed into a cuboid and placed in a furnace at temperature to initiate the reaction. The last two samples were cold pressed and placed between press rams: one unconstrained at the edges and another in an Inconel tube. Thermocouples placed in holes in the samples recorded the temperature.

Optimising the SHS process for the production of Ti_3SiC_2 was studied by El-Saeed *et al.* [109]. They compared several starting compositions for both SHS and pressureless sintering under flowing argon. A custom-built chamber with flowing argon was used, with the initiating source being a carbon electrode across the top of the sample. The samples undergoing pressureless sintering were placed in furnaces at 1500°C for 4 hours. The samples were then analysed using XRD. Comparing the SHS results, it was found that the highest concentration of Ti_3SiC_2 (88%) was formed from Ti, SiC and C with 20% excess Si. All of the SHS reactions produced ancillary phases, and pellets containing TiC could not be initiated. It was theorised that TiC takes too long to react and the SHS propagation stops. For comparison, the furnace sample generally had higher purities. Several of the compositions yielded ~100% pure samples: Ti+Si+C, Ti+TiC+Si, and Ti+SiC+C, each with 30% excess silicon. 50% excess silicon yielded large quantities of $TiSi_2$ not present in other samples. They concluded that although SHS is far quicker than other methods, the yields of MAX phase are typically too low.

Molten Salt Synthesis

A common method for synthesis of ceramic powders is Molten Salt Synthesis (MSS). It is similar to pressureless sintering, where reactant powders are initially cold pressed and then heated in a furnace to 'reaction sinter' a dense product. However a large amount of a salt with a low melting point is added to the initial mix of powders (usually around 1:1 [110]). The reactant/salt pellet is then heated above the melting point of the salt which forms a flux, dissolving the powders and increasing diffusion. The resulting pellet is then crushed and washed of salt, leaving only product powders which can then be milled and sintered. Powder morphology can often be controlled by time, temperature and type and concentration of salt.

The correct ratio of salt to powder is imperative to achieving high purity products. Too little salt lessens the effect of a flux, while too much can lead to liquid salt escaping from the pellet, removing reactants and some flux from the reaction. Typical furnace temperatures are 800—1100°C for times of 30—60 minutes. The corrosive nature of molten salts is beneficial in this context, as it strips material off of the reactant powders, allowing them to form new products, which can then precipitate out of solution. Despite MSS being a well-established method for the production of ceramic powders, relatively little research has been done into the synthesis of MAX phases through MSS.

Tian *et al.* were the first to synthesize MAX phases (Cr_2AlC) using molten salt synthesis [111]. Cr, Al and C powders were milled along with NaCl and KCl for 8 hours in ethanol and then dried. The powders were then pressed and heated in an alumina crucible under vacuum between 900—1200°C for 1 hour. Two compositions were used, one with excess aluminium, and they were mixed with salt in differing

ratios. The resulting powders, washed of salt were analysed by XRD and SEM. The optimum composition had extra aluminium, with twice the amount of salt as powder, synthesised at 1000°C. Tian *et al.* suggested that the excess aluminium, which would be liquid at the temperatures used, increased the reaction rate by adding extra flux to the pellet. It was also found that having a larger liquid phase (salt content) resulted in larger crystals of Cr_2AlC forming. Small amounts of Cr_7C_3 and Cr_2Al were detected. The powders were then hot pressed to determine stability and how well they densified. The pellets were similar in composition to the powder, suggesting stability. However the surfaces of the pellets were slightly porous, which Tian *et al.* believed was due to the large particle size (~5µm), so a milling step may be required to reduce the particle size.

Guo *et al.* attempted the synthesis of Ti_3SiC_2 using the molten salt method [112]. Elemental powders with 20% excess silicon were milled with NaCl. These were milled, dried, pressed, and then sintered in alumina crucibles between 1000—1300°C under flowing argon and held for 2 hours. Samples sintered without salt had very weak peaks corresponding to Ti_3SiC_2. Strong peaks were observed in the samples with salt, with the optimum parameters being 1:1 powder: salt at a temperature of 1200°C. It was found that the percentage of Ti_3SiC_2 formed dropped off sharply with more salt than the 1:1 ratio. The plate-like grains were observed by SEM and found to be around 1—2µm in length (Fig. 2.2.6).

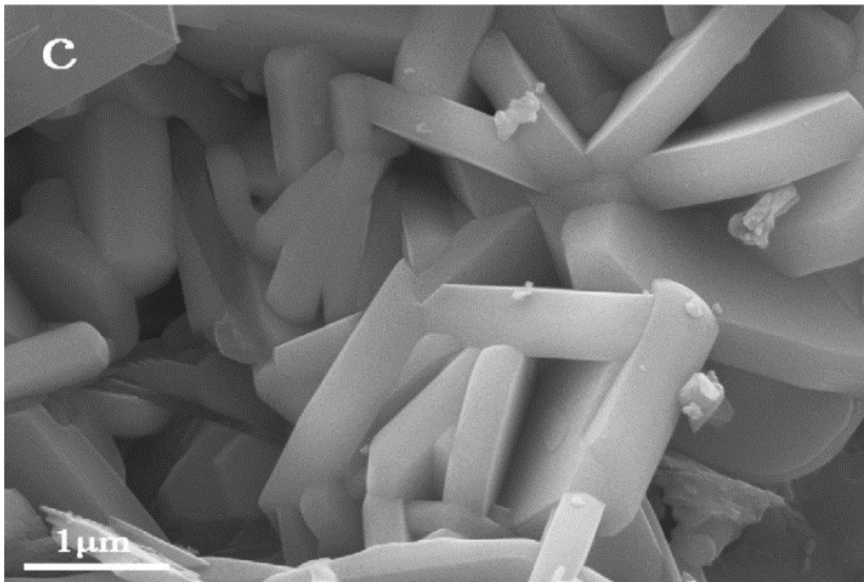

Fig. 2.2.5 – Ti_3SiC_2 grains synthesised via the molten salt method by Guo et al.

Other Methods

A novel method worth noting here is the use of a high powered laser to rapidly synthesis Ti_3AlC_2 by Chen *et al.* [113]. From a ground mixture of Ti, Al and TiC powders (in a ratio of 1:1.2:2), they heated batches of the starting powder with a 5 kW CO_2 laser for durations of 15—60 seconds in a custom built laser furnace. It was found through XRD analysis that after 20 seconds Ti_3AlC_2 was the main phase present alongside TiC and Ti_2AlC. Longer periods of heating resulted in less target phase and more ancillaries, although the relationship with time and purity was not linear. Using SEM, Chen *et al.* discovered a small amount of TiAl that was not detected with XRD analysis. The average grain width of Ti_3AlC_2 was determined to be 1µm after 20 seconds, and 2µm after 60 seconds.

Summary

Based on the above literature, SHS is unlikely to be useful for synthesis of MAX phases for nuclear applications, due to small samples being preferential, and due to the high ancillary phase content. While SPS has been shown to produce high purity samples, hot pressing still represents the best option. It is one of the most extensively studied methods, and based on its success in synthesising Zr-containing and hybrid MAX phases, it is currently considered the most appropriate method for production of MAX phases for nuclear applications.

2.2.8 *Coating deposition*

Shape-forming techniques are crucial to transferring the desirable properties of a bulk material to a form suitable for industrial application. In this case, protective MAX phase layers may be applied to the outside of existing cladding tubes to provide extra resistance against oxidation. Note that, several of the coating methods discussed below may not be suitable for evenly coating cylindrical geometries (i.e. zirconium alloy-clad fuel rods), but have been included for comparison as they are well-established techniques.

Physical Vapour Deposition (PVD)

PVD involves vaporisation of a target and allowing the vapour to condense on a substrate, which differs from chemical vapour deposition (CVD) in that the target is made of the coating material, whereas in CVD the coating material is made on the substrate via reaction of deposited precursors.

Pulsed Laser Deposition (PLD) uses a laser to vaporise a target material in a chamber, ablated particles of which deposit onto a nearby substrate. Hu *et al.* used this technique to coat silicon substrate with

Ti_3SiC_2 thin films [114]. The target material was a hot-pressed pellet of Ti_3SiC_2, and was vaporised by a 248nm laser, pulsed for 20ns from 1—50Hz. Hu *et al.* report coating thicknesses of 250—500nm, with substrate temperatures of only 100°C and 300°C. Through XRD analysis they determine the coating to be highly oriented Ti_3SiC_2, with only the 008 and 102 peaks visible at 100 °C and 300 °C respectively. However, Bultmann *et al.* call into question the analysis by Hu *et al.* [115] arguing that their XRD patterns could be explained as TiC with some silicon substitution on the C sites.

Walter *et al.* explored magnetron sputtering as a possible method to coat steel with Cr_2AlC on a scale suitable for industry, while using a single MAX phase target [116]. Silicon substrates were used for coating when the substrate temperature was below ~530°C, otherwise aluminium was used, alongside an unspecified grade of stainless steel. The deposition time used was 10 minutes using a power density of 5.5W/cm^2, which resulted in a coating ~500nm thick. In the tested substrate temperature range of 450—850°C the deposited coating was crystalline; below this range the coating was amorphous. For the sample coated with a substrate temperature of 850°C, XRD analysis shows the coating is greater than 95% Cr_2AlC, and for the stated temperature range the proportion of MAX phase remains above 90%. Finally, a steel sample was coated for 20 minutes at 500°C, and compared the XRD of the uncoated substrate to the back of the coated substrate. They found no difference in the structure of steel.

Electrophoretic Deposition (EPD)

Electrophoretic Deposition (EPD) is a well-established industrial coating technique, used because it allows even deposition on complex geometries, and it can be performed relatively inexpensively in a range of liquid media (including water) [117]. A schematic is shown in fig. 2.2.7.

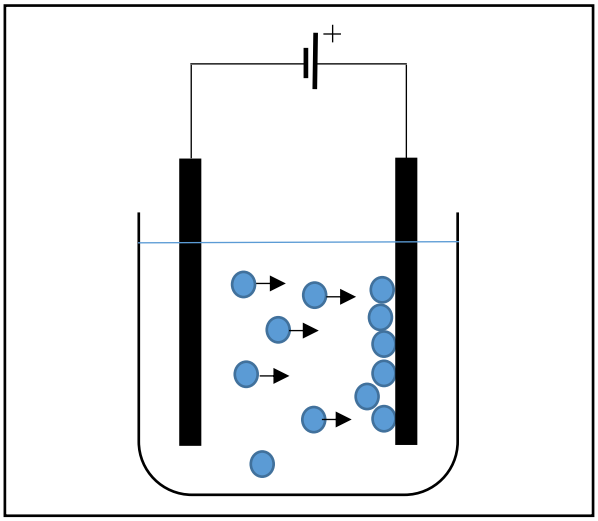

Fig. 2.2.7 – Schematic representation of EPD

A liquid containing a suspension of small particles is known as a colloid. In order for colloids to be stable, the individual particles must repel one another in the medium, otherwise particles can agglomerate into larger bodies which can then separate out under gravity [118]. This particle repulsion is governed by a property called the Zeta potential. Particles in suspension exhibit an electrostatic surface charge, which in turn attracts a surrounding layer of ions of the opposite charge. These ions then also attract a layer of oppositely charged ions (same charge as particle). This tightly bound layer is known as the electrical Double Layer (DL) and will remain around a particle as it moves [119]. Beyond the double layer, the surrounding ions are less tightly bound and will not necessarily move as the particle does. This boundary is called the slipping layer, and it is at this point where the zeta potential is measured. Zeta potential is not an innate quality of a particle, as it varies with the suspension pH. Typically making a medium more alkaline lowers the Zeta potential (which can be negative), and acidity raises it. A large Zeta potential (positive or negative) is required to form a stable colloid, as the electrostatic repulsion is greater than any attractive forces. There exists a pH which reduces the Zeta potential to zero, which means the colloid is at its least stable and will likely separate. This pH is referred to as the Isoelectric Point (IEP) [120].

Electrophoresis is a phenomenon in which charged particles will move towards oppositely charged electrodes when an electric field is present. Particle velocity is governed by Henry's formula, given by:

$$U_e = \frac{2\varepsilon\varepsilon_0\zeta f(\kappa\alpha)}{3\eta} \quad (2.2.1)$$

Where U_e is the electrophoretic mobility , ε is the dielectric constant of the liquid, ε_0 is the vacuum permittivity, ζ is the zeta potential, $f(\kappa\alpha)$ is called Henry's function, and η is the liquid viscosity [121]. Henry's function is the ratio of the particle diameter (α) to the thickness of the electrical double layer (κ) and can be approximated as 1.5 for a polar liquid such as water (Smoluchowski approximation). Multiplying the mobility by the applied field strength will give the particle velocity.

EPD is an application of electrophoresis whereby one of the electrodes used is the body to be coated. A suspension of coating is prepared in a solvent by adjusting the pH and with the possible aid of a dispersant (to improve colloid stability). An applied voltage causes electrophoresis and the particles move towards and deposit themselves on the electrode. Anodic deposition requires negatively charged particles, while cathodic deposition requires positive surface charges. When the process is finished the electrode is removed and left to dry before densification can take place.

Liang *et al.* used EPD to coat indium tin oxide glass with $Ti_3Si_{0.95}(Al_{0.05})C_2$ particles [122]. The MAX phase powder was milled down to an average particle size of 3.3µm. The Zeta potential of the powder in water was measured over a range of pH values, and it was determined that $Ti_3Si(Al)C_2$ has a negative

surface charge over most of the pH range, and the maximum absolute Zeta potential occurs at around pH 9. A solution of 1vol.% of the powder in water was made at pH 9 (adjusted with NaOH and HCl) by stirring and sonicating of the mixture to form a colloid. The mixture remained stable for around 2 hours, which was time enough to complete the deposition. The cathode (platinum mesh) and anode (ITO glass) were placed in the colloid 1cm apart and 3V was put across them for time between 1—10 minutes. The resulting green deposits were left to dry and then characterised with XRD and SEM. The results showed the initial deposits (when deposition time was short) had a preferred orientation, which decreased as deposition times increased. The Lotgering orientation factor for 2 minutes of deposition was 0.76, while by 10 minutes the factor had dropped to 0.67. A coating 10µm thick was obtained by partially drying the deposit and repeating the EPD process three times.

Mishra *et al.* have kept the orientation of the grains high throughout the deposit by conducting the deposition in a high magnetic field [120]. They also investigated the use of Polyethyleneimine (PEI); a branched chain polymer, as a dispersant. Measurements of Zeta potential at differing pH levels were in agreement with Liang *et al.*: a negative surface charge peaking at pH 9. With small amounts of PEI, the mixture had a high positive surface charge (absolute value higher than with no dispersant) which continued up until pH 10—11 where it became negative. Voltages between 2—50V were used for 10 minute depositions, in water, ethanol and a 50% ethanol solution. Several electrode materials were used: palladium sheet, steel, ITO glass and polymer coated alumina. The EPD was carried out in a 12T magnetic field, in an attempt to orient the particles.

Unable to verify the previous work by Liang *et al.* by repeating their experiment, Mishra *et al.* used PEI and cathodic deposition. At pH 5 (highest Zeta potential) the quality of the deposits was poor, and often cracked. This is probably due to particle repulsion from high Zeta potential. pH 7 yielded better results, using 25V and 50% ethanol solution (to prevent electrolysis) on ITO glass; a deposit 0.5cm thick was achieved with a density of 47.5% of the theoretical density. After drying, the Lotgering orientation factors were 0.35 for the top and 0.75 for the side, showing that the method is valid for orienting MAX phase grains. Mishra *et al.* also reported on the phenomenon of pH localisation, the process by which the particles deposit themselves [123]. They reported on a change in the local pH around the electrodes: a decrease around the anode and an increase around the cathode, due to the movement of H^+ and OH^- ions in the liquid. They propose that this pH change will take the suspended particles through their IEP causing them to lose their charge and flocculate (the agglomeration of fine particles formerly in suspension) on the electrode. As the deposit thickens, the effect is reduced due to lack of proximity to the electrode, which causes deposition to slow.

Abdelkader *et al.* repaired crack damage in MAX phase ceramics using EPD [124], however the cracks were repaired using alumina and titanium carbide, rather than MAX phase powder. Cracks were induced in Ti_2AlC using a Vickers indenter and a load of 200N, causing cracks up to 60µm to appear. Al_2O_3 (average particle size 1µm) was dispersed in ethanol and charged using a *keto-enol equilibrium* reaction: acetone, iodine and water are added, causing some of the acetone to change to its '*enol*' form, which then reacts with iodine and liberates a hydrogen ion [125]. These H^+ ions then gather around the alumina particles, giving them an overall positive charge. Using 20V for 5—15minutes Abdelkader *et al.* managed to fill the cracks almost completely with alumina, which they believe will sinter and diffuse when the MAX phase is brought up to (presumably) operational temperature, fixing the crack and restoring the original properties of the ceramic. A similar deposition of TiC in cracks was achieved, once the carbide was milled down to a smaller particle size.

De Riccardis *et al.* reported on a method for densifying electrophoretic deposits using electron beam sintering [126]. They deposited alumina or an alumina-zirconia mixture onto stainless steel electrodes from a 5wt.% solution in ethanol. The electrodes were either 'as-received', sandblasted to roughen the surface, or coated with a thin sputter-coated layer of titanium. Deposition times were up to 5 minutes under a field of 20V/cm or 40V/cm. This resulted in thin deposits of 3.5 mg/cm^2 which were then dried for 24 hours. Some samples then received pre-sinter heat treatments at 900°C or 550°C for 1 hour in flowing nitrogen or air. The samples were then subjected to scanning e-beam treatments with fluences of 5.5—13.75J/mm^2. The coatings were then subjected to a qualitative scratch test and a more thorough pull test to determine adhesion. The pull test involved gluing a stub to the sintered coating and applying increasing force until the stub came away. The untreated steel lost its coating easily (3MPa of stress) whereas the Ti-coated sample and the sandblasted sample performed better (4MPa and 7MPa respectively). For comparison, an un-sintered deposition was dislodged with 46KPa, demonstrating that sintering had definitely occurred. The stress values recorded were qualitative, based on the researcher's determination of when coating delamination had occurred, and are only useful for comparison within this study.

Other Methods

An alternative route of deposition and densification in one step is Pulsed Electrospark Deposition (PED). The process uses a sacrificial anode made of the coating material, which is then brought into close proximity to the surface cathode to be coated. Pulsing a high electric current across the electrodes causes arcing, which deposits some of the anode onto the cathode in a manner similar to arc welding [127]. High frequency and short duration pulses ensure that the local heating of the

substrate is not too great, and the anode can be scanned across the surface to build up a layer of deposit. This is potentially useful for applying a coating to zirconium alloy tubes, as zirconium undergoes a phase transition at 862°C from hexagonal close packed (hcp) to body centred cubic (bcc) [128], which is undesirable for the fuel cladding to retain strength.

Only one paper was found to have used PED (a relatively established technique with other materials) to deposit MAX phases onto a surface. Zamulaeva *et al.* used a Cr_2AlC anode to deposit films onto a flat OT4-1 (a titanium alloy) surface [129]. Cr_2AlC was chosen because its decomposition products (Cr_7C_3 for example) are refractory in nature and so would suit high temperature applications. Short pulses of 10^{-6}—10^{-3}s were used to avoid overheating of the titanium alloy, and two current settings were used: 500A and 170A. Deposition took place in both air and a chamber with flowing argon for up to 10 minutes. The anode and cathode were weighed before and after to determine mass transfer and transfer efficiency, and were analysed with XRD and SEM.

The mass loss from the anodes in air and argon were comparable, but the mass gain of the surface in argon was much greater than in air. Zamulaeva *et al.* propose that there was a high oxidation and decomposition of the anode material in transit in air. The optimum mass transfer efficiency was found to be 68% for 170A (Ar). XRD of the unspent anode showed it to be pure Cr_2AlC, while after deposition revealed Cr_2AlC with slightly different lattice parameters, and also a Cr_2AlC phase with largely different lattice parameters (dubbed by Zamulaeva *et al.* as Cr_2AlC-II). The author attributes this difference to many dislocations arising from the nature of the deposition. The substrate after deposition at 170A revealed Cr_2AlC with usual lattice parameters to be the main phase, along with some TiC, Al_2O_3 and other ancillary phases. 500A deposition resulted in the Cr_2AlC-II phase being present as well. However it was shown that Ti from the surface pervades the coating in low current deposition, whereas in high current deposition, the layer of TiC stops close to the surface, leaving the coating separate but adhered. A deposition thickness of ~60µm was obtained.

Gutzmann *et al.* used a cold spraying technique to deposit layers of Ti_2AlC onto copper, steel (S235) and titanium substrates [130]. Using a feedstock of pre-synthesised Ti_2AlC with D50 = 34.3µm and a process gas of nitrogen at 4MPa, the powder was sprayed at the substrates with 1—5 to try and build up thicker coatings. The gas temperature used was 600°C for initial testing, however most of the MAX phase particles did not adhere to the surface, and merely dented the surface. Increasing the temperature to 1000°C improved the adhesion between coating particles and substrate. A single pass resulted in a coating thickness of 30—50µm, which increased to 110—155µm after 5 successive coatings. However Gutzmann *et al.* estimate the top third to be very loosely adhered. By using a lower temperature process gas than thermal spraying techniques, the coating was determined by XRD to

still be Ti_2AlC, and with a slightly higher oxygen content that the powder feedstock (1.58wt.% up from 0.94wt.%).

A different method to mitigate the effect of high temperatures used in thermal spraying is to deliver the feedstock powder in a liquid steam (known as liquid plasma spraying or LPS). Yu *et al.* deposited Ti_3AlC_2 onto stainless steel substrates using plasma spraying with 10wt.% feedstock in pH-adjusted deionised water and a 1:1 water: ethanol mixture [131]. These were then compared to plasma sprayed coatings without a liquid delivery method. A 15kW spraying system was used with an argon/hydrogen plasma. It was found after the normal plasma spraying, the majority of the sprayed MAX phase (Yu *et al.* report ~80%) had decomposed, with TiC becoming the main phase. However, using water, with an acidic or neutral pH to inject the powder into the plasma stream resulted in coating XRD patterns "indistinguishable" from the feedstock XRD approximately 10—20µm thick. Yu *et al.* determined no oxidation products in the XRD patterns of the LPS coating, but Raman analysis indicated the presence TiO_2, which they posited was too small a fraction of the coating to be visible on XRD patterns. The water/ethanol mixture ignited in the plasma stream, resulting in a poor coating.

2.2.9 *Shape forming*

To completely replace zirconium alloy cladding, a method for producing dense MAX phase tubes of a similar geometry to fit in PWR assemblies. Further to this, a purely MAX phase cladding may be feasible if a suitable phase was identified and tube formation possible. Other parts of the fuel assembly, such as spacer grids or endcaps could also be replaced with MAX phases.

Slip casting

A technique well-established for ceramic processing is slip casting, used currently to create, amongst other things, ceramic toilets and sink units. Used for hundreds of years, a slurry of fine ceramic particles in water (sometimes with additives to improve stability and green body strength) is poured into a porous mould. Capillary action draws the water into the mould, while coating the inside with a time-dependant layer of the particles. Once the piece has been left to dry it can be de-moulded and sintered as appropriate [132]. This is of particular interest to the project as it is a method that could possibly be employed to cast ceramic cladding tubes on an industrial scale.

Little published work exists on the slip casting of MAX phases. El-Raghy and Barsoum applied for a patent on slip casting and gel casting of MAX phases with specific applications as glove and condom formers [133], but are vague on the constituents of their slurry. This does at least show that Ti_3SiC_2

can be slip cast. Hu *et al.* have used so-called "slip casting" in a magnetic field to cast oriented pellets of MAX phase for densification by SPS (see above) [134]. However, the slips used had a very low solids loading of only a few wt.%, and the process seems more dependent on gravitational settling of particles. Bowen *et al.* used thick Ti_2AlC slips to cast MAX phase foams around macropore polyurethane foam [135]. Although not technically slip casting, as the water is removed via air drying rather than capillary action, the slip formulation is relevant. Bowen *et al.* used polyethylene glycol, methylcellulose and proprietary Dispex GA40 to improve the qualities of their slip, and tested various solids loading ratios with water to determine the best slip. A slurry of Ti_2AlC (With D_{90} 20µm), 2wt.% PEG, 1.2wt.% Dispex, 2.4wt.% MC and 52wt.% water was found to have the most suitable properties. Polyurethane foam pieces were dipped in the slip, wrung and re-dipped to ensure thorough permeation and left to dry for 24 hours. A burnout stage from 200—800°C was used to remove the additives, after which the foams were sintered at 1400°C for 5 hours. This resulted in densified material with large pores of 1—3mm in diameter, mimicking the previously underlying foam.

Sun *et al.* demonstrated Ti_3AlC_2 could be slip cast and sintered, and examined the surface chemistry and rheology of water based Ti_3AlC_2 slips [136]. Polyacrylic acid (PAA) was used as a dispersant, and Sun *et al.* found that 2dwb% of PAA in an acidic slip between pH 4.5—6 allowed for a high solid loading of 30vol.% (approximately 64wt.%) of MAX phase and still retain enough fluidity to be poured into a mould. After drying, the cast pieces were demoulded and sintered in flowing argon at 1420°C for 1.5 hours. The final pieces were found to be 96% of the max density for Ti_3AlC_2.

A specific technique used to cast long thick ceramic tubes is known as Centrifugal Slip Casting (CSC) [137]. This involves an axially rotating mould with input ports at the ends to fill with slip, or can involve spinning a mould away from the axis of rotation to create flat parts [138]. Combining centrifugal pseudo-force with capillary action of the mould allows for higher green-density parts to be produced, and reduces bubbles and defects therein. It also allows for composite that have a gradient through them, due to differential mass separation from the rotation [132]. Oriented structures may also be cast from platelet materials (such as MAX phases) [139].

Extrusion

A method for producing ceramic tubes exists in the form of extrusion. The ceramic particles are suspended in a highly viscous paste, which is then forced through a die or annulus to produce the corresponding cross section [140]. Once dry this can be sintered as appropriate. An advantage of this is that tubes could be extruded as long as needed, meaning that production of a thin 4m one piece cladding tube could be possible. A patent by Li *et al.* has been filed for production of MAX phase tubes

via extrusion, but is vague on the suspension preparation and details [141]. Work on ceramic extrusion in the scientific literature has been in pursuit of porous ceramic tubes for uses not limited to catalysis or filtration [142] [143]. However the technique can still be used to create dense parts, and is used industrially by Sandvik Kanthal to produce tube from their Maxthal® products (Maxthal 312 impure Ti_3SiC_2 and Mathal 211 impure Ti_2AlC [144]). It was stated in response to a question that it was believed extruding a 4m long tube would be possible, though a longer furnace would then be required for sintering, with 1m being the maximum length able to be produced in their sintering furnaces at the time (2014).

Other shape forming methods

Murugaiah *et al.* demonstrated that Ti_3SiC_2 could be tape cast from a slurry and densified resulting in highly oriented samples [145]. Ti_3SiC_2 with an average particle size of 5µm was used in a 35wt.% slurry with water, 0.25wt.% Darvan C commercial deflocculant, 0.5wt.% polyethylene glycol and 3wt.% hydroxypropylmethylcellulose. The PEG and HPMC act as a dispersant and a binder respectively. 400µm tapes were cast, which reduced in thickness to ~100µm after drying. The tape was then cut into sections and stacked to a thickness of 10mm. After prepressing and a binder burnout phase at 500°C the samples were sintered under argon at 1600°C for 3 hours. The sintered samples were at full density and contained highly oriented grains of Ti_3SiC_2, however the fraction of TiC increased. In an attempt to mitigate this, Murugaiah *et al.* repeated the process, sintering in a C or Si rich atmosphere. They found that C increased the fraction of TiC, while Si resulted in the formation of titanium silicides, both of which prevented large grain growth. Finally it should be noted that although tape casting constitutes a shape forming method, it is unlikely to be used for the production of tubes, however the sintering procedure is relevant.

As noted in the Synthesis Section, hot pressing, HIP and SPS are capable of producing simple geometry small components but are not considered further in this review as a shape forming technique as they are not foreseen to be capable of producing long cladding tubes.

2.3 References

[1] N. Mayhew, “URAM-2018 Wraps Up: The Future of Uranium as a Sustainable Source of Energy.” [Online]. Available: https://www.iaea.org/newscenter/news/uram-2018-wraps-up-the-future-of-uranium-as-a-sustainable-source-of-energy.

[2] R. Cameron and J.-H. Keppler, “The system costs of different power generation technologies: A new look at the competitiveness of nuclear power. - Paper and presentation,” in *European Nuclear Conference, Manchester, 9th-13th December*, 2012.

[3] B. W. Brook, A. Alonso, D. A. Meneley, J. Misak, T. Blees, and J. B. van Erp, “Why nuclear

energy is sustainable and has to be part of the energy mix," *Sustain. Mater. Technol.*, vol. 1, pp. 8–16, 2014.

[4] J. M. Deutch, C. Forsberg, A. C. Kadak, M. S. Kazimi, and E. J. Moniz, "Update of the MIT 2003 Future of nuclear power," 2009.

[5] J. Buogiorno, J. Parsons, M. Corradini, and D. Petti, "The Future of Nuclear Energy in a Carbon-Constrained World: An Interdisciplinary MIT study," 2018.

[6] D. Bodansky, *Nuclear Energy: Principles, Practices, and Prospects*, vol. 65. 1997.

[7] V. Nian, "Progress in Nuclear Power Technology," in *Encyclopedia of Sustainable Technologies*, no. August, Elsevier, 2017, pp. 87–106.

[8] IAEA - International Atomic Energy Agency, "IAEA Power Reactor Information System," 2018. [Online]. Available: IAEA.org/pris. [Accessed: 13-Apr-2018].

[9] G. A. Brennecka, L. E. Borg, I. D. Hutcheon, M. A. Sharp, and A. D. Anbar, "Natural variations in uranium isotope ratios of uranium ore concentrates: Understanding the238U/235U fractionation mechanism," *Earth Planet. Sci. Lett.*, vol. 291, no. 1–4, pp. 228–233, 2010.

[10] "Uranium Enrichment." [Online]. Available: http://www.world-nuclear.org/information-library/nuclear-fuel-cycle/conversion-enrichment-and-fabrication/uranium-enrichment.aspx.

[11] "World Nuclear: Nuclear reactors." [Online]. Available: http://www.world-nuclear.org/information-library/nuclear-fuel-cycle/nuclear-power-reactors/nuclear-power-reactors.aspx. [Accessed: 16-Apr-2018].

[12] A. E. Waltar and A. B. Reynolds, *Fast Breeder Reactors*, 1st ed. Pergamon Press, 1981.

[13] E. Nonboel, *Description of the Advanced Gas Cooled Type of Reactor (AGR)*. IAEA, 1996.

[14] "Nuclear fuel." [Online]. Available: https://www.nuclear-power.net/nuclear-power-plant/nuclear-fuel/. [Accessed: 08-Sep-2018].

[15] T. R. Allen, R. J. M. Konings, and A. T. Motta, *Corrosion of Zirconium Alloys*, 1st ed., vol. 5. Elsevier Inc., 2012.

[16] F. J. Erbacher and S. Leistikow, *A review of Zircaloy fuel cladding behavior in a loss-of-coolant accident*, no. September. Kernforschungszetrum Karlsruhe GmbH, 1985.

[17] H.-G. Kim, I. Kim, B. Choi, and J. Park, "A study of the breakaway oxidation behavior of zirconium cladding materials," *J. Nucl. Mater.*, vol. 418, no. 1–3, pp. 186–197, Nov. 2011.

[18] M. Yamato, F. Nagase, and M. Amaya, "Reduction in the onset time of breakaway oxidation on Zircaloy cladding ruptured under simulated LOCA conditions," *J. Nucl. Mater.*, vol. 445, no. 1–3, pp. 78–83, 2014.

[19] M. Billone, Y. Yan, T. Burtseva, and R. Daum, "Cladding embrittlement during postulated loss-

of-coolant accidents," 2008.

[20] J. Yanez, M. Kuznetsov, and A. Souto-Iglesias, "An analysis of the hydrogen explosion in the Fukushima-Daiichi accident," *Int. J. Hydrogen Energy*, vol. 40, no. 25, pp. 8261–8280, 2015.

[21] G. Steinhauser, A. Brandl, and T. E. Johnson, "Comparison of the Chernobyl and Fukushima nuclear accidents: A review of the environmental impacts," *Sci. Total Environ.*, vol. 470–471, pp. 800–817, 2014.

[22] J. Majevadia, "Hydrogen-enhanced localised plasticity – a mechanism for hydrogen embrittlement," *Nucl. Futur.*, vol. 8, no. 3, pp. 46–51, 2012.

[23] P. A. Raynaud, D. A. Koss, and A. T. Motta, "Crack growth in the through-thickness direction of hydrided thin-wall Zircaloy sheet," *J. Nucl. Mater.*, vol. 420, no. 1–3, pp. 69–82, 2012.

[24] P. Ashcheulov, R. Škoda, J. Škarohlíd, A. Taylor, F. Fendrych, and I. Kratochvílová, "Layer Protecting the Surface of Zirconium Used in Nuclear Reactors," *Recent Pat. Nanotechnol.*, vol. 10, pp. 59–65, 2016.

[25] IAEA - International Atomic Energy Agency, "Delayed hydride cracking in zirconium alloys in pressure tube nuclear reactors," 2004.

[26] M. W. Barsoum, "MAX Phases: Properties of Machinable Ternary Carbides and Nitrides," in *Wiley-VCH*, vol. 1, Wiley-, 2013.

[27] W. Jeitschko, H. Nowotny, and F. Benesovsky, "Kohlenstoffhaltige ternaire Verbindungen (H-Phase)," *Monatshefte für Chemie*, vol. 332, pp. 2–6, 1963.

[28] M. A. Pietzka and J. C. Schuster, "Summary of constitutional data on the aluminum-carbon-titanium system," *J. phase equilibria*, vol. 15, no. 4, pp. 392–400, 1994.

[29] M. W. Barsoum and T. El-raghy, "The MAX phases: Unique new carbide and nitride materials," *Am. Sci.*, vol. 89(4), pp. 334–343, 2001.

[30] J. Wang, Y. Zhou, Z. Lin, and T. Liao, "First-principles investigation on chemical bonding and bulk modulus of the ternary carbide Zr2Al3C5," *Phys. Rev. B*, vol. 72, no. 5, p. 052102, Aug. 2005.

[31] B. Tunca, T. Lapauw, O. M. Karakulina, M. Batuk, T. Cabioc'h, J. Hadermann, R. Delville, K. Lambrinou, and J. Vleugels, "Synthesis of MAX Phases in the Zr-Ti-Al-C System," *Inorg. Chem.*, vol. 56, no. 6, pp. 3489–3498, 2017.

[32] K. Lambrinou, T. Lapauw, A. Jianu, A. Weisenburger, J. Ejenstam, P. Szak´los, J. Wallenius, E. Ström, K. Vanmeensel, and J. Vleugels, "Corrosion-Resistant Ternary Carbides For Use in Heavy Liquid Metal Coolants," in *The American Ceramic Society*, 2015, pp. 19–34.

[33] N. J. Lane, S. C. Vogel, E. N. Caspi, and M. W. Barsoum, "High-temperature neutron diffraction and first-principles study of temperature-dependent crystal structures and atomic

vibrations in Ti 3AlC2, Ti2AlC, and Ti5Al 2C3," *J. Appl. Phys.*, vol. 113, no. 18, 2013.

[34] N. J. Lane, M. Naguib, J. Lu, L. Hultman, and M. W. Barsoum, "Structure of a new bulk Ti 5Al 2C 3 MAX phase produced by the topotactic transformation of Ti 2AlC," *J. Eur. Ceram. Soc.*, vol. 32, no. 12, pp. 3485–3491, 2012.

[35] W. K. Pang, I. M. Low, B. H. O'Connor, A. J. Studer, V. K. Peterson, J.-P. Palmquist, and A. A. Bin Mohamed, "DIFFRACTION STUDY ON THE THERMAL STABILITY OF Ti[sub 3]SiC[sub 2]/TiC/TiSi[sub 2] COMPOSITES IN VACUUM," 2010, vol. 45, no. 1, pp. 44–48.

[36] P. O. Å. Persson, "P." [Online]. Available: https://people.ifm.liu.se/perpe/.

[37] J. P. Palmquist, S. Li, P. O. A. Persson, J. Emmerlich, O. Wilhelmsson, H. Hogberg, M. I. Katsnelson, B. Johansson, R. Ahuja, O. Eriksson, L. Hultman, and U. Jansson, "Mn+1AXn phases in the Ti-Si-C system studied by thin-film synthesis and ab initio calculations [74]," *Phys. Rev. B - Condens. Matter Mater. Phys.*, vol. 70, no. 16, pp. 1–13, 2004.

[38] D. Horlait, S. C. Middleburgh, A. Chroneos, and W. E. Lee, "Synthesis and DFT investigation of new bismuth-containing MAX phases," *Sci. Rep.*, vol. 6, no. November 2015, p. 18829, 2016.

[39] H. J. Matzke, *Science of advanced LMFBR fuels*. Netherlands: North Holland. Physics publishing, 1986.

[40] M. Radovic and M. W. Barsoum, "MAX phases: Bridging the gap between metals and ceramics," *Am. Ceram. Soc. Bull.*, vol. 92, no. 3, pp. 20–27, 2013.

[41] M. W. Barsoum, T. El-raghy, C. J. Rawn, W. D. Porter, H. Wang, E. a Payzant, and C. R. Hubbard, "Thermal properties of Ti3 SiC2," *J. Phys. Chem. Solids*, vol. 60, pp. 429–439, 1999.

[42] M. Barsoum, I. Salama, T. El-Raghy, J. Golczewski, H. Seifert, F. Aldinger, W. Porter, and H. Wang, "Thermal and electrical properties of Nb_2AlC, $(Ti,Nb)_2AlC$ and Ti_2AlC," *Metall. Mater. Trans. A*, vol. 33, no. 9, pp. 2775–2779, 2002.

[43] W. Tian, P. Wang, G. Zhang, Y. Kan, Y. Li, and D. Yan, "Synthesis and thermal and electrical properties of bulk Cr2AlC," *Scr. Mater.*, vol. 54, no. 5, pp. 841–846, 2006.

[44] M. W. Barsoum and M. Radovic, "Elastic and Mechanical Properties of the MAX Phases," *Annu. Rev. Mater. Res.*, vol. 41, no. 1, pp. 195–227, 2011.

[45] T. El-Raghy, A. Zavaliangos, M. W. Barsoum, and S. R. Kalidindi, "Damage mechanisms around hardness indentation in Ti3SiC2," *J. Am. Ceram. Soc.*, vol. 80, no. 2, pp. 513–516, 1997.

[46] M. W. Barsoum and T. El-Raghy, "Room-temperature ductile carbides," *Metall. Mater. Trans. A*, vol. 30, no. 2, pp. 363–369, Feb. 1999.

[47] D. Chen, K. Shirato, M. W. Barsoum, T. El-Raghy, and R. O. Ritchie, "Cyclic Fatigue-Crack

Growth and Fracture Properties in Ti3SiC2 Ceramics at Elevated Temperatures," *J. Am. Ceram. Soc.*, vol. 84, no. 12, pp. 2914–2920, 2001.

[48] S. Hwang, S. C. Lee, J. Han, D. Lee, and S. Park, "Machinability of Ti3SiC2 with layered structure synthesized by hot pressing mixture of TiCx and Si powder," *J. Eur. Ceram. Soc.*, vol. 32, no. 12, pp. 3493–3500, Sep. 2012.

[49] J. Ward, D. Bowden, E. Prestat, S. Holdsworth, D. Stewart, M. W. Barsoum, M. Preuss, and P. Frankel, "Corrosion performance of Ti3SiC2, Ti3AlC2, Ti2AlC and Cr2AlC MAX phases in simulated primary water conditions," *Corros. Sci.*, vol. 139, no. February, pp. 444–453, 2018.

[50] K. Pettersson, T. Billone, M.Fuketa, C. Grandjean, G. Hache, and L. Heins, *Nuclear Fuel Behaviour in Loss-of-coolant Accident (LOCA) Conditions*, no. 6846. OECD Nuclear Energy Agency, 2009.

[51] D. B. Lee, T. D. Nguyen, J. H. Han, and S. W. Park, "Oxidation of Cr2AlC at 1300°C in air," *Corros. Sci.*, vol. 49, no. 10, pp. 3926–3934, Oct. 2007.

[52] M. Haftani, M. Saeedi Heydari, H. R. Baharvandi, and N. Ehsani, "Studying the oxidation of Ti 2 AlC MAX phase in atmosphere: A review," *Int. J. Refract. Met. Hard Mater.*, vol. 61, pp. 51–60, Dec. 2016.

[53] X. H. Wang and Y. C. Zhou, "High-temperature oxidation behavior of Ti2AlC in air," *Oxid. Met.*, vol. 59, no. 3–4, pp. 303–320, 2003.

[54] M. Sundberg, G. Malmqvist, A. Magnusson, and T. El-Raghy, "Alumina forming high temperature silicides and carbides," *Ceram. Int.*, vol. 30, no. 7, pp. 1899–1904, 2004.

[55] B. Cui, D. D. Jayaseelan, and W. E. Lee, "Microstructural evolution during high-temperature oxidation of Ti2AlC ceramics," *Acta Mater.*, vol. 59, no. 10, pp. 4116–4125, Jun. 2011.

[56] Z. Feng, P. Ke, Q. Huang, and A. Wang, "The scaling behavior and mechanism of Ti 2 AlC MAX phase coatings in air and pure water vapor," *Surf. Coatings Technol.*, vol. 272, pp. 380–386, Jun. 2015.

[57] Z. Sun, Y. Zhou, and M. Li, "Oxidation behaviour of Ti3SiC2-based ceramic at 900-1300°C in air," *Corros. Sci.*, vol. 43, no. 6, pp. 1095–1109, 2001.

[58] D. J. Tallman, B. Anasori, and M. W. Barsoum, "A critical review of the oxidation of Ti2AlC, Ti3AlC2and Cr2AlC in Air," *Mater. Res. Lett.*, vol. 1, no. 3, pp. 115–125, 2013.

[59] D. Lee and T. Nguyen, "Cyclic oxidation ofCr2AlC between 1000 and 1300◦C in air.," *J Alloy. Compd.*, vol. 464, pp. 434–439, 2008.

[60] Z. Lin, M. Li, J. Wang, and Y. Zhou, "High-temperature oxidation and hot corrosion of Cr2AlC.," *Acta Mater.*, vol. 55, pp. 6182–6191, 2007.

[61] J. Varmuza, K. Katovsky, O. Stastny, and M. Zeman, "The spectrum of neutrons and its

importance for nuclear power engineering," *Proc. 2017 18th Int. Sci. Conf. Electr. Power Eng. EPE 2017*, 2017.

[62] Y. Dong, B. H. Sencer, F. A. Garner, and E. A. Marquis, "Microchemical and microstructural evolution of AISI 304 stainless steel irradiated in EBR-II at PWR-relevant dpa rates," *J. Nucl. Mater.*, vol. 467, pp. 692–702, 2015.

[63] D. J. Tallman, E. N. Hoffman, E. N. Caspi, B. L. Garcia-Diaz, G. Kohse, R. L. Sindelar, and M. W. Barsoum, "Effect of neutron irradiation on select MAX phases," *Acta Mater.*, vol. 85, pp. 132–143, 2015.

[64] D. J. Tallman, L. He, B. L. Garcia-Diaz, E. N. Hoffman, G. Kohse, R. L. Sindelar, and M. W. Barsoum, "Effect of neutron irradiation on defect evolution in Ti3SiC2and Ti2AlC," *J. Nucl. Mater.*, vol. 468, pp. 194–206, 2016.

[65] J. Ward, S. Middleburgh, M. Topping, A. Garner, D. Stewart, M. W. Barsoum, M. Preuss, and P. Frankel, "Crystallographic evolution of MAX phases in proton irradiating environments," *J. Nucl. Mater.*, vol. 502, pp. 220–227, 2018.

[66] C. Grove, D. Shepherd, M. Thomas, and P. Little, "Neutronics of MAX phase materials," *Struct. Mater. Innov. Nucl. Syst. (SMINS-4), Univ. Manchester*, 2016.

[67] T. Yang, C. Wang, C. A. Taylor, X. Huang, Q. Huang, F. Li, L. Shen, X. Zhou, J. Xue, S. Yan, and Y. Wang, "The structural transitions of Ti3AlC2 induced by ion irradiation," *Acta Mater.*, vol. 65, pp. 351–359, 2014.

[68] P. Song, J. Sun, Z. Wang, M. Cui, T. Shen, Y. Li, L. Pang, Y. Zhu, Q. Huang, and J. L??, "Irradiation resistance properties studies on helium ions irradiated MAX phase Ti3AlC2," *Nucl. Instruments Methods Phys. Res. Sect. B Beam Interact. with Mater. Atoms*, vol. 326, pp. 332–336, 2014.

[69] C. Wang, T. Yang, S. Kong, J. Xiao, J. Xue, Q. Wang, C. Hu, Q. Huang, and Y. Wang, "Effects of He irradiation on Ti3AlC2: Damage evolution and behavior of He bubbles," *J. Nucl. Mater.*, vol. 440, no. 1–3, pp. 606–611, 2013.

[70] M. K. Patel, D. J. Tallman, J. A. Valdez, J. Aguiar, O. Anderoglu, M. Tang, J. Griggs, E. Fu, Y. Wang, and M. W. Barsoum, "Effect of helium irradiation on Ti3AlC2 at 500°C," *Scr. Mater.*, vol. 77, pp. 1–4, 2014.

[71] Q. Qi, G. J. Cheng, L. Q. Shi, D. J. O'Connor, B. V. King, and E. H. Kisi, "Damage accumulation and recovery in C+-irradiated Ti3SiC2," *Acta Mater.*, vol. 66, pp. 317–325, 2014.

[72] W. Jiang, C. H. Henager, T. Varga, H. J. Jung, N. R. Overman, C. Zhang, and J. Gou, "Diffusion of Ag, Au and Cs implants in MAX phase Ti 3 SiC 2," *J. Nucl. Mater.*, vol. 462, pp. 310–320, Jul. 2015.

[73] J. C. Nappé, P. Grosseau, F. Audubert, B. Guilhot, M. Beauvy, M. Benabdesselam, and I.

Monnet, “Damages induced by heavy ions in titanium silicon carbide: Effects of nuclear and electronic interactions at room temperature,” *J. Nucl. Mater.*, vol. 385, no. 2, pp. 304–307, 2009.

[74] K. R. Whittle, M. G. Blackford, R. D. Aughterson, S. Moricca, G. R. Lumpkin, D. P. Riley, and N. J. Zaluzec, “Radiation tolerance of Mn+1AXn phases, Ti 3AlC2 and Ti3SiC2,” *Acta Mater.*, vol. 58, no. 13, pp. 4362–4368, 2010.

[75] Q. Huang, R. Liu, G. Lei, H. Huang, J. Li, S. He, D. Li, L. Yan, and J. Zhou, “Irradiation resistance of MAX phases Ti3SiC2 and Ti3AlC2: Characterization and comparison,” *J. Nucl. Mater.*, vol. 465, pp. 640–647, 2015.

[76] C. Wang, T. Yang, J. Xiao, S. Liu, and J. Xue, “Structural Transitions Induced by Ion Irradiation in V2AlC and Cr2AlC,” *J. Eur. Ceram. Soc.*, vol. 99, no. 5, pp. 1769–1777, 2016.

[77] E. N. Hoffman, D. W. Vinson, R. L. Sindelar, D. J. Tallman, G. Kohse, and M. W. Barsoum, “MAX phase carbides and nitrides: Properties for future nuclear power plant in-core applications and neutron transmutation analysis,” *Nucl. Eng. Des.*, vol. 244, pp. 17–24, 2012.

[78] Special Metals, “Inconel Alloy 617 Datasheet No. SMC-029 (2005),” *Special Metals*, 2005. [Online]. Available: http://www.specialmetals.com/assets/documents/alloys/inconel/inconel-alloy-617.pdf. [Accessed: 13-Apr-2017].

[79] E. Zapata-Solvas, S.-R. G. Christopoulos, N. Ni, D. C. Parfitt, D. Horlait, M. E. Fitzpatrick, A. Chroneos, and W. E. Lee, “Experimental synthesis and density functional theory investigation of radiation tolerance of $Zr_3(Al_{1-x}Si_x)C_2$ MAX phases,” *J. Am. Ceram. Soc.*, vol. 100, no. 4, pp. 1377–1387, 2017.

[80] M. W. Barsoum and T. El-Raghy, “Synthesis and Characterization of a Remarkable Ceramic: Ti3SiC2,” *J. Am. Ceram. Soc.*, vol. 79, no. 7, pp. 1953–1956, 1996.

[81] P. WANG, B. chu MEI, X. lin HONG, and W. bing ZHOU, “Synthesis of Ti2AlC by hot pressing and its mechanical and electrical properties,” *Trans. Nonferrous Met. Soc. China (English Ed.*, vol. 17, no. 5, pp. 1001–1004, 2007.

[82] W. Tian, K. Vanmeensel, P. Wang, G. Zhang, Y. Li, J. Vleugels, and O. Van der Biest, “Synthesis and characterization of Cr2AlC ceramics prepared by spark plasma sintering,” *Mater. Lett.*, vol. 61, no. 22, pp. 4442–4445, 2007.

[83] T. Lapauw, J. Halim, J. Lu, T. Cabioc’h, L. Hultman, M. W. Barsoum, K. Lambrinou, and J. Vleugels, “Synthesis of the novel Zr3AlC2 MAX phase,” *J. Eur. Ceram. Soc.*, vol. 36, no. 3, pp. 943–947, 2016.

[84] X. He, Y. Bai, C. Zhu, Y. Sun, M. Li, and M. W. Barsoum, “General trends in the structural, electronic and elastic properties of the M3AlC2 phases (M = transition metal): A first-principle study,” *Comput. Mater. Sci.*, vol. 49, no. 3, pp. 691–698, 2010.

[85] T. Lapauw, K. Lambrinou, T. Cabioc'h, J. Halim, J. Lu, A. Pesach, O. Rivin, O. Ozeri, E. N. Caspi, L. Hultman, P. Eklund, J. Rosén, M. W. Barsoum, and J. Vleugels, "Synthesis of the new MAX phase Zr2AlC," *J. Eur. Ceram. Soc.*, vol. 36, no. 8, pp. 1847–1853, 2016.

[86] T. Lapauw, D. Tytko, K. Vanmeensel, S. Huang, P. P. Choi, D. Raabe, E. N. Caspi, O. Ozeri, M. To Baben, J. M. Schneider, K. Lambrinou, and J. Vleugels, "(Nbx, Zr1-x)4AlC3 MAX Phase Solid Solutions: Processing, Mechanical Properties, and Density Functional Theory Calculations," *Inorg. Chem.*, vol. 55, no. 11, pp. 5445–5452, 2016.

[87] Z. Liu, L. Zheng, L. Sun, Y. Qian, J. Wang, and M. Li, "(Cr 2/3 Ti 1/3) 3 AlC 2 and (Cr 5/8 Ti 3/8) 4 AlC 3 : New MAX-phase Compounds in Ti-Cr-Al-C System," *J. Am. Ceram. Soc.*, vol. 97, no. 1, pp. 67–69, Jan. 2014.

[88] E. Zapata-solvas, M. A. Hadi, and D. Horlait, "Synthesis and physical properties of (Zr 1-x , Ti x) 3 AlC 2 MAX phases," *J. Am. Ceram. Soc.*, no. April, pp. 1–9, 2017.

[89] T. Lapauw, B. Tunca, D. Potashnikov, A. Pesach, O. Ozeri, J. Vleugels, and K. Lambrinou, "The double solid solution (Zr , Nb) 2 (Al , Sn) C MAX phase : a steric stability approach," *Sci. Rep.*, vol. 2, pp. 1–13, 2018.

[90] M. Dahlqvist, J. Lu, R. Meshkian, Q. Tao, L. Hultman, and J. Rosen, "Prediction and synthesis of a family of atomic laminate phases with Kagomé-like and in-plane chemical ordering," *Sci. Adv.*, vol. 3, no. 7, 2017.

[91] L. Chen, M. Dahlqvist, T. Lapauw, B. Tunca, F. Wang, J. Lu, R. Meshkian, K. Lambrinou, B. Blanpain, J. Vleugels, and J. Rosen, "Theoretical Prediction and Synthesis of (Cr 2/3 Zr 1/3) 2 AlC i -MAX Phase," *Inorg. Chem.*, vol. 57, no. 11, pp. 6237–6244, Jun. 2018.

[92] I. M. Low, *Advances in Science and Technology of Mn+1axn Phases*. 2012.

[93] Z. M. Sun, "Progress in research and development on MAX phases: a family of layered ternary compounds," *Int. Mater. Rev.*, vol. 56, no. APRIL 2011, pp. 143–166, 2011.

[94] N. F. Gao, J. T. Li, D. Zhang, and Y. Miyamoto, "Rapid synthesis of dense Ti3SiC2 by spark plasma sintering," *J. Eur. Ceram. Soc.*, vol. 22, no. 13, pp. 2365–2370, 2002.

[95] A. Zhou, C. Wang, and Y. Hunag, "Synthesis and mechanical properties of Ti 3 AlC 2 by spark plasma sintering," *Synthesis (Stuttg).*, vol. 8, pp. 3111–3115, 2003.

[96] J. Zhu and B. Mei, "Fabrication of high-purity Ti 3 SiC 2 by spark plasma sintering (SPS) of elemental powders," *Most*, no. c, pp. 889–890, 2003.

[97] F. Sato, J. Li, and R. Watanabe, "Reaction Synthesis of Ti3SiC2 from Mixutre of Elemental Powders," *Mater. Transations, JIM*, vol. 41, no. 5, pp. 605–608, 2000.

[98] W. B. Zhou, B. C. Mei, J. Q. Zhu, and X. L. Hong, "Rapid synthesis of Ti2AlC by spark plasma sintering technique," *Mater. Lett.*, vol. 59, no. 1, pp. 131–134, 2005.

[99] B. Y. Liang, S. Z. Jin, and M. Z. Wang, “Low-temperature fabrication of high purity Ti3SiC2,” *J. Alloys Compd.*, vol. 460, no. 1–2, pp. 440–443, 2008.

[100] H. Abderrazak, F. Turki, F. Schoenstein, M. Abdellaoui, and N. Jouini, “Influence of mechanical alloying on Ti3SiC2 formation via spark plasma sintering technique from Ti/SiC/C powders,” *Ceram. Int.*, vol. 39, no. 5, pp. 5365–5372, Jul. 2013.

[101] W. Tian, Z. Sun, Y. Du, and H. Hashimoto, “Synthesis reactions of Cr2AlC from Cr-Al4C3-C by pulse discharge sintering,” *Mater. Lett.*, vol. 62, no. 23, pp. 3852–3855, 2008.

[102] Y. Mizuno, K. Sato, M. Mrinalini, T. S. Suzuki, and Y. Sakka, “Fabrication of textured Ti3AlC2 by spark plasma sintering and their anisotropic mechanical properties,” *J. Ceram. Soc. Japan*, vol. 121, no. 1412, pp. 366–369, 2013.

[103] C. Hu, Y. Sakka, S. Grasso, T. Suzuki, and H. Tanaka, “Tailoring Ti3SiC2 ceramic via a strong magnetic field alignment method followed by spark plasma sintering,” *J. Am. Ceram. Soc.*, vol. 94, no. 3, pp. 742–748, 2011.

[104] H. B. Zhang, C. F. Hu, K. Sato, S. Grasso, M. Estili, S. Q. Guo, K. Morita, H. Yoshida, T. Nishimura, T. S. Suzuki, M. W. Barsoum, B. N. Kim, and Y. Sakka, “Tailoring Ti3AlC2 ceramic with high anisotropic physical and mechanical properties,” *J. Eur. Ceram. Soc.*, vol. 35, no. 1, pp. 393–397, 2015.

[105] C. Hu, Y. Sakka, T. Nishimura, S. Guo, S. Grasso, and H. Tanaka, “Physical and mechanical properties of highly textured polycrystalline Nb 4 AlC 3 ceramic,” *Sci. Technol. Adv. Mater.*, vol. 12, no. 4, p. 044603, 2011.

[106] A. Hendaoui, M. Andasmas, A. Amara, A. Benaldjia, P. Langlois, and D. Vrel, “SHS of High-Purity MAX Compounds in the Ti – Al – C System,” vol. 17, no. 2, p. 3862, 2008.

[107] Y. Khoptiar and I. Gotman, “Synthesis of dense Ti3SiC2-based ceramics by thermal explosion under pressure,” *J. Eur. Ceram. Soc.*, vol. 23, no. 1, pp. 47–53, 2003.

[108] Special Metals Corporation, “INCONEL 718 Datasheet no. SMC-045 (2007),” 2007. [Online]. Available: http://www.specialmetals.com/assets/smc/documents/inconel_alloy_718.pdf. [Accessed: 15-May-2015].

[109] M. A. El Saeed, F. A. Deorsola, and R. M. Rashad, “Optimization of the Ti3SiC2 MAX phase synthesis,” *Int. J. Refract. Met. Hard Mater.*, vol. 35, pp. 127–131, Nov. 2012.

[110] T. Kimura, “Molten Salt Synthesis of Ceramic Powders,” *Adv. Ceram. - Synth. Charact. Process. Specif. Appl.*, pp. 75–100, 2011.

[111] W. B. Tian, P. L. Wang, Y. M. Kan, and G. J. Zhang, “Cr2AlC powders prepared by molten salt method,” *J. Alloys Compd.*, vol. 461, no. 1–2, pp. 6–11, 2008.

[112] X. Guo, J. Wang, S. Yang, L. Gao, and B. Qian, “Preparation of Ti3SiC2 powders by the

molten salt method," *Mater. Lett.*, vol. 111, pp. 211–213, 2013.

[113] D. Chen, X. Tian, H. Wang, and Z. Huang, "Rapid synthesis of bulk Ti3AlC2 by laser melting," *Mater. Lett.*, vol. 129, pp. 98–100, 2014.

[114] J. J. Hu, J. E. Bultman, S. Patton, J. S. Zabinski, and T. Ti, "Pulsed laser deposition and properties of MAX phase formulated Ti3SiC2 thin films," *Tribol. Lett.*, vol. 16, no. February, pp. 1–2, 2004.

[115] J. E. Bultman, S. Patton, P. Eklund, O. Wilhelmsson, U. Jansson, J. Emmerlich, H. Ho, and L. Hultman, "Comment on ''Pulsed laser deposition and properties of M," *Tribol. Lett.*, vol. 17, no. 4, pp. 977–978, 2004.

[116] C. Walter, D. P. Sigumonrong, T. El-Raghy, and J. M. Schneider, "Towards large area deposition of Cr2AlC on steel," *Thin Solid Films*, vol. 515, no. 2 SPEC. ISS., pp. 389–393, 2006.

[117] L. Besra and M. Liu, "A review on fundamentals and applications of electrophoretic deposition (EPD)," *Prog. Mater. Sci.*, vol. 52, no. 1, pp. 1–61, 2007.

[118] "Zeta potential: An Introduction in 30 minutes," *Zetasizer Nano Serles Technical Note. MRK654-01*, vol. 2. pp. 1–6, 2011.

[119] L. Bergstrom, "Colloidal Processing of Ceramics," in *Handbook of Applied Surface And Colloid Chemistry*, K. Holmberg, Ed. John Wiley & Sons, 2001, pp. 201–217.

[120] M. Mishra, Y. Sakka, C. Hu, T. S. Suzuki, T. Uchikoshi, and L. Besra, "Electrophoretic deposition of Ti 3 SiC 2 and texture development in a strong magnetic field," *J. Am. Ceram. Soc.*, vol. 95, no. 9, pp. 2857–2862, 2012.

[121] J. W. Swan and E. M. Furst, "A simpler expression for Henry's function describing the electrophoretic mobility of spherical colloids," *J. Colloid Interface Sci.*, vol. 388, no. 1, pp. 92–94, 2012.

[122] Y. Liang, Z. Sun, J. Chen, X. Liu, and Y. Zhou, "Electrophoretic Deposition of Ti 3 Si(Al)C 2 from Aqueous Suspension," *J. Am. Ceram. Soc.*, vol. 1921, no. 26735, pp. 1916–1921, 2010.

[123] M. Mishra, Y. Sakka, T. Uchikoshi, and L. Besra, "PH localization: A case study during electrophoretic deposition of ternary MAX phase carbide-Ti3SiC2," *J. Ceram. Soc. Japan*, vol. 121, no. 1412, pp. 348–354, 2013.

[124] A. M. Abdelkader, S. J. Garcia, and S. Van Der Zwaag, "Filling of surface cracks in MAX phase ceramics using cathodic electrophoretic deposition," *Ceram. Int.*, vol. 39, no. 3, pp. 3429–3433, 2013.

[125] S. Okamura, T. Tsukamoto, and N. Koura, "Fabrication of Ferroelectric BaTiO 3 Films by Electrophoretic Deposition," *Jpn. J. Appl. Phys.*, vol. 32, no. Part 1, No. 9B, pp. 4182–4185,

1993.

[126] M. F. De Riccardis, D. Carbone, E. Piscopiello, and M. V. Antisari, “Electron beam treatments of electrophoretic ceramic coatings,” *Appl. Surf. Sci.*, vol. 254, no. 6, pp. 1830–1836, 2008.

[127] R. J. Wang, Y. Y. Qian, and J. Liu, “Structural and interfacial analysis of WC92-Co8 coating deposited on titanium alloy by electrospark deposition,” *Appl. Surf. Sci.*, vol. 228, no. 1–4, pp. 405–409, 2004.

[128] I. Schnell and R. C. Albers, “Zirconium under pressure: Phase transitions and thermodynamics,” *J. Phys. Condens. Matter*, vol. 18, no. 5, pp. 1483–1494, 2006.

[129] E. I. Zamulaeva, E. A. Levashov, T. A. Sviridova, N. V. Shvyndina, and M. I. Petrzhik, “Pulsed electrospark deposition of MAX phase Cr2AlC based coatings on titanium alloy,” *Surf. Coatings Technol.*, vol. 235, pp. 454–460, 2013.

[130] H. Gutzmann, F. Gärtner, D. Höche, C. Blawert, and T. Klassen, “Cold spraying of Ti2AlC MAX-phase coatings,” *J. Therm. Spray Technol.*, vol. 22, no. 2–3, pp. 406–412, 2013.

[131] H. Yu, X. Suo, Y. Gong, Y. Zhu, J. Zhou, H. Li, P. Eklund, and Q. Huang, “Ti3AlC2 coatings deposited by liquid plasma spraying,” *Surf. Coatings Technol.*, vol. 299, pp. 123–128, Aug. 2016.

[132] G. A. Steinlage, R. K. Roeder, K. P. Trumble, and K. J. Bowman, “Centrifugal slip casting of components,” *American Ceramic Society Bulletin*, vol. 75, no. 5. pp. 92–94, 1996.

[133] T. El-Raghy and M. W. Barsoum, “Max Phase glove and condom formers,” US 2004/0250334 A1, 2004.

[134] C. Hu, Y. Sakka, H. Tanaka, T. Nishimura, and S. Grasso, “Fabrication of textured Nb4AlC3 ceramic by slip casting in a strong magnetic field and spark plasma sintering,” *J. Am. Ceram. Soc.*, vol. 94, no. 2, pp. 410–415, 2011.

[135] C. R. Bowen and T. Thomas, “Macro-porous Ti2AlC MAX-phase ceramics by the foam replication method,” *Ceram. Int.*, vol. 41, no. 9, pp. 12178–12185, 2015.

[136] Z. Sun, M. Li, L. Hu, X. Lu, and Y. Zhou, “Surface chemistry, dispersion behavior, and slip casting of Ti3AlC2suspensions,” *J. Am. Ceram. Soc.*, vol. 92, no. 8, pp. 1695–1702, 2009.

[137] G. A. Steinlage, R. K. Roeder, K. P. Trumble, and K. J. Bowman, “Textured ceramic tubes via centrifugal slip casting,” in *Textures of Materials*, 1996, pp. 1045–1050.

[138] W. Huisman, T. Graule, and L. J. Gauckler, “Centrifugal slip casting of zirconia (TZP),” *J. Eur. Ceram. Soc.*, vol. 13, no. 1, pp. 33–39, 1994.

[139] G. A. Steinlage, K. P. Trumble, and K. J. Bowman, “Process for slip casting textured tubular structures,” US 6,335,065 B1, 2002.

[140] N. Vitorino, C. Freitas, M. J. Ribeiro, J. C. C. Abrantes, and J. R. Frade, “Applied Clay Science Extrusion of ceramic emulsions : Plastic behavior,” *Appl. Clay Sci.*, vol. 101, pp. 315–319, 2014.

[141] S. Li, J. Xue, L. T, H. Huang, R. Li, and S. Gao, “Preparing MAX phase ceramic tube comprises e.g. adding binder, plasticizer and fiber toughening phase into deionized water, adding suspension into MAX phase nanopowder, extruding and molding slurry and performing pressure-less sintering,” CN108147828–A, 2017.

[142] X.-Y. Dai, F. Shen, J.-Y. Ji, S.-L. Wang, and M. Xu, “Study on extrusion process of SiC ceramic matrix,” *IOP Conf. Ser. Mater. Sci. Eng.*, vol. 265, 2017.

[143] N. Vitorino, C. Freitas, M. J. Ribeiro, J. C. C. Abrantes, and J. R. Frade, “Porous hollow tubes processed by extrusion of ceramic emulsions,” *Appl. Clay Sci.*, vol. 105–106, pp. 60–65, 2015.

[144] M. Ivermark, “Presentation of Maxthal (Attended by D. Shepherd),” in *CARAT 2nd Annual Meeting, Manchester. 16th-17th October*, 2014.

[145] A. Murugaiah, A. Souchet, T. El-Raghy, M. Radovic, M. Sundberg, and M. W. Barsoum, “Tape Casting, Pressureless Sintering, and Grain Growth in Ti 3 SiC 2 Compacts,” *J. Am. Ceram. Soc.*, vol. 87, no. 4, pp. 550–556, 2004.

3. Standard experimental procedure

Several generic experimental techniques were utilised in all results chapters. For simplicity, these are described below with more specialised techniques such as laser sintering and electrophoretic deposition discussed at the beginning of the pertinent chapters. Sources of error and their partial mitigation are covered in Section 10. Treatment of errors.

X-Ray Diffraction (XRD)

X-Ray Diffraction (XRD) is a highly useful characterisation technique for analysing crystalline samples. In principle, x-ray diffractometers rely on satisfaction of Bragg's Law as follows:

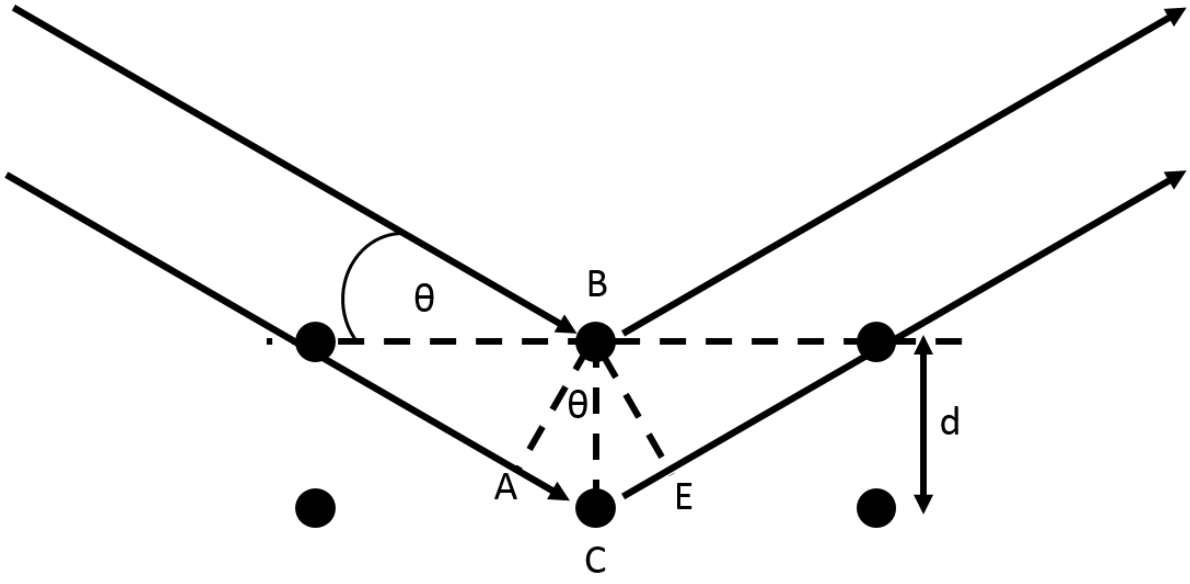

Fig. 3.1 – Diagram of monochromatic parallel X-rays incident at angle θ *on crystal lattice planes separated by distance d.*

With reference to the diagram in Fig.3.1, the top ray is scattered from an atom in the top layer (*B*), while the lower ray scatters from the lower layer atom *(C)*. If the incident x-rays are in phase and parallel, the scattered x-rays will be out of phase (that is they will not constructively interfere with one another to produce a detectable signal) due to the path difference *(ACE*), except in the case where the path difference is equal to a multiple of the wavelength λ:

$$ACE = \mathrm{n}\lambda \quad (3.1)$$

Which is equivalent to:

$$AC = CE = \frac{n\lambda}{2} \quad (3.2)$$

Using trigonometry, the length *AC* can be found:

$$AC = d \sin\theta \quad (3.3)$$

$$d \sin\theta = \frac{n\lambda}{2} \quad \rightarrow 2d \sin\theta = n\lambda \quad (3.4)$$

Therefore detectable 'in-phase' scattered x-rays are only produced when Bragg's Law is fulfilled by certain angles of incident x-rays for different atomic spacings [1].

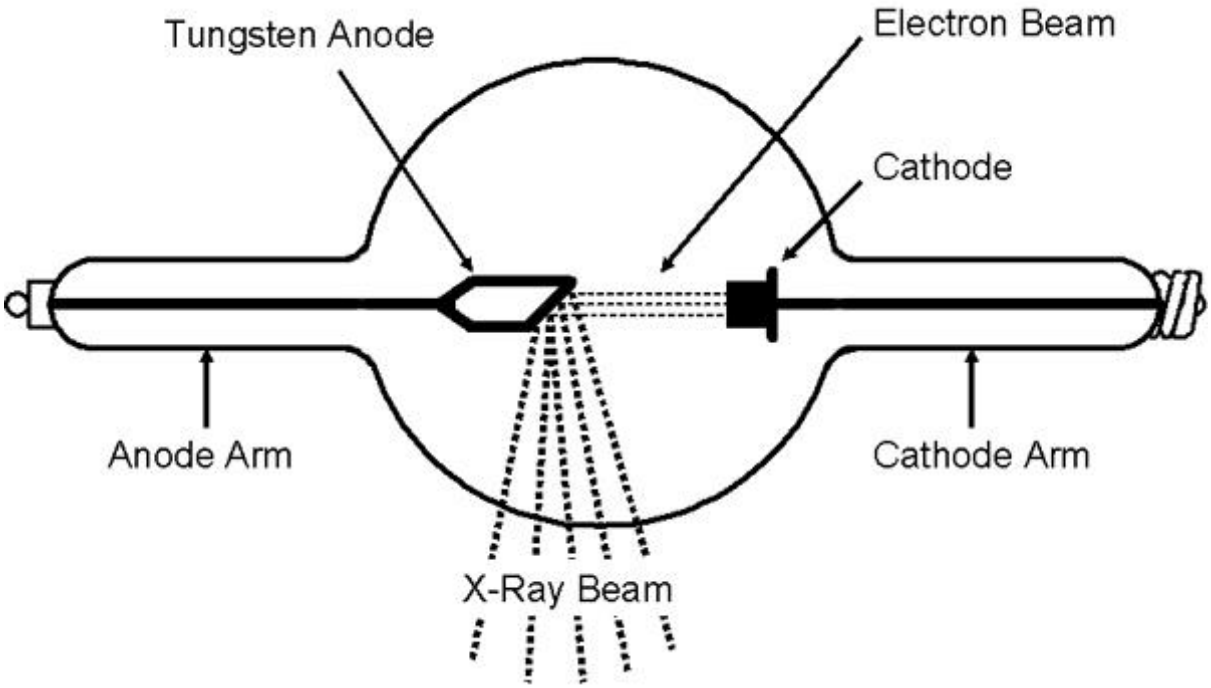

Fig. 3.2 – An example diagram of an x-ray source [2].

In practice, x-ray diffractometers contain an x-ray source, which comprises an evacuated tube with two electrodes within (Fig.3.2). A high voltage is applied across the electrodes, and electrons from the cathode are liberated and impact the anode, emitting photons in the x-ray spectrum as *Bremsstrahlung* and heating up the anode. The wavelength of the photons is dependent on the accelerating voltage and the anode material. Copper is often used due to its high thermal conductivity to prevent overheating.

The emitted x-rays are collimated and made monochromatic by filters that absorb wavelengths other than that targeted. These x-rays strike the sample surface at angle θ, scatter and are recorded by a detector. The detector is on a gantry that rotates around the sample, recording the angle 2θ and the

intensity at that point. The sample itself also rotates to remove any bias from oriented samples. Information gained from XRD is in the form of a spectrum of measured intensity over the angle range tested, and can be used to give information on the crystal structure and hence potentially identify the material phase.

The Bruker D2 Phaser (using Copper Kα radiation) was used primarily in this work for characterisation of synthesis samples and to check if any thermal decomposition occurred post-heating. Standard operating parameters were as follows: $10°<2\theta<70°$, 0.02° step size, dwell time 1s (total time approx. 50min). These parameters were chosen to optimise signal-to-noise ratio, while the scan range covered the characteristic peaks for Ti_3SiC_2 and other common MAX phases. Bruker EVA and ICCD PDF4+ software were used for peak identification.

Rietveld refinement is an analysis technique whereby XRD data is simulated based on input parameters (crystal structure for any included phases) and compared to collected data. By refining values for these parameters using a least squares algorithm, the simulated data can be very closely matched to collected data. From this, information such as the mass fractions of different materials (in a multiphasic sample) can be determined to a reasonable degree of accuracy. In this project Rietveld Refinement was undertaken using GSAS and EXPGUI.

Powder samples were briefly ground using an agate mortar and pestle with isopropanol (IPA) to reduce any dust generation. Once dry samples were placed in a holder and brought to the correct height by removing excess powder with a glass slide. Bulk samples were affixed to the holder with putty and the height was again checked with a glass slide.

Scanning Electron Microscopy (SEM)

Scanning Electron Microscopy (SEM) involves firing a highly collimated beam of electrons onto a sample typically in a vacuum (advanced 'Environmental' SEM (ESEM) can examine samples in a gas atmosphere in the chamber which is isolated from the evacuated column of the electron gun). Each point on the surface is irradiated by electrons, while a charged detector attracts and detects electrons created by different means (see below). The beam then scans the surface point by point allowing for a 2D image or map of surface. Because high energy electrons have a smaller De Broglie wavelength than is achievable with optical microscopy, electron microscopes have superior resolution. SEM also has a greater depth of field than optical microscopy.

Typically electron sources for electron microscopes comprise either a kinked filament made from tungsten or a very fine pointed electrode known as a Field Emission Gun (FEG), both in a high vacuum. These are held at a very high electric potential with an oppositely charged electrode near to the tip. The voltages are high enough to cause thermionic emission of electrons (for filament) or the emission

of electrons via quantum tunnelling (FEG), which accelerate towards the anode. Emitted electrons are then accelerated by a set voltage, collimated and focused by electromagnetic lens to produce a small electron beam that impacts the sample surface.

An electron microscope can be set to detect secondary electrons (SE), which are electrons liberated from the surface by the incident beam, which gives a high resolution image of the surface. Backscattered Electrons (BSE) are electrons from the incident beam that have scattered from a collision with sample nuclei. The energy of backscattered electrons is highly dependent on the mass of the scattering nuclei, and so significant contrast in images comes from differences in atomic number (Z) density. As well as detected electrons, some electron microscopes have one or more x-ray detectors, to detect characteristic x-rays emitted when incident electrons remove electrons from the sample. The transition of electrons to fill these gaps produces x-rays which correspond to different elements. One form of detection is Energy Dispersive X-ray Spectroscopy (EDX or EDS), whereby spectra, scans or maps can be created of the concentrations of various elements within the sample [3]. Fig. 3.3 shows a schematic diagram of a typical SEM.

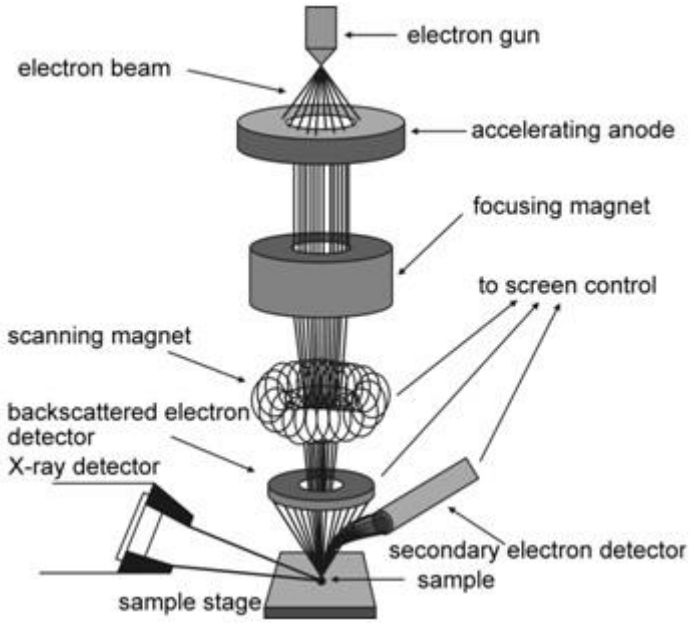

Fig. 3.3 – Schematic diagram of a typical SEM and associated detectors [4]

An FEI Inspect-F and a Hitachi TM3030 were used for SEM imaging throughout the project. The Inspect-F was used primarily for higher resolution images, with an accelerating voltage of 10kV unless otherwise stated, while the Hitachi TM3030 was used to obtain EDX spectra mapping (using built-in detector), using an accelerating voltage of 15kV. Bruker Quantax 70 software was utilised for EDX spectra mapping. Samples where appropriate were affixed to conductive carbon adhesive pads on metal stubs. Powder samples were blown with compressed air to remove any loose particles.

Due to the excellent electrical conductivity of MAX phases no further preparation was necessary, however in the case of samples that required mounting, Buehler Epoxicure 2 resin was used according to the manufacturer's instructions. Samples to be mounted were placed in a small petroleum jelly-lined mould with a removable bottom, and a mixed resin was carefully poured over the top. After curing overnight, the sample was de-moulded, cleaned of any residual jelly and polished according to standard surface preparation (see below). As the resin was non-conductive, mounted samples were carbon coated using an Agar 108CA coater, using 5V for 5s and then the surface was connected to the stub via a line of silver dag (Acheson Electrodag 1415).

Raman Spectroscopy

Different frequencies of Electromagnetic (EM) radiation can be used to excite various constituents of matter, such as atomic nuclei in Nuclear Magnetic Resonance (NMR) being excited by radio wave frequencies. This radiation is absorbed to excite the nuclei to a higher energy level, and radiation of a different characteristic frequency is emitted when the nuclei relax. In the case of Raman spectroscopy, visible light is used to excite atoms or molecules in a sample, and causes vibrations. The vast majority of these are scattered elastically, leaving the collision at the same wavelength as the incident light (referred to as Rayleigh scattering). However, a very small amount of the excited atoms or molecules do not return to the ground state in one transition, and so emit photons of a lower wavelength than the incident (Stokes-Raman scattering). Another scenario arises if the incident photon hits an already excited molecule and forces it down to a de-excited state, in which case a photon of higher than incident energy is emitted (Anti-Stokes scattering). Fig. 3.4 shows a Jablonski diagram for the aforementioned transitions. It is the latter two scattering regimes that Raman spectroscopy detects [1]. Thus for given transition at frequency f, deviations from the laser light frequency f_0 can be seen as f_0+f for Anti Stokes scattering and f_0-f for Stokes Raman Scattering.

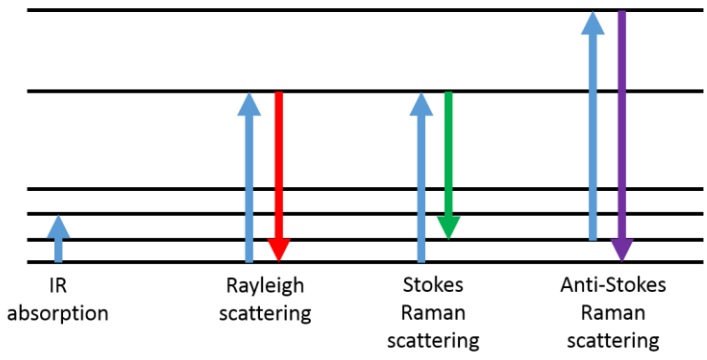

Fig. 3.4 – Jablonski diagram for different scattering regimes when photons interact with atoms or molecules. Redrawn from [5].

For EM radiation, wavelength (λ) and frequency (f) and the energy (E) are related by the following:

$$\lambda = \frac{c}{f} \quad (3.5)$$

$$f = \frac{E}{h} \quad (3.6)$$

Where c is the speed of light and h is Planck's constant.

Raman spectroscopy measures the energy change indirectly and displays results in terms of wavenumbers (ω), with units of cm^{-1} [6].

$$\omega = \frac{1}{\lambda} = \frac{f}{c} \quad (3.7)$$

The light in Raman scattering (typically a visible laser) causes vibrational and rotational excitation of the bonds in materials, leading to characteristic peaks for different bonds, which give peaks in the signal at specific wavenumbers. For MAX phases (of the 312 variety), there are six Raman active modes, and the vibrations in the unit cell that cause these are displayed in Fig. 3.5.

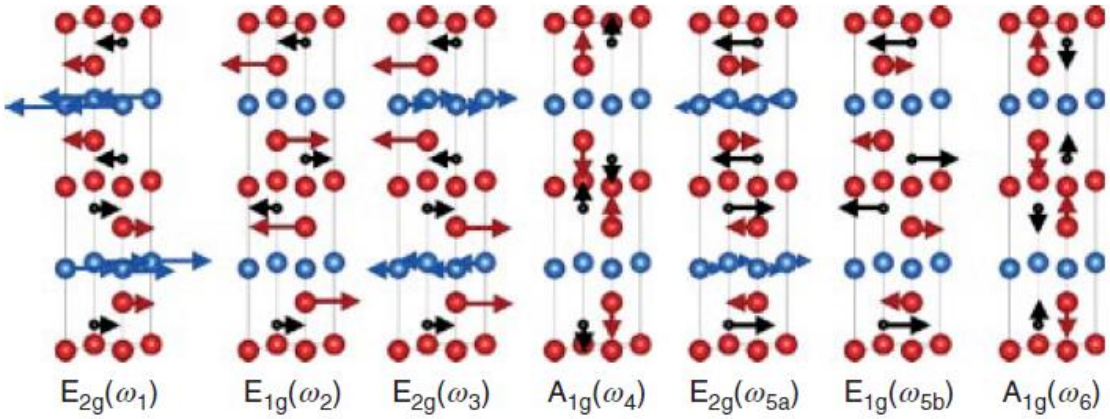

Fig.3.5 – The six Raman vibration modes in 312 MAX phases [7]*. Actual wavenumber values vary between MAX phases based on their composition.*

The Renishaw InVia Raman microscope was used for characterisation of phase composition. A 625nm 20mW laser was used with standard parameters to obtain 10 cumulative 10s scans, as this results in excellent signal-to-noise ratio in a short period of time. Peak positions were compared with literature values for identification. Raman uses a focused beam that covers a small area (~2μm diameter) and therefore regions characterised by Raman were selected by attempted random movement of the XY table by the operator of the control joystick to try and reduce any bias.

Sample Surface Preparation

Polishing of bulk samples was performed using a Buehler Ecomet 250 (140rpm), with an Automet 250 automatic polishing head (50 rpm, contrary rotation for grinding, complimentary for polishing). The samples were ground using P260 and P600 Diamond Grinding Discs (Metprep Cameo Platinum series) using water lubrication. Polishing was carried out using a 3 µm Apex Diamond Grinding disc (Buehler) and if necessary 3 µm and 1 µm water-based diamond suspensions (Metprep monocrystalline) were used on cashmere polishing cloth (Metprep). Samples were ultrasonic cleaned in water to remove any grinding media or loose particulates and then air dried.

Furnace operation

An inert or vacuum atmosphere was required for sintering and heat treatment of MAX phases. Flowing argon served as the inert gas within a tube furnace (Carbolite STF 15/75/450), and was set up to flow at a rate of approximately 0.25L/min, through both a wet and dry bubbler on the inlet and outlet. Once the furnace caps were sealed and the argon turned on, the furnace was left to purge for an hour before beginning the programme. For vacuum sintering (Elite TSF15-50/180-2416), the pump (Edwards RV3, $2x10^{-3}$ mbar ultimate pressure) was turned on and the system was once again left for an hour to evacuate before running the program, with the pump remaining on during the run. In all cases, furnaces were ramped from room to the dwell temperature at a rate of 3°C/min or 5°C/min (depending on the furnace used). Upon completion of the dwell time, furnaces were cooled to room temperature at the same rates.

Particle size analysis

Particle size analysis was performed on a Malvern Mastersizer 3000, in water. Due to the platelet shaped grains of Ti_3SiC_2 Mie Scattering settings for non-spherical particles were used, and an obscuration level of 2.75% in water. Values for refractive index were estimated from work done by Ali *et al*. [8], and absorption was taken to be 1.

References

[1] A. R. West, *Solid State Chemistry*, 2nd ed. Wiley, 2014.

[2] “Coolidge X-ray tubes.” [Online]. Available: https://www.orau.org/ptp/collection/xraytubescoolidge/coolidgeinformation.htm.

[3] L. Reimer, *Scanning Electron Microscopy: Physics of Image Formation and Microanalysis*, 2nd ed. Springer-Verlag, 1998.

[4] “SEM diagram.” [Online]. Available: http://www.technoorg.hu/news-and-

events/articles/high-resolution-scanning-electron-microscopy-1/.

[5] “Jablonski Diagram for Raman.” [Online]. Available: http://chyscience.blogspot.com/2012/09/.

[6] E. Smith and G. Dent, *Modern Raman Spectroscopy – A Practical Approach*. John Wiley & Sons, 2005.

[7] M. W. Barsoum, “MAX Phases: Properties of Machinable Ternary Carbides and Nitrides,” in *Wiley-VCH*, vol. 1, Wiley-, 2013.

[8] M. S. Ali, A. K. M. a. Islam, M. M. Hossain, and F. Parvin, “Phase stability, elastic, electronic, thermal and optical properties of Ti3Al1−xSixC2 (0≤x≤1): First principle study,” *Phys. B Condens. Matter*, vol. 407, no. 21, pp. 4221–4228, 2012.

4. Characterisation and synthesis of MAX phases

This section covers initial characterisation of proprietary MAX phase Ti_3SiC_2 (Maxthal 312, Sandvik Kanthal) as well as attempts at reactive SPS synthesis of Ti_3SiC_2. MSS was also used in-house to attempt the synthesis of Ti_3SiC_2, Ti_3AlC_2 and Ti_2AlC with supporting characterisation. Finally an attempt to synthesize new hybrid MAX phases (M-site substitution) considering the elemental recommendations of Grove *et al.* [1] with potentially better neutronic properties was undertaken using MSS and SPS.

4.1 Characterisation of Maxthal 312

Maxthal 312, sold by Sandvik Kanthal, is a commercially available Ti_3SiC_2. It is used in the context of this thesis as a stock MAX phase to study potential net-shape forming routes, due to its availability and prolific appearances in the literature. However, it is an unlikely candidate for nuclear applications as its oxidation resistance is worse than some aluminium containing MAX phases and is not optimum from a neutronics perspective (see Literature Review). Fig. 4.1.1 shows the XRD pattern of the as-received Ti_3SiC_2, which contains 10-15 vol.% TiC as an ancillary phase. According to the packaging, the material was synthesised using SHS.

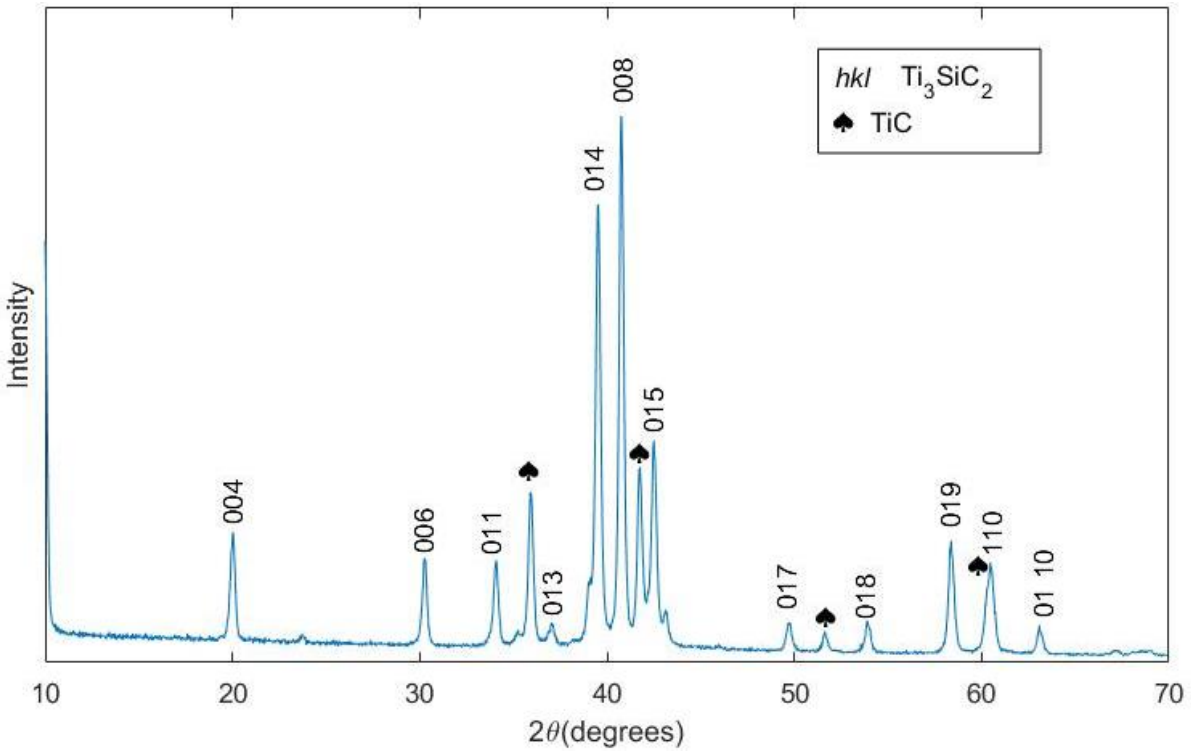

Fig. 4.1.1 –XRD spectrum of the as-received Maxthal 312.

The results of Raman analysis are displayed in Fig. 4.1.2. The characteristic peaks of single crystal Raman spectroscopy of Ti_3SiC_2 are labelled ω_{1-5} [2], while a broad TiC peak can be seen around 420 cm^{-1} [3].

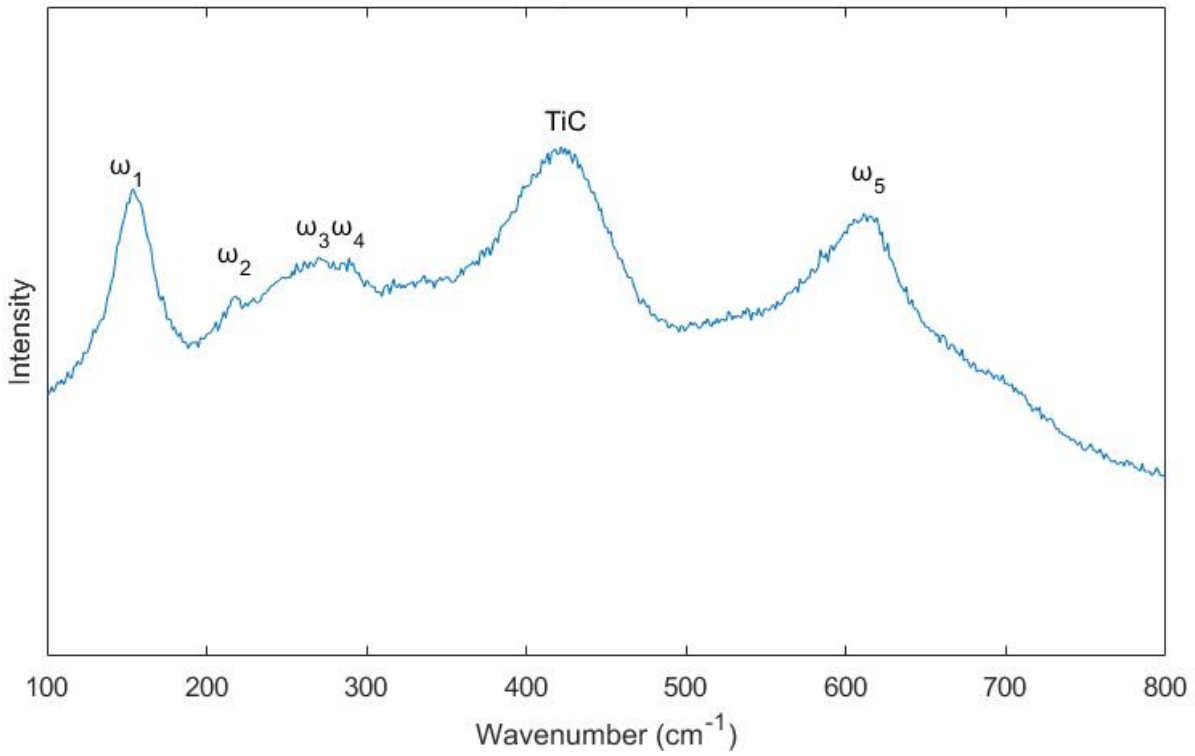

Fig. 4.1.2 – Raman analysis of Maxthal 312. Characteristic Ti_3SiC_2 peaks are marked with ω.

The powder morphology is shown in Fig. 4.1.3, using the FEI Inspect F microscope with an accelerating voltage of 20kV. The powder is irregularly shaped (consistent with SHS after milling [4]) and the nanolaminate nature of the material can clearly be seen.

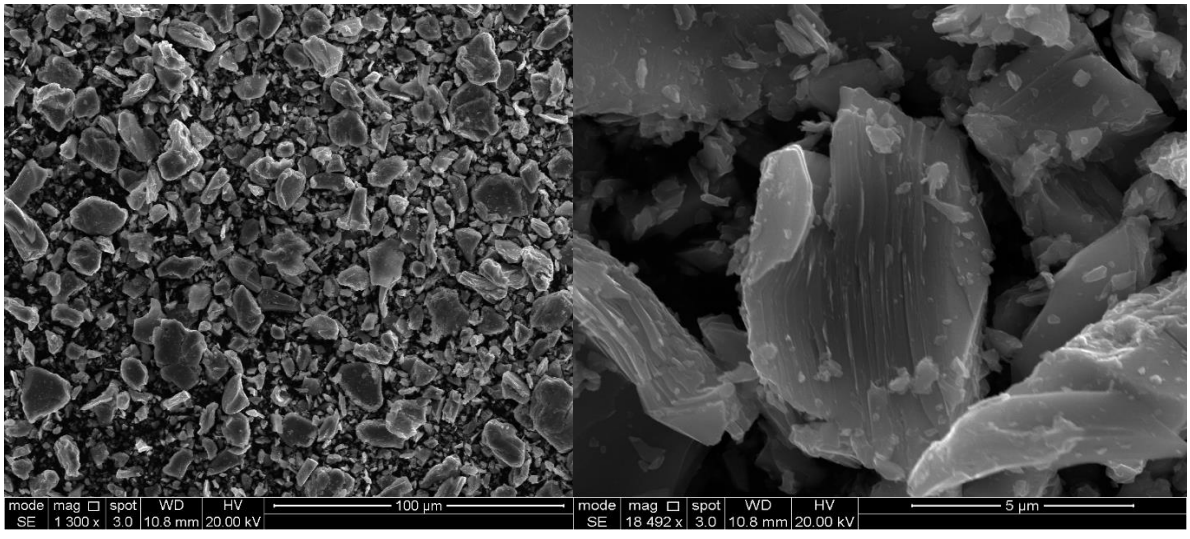

Fig. 4.1.3– Secondary electron (SE) SEM images of the as-received Maxthal 312

Particle size analysis was performed on a Malvern Mastersizer 3000, in water (see Standard Procedure section). The particle size profile is shown in Fig. 4.1.4 and the median particle size (D_{50}) was 7.07 ±0.30µm.

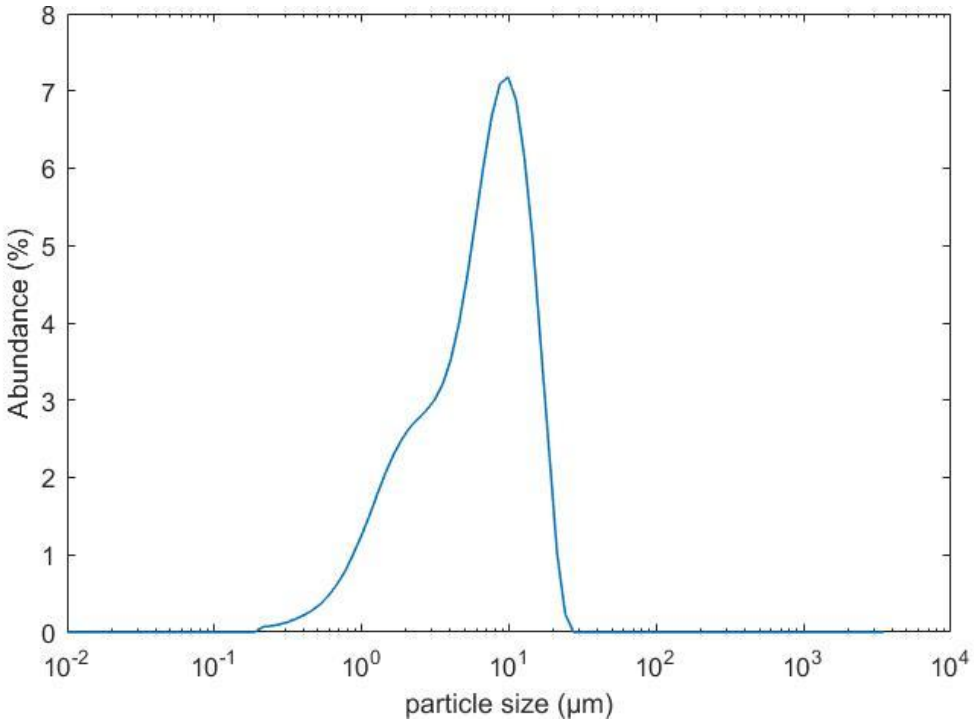

Fig. 4.1.4 – Particle size analysis of as-received Maxthal 312.

The Maxthal 312 was used for initial training and to test some parameters on the SPS furnace before attempting synthesis. It was used in further experiments in subsequent sections as a generic MAX phase in place of reactor appropriate phases.

4.2 Reactive SPS synthesis of Ti_3SiC_2

Reactive Spark Plasma Sintering was undertaken due to its prevalence in the literature and the high degree of success reported. Samples were synthesised from elemental powders Ti, Si and C, as well as from TiC, Si and Ti. Synthesis dwell temperatures were between 1300 and 1400 °C based on the literature. Dwell times were between 10 and 15 minutes.

4.2.1 Method and materials

Titanium powder (Alfa Aesar, >74µm, 99.5% pure), silicon powder (Sigma Aldrich, >44µm, 99% pure), crystalline graphite powder (Alfa Aesar, >44µm, 99% pure) and titanium carbide (Alfa Aesar, 2µm, 99.5% pure) were used. For the elemental powder synthesis, Ti, Si and C were combined in a 3:1.2:2 molar ratio, while the TiC, Si, Ti based samples were combined in the molar ratio 2:1.2:1, to give the same elemental molar ratio. The 20% excess of the A element, silicon in this case, is a common

addition in the literature when synthesising MAX phases to allow for some volatilisation during heating. The elemental reactant samples were milled in a planetary ball mill (Fritsch Pulverisette 6, yttria-stabilised ZrO_2 pot and spherical ZrO_2 media) for 10 minutes in IPA, and subsequently dried in a 90°C oven (Memmert 100-800) for 2 hours. Due to its high hardness, the reactant mixtures containing TiC were roller milled (Brook Crompton TYP T-DA63MB-D) for 24 hours with yttria-stabilised ZrO_2 cylindrical media (1cm diameter, 1.5cm length, rounded ends) to prevent damage and contamination from the mill bowls.

For the synthesis, 5g of the reactant mixes were loaded into graphite foil-lined 20mm diameter graphite dies with two layers of graphite foil between each of the punches and the powder. The punch and die assembly containing the powder was uniaxially pre-pressed at 160MPa for 5 minutes, and then loaded into the SPS furnace (FCT Systeme). Sintering was performed under vacuum (pressure not measured), with a uniaxial force of 10kN and a heating rate of 100°C/min. Separate samples were held at 1300°C for 10 and 15 minutes, at 1350°C for 10 minutes and at 1400°C for 10 minutes. After the dwell temperature and time, the samples were left in the chamber for 10 minutes to cool unassisted. Following this, the adhered graphite foil was removed with a sharp knife where possible, with remaining foil removed during the grinding/polishing process (see Standard Procedure section). XRD was performed and SEM-EDX using the Hitachi TM3030. Vickers hardness measurements were performed using a Mitutoyo nanoindenter under 1N load for 10 seconds.

4.2.2 Results

Fig. 4.2.1 displays the XRD patterns for the samples synthesised using elemental powders between 1300 and 1400 °C. Ti_3SiC_2 is present, alongside TiC, $TiSi_2$ intermetallic and graphite. The graphite intensity decreases as the temperature increases, along with an increase in intensity from the 014 Ti_3SiC_2 peak, but even at higher temperatures the synthesis result is not phase pure. Fig. 4.2.2 shows the characterisation results for the samples made with TiC as a reactant. There are two anomalous graphite peaks in the samples synthesised at 1300°C (15 minutes) and 1400 °C (10 min) which may be unreacted source powder, diffusion from the graphite dies or an inclusion of some of the graphite foil. At 1300°C there are strong TiC peaks, likely unreacted material, alongside some MAX phase, and $TiSi_2$. The samples synthesised at 1350°C showed a marked decrease in ancillary phases, as well as some of the MAX phase peaks relative to the 014 Ti_3SiC_2 peak. This latter suggests some orientation of the MAX phase crystals, which has been shown to occur in reactive SPS [6]. However, once again the samples are not phase pure.

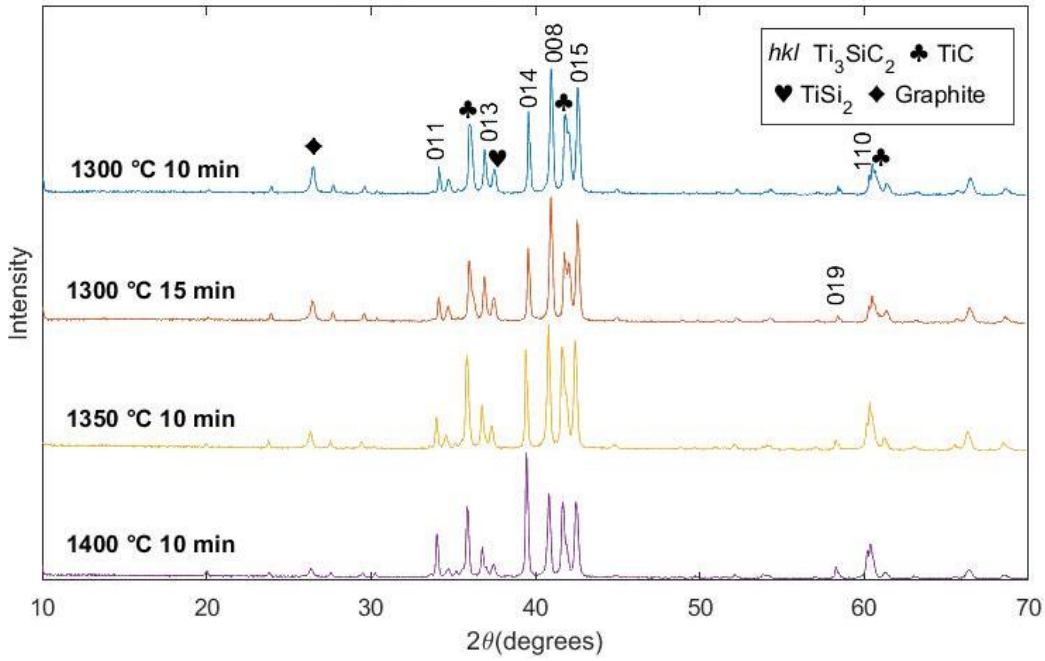

Fig. 4.2.1– XRD spectra of reactive SPS results from elemental powders.

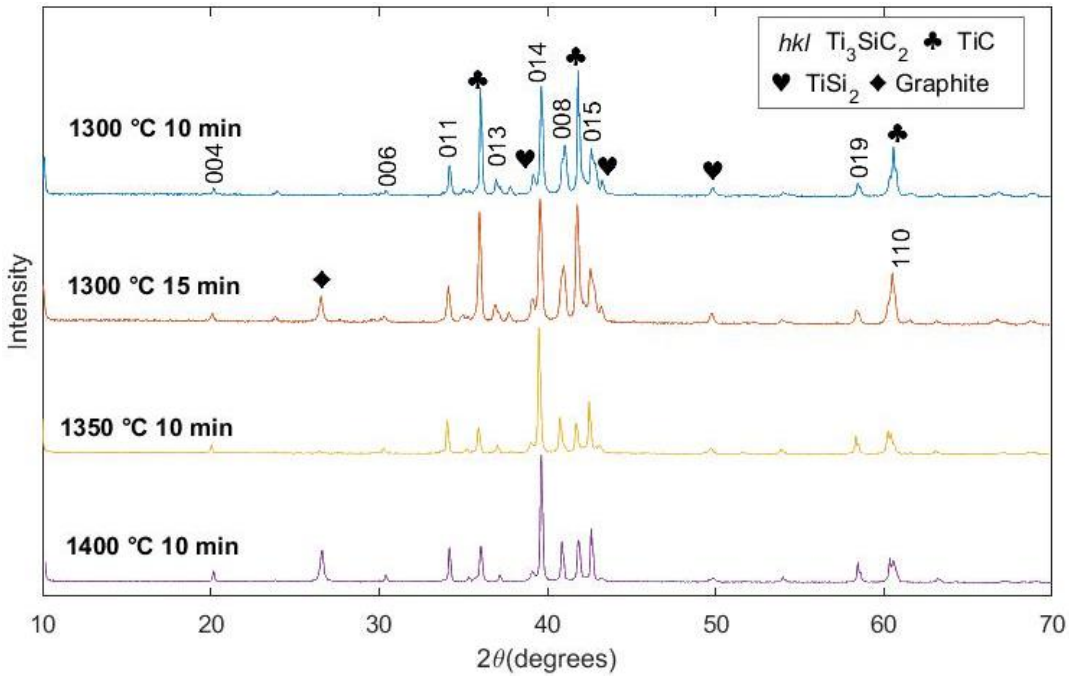

Fig. 4.2.2 – XRD spectra of reactive SPS results from TiC, titanium and silicon.

The ground and polished surface of the SPS pellets synthesised at 1300°C (10 min) and 1400°C (10 min) from elemental powders are shown in Fig. 4.2.3. In both cases, the material has large grains of graphite in a titanium and silicon matrix. EDX spectra analysis confirms that the dark regions are carbon and not voids, and also reveals some $TiSi_2$ present (Fig. 4.2.3).

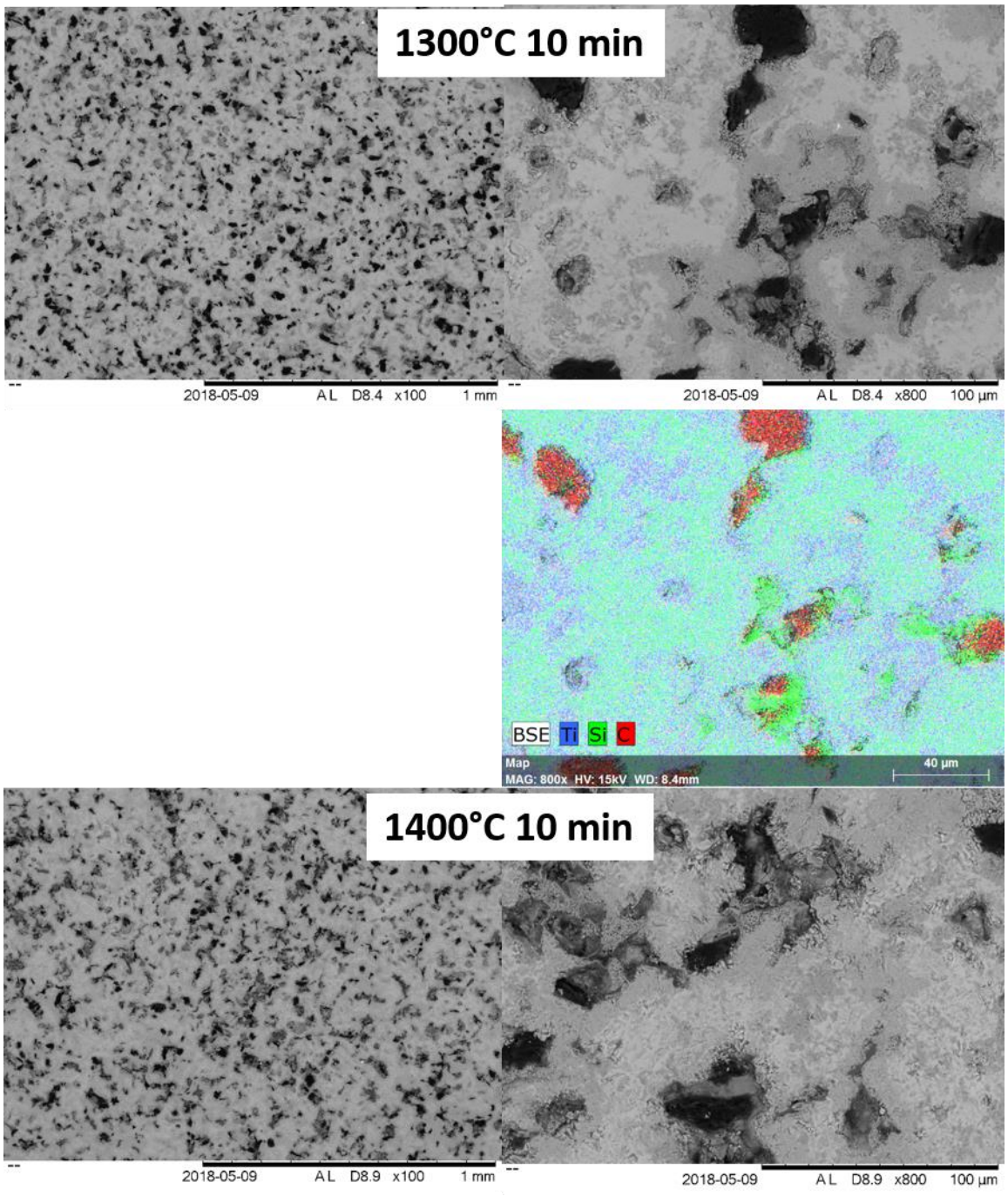

Fig. 4.2.3 – SE images of polished SPS samples made from elemental powders; EDX spectra analysis shown of 1300 °C 10 minute sample under relevant image.

The surface morphologies of the samples synthesised with TiC as a reactant differ from the elemental synthesis (Fig. 4.2.4). After 1300°C for 10 minutes, the sample is also multiphase, and contains silicon-rich areas surrounding titanium particles. Some small micron-scale grains are visible in areas of low density, which may correspond to unreacted TiC. However, silicon-surrounded titanium particles are absent in the sample after 1400 °C for 10 minutes, suggesting the reaction between Ti and Si to form $TiSi_2$ has now gone to completion, but that the reaction to form Ti_3SiC_2 was incomplete.

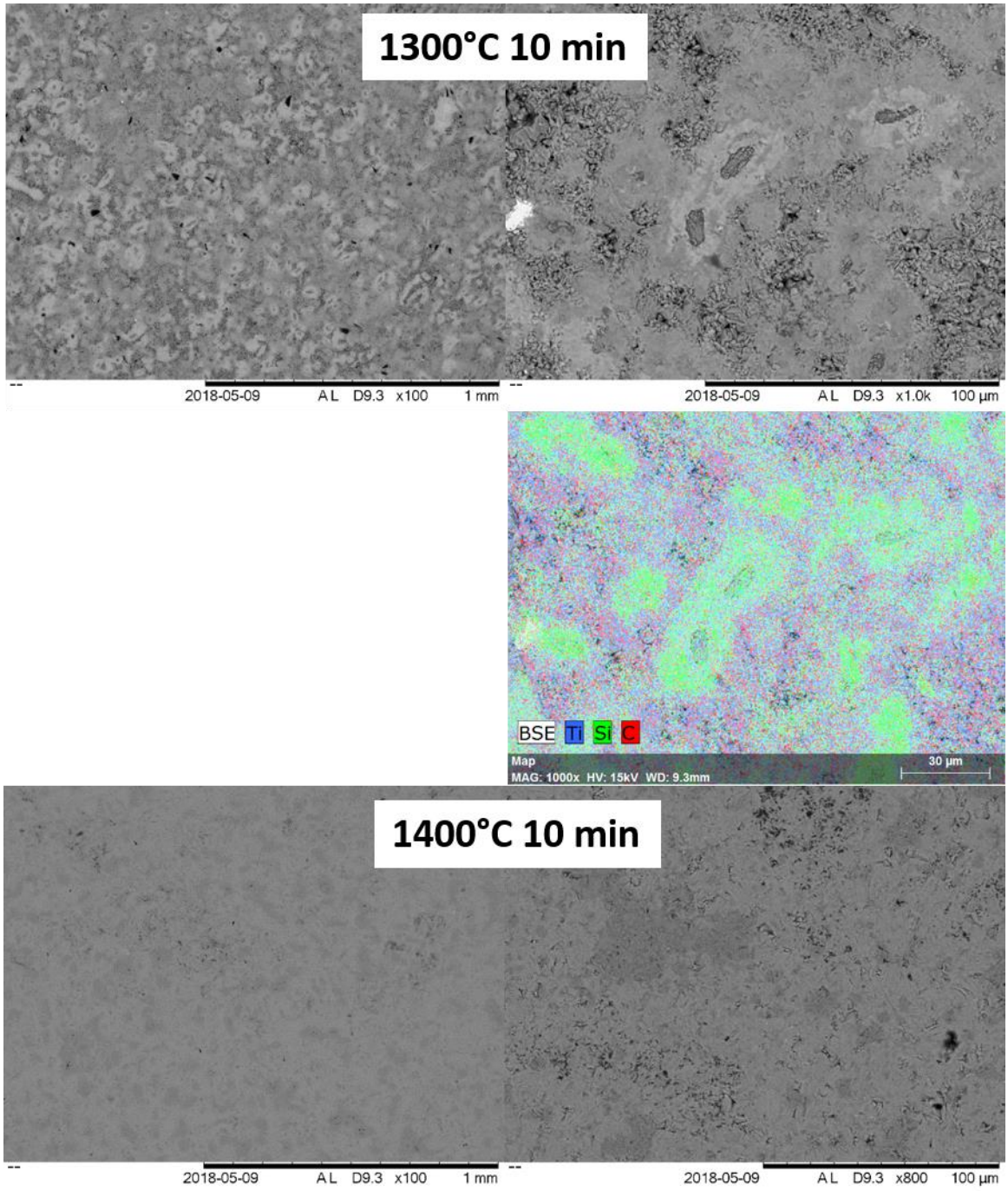

Fig. 4.2.4 – SE images of polished SPS samples made from TiC, Ti and Si; EDX spectra analysis of the 1300 °C 10 minute sample under relevant image.

Vickers hardness tests were performed and values are displayed in Fig.4.2.5. There is large variation in the recorded values, and this is due to the heterogeneity of the pellets. Individual measurements and mean values are displayed in Fig. 4.2.5.

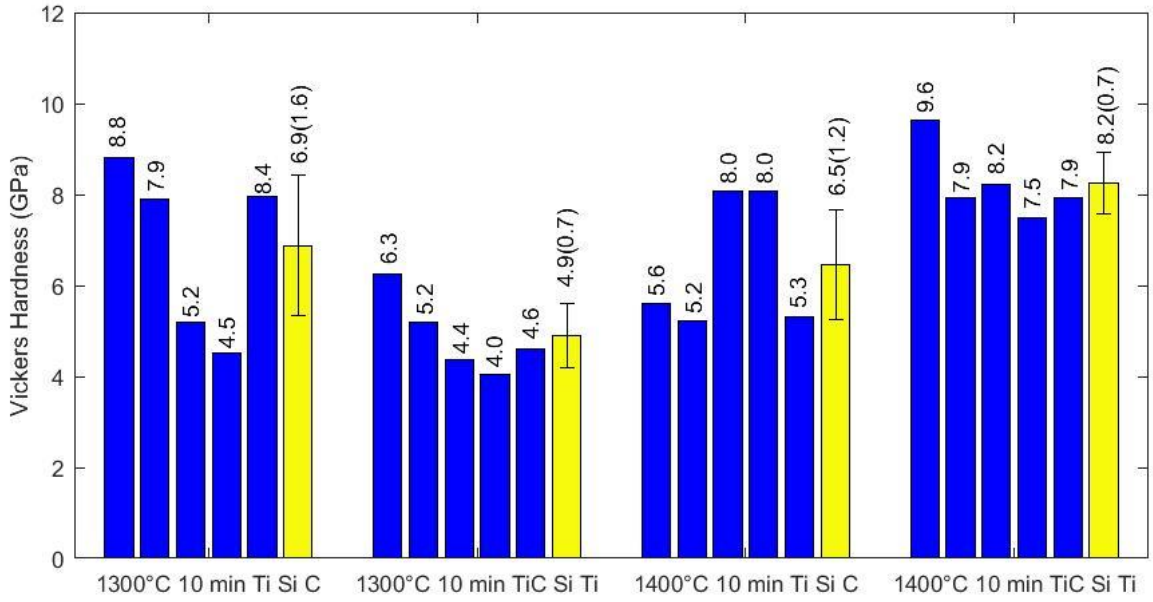

Fig.4.2.5 – HV_1 values for synthesised Ti_3SiC_2 pellets. Mean values displayed in yellow. Spread bars on mean columns and values in brackets after mean values show standard deviation.

4.2.3 Discussion

The purity of the samples synthesised with elemental powders was lower than expected. Under SEM, it was seen that large flakes of graphite were not entirely consumed during the reaction step, resulting in silicides. As the temperature was increased, the product phases changed little in their intensity, so further size reduction of the particles and increase in specific surface area, for graphite in particular, might improve the synthesis.

The TiC based samples were overall more successful than the elemental powder syntheses. The reason for this is likely threefold: using TiC removed the large graphite particles, and instead was very fine (2µm) which provided superior surface area for reaction; difference in milling times; and by having TiC present immediately, the initial formation of TiC from titanium and carbon can be bypassed. However, the 'TiC' sub-lattice of Ti_3SiC_2 is actually sub-stoichiometric Ti_3C_2 (Titanium sesquicarbide which can expressed as $TiC_{0.67}$), which likely would have served as a better reactant. Riley and Kisi worked on crystalline precursors for MAX phase synthesis, and found that Ti_3AlC_2 can be formed at lower than usual temperatures by starting with Ti_3C_2 and aluminium [7] [8]. By starting with Ti_3C_2, the reaction eliminates the need for metallic titanium and skips onto another formative step, improving the overall purity. Another possibility is the difference in milling techniques used on the two reactant batches. The elemental samples were milled for only 10 minutes, albeit with a much higher-energy milling technique, while the TiC containing batch was milled for 24 hours. A longer milling of the elemental powders may have reduced the size of the graphite, resulting in more of the reaction taking place.

The Vickers hardness literature value for polycrystalline Ti_3SiC_2 is 4-6GPa, depending on the applied load [2]. The hardness values for the elemental synthesis were found to fall into two distinct groups, which is likely due to the uneven composition and density of the pellet surfaces, visible under SEM. The TiC based samples were more consistent, and showed a higher hardness than expected, attributed to the higher ceramic TiC content.

4.2.3 Conclusions

Ti_3SiC_2 was synthesised through a reactive SPS procedure from elemental powders, and also TiC, Ti and Si. Synthesis from elemental powders was partially successful, but contained ancillary silicides and carbides, and under SEM it was found that large particles of graphite had not reacted, and were instead embedded in a Ti-Si matrix. Removing the graphite and using TiC instead resulted in a more complete reaction, but still with some extraneous TiC and $TiSi_2$.

4.3 Molten salt synthesis of Ti_3SiC_2

After SPS was unsuccessful at producing phase pure MAX phases, MSS was attempted, due to its relative novelty in the literature, its ease of reproduction and because it results in a powder product, removing the need for an intensive milling step to powder SPS pellets so they can be used for coating procedures. The methodology for this experiment was based on that of Guo et al. for MSS of Ti_3SiC_2 [9], who found the optimum synthesis temperature was 1200 °C with an even weight of salt and reactants.

4.3.1 Methods and materials

Ti (Alfa Aesar, >74 µm, 99.5% pure), Si (Sigma Aldrich, >44 µm, 99% pure) and C (Alfa Aesar, >44 µm, 99% pure) were combined in a 3:1.2:2 molar ratio. Samples were also made from Ti, SiC (Sigma Aldrich, 37–74µm, no purity given) and C in the molar ratio of 3:1.2:1. These reactant powder samples were then combined in a 1:1 weight ratio (1g each) with NaCl (Alfa Aesar, 99.5% pure, powder size not supplied) and milled in a Fritsch Pulverisette 23 vertical shaker mill (1800 oscillations per minute, 10 minutes, stainless steel mill pot and media) in heptane; a non-polar solvent instead of ethanol to prevent any absorbed water dissolving the salt. The milled powder was dried in a 90°C oven (Memmert 100-800) for 8 hours, and then uniaxially pressed into 13mm diameter pellets under 200MPa. The samples were placed on an alumina crucible boat and heated in a tube furnace under flowing argon (~0.25L/min) at 1200 °C for 2 hours. A sample was also held at 1200°C for 20h, to try and complete the reaction. Two samples were also held at 900°C for 2 and 20 hours. These low temperature

experiments were to determine how catalysing the effect of molten salt was well below the accepted synthesis temperature. After being in the furnace, the samples were crushed by hand in an agate mortar and pestle, and washed through a Büchner funnel with water several times to remove any salt. Finally the powders were dried again at 90°C overnight before being characterised by XRD. Rietveld refinement was performed using GSAS [10] and EXPGUI [11].

4.3.2 Results

The XRD patterns of the samples synthesised with elemental powders are shown in Fig. 4.3.1. Samples made with SiC resulted in no product phase in any of the samples, so have been omitted. At 900°C, titanium silicide phases and TiC are the main phases present, as well as a small amount of unreacted graphite. No identifiable Ti_3SiC_2 peaks are visible after 2 or 20 hours at 900°C. When the dwell temperature is increased to 1200°C for 2 hours, Ti_3SiC_2 is present, alongside $TiSi_2$, Ti_5Si_3 and TiC. After 20 hours, the Ti_5Si_3 intensities are reduced, likely from Si volatilisation, but the sample purity did not improve. Rietveld refinement was performed on the 1200°C, 20 hour sample (difference profile shown in Fig. 4.3.1), and it was found to contain by weight 39% Ti_3SiC_2, 34% TiC, 15% Ti_5Si_3 and 12% $TiSi_2$. The fit had a χ^2= 3.362 and a weighted Rp value of 0.107.

Examining the powders (1200°C 2 hours) under SEM reveals the needle-like grains of Ti_3SiC_2, which are morphologically similar to those synthesised by Guo *et al.* and the laminar nature is clearly visible (Fig. 4.3.2). The grains are approximately 1µm in width, and appear to have grown via templating off of one of the reactants (growth on the surface of another phase) or a non-target phase.

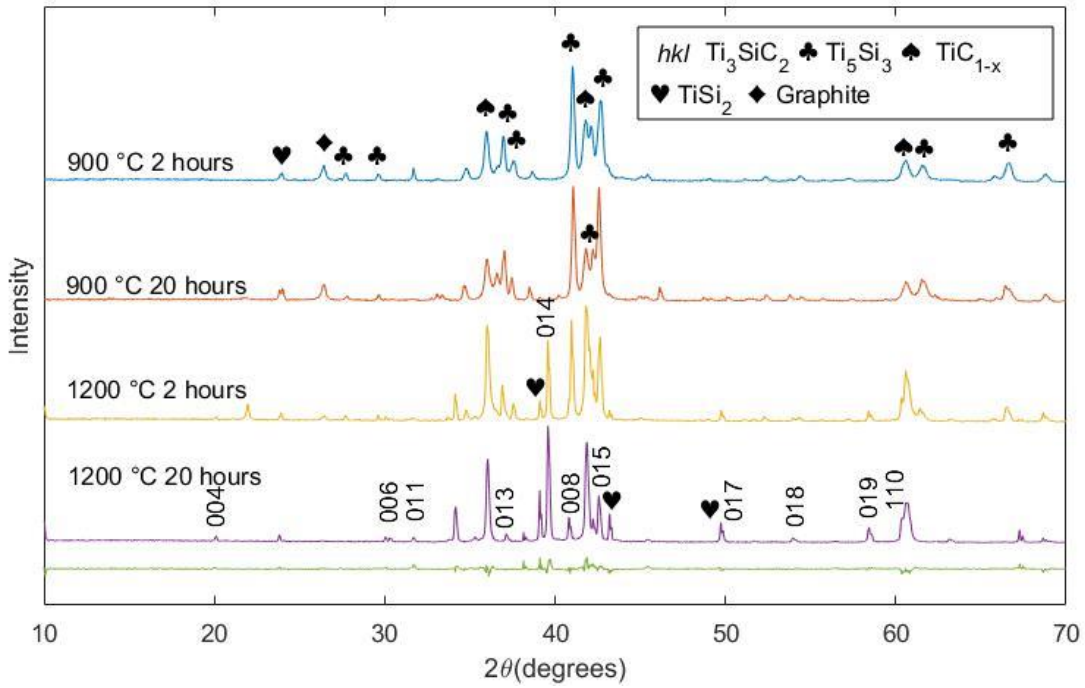

Fig.4.3.1 – XRD spectra for molten salt synthesised Ti_3SiC_2. Rietveld refinement difference in green.

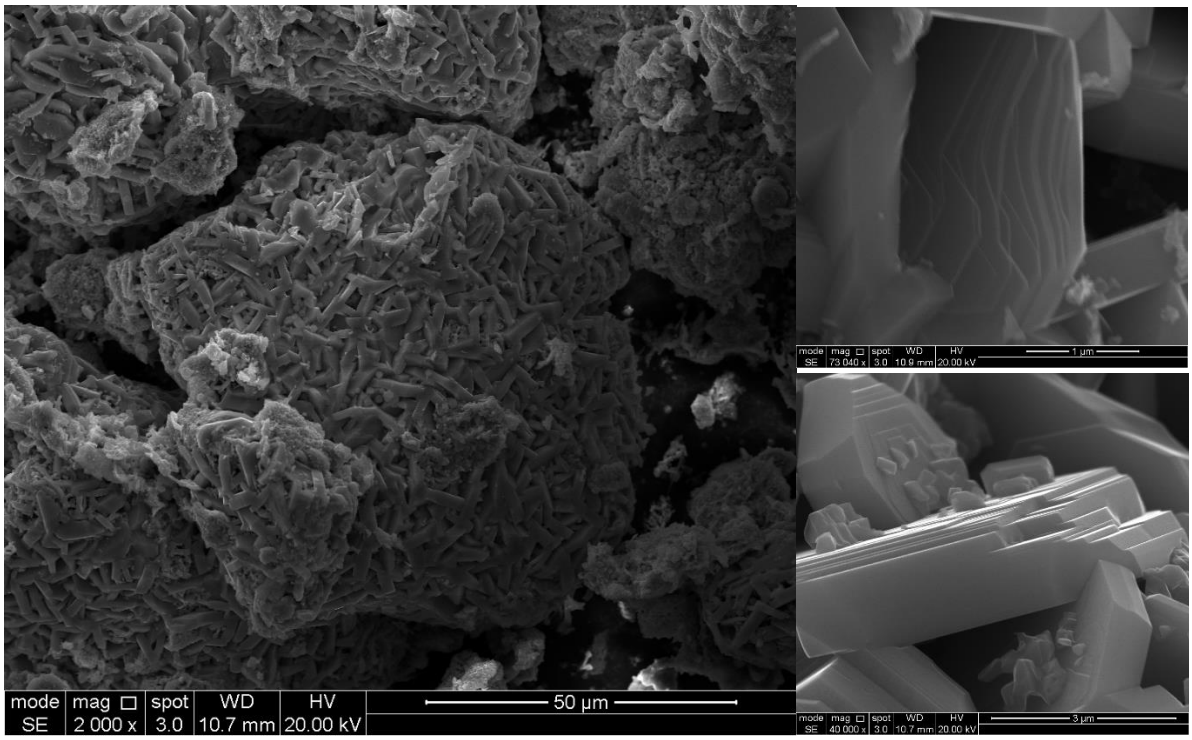

Fig. 4.3.2 – SE images of Ti_3SiC_2 synthesised in NaCl at 1200°C for 2 hours. Note the individual layers visible in the images on the right.

4.3.3 Discussion

The samples made with SiC failed to yield any MAX phase. The most likely reason for this is that structurally Ti_3SiC_2 does not resemble SiC; the Si is in fact bonded to Ti between layers of Ti_3C_2, meaning this was not a useful way to provide Si and some of the C for the reaction. The samples from elemental powders resulted in a partial success at 1200 °C, and did not improve after 20 hours of dwell time. Despite using similar reagent particle sizes and following the procedure, the results Guo *et al.* achieved were not able to be replicated. Their reactants were milled for 10 hours in ethanol with ZrO_2 media, which was assumed to be roller milling where such longer milling times are typical. In this work, a higher energy milling technique (vertical shaking) was used for a shorter time in an attempt to replicate a long low energy milling step, but it may have failed to reduce particle sizes enough to facilitate a full synthesis during the 2 hour dwell. After 20 hours some of the salt and the silicon would have evaporated from the sample, which is why the purity after a long dwell was not superior to the short.

4.3.4 Conclusion

Ti_3SiC_2 was successfully synthesised by MSS at 1200°C for 2 hours and 20 hours from elemental powders and NaCl. The sample contained a large portion of ancillary phases, mainly TiC and titanium silicides. The 20 hour sample was found to be 39% Ti_3SiC_2 by weight. A novel reactant composition using SiC as a source of silicon were unsuccessful at the temperatures and times used. The layered morphology of the needle-like grains was seen by SEM, with crystals growing to approximately 1µm thick and several microns long.

4.4 Molten salt synthesis of Ti_2AlC and Ti_3AlC_2

A more in-depth analysis on the synthesis of Ti_2AlC via the molten salt method was undertaken due to an apparent gap in the literature. The experiment varied dwell temperature, time and type of salt used. Changing the stoichiometry and increasing the temperature was also performed to synthesise Ti_3AlC_2. The results of the smaller scale trials were published [12].

When synthesising materials in molten salt, two separate reactions can occur: templating and dissolution-precipitation [13]. Templating occurs when one of the reactants is soluble in molten salt and reacts on the surface of an insoluble reactant, while dissolution-precipitation occurs when all the reactants dissolve, react in solution and precipitate a product phase. Templated products will bear some resemblance to the morphology of the precursor powders, while dissolution-precipitation is

independent of starting material morphology. The reaction pathway was determined by comparing the morphology of the reactant powders to product powders, and EDX was used to confirm these findings.

4.4.1 Methods and materials

Ti (Alfa Aesar, 74µm, 99.5% pure), Al (Alfa Aesar, 44–420µm, 99.8% pure) and graphite powder (Alfa Aesar, 44µm, 99% pure) were used as reactants, and NaCl (Alfa Aesar, 99.5% pure, powder size not supplied) and KCl (Sigma Aldrich, 99% pure, powder size not supplied) were used as fluxes. Synthesis was carried out separately using NaCl only, KCl only, and an equal mix of the two, which forms a low temperature eutectic which melts at 658°C [14], referred to from here on as NaKE. For synthesis of Ti_2AlC, a molar ratio of 2:1.2:1 was used, while 3:1.2:2 was used for Ti_3AlC_2 synthesis. For each sample, the molar ratio of reactants were combined with the salt in a 1:1 weight ratio (1g each) and subjected to the same milling, pressing and heating regime as described in the previous section above. Dwell temperatures for the furnace in this experiment were generally lower than with Ti_3SiC_2, as it was hoped that the molten aluminium present during the process would further aid diffusion and synthesis. Separate Ti_2AlC reactant samples were heated to 900°C, 950°C, 970°C and 1000°C for 2 hours, while an additional sample was heated to 970°C for 5 hours to try and demonstrate sub-1000 °C synthesis. The Ti_3AlC_2 reactant samples were heated to 1300°C for 2 hours. The resulting powders were analysed using XRD and SEM. To demonstrate the ability to scale up the process, another batch was created using KCl as the salt flux with a total salt and reactant weight of 20g. This was processed exactly as described above, but pressed into two 10g, 20mm diameter pellets and held in the furnace at 1000°C for 2 hours. After crushing, washing and drying the product pellets, the sample was characterised by XRD and compared to the smaller batches. Rietveld refinement was performed using GSAS [10] and EXPGUI [11].

To determine the reaction path for Ti_2AlC in molten salt, SEM images of the milled reactants were captured to determine their morphology. Some product powders were then set in resin, polished and analysed using SEM (Hitachi TM3030) to determine morphological similarities. EDX was also performed to investigate homogeneity of the product.

4.4.2 Results

Fig. 4.4.1 shows the XRD patterns for samples synthesised with NaCl over the range of temperatures. Surprisingly some Ti_2AlC is present in the 900°C sample, alongside titanium aluminides, TiC and graphite. As the dwell temperature increases, the ancillary phases decrease in intensity relative to the

MAX phase peaks. In particular, between 970°C (2 hours) and 970°C (5 hours), the intensity of the TiAl peaks relative to the 013 Ti_2AlC peak substantially diminish. At 1000°C the sample consists of only Ti_2AlC and a small amount of TiAl. Rietveld refinement of the NaKE-synthesised sample at 1000°C gives the sample composition of 88% Ti_2AlC and 12% $Ti_{0.9}Al_{1.1}$, with χ^2 value of 4.919 and a weighted R factor of 0.1337. Refining the structure also revealed the presence of an unknown minor phase with peaks at ~41.7° and 42.6°, leading to the higher χ^2 and weighted R-factor values.

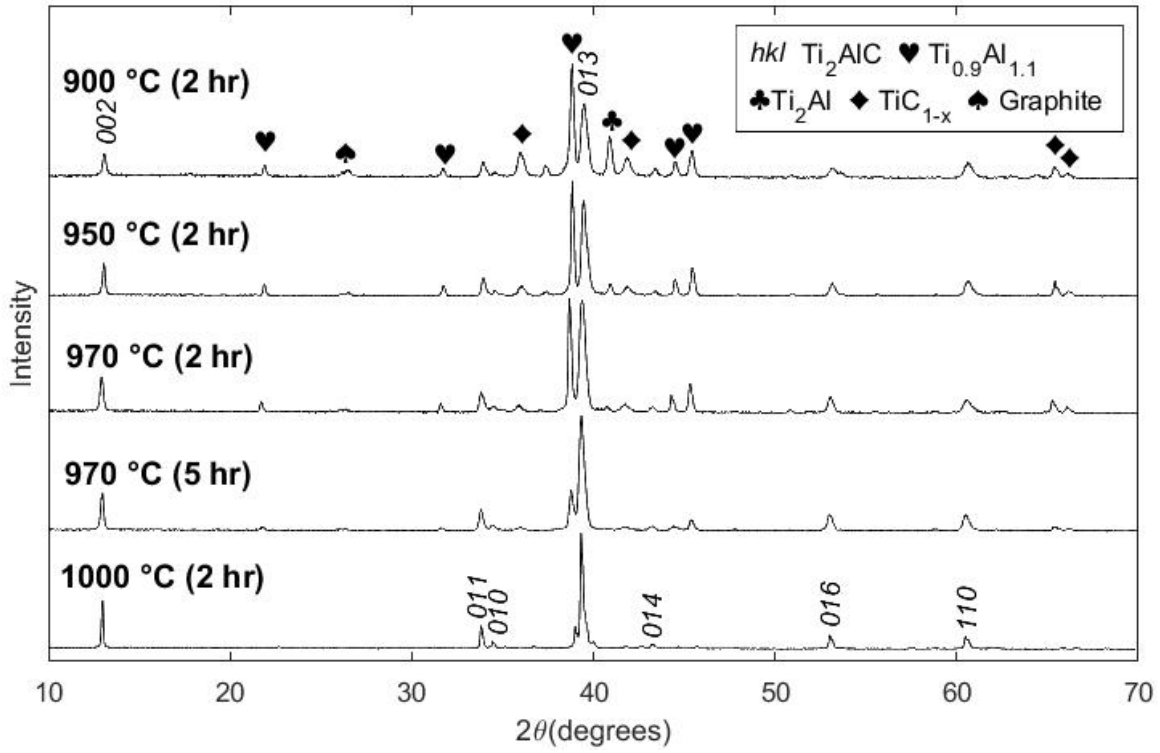

Fig. 4.4.1 – XRD spectra of samples synthesised with NaCl as the salt flux.

Among the salt combinations used, there was little difference in the results other than a small carbon signature in the KCl synthesised sample (likely unreacted graphite); Fig. 4.4.2 shows the samples synthesised at 1000°C using the different salt fluxes.

The XRD patterns for the Ti_3AlC_2 synthesis are shown in Fig.4.4.3. Ti_3AlC_2 is present, along with sub-stoichiometric TiC and the 211 phase Ti_2AlC. Rietveld refinement was performed on the NaKE-synthesised sample with Quantitative Phase Analysis (QPA) giving the composition by weight at 61% Ti_3AlC_2, 21% Ti_2AlC and 18% TiC, with a χ^2 value of 2.603 and a weighted R-factor of 0.0997.

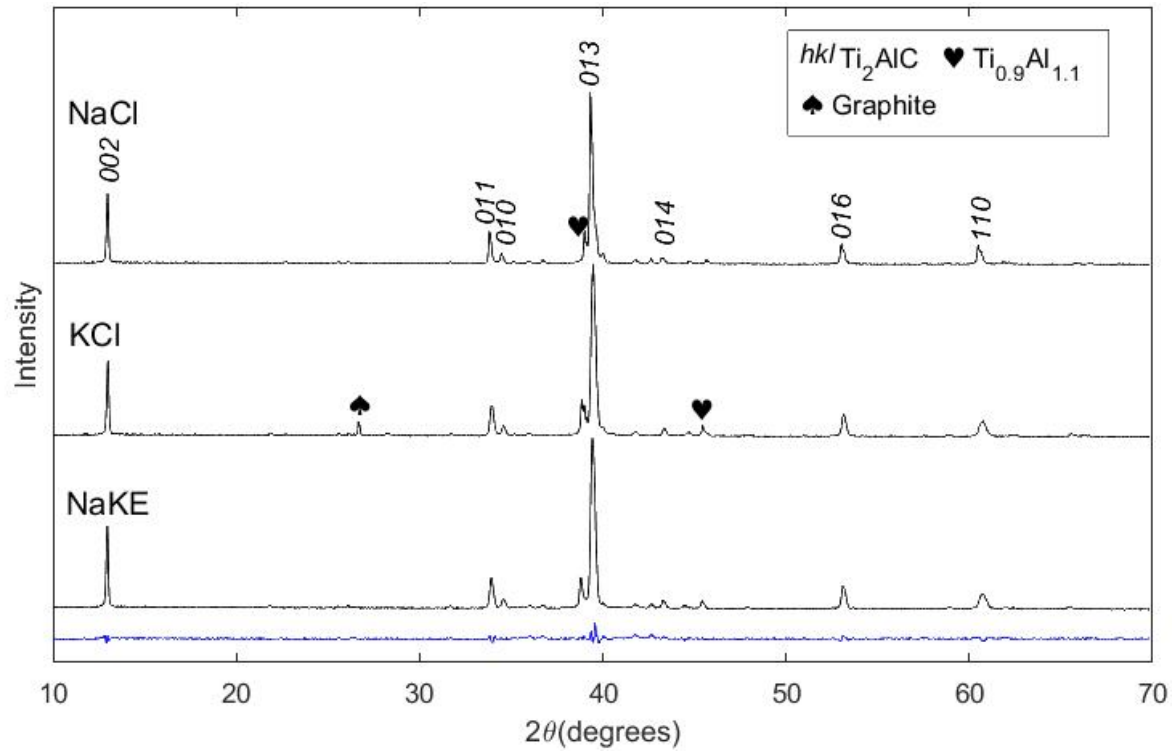

Fig. 4.4.2 – XRD spectra of samples synthesised at 1000°C for 2 hours using different salts. Difference profile for Rietveld refinement of NaKE sample shown in blue.

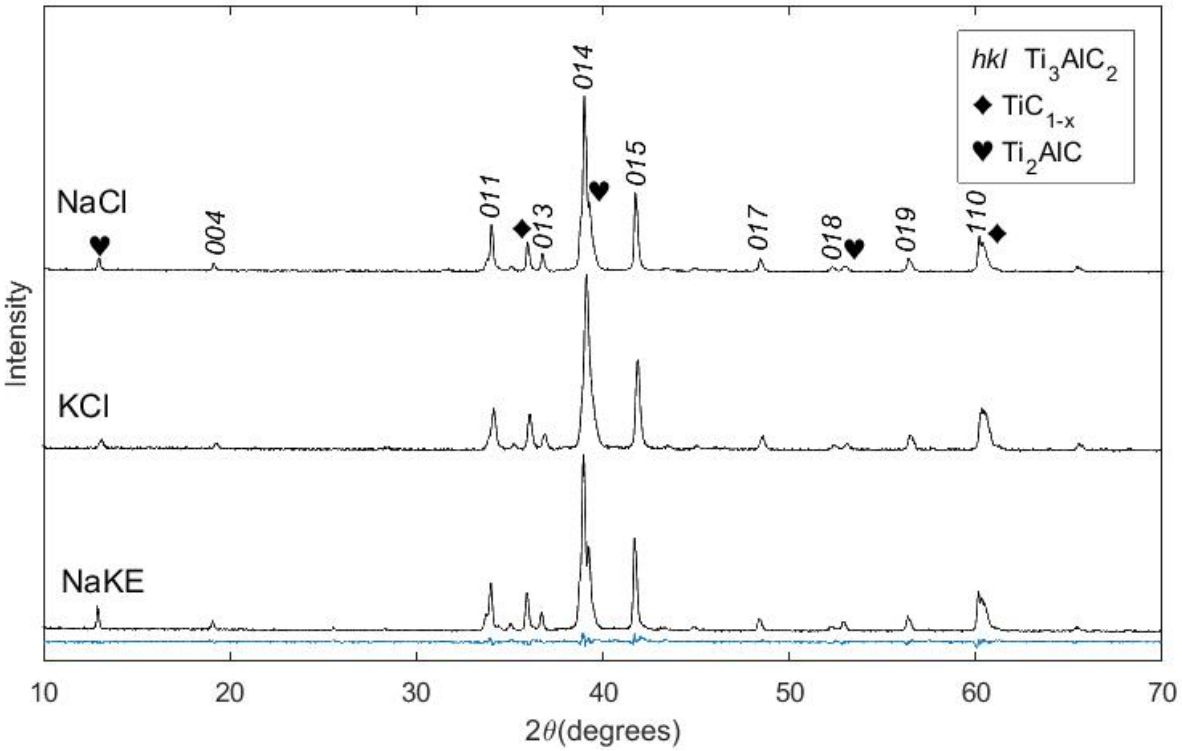

Fig. 4.4.3 - XRD spectra of Ti_3AlC_2 samples synthesised at 1300°C. Difference profile for Rietveld refinement of NaKE sample shown in blue.

Finally, the scaled-up synthesis of Ti_2AlC pattern is shown in Fig.4.4.4. The sample is still largely the target phase but contains sub-stoichiometric TiC as an ancillary phase instead of TiAl. The sample also contains some alumina, which may have arisen from improper purging of the furnace, or some pickup from the alumina crucibles dissolving in the salt from the larger pellets; given the absence of TiAl, it is likely the former.

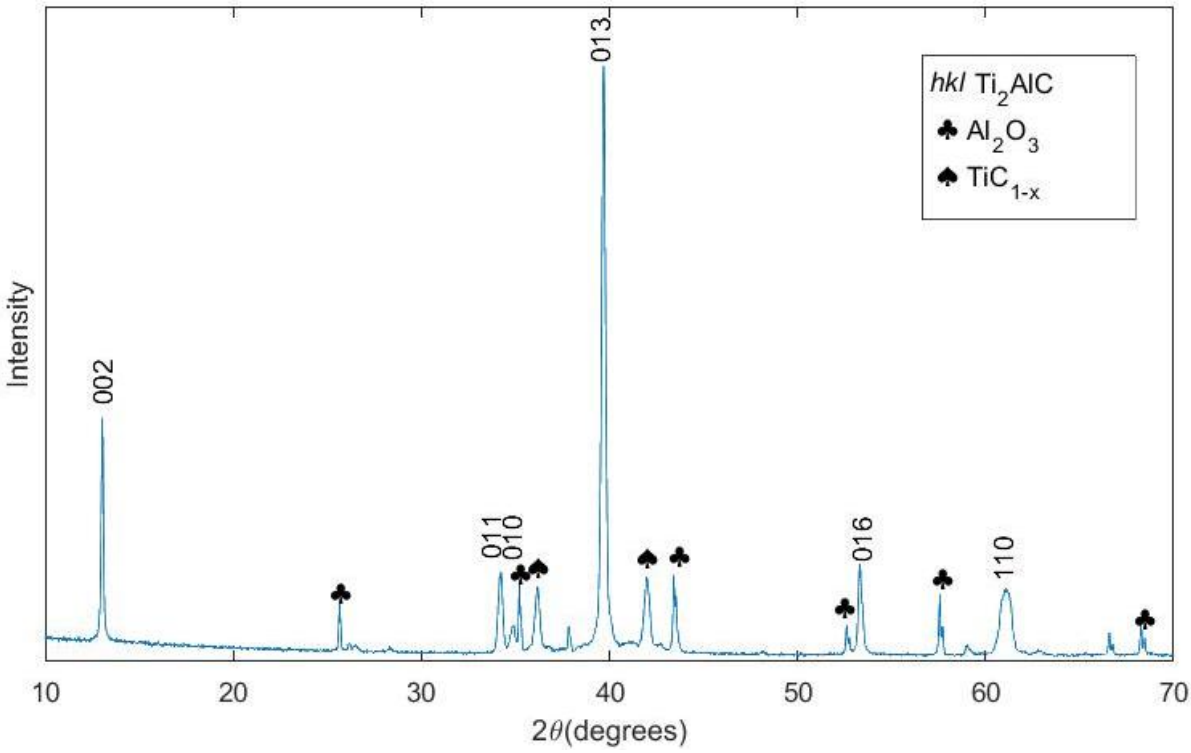

Fig. 4.4.4 - XRD spectrum from a 10g batch of Ti_2AlC, synthesised as with the previous samples.

Reaction pathway

Backscatter electron (BSE) images of the milled reactants are shown in Fig.4.4.5. The titanium is in small irregular pieces with a mean particle size of 31µm, the graphite flakes have a mean size of 21µm, but there are pieces as large as ~40µm. The aluminium, which had a much larger initial particle size has been pounded into large flakes ~120µm wide, with small graphite and titanium inclusions. However due to the synthesis temperature, the aluminium will be molten and so its morphology will not be apparent in the product.

After synthesis at 900°C and 1000°C, the powder morphologies are shown in Fig. 4.4.6, along with the Ti_3AlC_2 morphology. The 900°C sample is clearly not single phase with sub-micron grains clustered in larger particles, which could indicate templating. At 1000°C, the globular grains of Ti_2AlC are much more pronounced, and exhibit a morphology reminiscent of MSS-Cr_2AlC in the paper by Tian et al. [15]. The morphology of Ti_3AlC_2 is radically different from the 211 phase, consisting of long, needle-

like grains, which actually appear similar to MSS-Ti_3SiC_2 grains in the previous section, suggesting there is some similarity to the formation of this MAX phase in molten salt.

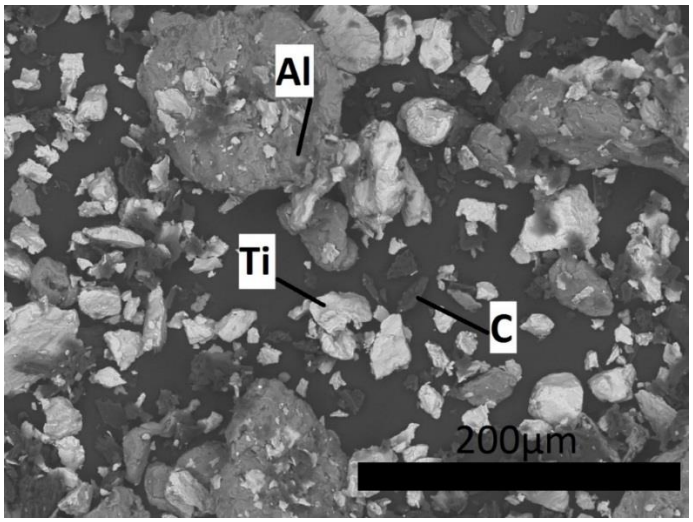

Fig. 4.4.5 – BSE image of the milled reactants for Ti_2AlC.

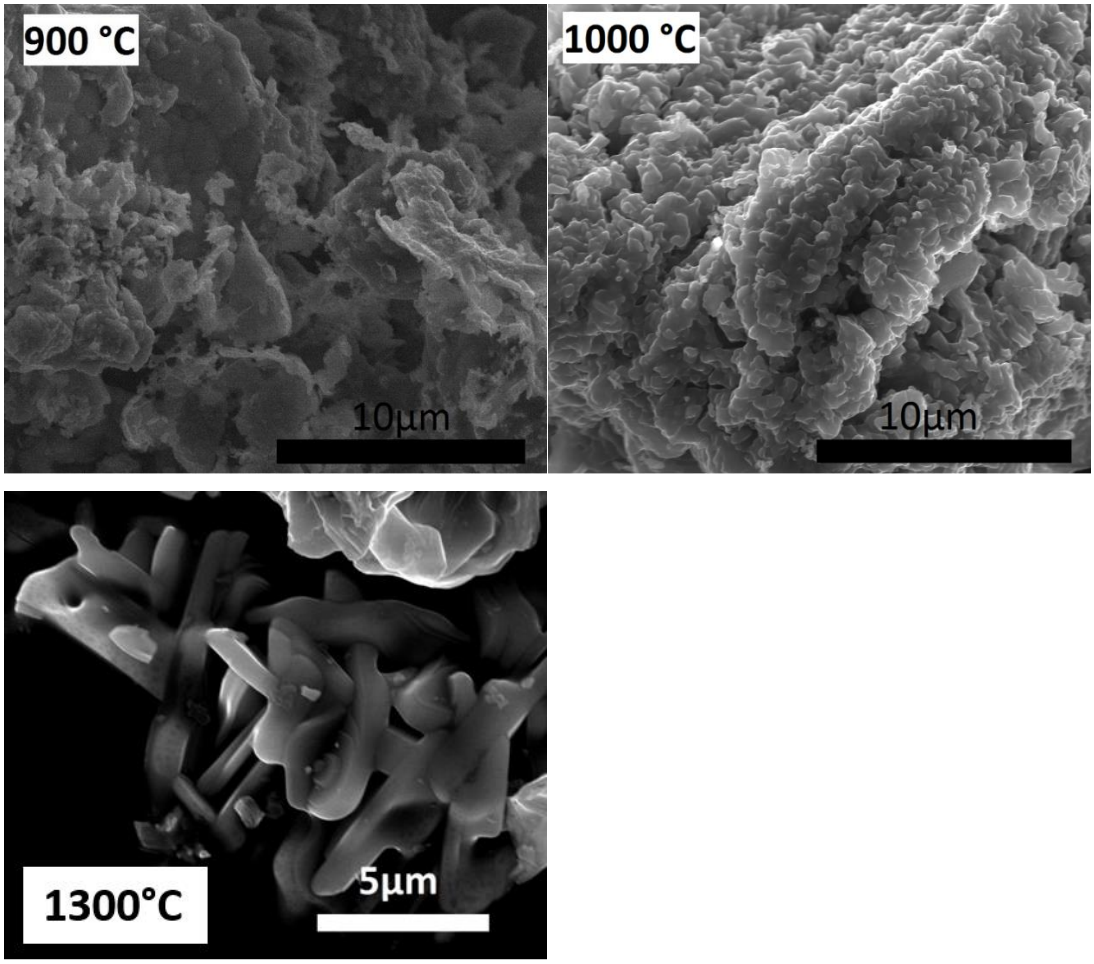

Fig. 4.4.6 - SE images showing the morphologies of Ti_2AlC at different temperature (top) and the morphology of Ti_3AlC_2 (bottom).

The EDX spectra maps are shown in Fig.4.4.7. At 900°C, Ti and Al are visibly present around what appears to be a particle of graphite. Due to the carbon coating and the carbon based resin, EDX was unable to accurately determine the nature of the black area, therefore the carbon coating was removed and Raman analysis was performed on a known area of unpopulated resin, and on the centre of one of the 'rings', shown in Fig.4.17, showing a strong peak at 1350cm^{-1}, corresponding to the D-band of disordered graphite, which occurs during milling [16]. At 1000°C, the sample was more homogeneous and coated particles were not observed.

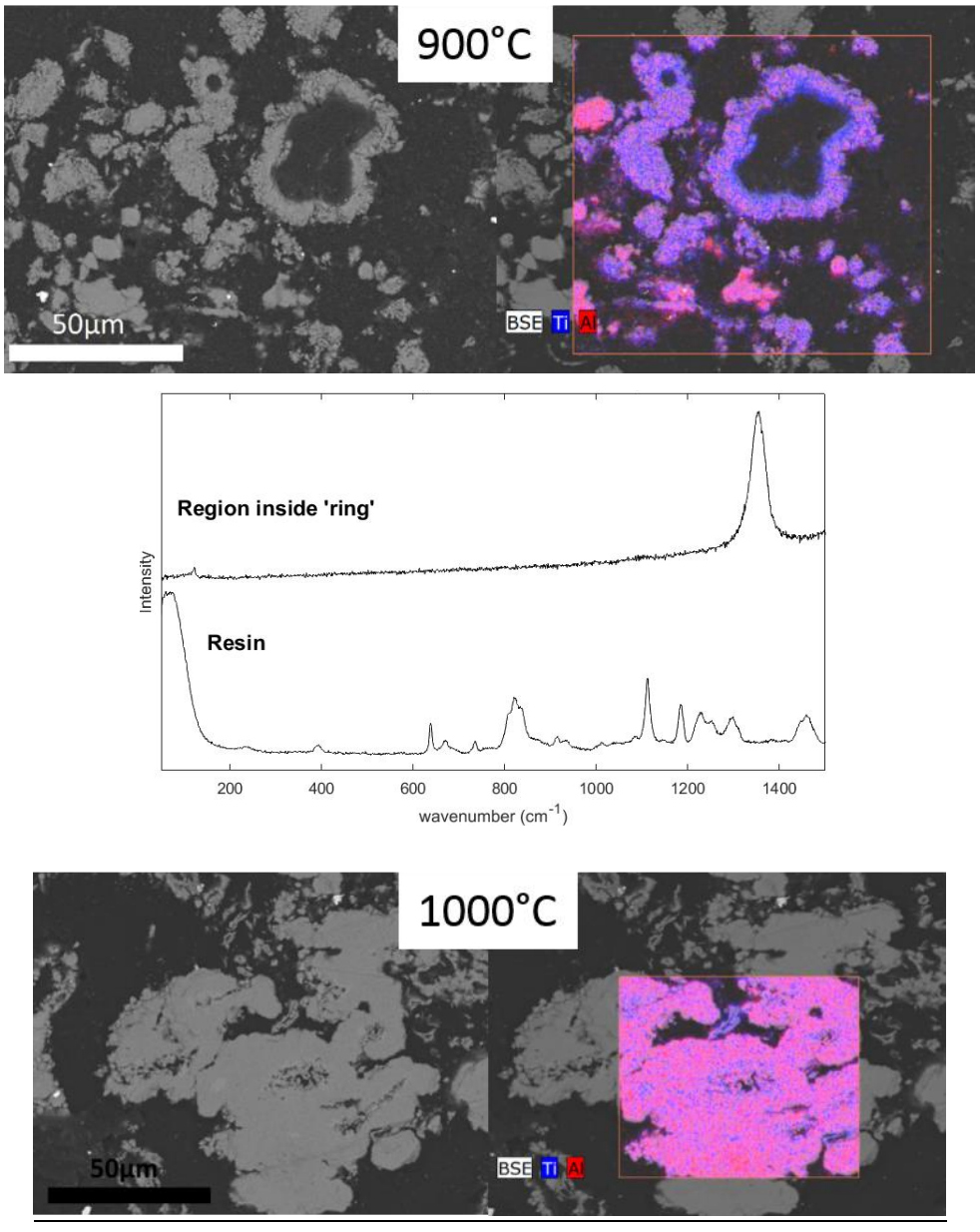

Fig.4.4.7 – EDX spectra maps of polished samples. Raman spectrum of known resin, and of centre of ring region in the top right.

4.4.3 Discussion

The proposed reaction pathway for Ti_2AlC formation is the initial formation of TiC and TiAl intermetallic compounds when the aluminium is molten. These two compounds then react to form the product Ti_2AlC, which is in agreement with the reaction pathway proposed by Wang *et al.* [17] who synthesised Ti_2AlC via hot pressing. After the synthesis, the pellets largely retained their shape, albeit with some cracking and expansion evident, therefore there was no large scale dissolution of reactants into the molten salt or the pellet would have collapsed. This suggests templating, or that the salt solvent became saturated before enough of the solid material had dissolved to compromise the pellet integrity. As seen in the resin mounted powders made at 900°C, templating of Ti and Al occurs around flakes of graphite, which are consumed by the reaction at higher temperatures.

After the synthesis of Ti_3AlC_2, it should be noted that a large fraction of the salt evaporated out of the samples and condensed on the inside of the tube furnace, so it is unclear how much of the reaction was assisted by the salt before it evaporated. As such, the results here are less pure than the 211 synthesis, and probably indicate a temperature ceiling for this process.

4.4.4 Conclusion

Ti_2AlC and its 311 counterpart Ti_3AlC_2 were successfully synthesised in molten salt for the first time in the literature. Ti_2AlC was present after dwell temperatures as low as 900°C, but becomes nearly phase pure at 1000°C with some small TiAl fraction. Ti_3AlC_2 was also synthesised at 1300°C, but with Ti_2AlC and TiC as ancillary phases, likely due to salt evaporation at high temperatures. The reaction pathway was determined to be TiAl formation from liquid aluminium and titanium, and TiC along with some templating onto graphite flakes. At higher temperatures, these react and form the product phase. A larger batch was prepared using the same method, and yielded similar results, but with ancillary TiC and Al_2O_3 instead of TiAl, likely due to poor purging of the furnace or oxidised reactants.

4.5 Hybrid synthesis MSS and SPS

An attempt was made to try and synthesise hybrid ‘211’ max phases with some M-site substitutions. The elements used were all potentially reactor suitable from a neutronics point of view and had the potential to form well adhered oxide layers. Aluminium and carbon were used for the A and X elements respectively. The M elements for this experiment were chosen to be Zr, Nb and Cr. Nb_2AlC and Cr_2AlC are well established as stable phases, while Zr_2AlC has been reported [18].

4.5.1 Materials and methods

Chromium (Alfa Aesar, 44µm, 99% pure), niobium (Alfa Aesar, 44µm, 99.8% pure), zirconium hydride (ZrH_2, Sigma Aldrich, 44µm, 99% pure), aluminium (Alfa Aesar, 44–420µm, 99.8% pure) and graphite powder (Alfa Aesar, 44µm, 99% pure) were used for this experiment. Zirconium hydride was used as it less sensitive to oxidation than pure zirconium, and it decomposes to zirconium at 1020 °C [19]. KCl was used as a flux to attempt MSS, while another batch of samples were SPS synthesised at a higher temperature. The general formula for reactant batches was $(M^1_x\ M^2_{1-x})_2Al_{1.2}C$, where M^1 and M^2 are two elements from Nb, Zr, and Cr, and x represents the fraction of substitution. As with previous experiments, the formula is super-stoichiometric with respect to aluminium to mitigate volatilisation. After synthesis, the samples were examined via XRD to determine the phase composition, and if there were any peak shifts corresponding to changes in the unit cell parameters.

The MSS procedure closely followed the previous work. The reactants were combined according to the above formula and milled with a 1:1 weight ratio of KCl. After drying and pressing, the samples were heated to 1100 °C in the tube furnace under flowing argon (~0.25L/min) for 2 hours, after which the pellets were crushed, washed and dried. Values for x used are displayed in Table 4.5.1. Zr+Cr was of particular interest, as a chromia/alumina scale could provide excellent oxidation resistance to a Zr-based max phase, so a broader range of x values were used.

M elements	x values targeted via MSS	x values targeted via SPS
Nb_xCr_{1-x}	0.05, 0.1, 0.9, 0.95	0.1, 0.9
Zr_xNb_{1-x}	0.05, 0.1, 0.9, 0.95	0.1, 0.9
Zr_xCr_{1-x}	0.05, 0.1, 0.25, 0.4, 0.6, 0.75, 0.9, 0.95	0.1, 0.9

Table 4.5.1 – The hybrid MAX phases targeted via MSS and SPS

These were chosen due to the discovery of some hybrid phases in the Ti-Cr-Al-C system by Liu *et al.* [20] and because Zr and Ti have similar chemical properties and crystal structure behaviour with respect to temperature.

To achieve a higher temperature of synthesis without the loss of salt, a batch of the samples were prepared without salt for SPS. The powders were combined according to the formulae above and planetary milled in a Fritsch Pulversitte 23 (1800 oscillations per minute, 10 minutes) in IPA and allowed to dry at 90°C for 8 hours (Memmert 100-800). 5g samples were then loaded into SPS graphite 20mm dies lined with graphite foil, and pre-pressed uniaxially under 160MPa for 5 minutes. The SPS furnace was run under vacuum (pressure not measured), with a 20 minute dwell time at 1300°C (16kN). After the dwell, the sample was allowed to cool naturally in the furnace for 10 minutes, before having the graphite foil removed, and then was polished for analysis. x values are displayed in Table 4.5.1.

4.5.3 Results

Molten Salt Synthesis

Fig. 4.5.1 shows the XRD for Cr+Nb molten salt samples with identifiable peaks. At low chromium content, the sample is primarily $NbAl_3$, Nb_2AlC and $(Nb_{0.9}Cr_{0.1})C$ with no evidence of peak shifting consistent with some chromium uptake in the niobium MAX phase. At the high chromium end, the sample contains Cr_2AlC and some $NbAl_3$.

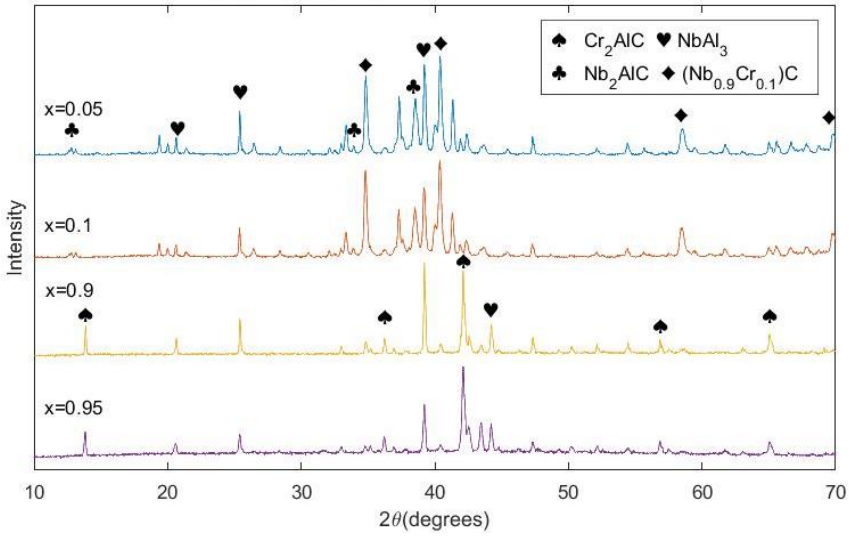

Fig. 4.5.1 – XRD spectra of $(Cr_xNb_{1-x})_2AlC$ synthesis in KCl for x= 0.05, 0.1, 0.9 and 0.95.

The Zr+Nb samples are shown in Fig. 4.5.2. With high niobium, the reaction formed Nb_2AlC and $NbAl_3$, along with ZrC, while the high zirconium samples formed Zr_2Al_3 and ZrC, with a faint peak from Nb_2AlC. Again, there is no evidence of shifts in the peaks within XRD patterns for Nb_2AlC.

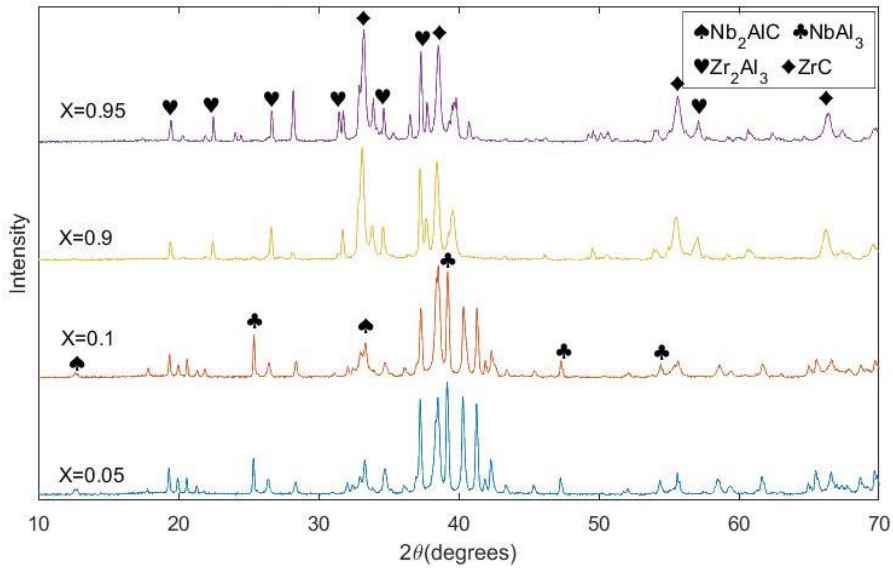

Fig. 4.5.2 – XRD spectra for $(Zr_xNb_{1-x})_2AlC$ synthesis with x= 0.05, 0.1, 0.9 and 0.95.

Finally, the characterisation of Zr+Cr samples are shown in Fig. 4.5.3. High zirconium results in ZrC and $ZrAl_2$ intermetallic, with no peaks corresponding to a MAX phase structure, shifted or otherwise. Cr_2AlC and Cr_2Al are present at high chromium content, and as the zirconium content increases, ZrC and Zr_2Al ancillary phases are present.

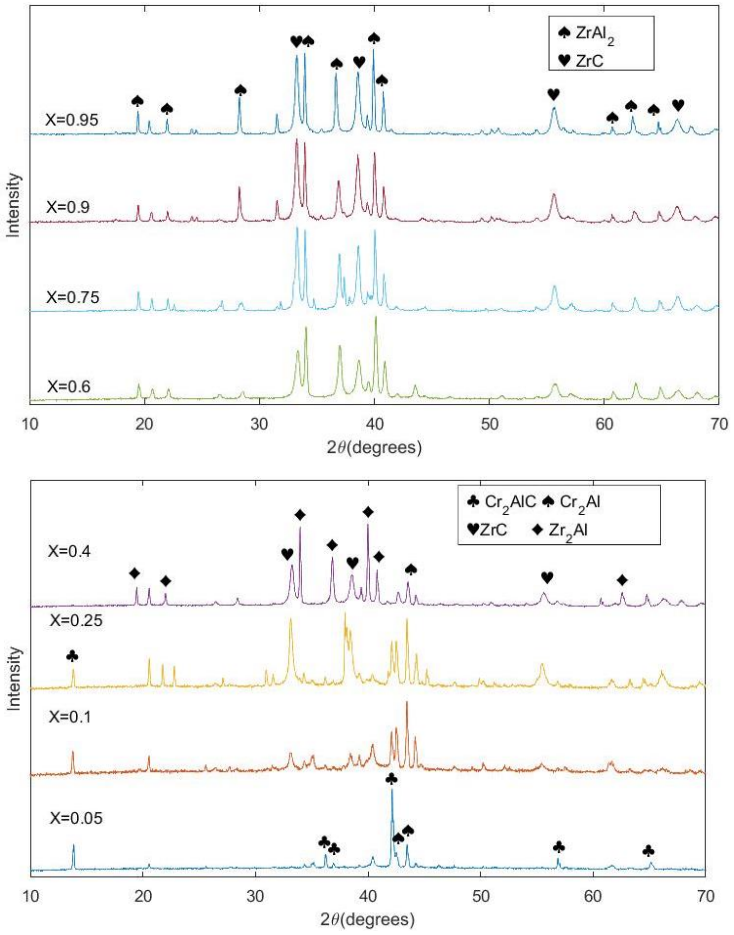

Fig. 4.5.3- XRD spectra for $(Zr_xCr_{1-x})_2AlC$ for x=0.95, 0.9, 0.75 and 0.6 (top), and x=0.4, 0.25, 0.1 and 0.05 (bottom).

Reactive SPS

Fig. 4.5.4 displays the XRD patterns for the samples made through SPS. The Cr+Nb sample with x=0.9 formed a liquid phase and leaked from the SPS die. This was repeated and the sample liquefied again. However, for Cr+Nb, x=0.1, some Nb_4AlC_3 was formed, along with Nb_2AlC, NbC, and unreacted graphite (or graphite foil). The Zr+Cr samples formed Cr_2AlC at high chromium, and ZrC at high zirconium, again with some graphite signal detected. Some Nb_2AlC is present in the Zr+Nb sample at high niobium, with some ancillary Zr_4AlC_3 413 MAX phase. The high zirconium sample produced no discernible MAX phase peaks, and was primarily graphite, Zr_2Al and ZrC.

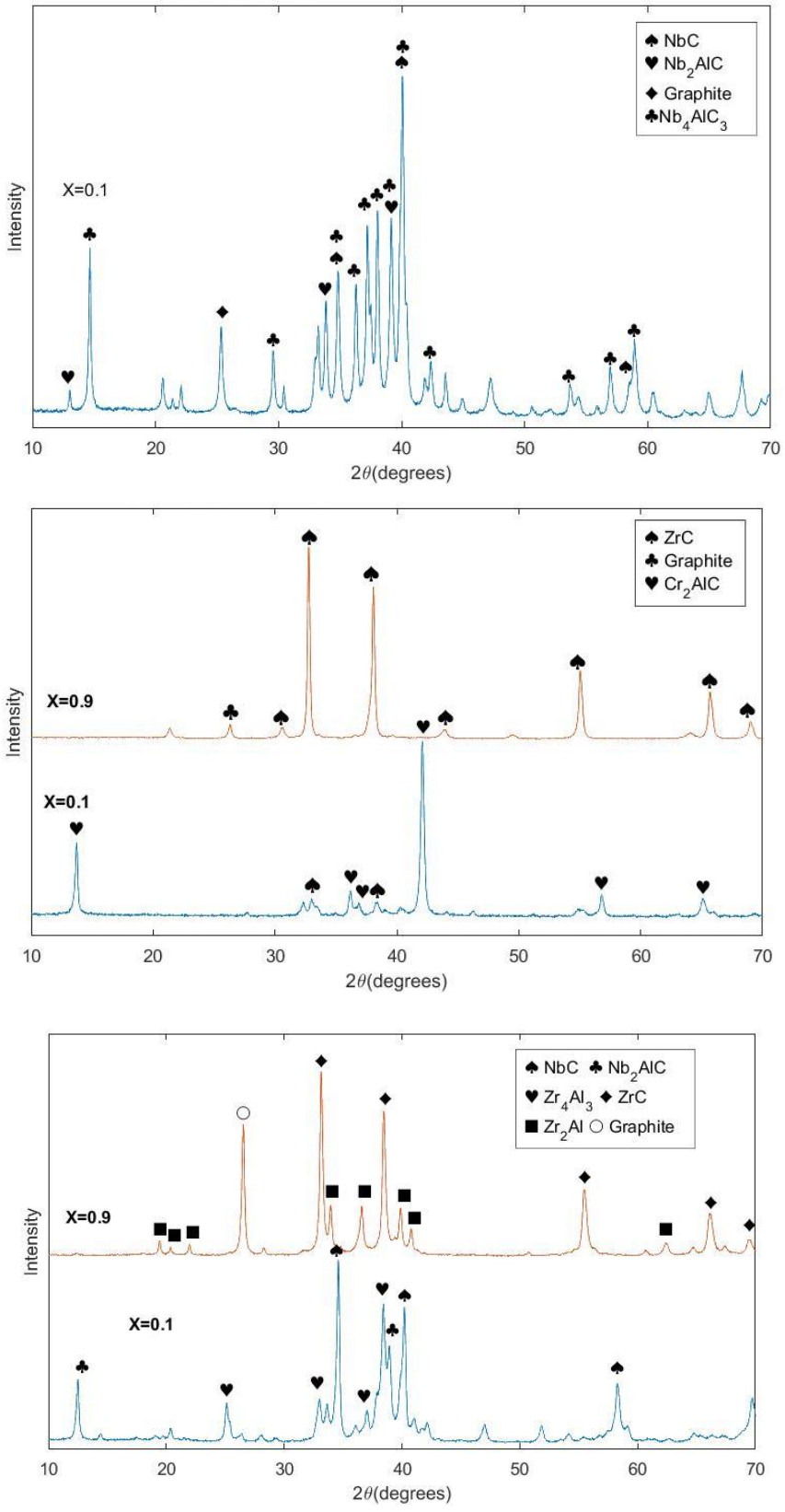

Fig 4.5.4 – XRD spectra for attempted hybrid MAX phase syntheses via reactive SPS.

4.5.3 Discussion

Unfortunately, no hybrid phases were found to exist via MSS, although a previously known hybrid binary carbide was found in the high niobium Cr+Nb samples. Several of the high chromium samples formed Cr_2AlC, which have been previously synthesised by Tian *et al.* [15]. Some Nb_2AlC is also present in the high niobium samples, which has not been synthesised via the molten salt method in the literature at the time of writing. Some dedicated synthesis experiments targeting this phase could result in improved purity. No Zr_2AlC formed in the high zirconium samples, which has previously been synthesised at ~1500 °C [18] so was unlikely to form at 1100 °C, even with the salt flux. Reactive SPS was also unsuccessful at producing hybrid phases. Cr_2AlC, Nb_2AlC and Nb_4AlC_3 were present in some of the samples, with no evidence of Zr_2AlC though some minor presence of Zr_4AlC_3 was detected. The Cr+Nb composition with x=0.9 was found to liquefy *in-situ* during the SPS procedure at around 1300°C. This is below the melting point of chromium and niobium and no binary eutectic exists around these conditions [21], so it could be due to the formation of a ternary Nb-Cr-Al eutectic. Overall, this suggests that both molten salt synthesis and spark plasma sintering are not appropriate methods to synthesise hybrid phases. More success has been had in the literature with hot pressing (see lit review) to synthesise hybrid phases, so it is likely that this is the best synthesis route to pursue future hybrid phase synthesis.

4.5.4 Conclusions

Novel attempted synthesis of hybrid (m-site substitution) MAX phases containing chromium, zirconium and niobium was conducted using MSS at 1100°C and Reactive SPS at 1300°C. Although some MAX phase phases were present, including Cr_2AlC, Nb_2AlC and Nb_4AlC_3, no evidence of any hybrid MAX phases were found.

4.6 References

[1] C. Grove, D. Shepherd, M. Thomas, and P. Little, “Neutronics of MAX phase materials,” *Struct. Mater. Innov. Nucl. Syst. (SMINS-4), Univ. Manchester*, 2016.

[2] M. W. Barsoum, “MAX Phases: Properties of Machinable Ternary Carbides and Nitrides,” in *Wiley-VCH*, vol. 1, Wiley-, 2013.

[3] B. H. Lohse, A. Calka, and D. Wexler, “Raman spectroscopy as a tool to study TiC formation during controlled ball milling,” *J. Appl. Phys.*, vol. 97, no. 11, 2005.

[4] F. Meng, B. Liang, and M. Wang, “Investigation of formation mechanism of Ti3SiC2 by self-propagating high-temperature synthesis,” *Int. J. Refract. Met. Hard Mater.*, vol. 41, pp. 152–161, 2013.

[5] M. S. Ali, A. K. M. a. Islam, M. M. Hossain, and F. Parvin, “Phase stability, elastic, electronic, thermal and optical properties of Ti3Al1−xSixC2 (0≤x≤1): First principle study,” *Phys. B Condens. Matter*, vol. 407, no. 21, pp. 4221–4228, 2012.

[6] A. Zhou, C. Wang, and Y. Hunag, “Synthesis and mechanical properties of Ti 3 AlC 2 by spark plasma sintering,” *Synthesis (Stuttg).*, vol. 8, pp. 3111–3115, 2003.

[7] D. P. Riley and E. H. Kisi, “The design of crystalline precursors for the synthesis of M n-1AXn phases and their application to Ti 3AlC2,” *J. Am. Ceram. Soc.*, vol. 90, no. 7, pp. 2231–2235, 2007.

[8] E. H. Kisi and D. P. Riley, “Crystalline ternary ceramic precursors,” 2009.

[9] X. Guo, J. Wang, S. Yang, L. Gao, and B. Qian, “Preparation of Ti3SiC2 powders by the molten salt method,” *Mater. Lett.*, vol. 111, pp. 211–213, 2013.

[10] A. . Larson and R. . Von Dreele, “General Structure Analysis System (GSAS),” 2000.

[11] B. H. Toby, “EXPGUI , a graphical user interface for GSAS EXPGUI , a graphical user interface for GSAS,” *J. Appl. Cryst.*, vol. 34, pp. 210–213, 2001.

[12] T. Galvin, N. C. Hyatt, W. M. Rainforth, I. M. Reaney, and D. Shepherd, “Molten salt synthesis of MAX phases in the Ti-Al-C system,” *J. Eur. Ceram. Soc.*, vol. 38, no. 14, pp. 4585–4589, 2018.

[13] M. L. Hand, M. C. Stennett, and N. C. Hyatt, “Rapid low temperature synthesis of a titanate pyrochlore by molten salt mediated reaction,” *J. Eur. Ceram. Soc.*, vol. 32, no. 12, pp. 3211–3219, 2012.

[14] G. J. Janz, *Molten Salts Handbook*. Academic Press, 1967.

[15] W. B. Tian, P. L. Wang, Y. M. Kan, and G. J. Zhang, “Cr2AlC powders prepared by molten salt method,” *J. Alloys Compd.*, vol. 461, no. 1–2, pp. 6–11, 2008.

[16] T. Xing, L. H. Li, L. Hou, X. Hu, S. Zhou, R. Peter, M. Petravic, and Y. Chen, “Disorder in ball-milled graphite revealed by Raman spectroscopy,” *Carbon N. Y.*, vol. 57, pp. 515–519, 2013.

[17] P. WANG, B. chu MEI, X. lin HONG, and W. bing ZHOU, “Synthesis of Ti2AlC by hot pressing

and its mechanical and electrical properties," *Trans. Nonferrous Met. Soc. China (English Ed.*, vol. 17, no. 5, pp. 1001–1004, 2007.

[18] T. Lapauw, K. Lambrinou, T. Cabioc'h, J. Halim, J. Lu, A. Pesach, O. Rivin, O. Ozeri, E. N. Caspi, L. Hultman, P. Eklund, J. Rosén, M. W. Barsoum, and J. Vleugels, "Synthesis of the new MAX phase Zr2AlC," *J. Eur. Ceram. Soc.*, vol. 36, no. 8, pp. 1847–1853, 2016.

[19] V. Z. Shemet, A. P. Pomytkin, V. A. Lavrenko, and V. Z. Ratushnaya, "Decomposition of metal hydrides in low temperatures and in high-temperature oxidation," *Int. J. Hydrogen Energy*, vol. 18, no. 6, pp. 511–516, 1993.

[20] Z. Liu, L. Zheng, L. Sun, Y. Qian, J. Wang, and M. Li, "(Cr 2/3 Ti 1/3) 3 AlC 2 and (Cr 5/8 Ti 3/8) 4 AlC 3 : New MAX-phase Compounds in Ti-Cr-Al-C System," *J. Am. Ceram. Soc.*, vol. 97, no. 1, pp. 67–69, Jan. 2014.

[21] C. Schmetterer, A. Khvan, A. Jacob, B. Hallstedt, and T. Markus, "A new theoretical study of the Cr-Nb system," *J. Phase Equilibria Diffus.*, vol. 35, no. 4, pp. 434–444, 2014.

5. MAX phase coating deposition and densification

The following section covers the deposition of Ti_3SiC_2 (Maxthal 312) via EPD and subsequent densification by conventional sintering and rapid laser sintering. These experiments aimed to serve as a proof of concept for a coating method that could, with an appropriate MAX phase and further refinement of the laser sintering, form the basis of an industrial process to coat fuel rods or spacer grids.

5.1 Initial EPD experiments

The particle size of Maxthal 312 was analysed and compared with milled samples to observe the change in median particle size (D_{50}). Initial depositions were carried out onto small copper foil plates in parallel sample holders and onto graphite rods with a cylindrical sample holder and tubular copper electrode (Fig.5.1.1). Parallel plates were used for ease of characterisation, while the graphite rods were to simulate cylindrical deposition onto fuel rod cladding. Various dispersants were tested based on the literature on their ability to improve suspension stability.

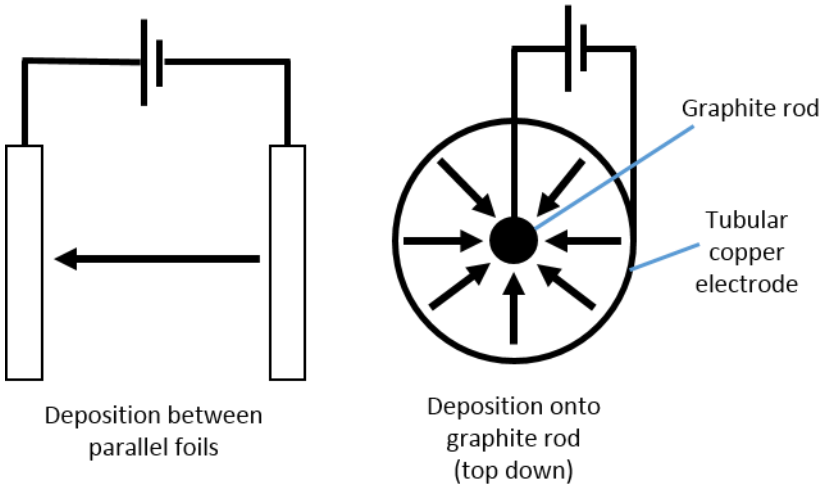

Fig. 5.1.1 – Schematics of initial depositions.

5.1.1 Materials and methods

Ti_3SiC_2 was used as the feedstock for the experiments, and copper foil (rolled from in-house stock, purity not measured) was used as a flat substrate. 10cm sections of graphite rods (Alfa Aesar, 6.3mm diameter, 99% pure) were also used to demonstrate the ability to coat cylindrical geometry evenly. Distilled water (produced in-house) was used as the liquid medium, as well as a 1:1 water:ethanol (VWR Scientific, anhydrous) mix as used by Mishra *et al.* [1] who successfully deposited Ti_3SiC_2 via EPD. Polyethyleneimine (PEI, Sigma Aldrich, Molecular weight M_w 25,000, <1% water) and Darvan CN

(Vanderbilt Minerals LLC, 25wt% ammonium polymethacrylate in water) were also tested for their efficacy as dispersants.

Sample holders

Custom PTFE and steel sample holders were initially used to support pieces of copper foil in a parallel position 20 mm apart, with an aperture diameter of 10 mm for deposition, as shown in Fig.5.1.2. However, part of the PTFE at the front was very thin and slightly warped during experiments, which resulted in water being trapped when the sample holders were removed from the suspension. This water often washed some of the fragile deposits away during sample removal, so some modified holders were designed (modelled in FreeCAD V0.15) to work with the existing steel parts. These modified parts were subsequently used for the work presented here.

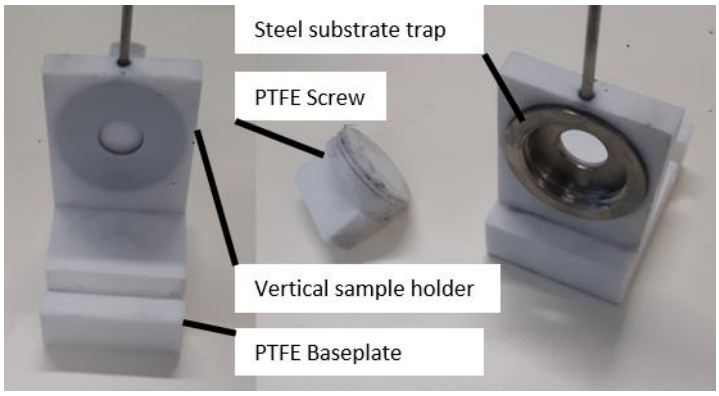

Fig. 5.1.2 – Image of the parallel deposition sample holders.

Fig. 5.1.3 shows the CAD models of the two designed sample holders. The holder for maintaining a flat geometry is similar to the previous holder but with a thicker front section to reduce warping. They were designed to fit in the same holder as the previous ones, but another holder was designed to hold the samples 10 mm apart. A second holder was designed to hold graphite rods upright, with two ridges onto which foil electrodes could be wrapped around, while still allowing a good flow of suspension. The diameters of the rods were 26.3 mm and 46.3 mm to give a distance between the two electrodes of 10 mm and 20 mm, respectively. The sample holders were manufactured from PTFE by CS Press Tools Ltd.

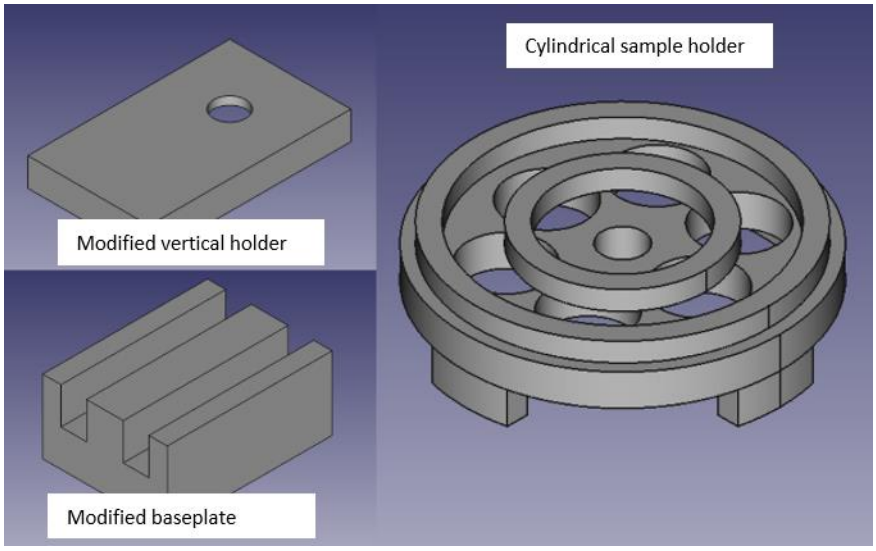

Fig. 5.1.3 – CAD models of sample holders rendered in FreeCAD.

Powder preparation

The sample of Ti_3SiC_2 (150g) was attritor milled (Szegvari Attritor System Type 8, 01HD) in isopropanol with spherical ZrO_2 (3mm diameter). The sample was milled at 300rpm for 90 minutes, with some being removed from the mill at 30 and 60 minutes for particle size analysis (PSA). Another sample was roller milled for 24 hours in IPA with cylindrical ZrO_2 media (1cm diameter, 1.5cm length, rounded ends). Both samples were allowed to dry, subjected to PSA using a Malvern Mastersizer 3000 (see Standard Procedures) and compared to the unmilled Maxthal 312. Particle size measurements were carried out using the wet cell, and ultrasonically agitated to break up agglomerates prior to testing.

Suspension preparation

The sample preparation was modelled on the experiments of Liang *et al*.[2] and Mishra *et al*. [1] Liang *et al.* used $Ti_3Si_{0.95}Al_{0.05}C_2$ in a 1vol.% suspension in water at pH9, while Mishra *et al.* used 10 vol.% Ti_3SiC_2 in 50:50 water: ethanol with $10mg/g_{MAX\ phase}$ of PEI. Both suspensions were replicated and used for deposition to determine which was the more effective. Suspensions were also created using Darvan CN as a dispersant.

The general suspension preparation was as follows: the appropriate quantity of MAX phase was weighed out into a beaker, to which distilled water or water/ethanol was added carefully until all the powder was wetted. PEI is highly viscous, and forms long strings when scooped out of the container. To mitigate this, the appropriate quantity was weighed into a separate beaker, to which a known quantity of hot water was added to dissolve the PEI. Once dissolved the sample was added to the rest of the suspension liquid. The suspensions were stirred for ~3 minutes with a glass rod to remove any large clumps and to scrape any settled material from the bottom of the beaker. The samples were

then ultrasonically agitated for 5 minutes to break up any micro-agglomerations, after which they were briefly stirred manually once more. In between deposition runs, samples were kept moving with a magnetic stirrer and stir bar (IKA Werke, RCT type B, 2cm bar, setting 6/10).

EPD was carried out using a power supply (Kikusui PAS500-0.6) set to constant voltage mode with applied voltages between 1 and 20V. Deposition times ranged from 1 to 10 minutes. Copper substrates were cleaned with IPA to remove any smears or debris before deposition. After deposition, the sample holders were removed from the suspension and the coated foil electrode taken out of the sample holder and left to dry on a flat surface. The 'green' deposit (i.e. unsintered, not its colour) was imaged by SEM (Hitachi TM3030).

Zeta-Potential

After initial test runs, it was decided to quantitatively pinpoint the optimum conditions for deposition of Ti_3SiC_2. To achieve this, the zeta potential of the MAX phase was measured in pure water, and with 1wt.% PEI (dry weight basis or DWB) added on a Malvern Zetasizer at a range of pH values. As with PSA, Mie scattering settings were used with refractive index of 3.6 and absorption of 1. An obscuration value of 2.75% was used, and 5 measurements for each pH were automatically logged. 0.1 M solutions of NaOH and HCl were used to adjust the pH.

5.1.2 Results

Particle Size Analysis

The PSA graphs of the milled Ti_3SiC_2 are shown in Fig. 5.1.4, and compared to unmilled. The D_{50} (Mass median diameter or median particle size) values for each sample are given in Table 5.1.1. The median particle size appears to increase during the first 60 minutes of attritor milling, but this is unlikely to be the case (see 5.1.3 Discussion). After 90 minutes of attritor milling, the median size had reduced to 6.06µm, but roller milling reduced the D_{50} by over 2µm to 4.79µm. Therefore the roller milled powders were used for subsequent deposition experiments. Potentially a smaller powder size could have been achieved with further attritor milling, as a minimum may not yet have been reached.

Process	**D_{50} (µm)**
As-received	7.01±0.35
30 minute attritor mill	7.59±0.38
60 minute attritor mill	7.71±0.39
90 minute attritor mill	6.06±0.30
24 hour roller mill	4.79±0.24

Table 5.1.1 – D_{50} for milled Ti_3SiC_2

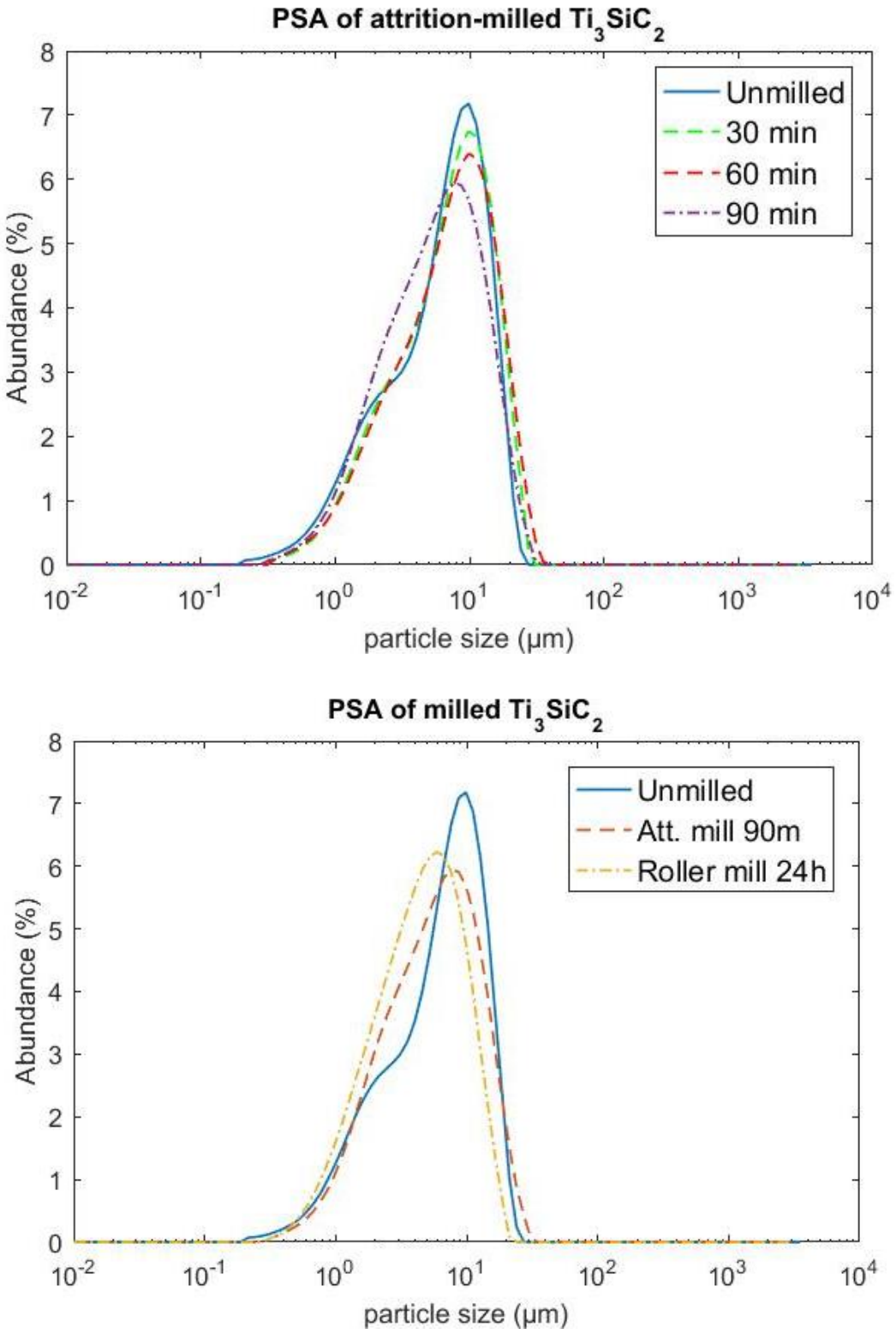

Fig. 5.1.4 – Particle size profiles for unmilled, roller milled and attritor milled Ti_3SiC_2.

Initial deposition

Following the procedure of Liang *et al.* some deposition was achieved, albeit at a very slow rate. In their paper, Liang *et al.* reported using 3.5V for deposition, but results were improved when the voltage was increased to 10V for 10 minutes. Above 10V, electrolysis was producing noticeable bubbles on the surface, and left the depositions pock-marked and discoloured the substrates. The deposition occurred on the positively charged substrate, indicating that Ti_3SiC_2 has a negative zeta-potential in water. An example deposition carried out using this method on both copper and graphite is shown in Fig. 5.1.5. Initially, it was hoped that EPD onto a graphite rod could build up (potentially through repeated depositions) a thick green coating on the order of ~mm thickness, and that after sintering and removal or burnout of the rod, a freestanding MAX phase tube could be produced. The resultant deposits were far thinner than expected however, and so other methods were sought to produce the tubes (see Chapter 6). Results from following the protocol from Mishra *et al.* were very inconsistent, and due to either the high solids loading or the PEI, the sample clumped and settled out far quicker than the previous solution. Small additions (1–2% of dry weight) of Darvan CN instantly caused the MAX phase powder to fall out of suspension, which indicating that it works best for particles with a positive surface charge, and so this was not pursued further. It should also be noted that the small apertures in the sample holders often held a droplet or a meniscus of water when removed from the suspension, which then disrupted the fragile deposition. This was partially mitigated by introducing a small strip of laboratory blue roll to wick some away, but it was largely a problem with holder design. Depositions were consistently better when using shorter separation between electrodes. Some observations from initial tests are displayed in table 5.1.2.

Conditions	Observations
- Copper electrodes, cleaned with ethanoic acid and isopropanol. - 4V, 10 minutes, 1%vol. suspension with distilled water. - 15 mm separation, screw holders.	- Deposition very thin, mostly washed off by water meniscus. - Repeated with incremental voltages up to 12V, 10V gives thicker coverage, while voltages above 10 resulted in electrolysis and bubbles disrupting the surface. - Using newer sample holders (with 10 mm separation) gave thicker looking deposits, although still issue with meniscus.
- Copper electrodes, cleaned with ethanoic acid and isopropanol. - 10V, 10 minutes, laboratory tap water, 1%vol. suspension - 15 mm separation, screw holders.	- Lots of electrolysis (bubbling) – likely too many ionic compounds in tap water. Copper electrodes discoloured from electrolysis. - No noticeable deposition
- Copper electrodes, cleaned with ethanoic acid and isopropanol. - 50% ethanol solution used by Mishra *et al.*[1] - 10mm separation. - 10–20V, 10 minutes	- Inconsistent results, suspension settled relatively quickly. Sometimes results in deposition but not noticeably thicker than other suspensions. - High current flow on the PSU indicates electrolysis/short circuiting through settled MAX phase.
- 1% Vol. suspension using 1% dwb of Darvan CN	- Suspension immediately flocculated and settled. Based on surface charge analysis of powder, Darvan CN must be designed for use on only positively charged particles in suspension.

Table 5.1.1 – Some observations of initial test runs.

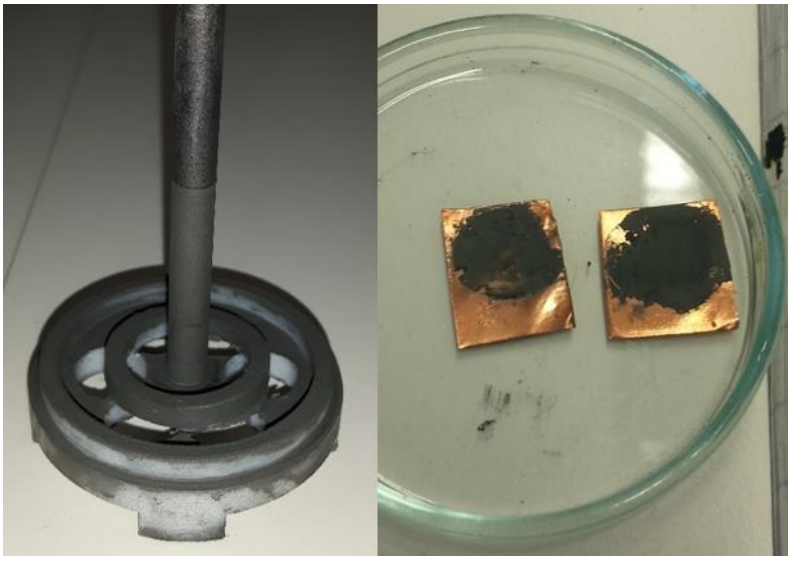

Fig. 5.1.5 – Examples of deposition with 1vol.% Ti_3SiC_2 in pH 9 water

SEM images of the copper substrate are shown in Fig. 5.1.6. There is some exposed copper in places, due to the 'washing' effect of water trapped on the sample holder. The presence of some large >10µm

particles of MAX phase can be seen despite the majority of these settling out but most deposited particles were <5µm.

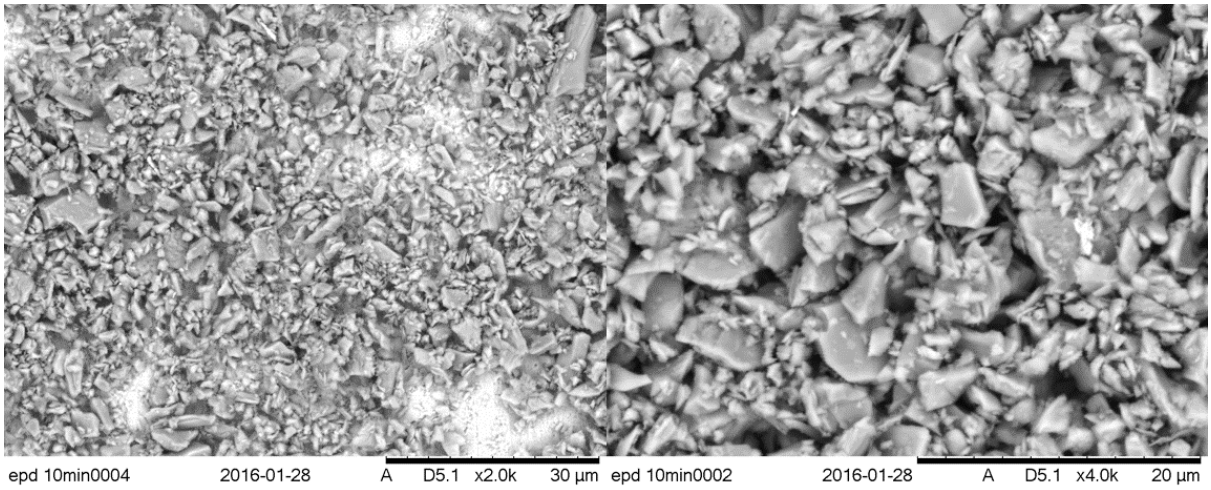

Fig. 5.1.6 – SEM images of EPD Ti_3SiC_2 on copper foil.

Zeta potential

The recorded values of zeta potential for the two samples are shown in Fig. 5.1.6. The maximum zeta potential for Ti_3SiC_2 was around pH9 and confirms that the material has a negative surface charge at most pH values. The addition of PEI changes the surface charge to positive over a wide range of pH values, but is generally highest between pH 3–6. The Isoelectric Point (IEP) for Ti_3SiC_2 is at pH 5, while the addition of 1wt.% PEI moves it to pH ~10.9.

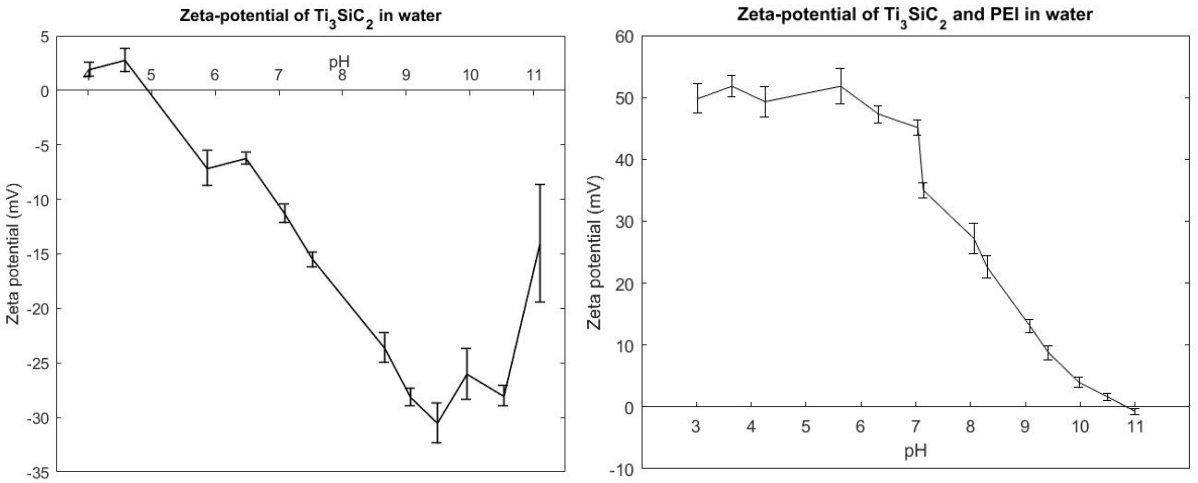

Fig. 5.1.6 – Zeta potential measurements for Ti_3SiC_2 suspensions. Spread bars show standard deviation.

5.1.3 Discussion

The first 60 minutes of attritor milling appeared to increase the median particle size which could be for several reasons. The first is preferential milling of a small fraction of very large particles which initially gives rise to larger particles than the median. This was eventually mitigated after 90 minutes. Another possibility is prior contamination of the attritor mill or contamination from pieces of milling media. Finally, agglomerations of small particles during the PSA process can give false readings for large particles. Of these the first is most likely, as particles present on the depositions can be seen in excess of 20µm in length, and the PSA samples were specifically ultrasonically agitated to remove any agglomerates.

Another explanation may be the heterogeneous distribution of particle sizes within the attritor mill during milling. Samples were extracted from the top of the mill bowl, which may have contained more material of a larger size. This possibility is supported by a technical report [3] conducted by NNL on behalf of Sellafield Ltd (SL) on attritor milling of UO_2 ceramic powder using a mill from the same manufacturer as the work reported in this Thesis Section (SL are acknowledged for their kind permission to supply and cite the report). This found during periodic unpacking of the mill that powder tends to compact onto the walls of the mill bowl during initial milling stages. Subsequent impacts from mill balls gradually remove this build up and reduce the particle size. The report found that the fine powder then settles to the bottom of the mill, where it remains until the mill is discharged. However, it should be noted that difference in procedures between those used in the report (which was conducted using dry milling with steel media at lower rotational speeds, with a larger mass of powder) and this work means that an exact comparison may not be drawn.

Initial tests of the EPD process were inconsistent due to the tendency of the flat sample holders to trap water on and around the substrate. Removal when wet often led to the deposition being washed off, while letting the samples dry in the holder often caused the deposit to flake off during removal. Wicking away some water with laboratory blue roll improved this problem, but less intrusive sample holders would be preferable. The cylindrical sample holder worked well and the graphite rod was easy to remove without disturbing the coating, and this is the case that is more applicable to deposition on tubular cladding.

Despite Mishra *et al.* reporting free-standing deposits with a thickness of up to 5mm, no such deposits were achieved here by an attempt to follow their method. Mishra *et al.* used PEI with an average molecular weight of 10,000, whereas the PEI used in this experiment had an average molecular weight of 25,000. This was the only available polymer and is likely the issue. The branch-chain polymer acts as a dispersant by absorbing to particle surfaces [4] similar to chelation (the bonding of organic molecules to metal containing species) on a macro scale, so a difference in molecular weight could

adversely affect deposition. As PEI changes the surface charge from positive to negative, the dosage is very important; too little PEI could result in both positive and negatively charged particles in the same suspension, leading to rapid flocculation. In contrast, Liang *et al.*'s method yields thin but reliable deposits, so their procedure was adopted for future experiments. The zeta potential measurements are generally in agreement with work done on suspensions of Ti_3SiC_2 (or $Ti_3Si_{0.95}Al_{0.05}C_2$ in the case of Liang *et al.*) and confirm that the best pH for Ti_3SiC_2 in water is 9.

5.1.4 Conclusion

Particle size analysis shows the best size reduction method for the as-received Ti_3SiC_2 to be roller milling for 24 hours. Initial experiments in EPD found the most reliable method for deposition was a 1vol.% suspension of Ti_3SiC_2 in pure water, adjusted to pH 9. An applied voltage of 10V for 10 minutes yields even deposits on copper and graphite without problematic hydrolysis (the splitting of water into hydrogen and oxygen gas which then escapes to atmosphere, bubbles of which can dislodge coating or react with the substrates), but the initial sample holder design meant deposition layers were disturbed during substrate removal. This disturbance was mitigated through the use of adjusted sample holders. The cylindrical geometry was not affected by this problem, and yielded even depositions. The highest absolute zeta potential for Ti_3SiC_2 in water was pH 9, while adding 1wt.% DWB of PEI altered the maximum zeta potential to pH 3–5.

5.2 – Deposition onto titanium and zirconium

After the initial experiments, the capability of deposition onto zirconium alloys needed to be tested. There was an initial delay obtaining zirconium alloys, and so titanium is used for the bulk of these experiments, due to its chemical and phase behaviour similarity to zirconium, as well as being a much more affordable substitute.

5.2.1 Materials and methods

Titanium plates (Alfa Aesar, 1mm thick, 99.2 % pure) were used as the deposition substrate for the bulk of this experiment, cut to 100x50mm with a guillotine. Some sections of ZIRLO® proprietary zirconium alloy tube and flat plates (200x100mm, 0.8mm thick) were also used as substrates, having been kindly donated by Westinghouse, an international fuel, cladding and reactor technology supplier. As in the previous experiments, the feedstock was Maxthal 312, and suspensions were based on in-house distilled water. NaOH was used to adjust the pH of the suspensions. A new sample holder was designed using SketchUp 2016 (Trimble Inc.) CAD software and 3D printed (Prusa I3 type, home built) in ABS plastic (Fig.5.2.1). The new holder held the plates 15 mm apart from the top of the substrates, along with a small baseplate. However, the baseplate negatively affected deposition, and so the top

piece was used on its own (Fig. 5.2.2). The suspension preparation followed the procedure outlined in the previous section, using a 1vol.% suspension of Ti_3SiC_2 in water, adjusted to pH 9. The substrates were once again cleaned with IPA, and the substrate surfaces were also roughened with P600 SiC grinding paper to provide better adhesion for the coating. Some observations of initial tests are displayed in table 5.2.1; these results were used in conjunction with zeta-potential data to determine the optimum conditions.

Conditions	**Observations**
- Titanium electrodes, cleaned with isopropanol. - 1%vol solution, unadjusted pH - 6V, 10 minutes, 10mm separation.	- 0.8–1 mA of current flow, poor deposition. - When voltage increased to 12V, 2.3mA flow. No observably better deposition. - At 15V (3.2mA) excessive bubbling and poor deposition due to electrolysis.
- Titanium electrodes, cleaned with isopropanol. Surface as received. - 10V, 10 minutes, pH 9 1%vol. suspension. - Printed sample holder with baseplate, 10mm separation.	- Surface deposits thin and appeared to wash off when lifted, small rivulets of removed deposit formed. - Baseplate disrupted the deposit at the bottom of the substrate, will be omitted in future depositions.
- As above with surface roughened with p600 grinding paper. - No baseplate in the sample holder.	- Deposition more even up to the edges, slightly thinner at air/water interface. - Less deposit washed off, appears to be better than previous results. Sample was left to dry and re-deposited
- Suspension as above, using sample with a deposition on it.	- Deposition appears thicker after second deposition. More even coating and deficient areas previously have been 'filled in'.

Table 5.2.1 – Some preliminary observations from EPD tests.

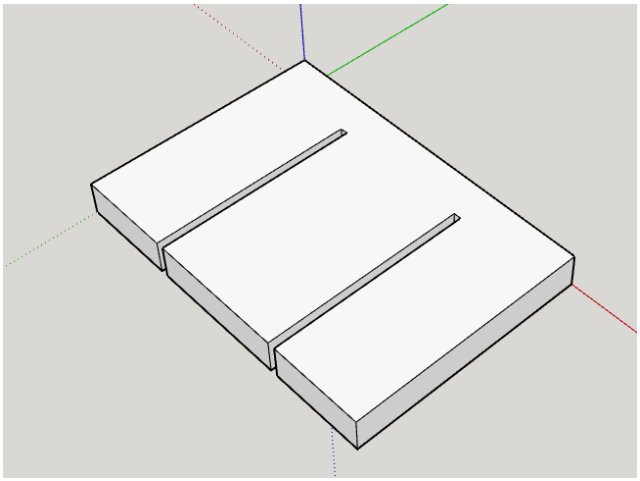

Fig. 5.2.1 – CAD model of sample holder, rendered in Sketchup.

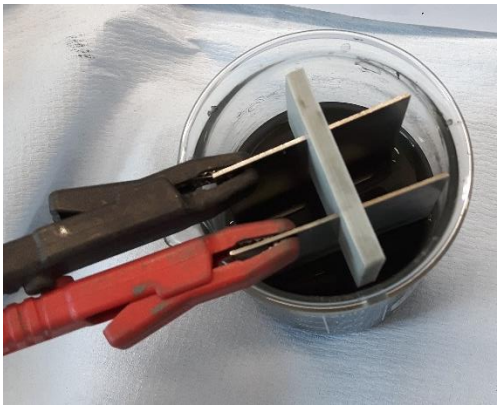

Fig. 5.2.2 – Experimental setup showing new sample holder.

Due to the delicate nature of the green deposits, directly measuring their thickness was difficult. Consequently, an area density measurement was used to measure the quantity of material deposited. The substrates were weighed prior to deposition, subject to EPD and left to dry. The substrates were weighed once again, and the deposited area measured using digital callipers. The mass difference and the area were used to give a surface density ρ of the coating, shown in equation 5.2.1.

$$\rho = \frac{M}{A} = \frac{m_2 - m_1}{x \times y} \quad (5.2.1)$$

Where M is the mass difference and A is the coating area (rectangular, found by measuring width x and length y). The mass difference is between m_2 and m_1, the post-coating and pre-coating mass respectively.

Further to this, a strip of titanium with green deposition was carefully mounted in resin and polished. However, despite attempts to pour the resin gently from behind the coated side, the viscous resin removed and dispersed the coating while it cured. This sample was polished, coated and analysed under SEM but no coating was visible on the titanium foil. A coated titanium plate was placed in the vacuum furnace and sintered at 1400 °C for 1 hour in an attempt to densify and adhere the coating.

5.2.2 Results

The surface density deposition graph is shown in Fig 5.2.3. The mass of deposited material increases over time; the surface density after 10 minutes on titanium is 1.89±0.26 mg/cm^2. During the deposition the current fluctuated slightly between 0.8-1mA, but largely remained stable. Photographs of deposition onto titanium and ZIRLO®, along with SEM images of the green deposit on Ti are shown in Fig. 5.2.4. The coating appears more uniform on Ti than with the small copper samples, and once again there are large (>10µm) particles visible.

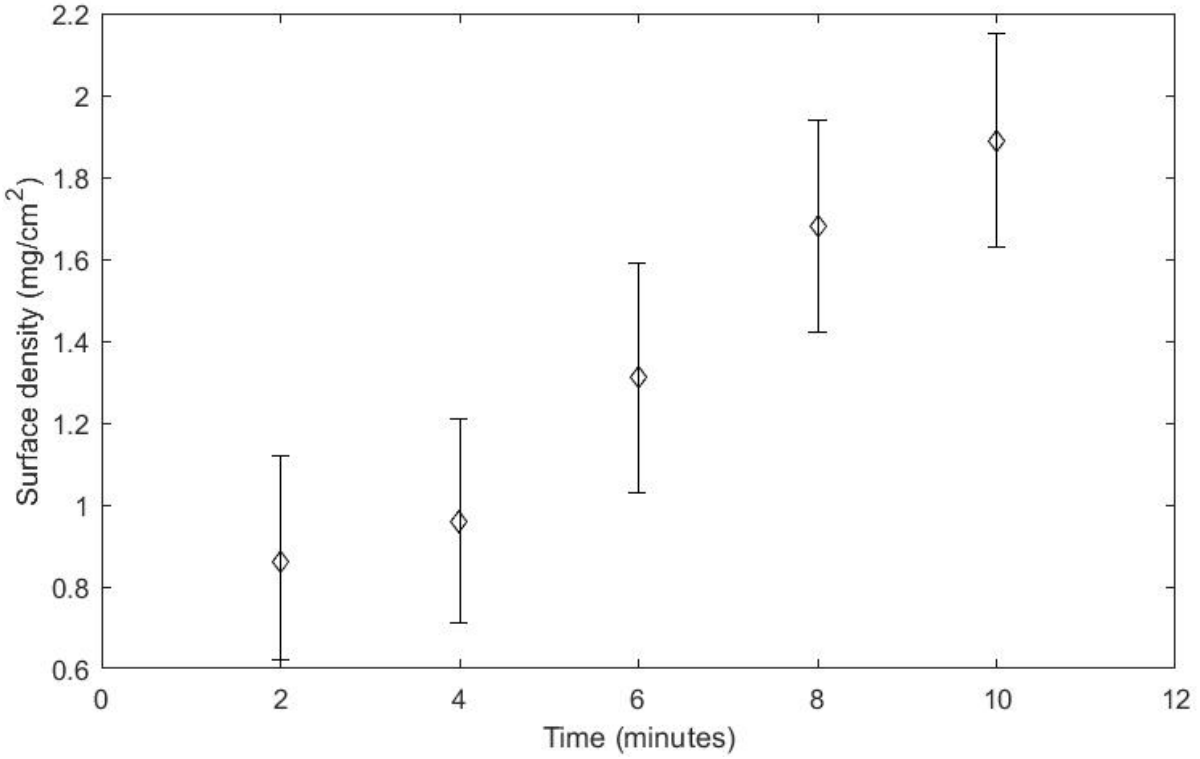

Fig. 5.2.3 – Surface density versus time for EPD of Ti_3SiC_2 onto titanium in water at pH 9, with 10 V applied.

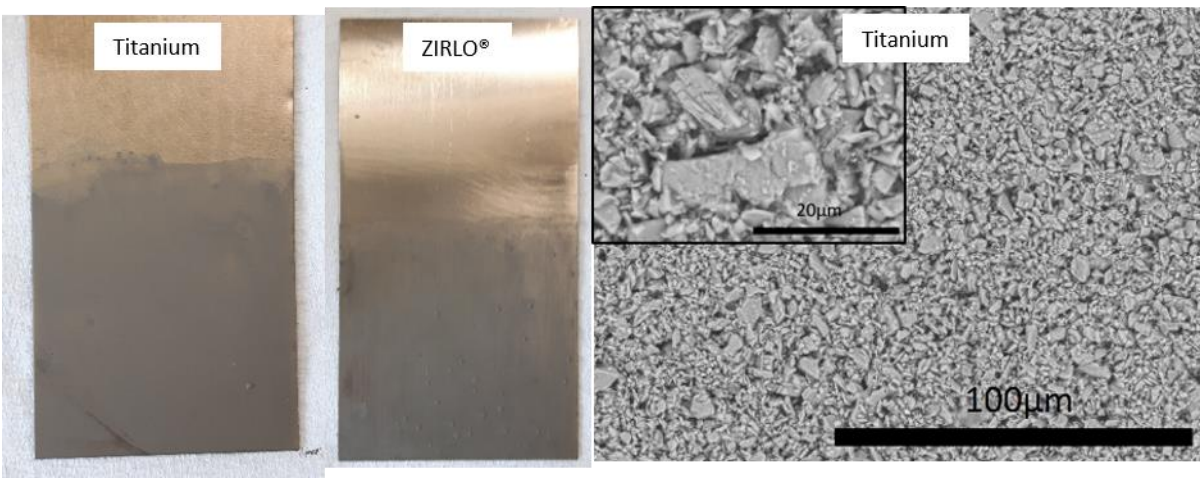

Fig. 5.2.4 – Photographs of depositions. SEM images of green depositions on titanium (right), with large particles visible.

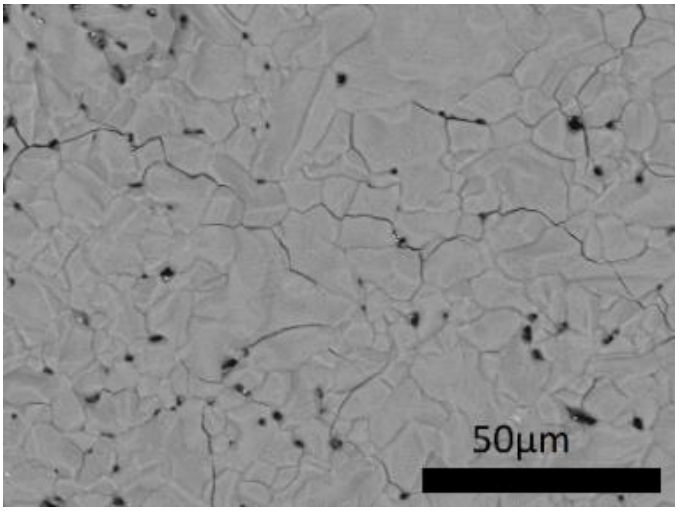

Fig. 5.2.5 – Spalled flake of densified MAX phase coating on Ti, after a 1400 °C 1 hour sinter under vacuum.

After sintering, the coating failed to adhere to the substrates at all, but instead formed large flakes. One of these flakes was placed on an SEM stub and imaged, Fig. 5.2.5. Although cracked, the coating appears dense, with some small porosity. However the titanium and ZIRLO® retained no densified coating.

5.2.3 Discussion

The new sample holders functioned better, and combined with larger deposition substrates, the coatings appeared uniform, with minimal suspension remaining on the surface when the substrates were removed. The time deposition graph was largely as expected, but in comparison with Liang *et al.*, the deposits produced in this work were approximately a factor of 2 thicker, most likely due to the use of 10V, whereas Liang *et al.* used 3V.

The deposited layers on titanium and ZIRLO® appeared more uniform than on the smaller copper substrates. However, deposited layers at the very top of the plate, corresponding to the surface of the suspension were visibly thinner than those in the bulk. This is likely due to the beginning of the suspension settling. After sintering, the coating densified at 1400°C but failed to adhere to the substrate. Unfortunately in the case of zirconium alloys, heating the cladding to this temperature is unfeasible due to a phase change at 862°C [5]. Some deposited samples of copper, graphite and titanium were vacuum sintered at 800°C for up to 20 hours, but none resulted in any densification.

5.2.4 Conclusion

Using the suspension characteristics determined in the previous experiment (1vol.% Ti_3SiC_2 in pH 9 water), deposition surface densities of 1.89±0.26mg/cm^2 were achieved after applying 10V for 10 minutes across titanium plates 15mm apart. It was assumed that the deposition results were similar on the ZIRLO® substrates as they were similar in appearance. SEM shows the presence of large (>10μm) particles in the deposition which is unexpected. Attempts to densify the coating to the substrate while remaining adherent were unsuccessful with conventional sintering methods.

5.3 – Rapid laser sintering

After unsuccessful attempts at densifying the coating conventionally, a more novel approach was taken using the 200W laser in a Renishaw SLM 3D printer to rapidly sinter the coating and adhere it to the substrate. With this approach, the coating was densified and partially adhered, although overall coverage was less than complete.

5.3.1 Materials and methods

Coated titanium and ZIRLO® plates were used from the previous experiment (see above). No preparations were performed before laser sintering other than letting the plates dry in a fume cupboard for at least 2 hours. A Renishaw AM250 Selective Laser Melting (SLM) 3D printer was used as a laser source (1080nm wavelength). The AM250 is a pulsed laser system which scans an area with rapid static pulses of emission which overlap slightly. Under normal operation this would fuse metal powder in a powder bed, which is subsequently covered with another layer of metal powder and the laser scans again, during which the metal baseplate is lowered, allowing 3D metal structures to be printed. However for this experiment the powder feedstock was removed, along with the wiper which spreads layers of powder. The baseplate was lowered to compensate for the thickness of the coated plate, and the system was paused after one 'layer' meaning that the coating was scanned by the laser only once. The sintering takes place in an argon environment. Using the Renishaw Materials Development Module (MDM), matrices of squares were set up to test a ranges of two parameters affecting the energy density, namely laser power (W) and laser focus (mm) which raises the focal point of the laser above the surface of the plate, resulting in a wider spot. Unfortunately the AM250 was not available for use on the coated ZIRLO® samples, so a different model of SLM printer, the AM125 (Renishaw, 1064nm wavelength) was used to sinter them.

After the laser sintering process, the samples were sectioned using a Secotom-50 (Struers) running at 3000rpm and a feed rate of 0.1mm/s with a non-ferrous cut-off wheel 10S20 (Struers). Water was

used for cooling and lubrication. Some samples were imaged using SEM (Hitachi TM3030 and FEI Inspect F) and characterised by Raman (Renishaw InVia microscope). Samples of particular interest were set in resin and polished, allowing SEM imaging of the cross section.

5.3.2 Results

Initial parameters for the laser sintering were: 10–200W across ten columns (21.11W increments), and the beam focus between 0–14mm across eight rows (2mm increments), resulting in eighty 5mm squares with a 1mm gap between them. A photo of the plate is shown in Fig. 5.3.1. Visually, there are three distinct regions on the test plate: a region of low power and wide focus which appears to have densifies the coating but not adhered to the substrate (region A), a region spanning low power and tight focus to higher power and wider focus which appears dense and adhered (region B), and a large section at the higher powers where the coating has been ablated by the laser (region C). Towards the increasing power end the plate was noticeably bent.

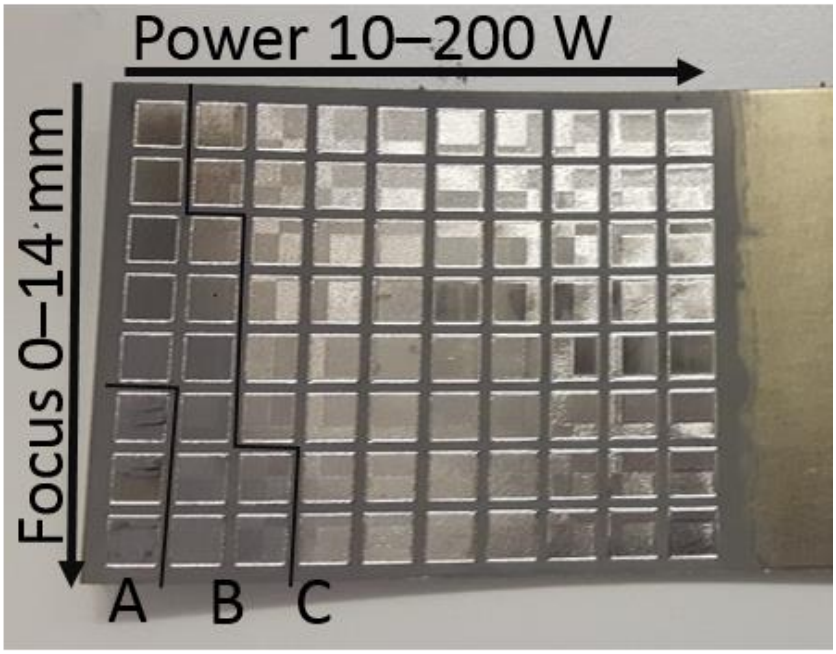

Fig. 5.3.1 – Outcome of initial laser sintering test on Ti substrate showing: dense but flaky coating (A), potentially dense and adhered coating (B), and ablated metal (C).

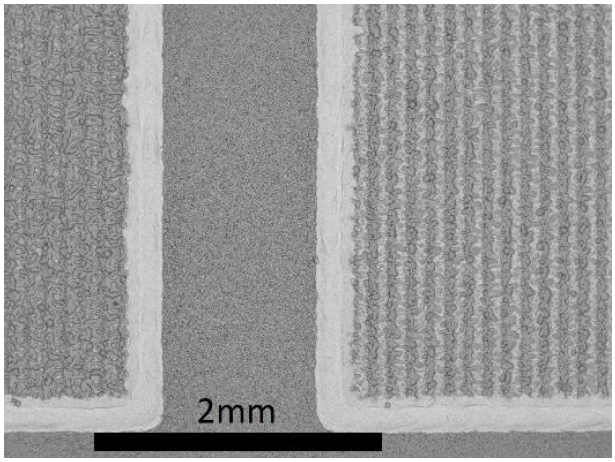

Fig.5.3.2 – SEM image showing morphology of the laser sintered test squares compared with the green region between. 10W, 6 mm focus (left) and 31.11W, 6 mm focus (right).

Fig. 5.3.2 shows an example of the coating morphology compared with the green coating between scans. The coating surface is globular, with some exposed lines, which correspond to the path of the laser. SEM images of the 2nd column, corresponding to 31.11 W are displayed in Fig. 5.3.3 showing the effect of widening the beam by defocussing. At a tight focus (0–6 mm) the path of the laser is clear, resulting in an ablated pathway with some densified regions to the periphery. As the beam is spread further (8–14 mm), less ablation takes place and the coating coverage starts to improve, although still with some gaps.

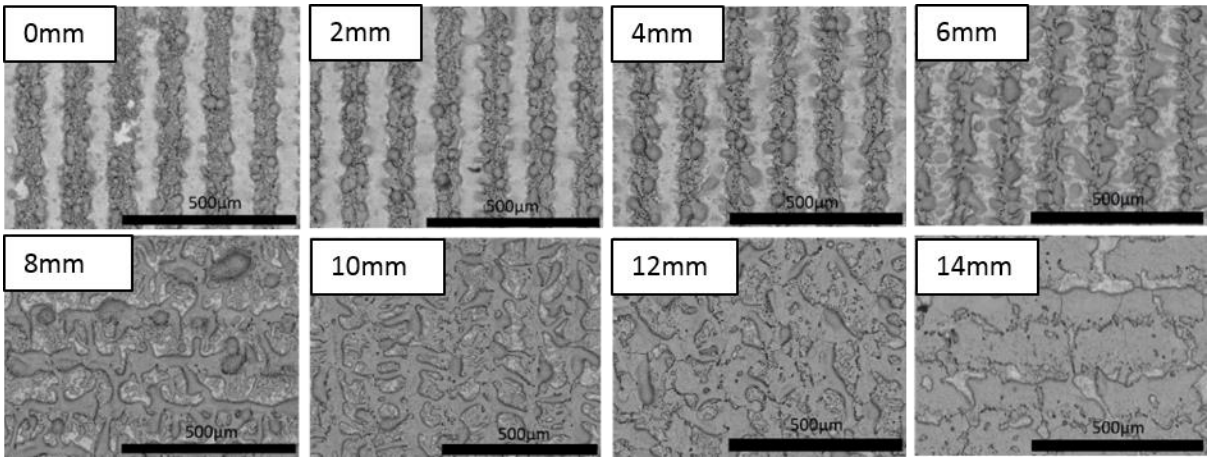

Fig.5.3.3 – SEM images comparing the effect of increasing beam defocus for a set power (31.11W).

From a purely visual inspection of the first plate, the power range was clearly too high, and so the next set of parameters used were honed in on the region B shown in Fig.5.3.1. The square size was increased to 10mm and the number of rows and columns halved. New parameters used were 5–50W powers, across 5 columns (11.25W increments) and focus parameters of 5–10mm and 5-20mm. Cross

sections of samples at 16.25 W (10mm focus), and 5 W (5mm focus) are shown in Fig. 5.3.4. The thickness is between 10–30µm, and the adhesion varies greatly. At 16.25W with a defocused beam (10mm focus), the coating layer is uniform in its coverage, however the adhesion to the substrate is poor, and there are cracks in the coating. At low power and narrow focus (5W, 5mm) the periodic strips of coating can be seen giving partial coverage, but these ridges are well adhered to the substrate. There is also a nodular surface phase on top of the densified coating that is cracked and not well adhered. EDX analysis of this surface phase reveals an absence of silicon due to volatilisation, resulting in TiC_{1-x} (Fig. 5.3.5). Generally speaking, wide focus results in a cross section morphology with good coverage but poor adhesion, while narrow focus gives rows of well adhered coating bands. High power and wide focus gives a 'best of both' situation with wider adhered bands with gaps. However the TiC_{1-x} surface phase is increased with higher laser power (Fig. 5.3.6).

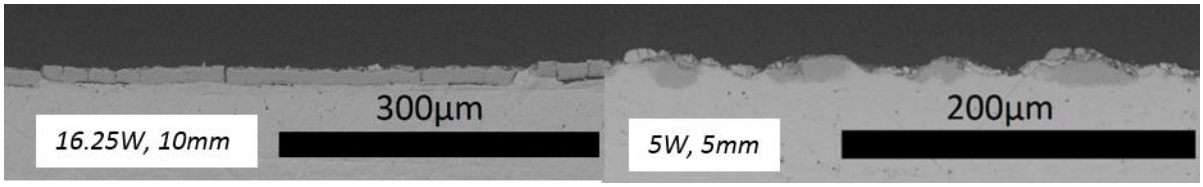

Fig. 5.3.4 – SEM (SE) images of coating cross sections on Ti.

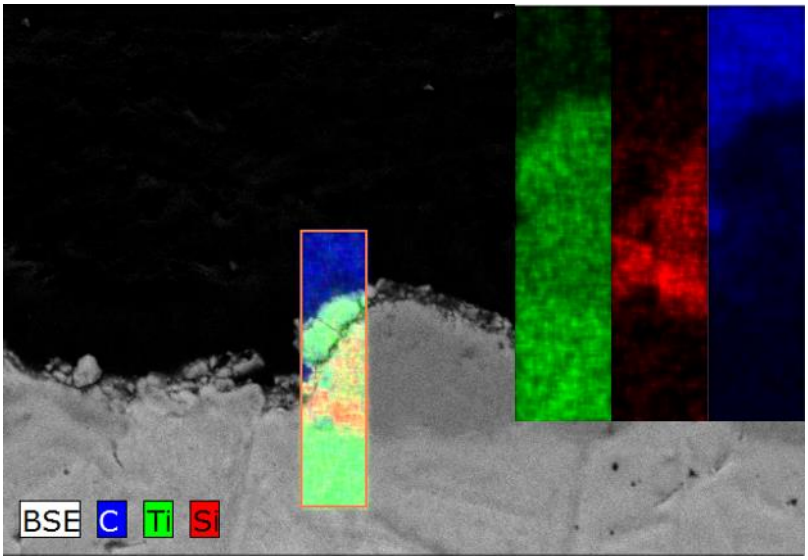

Fig. 5.3.5 – EDX spectra of the cross section of coating on Ti for 5W, 5mm focus.

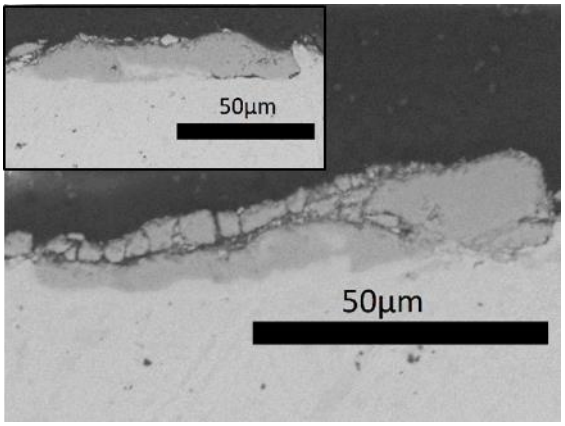

Fig. 5.3.6 – 50 W, 10 mm focus sample on Ti showing wider bands with increased TiC_{1-x} surface phase.

To confirm that the coating was not amorphised during the sintering process, Raman analysis was performed on both the surface (Fig 5.3.7) and the cross section (Fig. 5.3.8) of the coating. Raman from the surface of the coating still shows characteristic MAX phase peaks, while also displaying the two broad peaks associated with TiC_{1-x} [6]. While lower intensity (due to the small area), the cross sectional Raman scans still displayed some Ti_3SiC_2 peaks.

Unfortunately the samples sintered on the AM125 (both titanium and ZIRLO®) resulted in some densification but very poor adhesion, resulting in the coating being eroded by the saw coolant spray when sectioning was attempted. Raman of the zirconium plate was undertaken before sectioning, and Ti_3SiC_2 peaks were visible along with TiC_{1-x}.

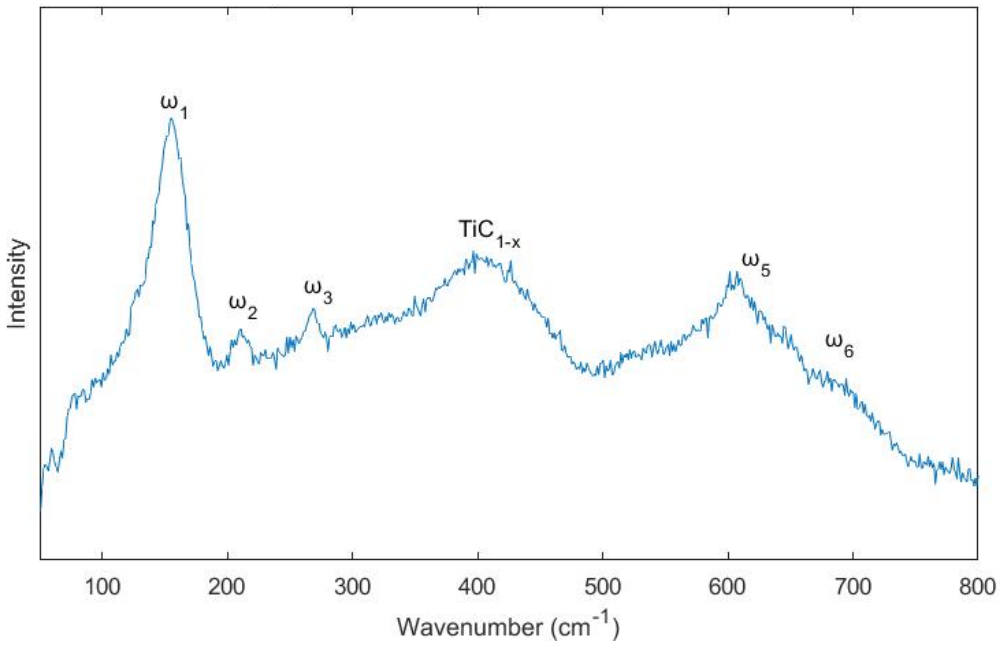

Fig. 5.3.7 – Raman analysis of laser sintered (38.75W, 10mm focus) Ti_3SiC_2 coating surface on Ti.

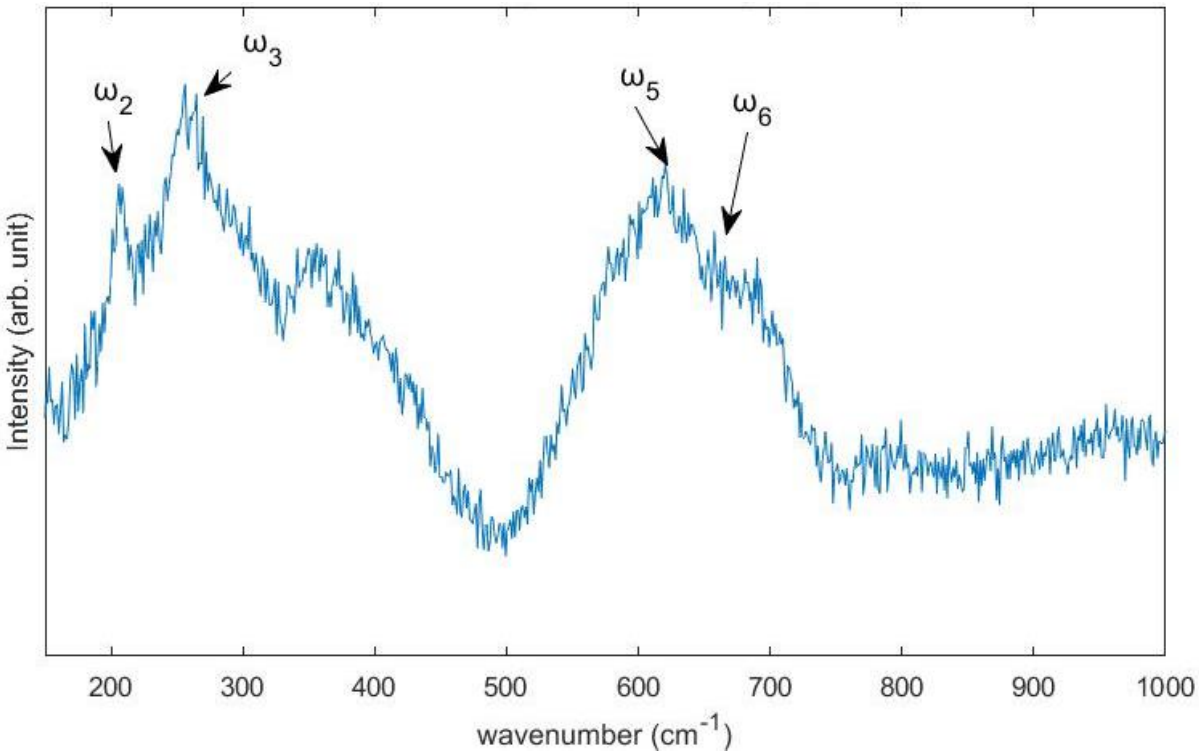

Fig. 5.3.8 – Raman analysis of laser sintered (50W, 15mm focus) Ti_3SiC_2 coating cross section on Ti.

5.3.3 Discussion

Unfortunately, the details of the optical set up of the AM250 and AM125 are not widely available. Without knowing the collimated beam width before focussing and the initial focal length (with focus parameter set to 0) the exact energy deposited by the laser per unit area cannot be quantitatively determined. Literature gives the spot size of the AM250 at ~70µm when focussed [7] [8], which is consistent with the first SEM image in Fig.5.3.3.

The samples sintered using the AM125 did not fully adhere to either the Ti or the ZIRLO® substrate. A possible reason this this is that the spot size on the AM125 is around half the size of the AM250 at ~35µm, increasing the intensity by a factor of 4 [9]. Further to this, the beam travel speed was slower, and the hatching distance was initially different; the AM250 left a gap of around 70µm between beam pathways, while the AM125 initially gave total scan coverage by laser. A subsequent run with a wider hatching distance on the AM125 still failed to densify the samples.

Ideal parameters for sintering with the AM250 on Ti involved a wider focus (10mm) coupled with a relatively low power (>20W), which resulted in the best coverage. A TiC interlayer pre-deposited may improve adhesion of the coating to the substrate, or perhaps ZrC and a Zr-based MAX phase in the

case of zirconium alloys. The use of a laser to densify MAX phase coatings has potential, and more work needs to be done on a wider range of parameters to optimise. As well as using an AM250, an alternate or bespoke CNC (Computer Numerical Control) laser may yield more quantitative results for the energy density required to densify and adhere quickly without ablating or volatilising the coating.

To apply this work/technique to a cladding-coating application, even coverage would be needed, as partial coverage would likely result in accelerated corrosion on the bare zirconium alloy and create weak regions. Adhesion is a critical factor as well, as any loss or removal of coating from damage associated with transport and insertion of the fuel assemblies would again present a region with accelerated corrosion.

5.3.4 Conclusion

Using a novel approach to MAX phase sintering, SLM 3D printers were used to rapidly densify EPD Ti_3SiC_2 coatings on Ti. At low power and narrow focus (5W, 5mm) the coating densified into well adhered bands, with some TiC_{1-x} surface phase, while increasing the power and widening the focus (16.25W, 10mm focus) results in better overall coverage but poorer adhesion. High power and wide focus (50W, 10 mm) gave wider adhered bands with some cracking and an increase in the surface phase. Raman spectroscopy indicates that some of the coating remained crystalline MAX phase. The work done on an older model, the AM125 was unable to replicate the results produced by the AM250, and as a result densified deposits were not obtained on ZIRLO, although it is assumed this is due to equipment problems rather than a fundamental problem.

5.4 References

[1] M. Mishra, Y. Sakka, C. Hu, T. S. Suzuki, T. Uchikoshi, and L. Besra, “Electrophoretic deposition of Ti 3 SiC 2 and texture development in a strong magnetic field,” *J. Am. Ceram. Soc.*, vol. 95, no. 9, pp. 2857–2862, 2012.

[2] Y. Liang, Z. Sun, J. Chen, X. Liu, and Y. Zhou, “Electrophoretic Deposition of Ti 3 Si(Al)C 2 from Aqueous Suspension,” *J. Am. Ceram. Soc.*, vol. 1921, no. 26735, pp. 1916–1921, 2010.

[3] C. D. Hartley, “Laboratory Scale Mill: Powder Location Tests,” *NNL 11764, Issue 2*, 2017.

[4] F. Tang, T. Uchikoshi, K. Ozawa, and Y. Sakka, “Effect of polyethylenimine on the dispersion and electrophoretic deposition of nano-sized titania aqueous suspensions,” vol. 26, pp. 1555–1560, 2006.

[5] I. Schnell and R. C. Albers, “Zirconium under pressure: Phase transitions and thermodynamics,” *J. Phys. Condens. Matter*, vol. 18, no. 5, pp. 1483–1494, 2006.

[6] B. H. Lohse, A. Calka, and D. Wexler, “Raman spectroscopy as a tool to study TiC formation

during controlled ball milling," *J. Appl. Phys.*, vol. 97, no. 11, 2005.

[7] W. S. Gora, Y. Tian, A. P. Cabo, M. Ardon, R. R. J. Maier, P. Prangnell, N. J. Weston, and D. P. Hand, "Enhancing surface finish of additively manufactured titanium and cobalt chrome elements using laser based finishing," *Phys. Procedia*, vol. 83, pp. 258–263, 2016.

[8] S. Ghouse, S. Babu, R. J. Van Arkel, K. Nai, P. A. Hooper, and J. R. T. Jeffers, "The influence of laser parameters and scanning strategies on the mechanical properties of a stochastic porous material," *Mater. Des.*, vol. 131, pp. 498–508, 2017.

[9] M. Król, L. A. Dobrzański, Ł. Reimann, and I. Czaja, "Surface quality in selective laser melting of metal powders," *Arch. Mater. Sci. Eng.*, vol. 60, no. 2, pp. 87–92, 2013.

6. Slip casting MAX phase tubes, densification and subsequent testing

Electrophoretic deposition failed to produce thick enough coatings on graphite rods to sinter and produce a tube, so another method was needed. Given the available equipment and its well-established nature, slipcasting was chosen. Although centrifugal slipcasting would likely result in a denser tube (see literature review) it requires bespoke equipment, so standard slipcasting was used to prove the concept. The following section covers suspension preparation, casting and sintering of tubes, finishing and final testing.

6.1 – Slip preparation, casting and sintering

Initial slip measurements were carried out qualitatively. Green slip bodies were cast and left to dry before sintering. Densification at a range of temperatures and different environments was carried out to sinter the tubes and burn out the additives. Cross sections of sintered tubes were characterised to determine density and composition after sintering.

6.1.1 Materials and methods

As with the previous experiments, Ti_3SiC_2 (Maxthal 312) was used as a placeholder for a reactor-suitable MAX phase. A second batch of Maxthal 312 was obtained with a stated mass-median-diameter (D_{50}) of 2.5µm to see if this aided casting. PEI (Sigma Aldrich, M_w 25,000, <1% water) was tested as a dispersant, while methylcellulose (Sigma Aldrich, viscosity of 4000 centiPoise (cP)) was used as a thickener; to increase the viscosity without further raising the solids loading. To construct the moulds, plaster of Paris (JW Superwhite) was used, alongside modelling clay to create a seal, and petroleum jelly and washing-up liquid to act as mould release.

Methylcellulose is hygroscopic and prone to clumping when added to water. However it has the unusual property of being insoluble in hot water (>50 °C) while having a high solubility in cold water. This, combined with the difficulty of using PEI (see previous section) led to the following procedure for slip preparation. To ensure proper dispersion, PEI was first weighed into a beaker, to which the necessary amount of water was added. The solution was placed on a hotplate (Jenway 1000) set to 70 °C while being intermittently stirred with a glass rod, until the strands of PEI had completely dissolved. The methylcellulose was then weighed into a weighing boat and quickly added to the beaker. The insolubility of the particles causes them to disperse and not gel in contact with the water. After being stirred again, the Ti_3SiC_2 was weighed and added with additional stirring. The still warm slip was then transferred to a small glass bottle (10ml) or a larger polypropylene mill bottle (250ml) depending on the quantity needed and the samples were kept moving while they cooled. The larger bottles were

placed on the roller mill (Brook Crompton TYP T-DA63MB-D), while the smaller samples were placed on a tube rotator (Cole Palmer) at 30rpm to ensure the thorough mixing of samples too small for a blunger[1].

Based on the literature and qualitative assessment, a slip consisting of Ti_3SiC_2, water and PEI in the mass ratio of 40:20:1 respectively was combined and agitated for 24 hours. The slip was then poured into an existing tubular one piece mould with a diameter of 3cm. After 2 minutes, the excess slip was poured from the mould, and the sample was left to dry for 2 weeks, which is much longer than traditional slip casting. The length of time was to ensure the small plaster moulds and the tube had dried fully, since initial attempts to de-mould pieces more quickly resulted in failure. Removing the part resulted in some cracking around the top, but a large portion remained intact. Based on the poor green body strength of this part, methylcellulose was added to subsequent slips. The use of small quantities (approx. 3% of dry weight or less) of methylcellulose were key, as addition of too much caused the slip to form a gelatinous mass which did not pour easily.

A more thorough investigation into the slip properties was carried out. Rheology measurements were performed on an AR2000 rheometer (TA instruments), using a 20mm plate and cone geometry. A pre-shear phase with constant shear rate of 1 s^{-1} was applied for each sample for 120 seconds. This was performed largely to ensure the sample was well distributed between the plates, and to check there were no large agglomerates or air bubbles. Then the shear rate was varied logarithmically between 0 and 100 s^{-1} with 10 seconds on each of 16 steps. The viscosity was measured as a function of time and of shear rate respectively. The slips tested are shown in Table 6.1, percentages are shown as a fraction by mass of the Ti_3SiC_2 (dry weight basis or DWB).

[1] An agitator used on larger quantities of slips, involving a rotating paddle in a chamber or bucket.

Slip Identifier	Water (%DWB)	PEI (%DWB)	Methylcellulose (%DWB)
A	46.0	4.0	0.0
B	46.0	4.0	0.5
C	46.0	4.0	1.0
D	50.0	4.0	0.0
E	50.0	4.0	0.5
F	50.0	4.0	1.0
G	52.0	4.0	0.0
H	52.0	4.0	0.5
J	52.0	4.0	1.0

Table 6.1.1 – Slip compositions tested with a rheometer. Percentages are as a fraction of the powder weight.

A more appropriate mould was made with a former roughly approximating the dimensions of a fuel cladding rod. The former was 11.5mm in diameter, 15cm in length, and had a bevel on the bottom edge to facilitate easier removal of parts. This former was used to make a one piece mould, as well as a 2 piece mould. The former was designed in FreeCAD v0.15 and reproduced in brass.

The new moulds made are shown in Fig. 6.1.1. The two part mould was created by setting half the former in modelling clay, and placing 3 modelling clay 'keys' on the face of one mould before covering in plaster and leaving to set. The mould was allowed to dry before being painted with a thin layer of washing-up liquid, replacing the former and pouring plaster over. The washing-up liquid acts as a water soluble mould release, as petroleum jelly or oil-based release agents could block water uptake in the mould. When the top half was set the two mould halves were separated and allowed to dry fully before washing the mould release away with water and allowing to dry again.

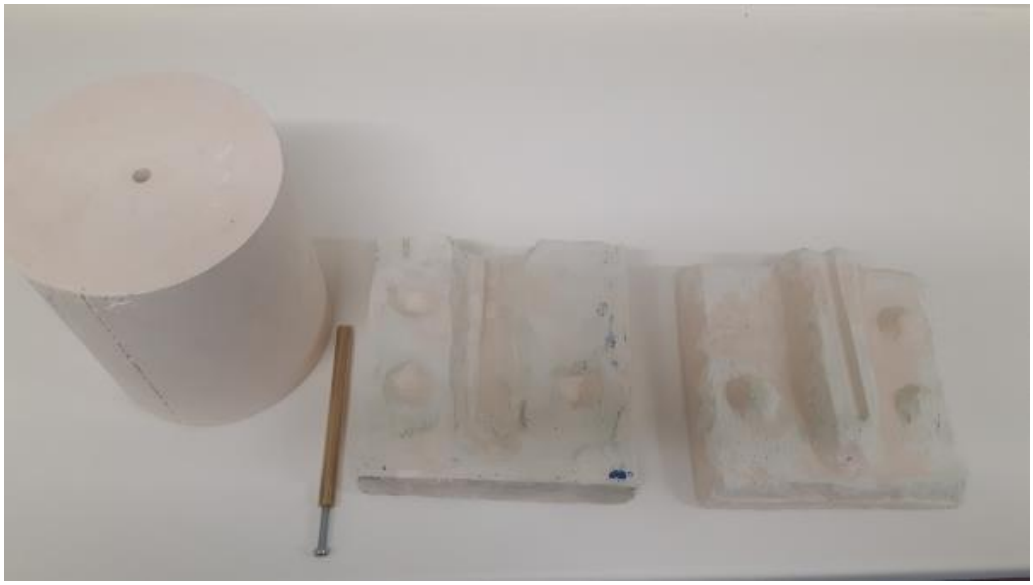

Fig. 6.1.1 – New moulds and the former made to be more dimensionally correct for fuel rods.

To sinter the green parts, they were subjected to a 2 hour dwell in a tube furnace under flowing argon (~0.25 L/min) or vacuum and temperatures between 1300 and 1450°C (see standard procedure). To burnout the polymers, a 1 hour interim dwell at 500°C was included in the furnace runs. A small sample of green body casting was subjected to TGA (PerkinElmer Pyris 1) in argon atmosphere up to 1000°C to try and determine if the polymer loss was noticeable. Samples were sectioned, resin mounted, polished and examined by SEM (Hitachi TM3030) with EDX. Sections were also characterised with XRD and Raman analysis. Density measurements were attempted using helium pycnometry and the Archimedes method with water (immersion density), but the samples contained a large amount of open porosity, so density/porosity measurements were estimated using ImageJ software (Version 1.51u, National Institute of Health).

6.1.2 Results

Fig. 6.1.2 shows the largest piece of the casting with the first slip tested. Despite being in the mould for a very short time, a thick layer had built up (~1cm) on the inside of the mould. This is much quicker than expected for slip casting which suggests this slip is not ideal. Too much water or a poor suspension can result in a fast water uptake as seen here. The part is visibly porous on the top broken edge, with the inclusion of macroscopic bubbles present in the slip. The wall thickness is relatively even, but there is a thinner section running the inside length of the tube, giving the whole a slight teardrop profile. This is likely due to a fault or crack down the inside of the mould.

Fig. 6.1.2 – Photographs showing the initial mould used (left), with the largest intact piece shown from the side (right) and the top (middle inset).

Fig. 6.1.3 shows the viscosity versus applied shear rate graphs for the 9 test slips. The rheological profiles fall into two distinct groups: 3 which behave as a Newtonian fluid (shear independent viscosity) and 6 which exhibit shear-thinning (pseudoplasticity) [1]. The Newtonian fluids correspond to the slips with no methylcellulose, with viscosity inversely proportional to water content. The methylcellulose-containing slips are much more viscous at rest but flow easier with increasing applied load. Increasing methylcellulose content increases viscosity, but lower water content did not always correspond to increased viscosity. For comparison, the viscosities at an arbitrary point ($10s^{-1}$) are replotted in Fig.6.1.4, with test slips in order of expected increasing viscosity. For the first 3 slips (no methylcellulose), the viscosity increases with decreasing water content, as it does with the first 3 methylcellulose containing slips. However looking at the 3 most viscous samples, the sample with the lowest water content (Slip C: 46%DWB water, 1%DWB PEI) is slightly less viscous than the preceding slip (Slip F, 50%DWB water, 15%DWB PEI). This is covered below in the Discussion Section.

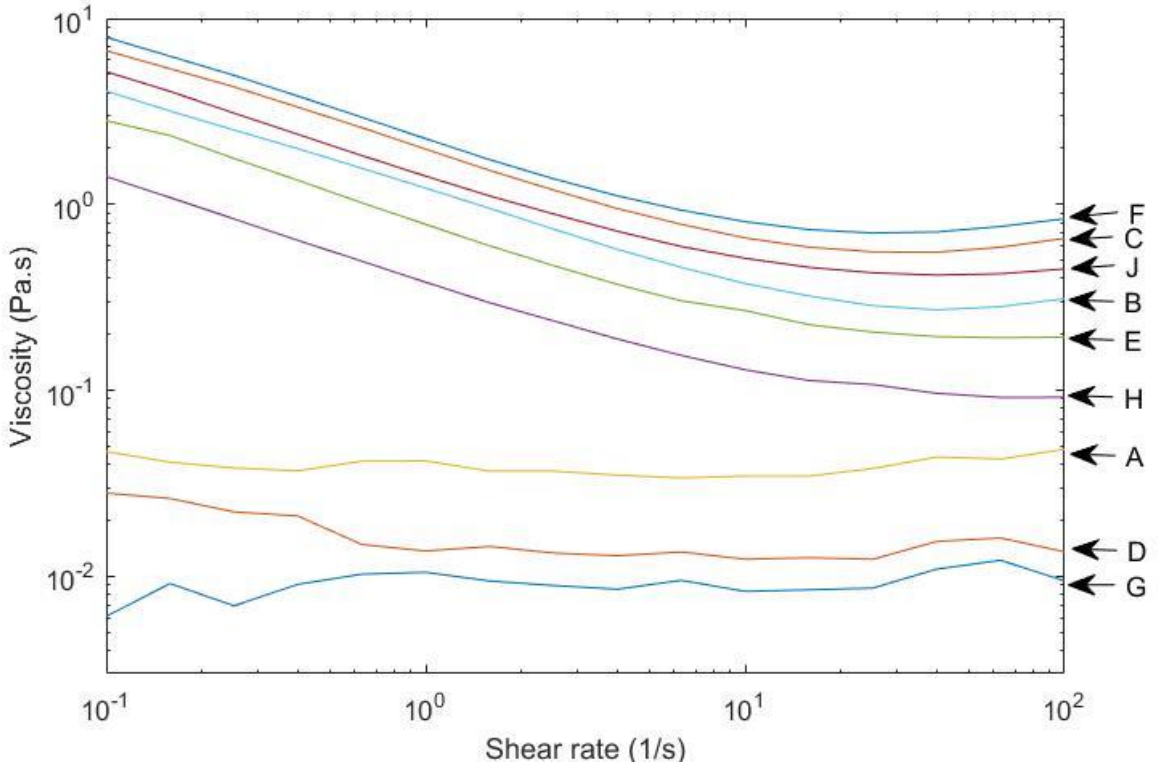

Fig. 6.1.3 – Viscosity measurements of the test slips for applied shear rates (each applied for 10s). Slip identifying letter corresponds to Table 6.1.1.

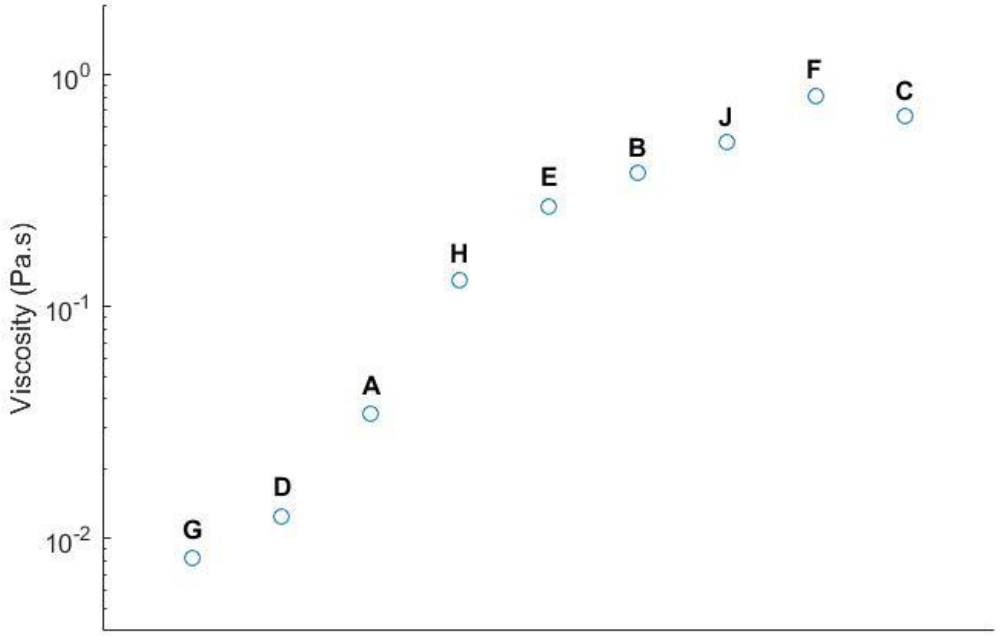

Fig. 6.1.4 – Viscosities for test slips at 10 s^{-1} shear rate. Slips ordered in expected increasing viscosity.

The mass change TGA results are shown in Fig. 6.1.5. Despite repeated runs under argon, the green Ti_3SiC_2 always began oxidising at ~400°C and continued sharply up to the maximum tested temperature. Although some mass loss was initially observed (maximum loss ~0.25%), it is likely the main burnout of the polymers was eclipsed by the oxidation of the MAX phase. This graph has been included to reiterate that Ti_3SiC_2 is not an ideal candidate for oxidation resistant cladding. XRD of the post-TGA sample revealed strong TiO_2 and SiO_2 peaks (not pictured). A burnout of 500°C was used to make sure the polymers were burnt out.

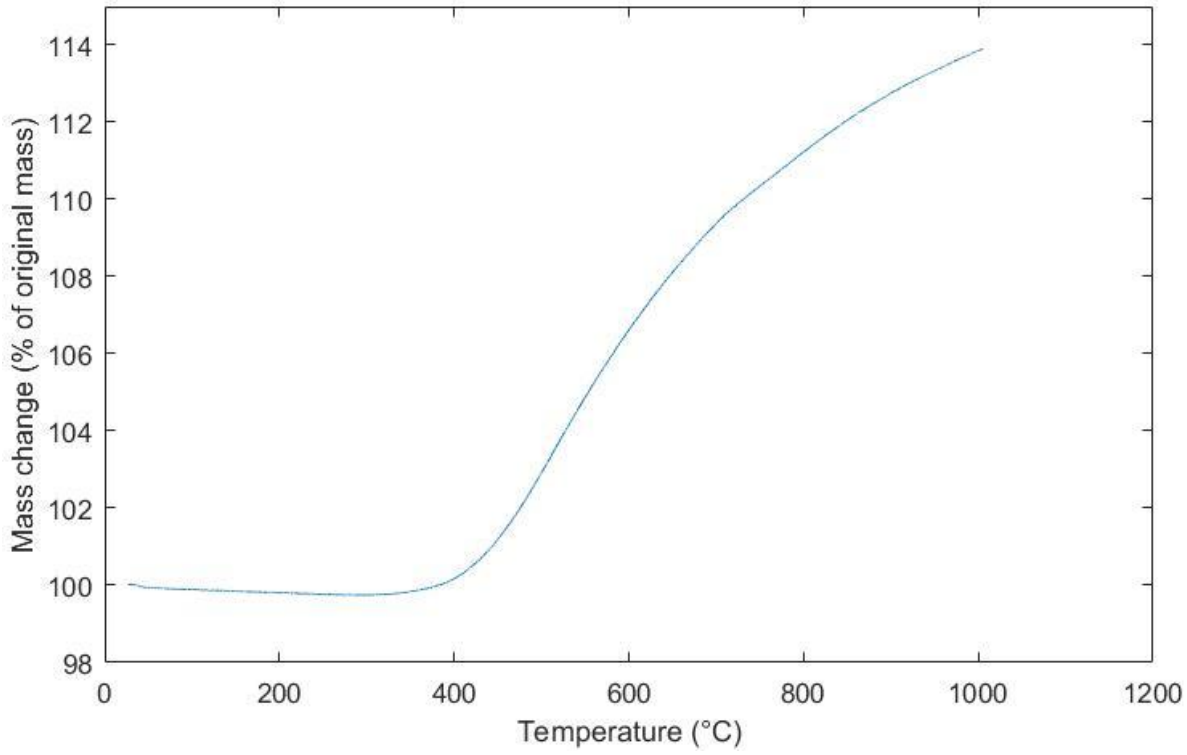

Fig. 6.1.5 – TGA of green Ti_3SiC_2 cast section.

XRD patterns of tube sections after sintering are shown in Fig. 6.1.5, including a sample that only received a burnout at 500°C for 1 hour. Samples under flowing argon failed to densify. Even after dwell temperatures of 1400–1450 °C, samples remained powdery and broke easily. Further to this, some TiO_2 (rutile) was present in the argon-sintered samples, caused by either an improper seal or purging of the furnace. Using the vacuum pump resulted in densification through sintering but from the XRD patterns the TiC peaks have increased in intensity. This is a common problem where the A element (silicon in this case) is more weakly bound, and so can volatilise at high temperatures, and this exacerbated by the vacuum.

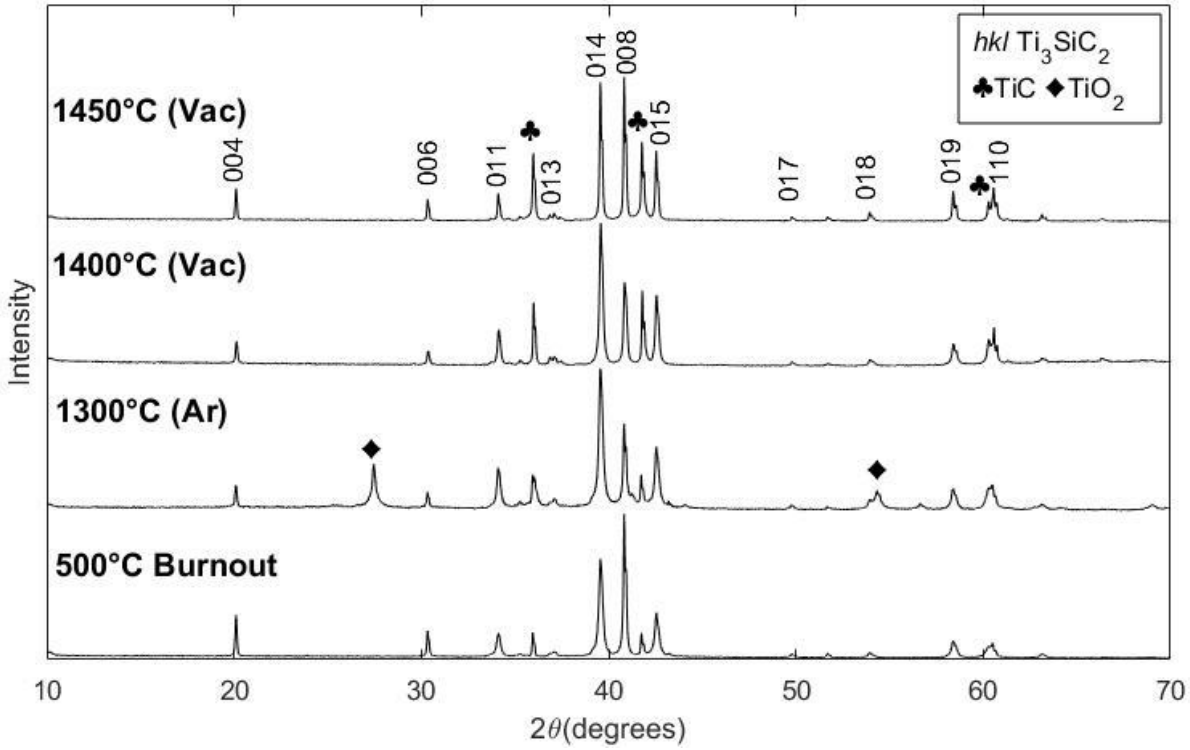

Fig. 6.1.5 – Example XRD patterns for slip cast samples sintered under flowing argon or vacuum. Argon sample shown did not densify.

Sintered samples were further cut into thin cross sections for characterisation by SEM and EDX. A sample of the first tube cast, sintered at 1450°C is shown in Fig. 6.1.6. The sample is riddled with macroscopic bubbles (some as large as 200µm) which were too big to 'sinter out'. Analysing a region without large bubbles with ImageJ yielded a surface density of 87.9%. Fig. 6.1.6 also shows an edge region of the tube, along with EDX analysis. This darker, porous region is ~150µm thick and deficient in silicon.

Raman analysis of the edge region is shown in Fig. 6.1.7. Compared with a central section of the tube, Ti_3SiC_2 characteristic peaks are visible in the centre, but there is no appreciable signal from the edge region. Although TiC is Raman inactive, it is expected that this edge region would be TiC_{1-x} based on the decomposition of MAX phases (see Discussion in Section 6.2.3).

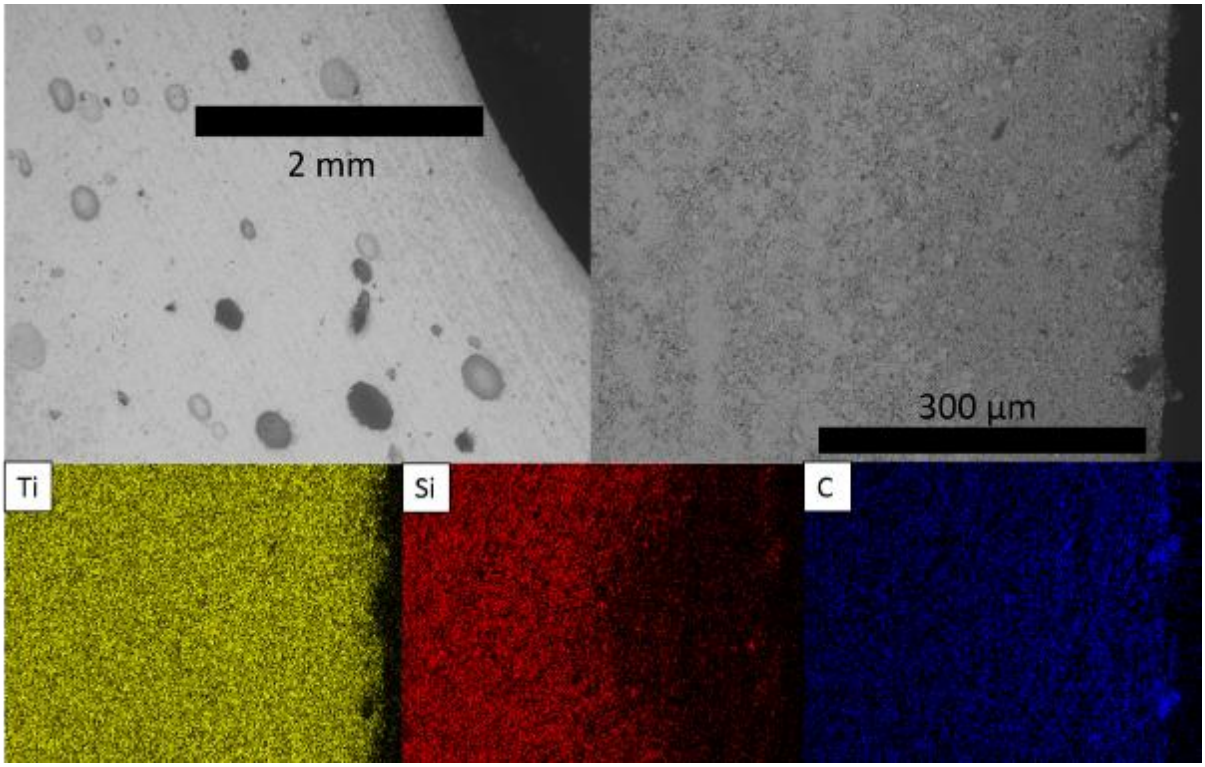

Fig. 6.1.6 – SEM images of bubbles in sintered tube (top left) and tube edge (top right). EDX spectra maps (bottom) of tube edge region.

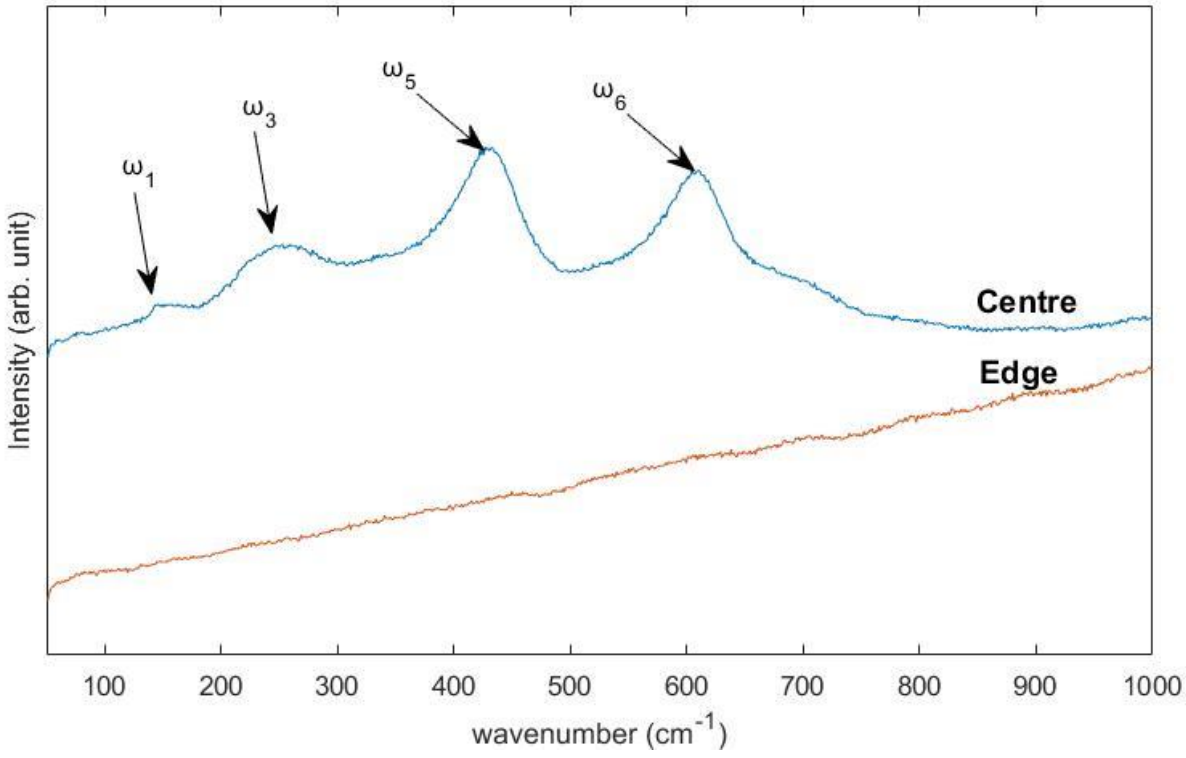

Fig. 6.1.7 – Raman analysis of central and edge regions of the tube cross section shown in Fig.6.2.4.

Removal of the green body from the new 1-piece narrow mould was impossible without destroying the cast part, but the 2-part mould yielded consistent casts, albeit with a few parts cracking upon removal. Using the 2-part mould with a degassing step before casting results in far fewer bubble inclusions in the final densified part (Fig. 6.1.8). The addition of methylcellulose as a thickener did slow down the water uptake, but it was still faster than traditional pottery slips. Tubes cast from the 2-part mould had large lateral 'sprues' running the mould seam, but these were removed after densification by grinding. ImageJ density estimates for a flat cross sectional region were 88.6%.

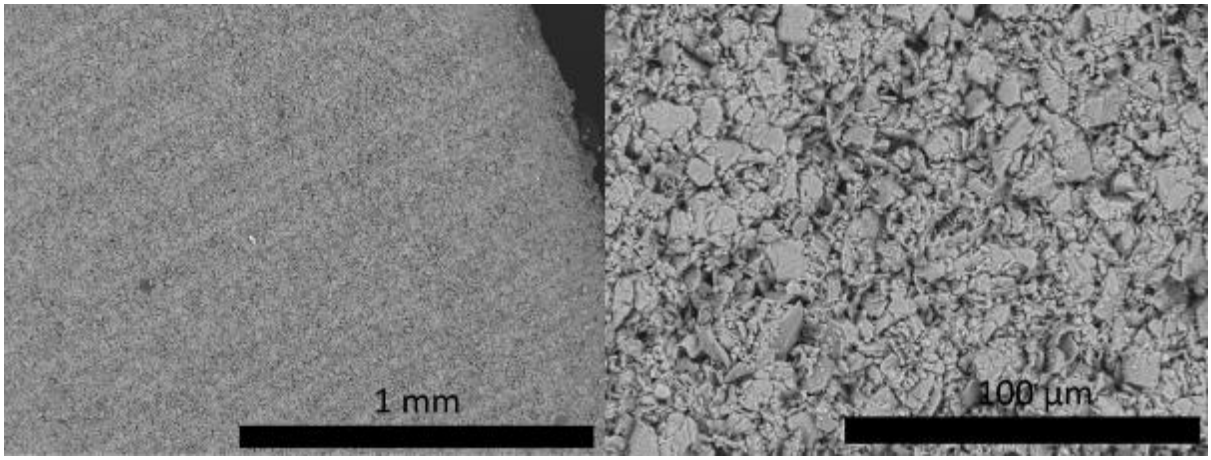

Fig. 6.1.8 – Sintered (1450°C, 2h under vacuum) slip cast tube cross section with new mould, methylcellulose containing slip. Slip was degassed before pouring.

6.1.3 – Discussion

Despite the first casting resulting in a section of green body tube, there were several problems. As previously mentioned the water uptake by the mould was very quick, meaning the suspension quality was poor. The speed at which suspended material aggregated on the mould interior is likely the reason for the trapped air bubbles. To mitigate this in the future, subsequent slips were subjected to a 5 minute degassing step in a vacuum desiccator connected to a pump (KNFlabs N86KT.18, 160mbar) between agitation and pouring. The low pressure was abruptly brought up to atmospheric pressure, which was hoped to burst any bubbles brought to the surface by the lower pressure.

The wider variation on the rheology graphs for PEI-only slips seems to reinforce the idea of a poor suspension; aggregations or uneven distribution of particles could result in inconsistent viscosity measurements. These samples also appeared to separate slightly under the plate and cone, with a more liquid region in the centre, surrounded by a thicker paste. Both may be a consequence of an improper molecular weight of PEI used (see Chapter 5).

The addition of methylcellulose seemed to help greatly with the overall suspension of the particles, and no separation was observed after testing. From Fig. 6.1.3 and 6.1.4, the slip with the 'expected' highest viscosity was actually slightly lower than the preceding slip. This may be due to user error, as a variation in the amount of material between the plates can offset results, as can any minor inclusions of air bubbles. Further to this, despite best efforts, methylcellulose is extremely hygroscopic in its powder form, and so may have absorbed extra water during slip preparation. However, the result is also indicative of a ceiling, where further addition of methylcellulose has less of an effect on the viscosity. Slip B (46%DWB water, 4%DWB PEI, 0.5%DWB methylcellulose) was chosen as the most appropriate to further explore; based on the rheological data, a pseudoplastic slip is preferable, as it is less viscous while being agitated and poured into the mould. This means the slip powder is better dispersed, and it can flow more easily into any mould detail. Once at rest in the mould, its viscosity increases, which helps slow down the passage of suspended particles and water uptake. Qualitatively, slips more viscous than Slip B were too thick to pour easily, and some of the highest viscosity slips were more paste-like and required a spatula to apply them to the rheometer.

The Raman analysis from the tube edge seems to suggest TiC rather than TiC_{1-x}, which is expected from silicon volatilisation from Ti_3SiC_2. A possible reason for this are that the ~10% TiC content in the Maxthal 312 are separate smaller particles, and so were more mobile and drawn to the mould surface first. Secondly, carbon-rich pyrolysis products from the polymer could have reacted with the substoichiometric TiC, although this is unlikely due to the relatively low temperature at which they are pyrolysed. However, the presence of surface ancillary phases are not a major problem, as parts could be made oversized and machined to the precise dimensions, removing this layer.

The improved slip composition gave a better water uptake speed and resulted in stronger green bodies. This in turn facilitated easier removal from the 2-part mould, although the process was far from lossless. Degassing the slip also helped reduce large scale porosity from trapped bubbles and indirectly help green-body strength. Many of the tubes had offset central holes after casting, and required careful drilling. This may be due to mould design, where one side was marginally thicker than the other, and so had more capacity for water uptake.

6.1.4 – Conclusion

A cracked yet largely intact tube was slip cast from a slip containing Ti_3SiC_2, 50%DWB water and 2.5%DWB PEI. After some further qualitative experimentation, the PEI content was increased to 4%DWB and the effect of water content and methylcellulose was investigated with a rheometer. PEI-only slips exhibited Newtonian responses to increasing shear rates, while the PEI + methylcellulose

slips exhibited shear thinning behaviour. Overall the PEI + methylcellulose slips were much more viscous, and a slip containing 46%DWB water, 4%DWB PEI and 0.5%DWB methylcellulose was selected as the most ideal slip for further testing. Two new moulds were made to cast tubes dimensionally appropriate for fuel rod cladding. Using a more suitable slip composition and a more appropriate sized 2-part mould, tubes were cast after a degassing step to reduce bubbles. The tubes were sintered up to 1450°C in a vacuum furnace, resulting in densification, alongside silicon loss from the surface.

6.2 – Tube finishing and testing

Using tubes cast and densified in the previous section, the samples were polished, sectioned and destructively tested to determine the maximum cylinder stress at failure.

6.2.1 – Materials and methods

MAX phase tubes produced in the previous section were used. To try and ensure consistency, all tubes in this section were produced from slip B (see above Section) using the 2 part mould. They were all subjected to sintering at 1400°C under vacuum for 2 hours. Due to lack of access to a lathe, the tubes were carefully hand polishing using SiC papers starting at P200 and finishing with P1800. The tube interiors were drilled out using 6mm tool steel bits on a pillar drill.

A bespoke hoop stress rig was designed (Fig.6.2.1). The three part rig consisted of a steel baseplate to which keys a 6mm diameter polyurethane bung. Finally a 6mm diameter ram axially compresses the bung which then expands radially inside the section of tube. Using a compression test rig (Zwick Roell Z050 with 50kN parallel platen load cell) the bung can be uniaxially compressed until the resulting radial expansion causes the tube sections to fail (brittle failure at room temperature [2], noting that ATF fuel clads would operate at around 350°C but testing at this temperature was unavailable for this). See Fig. 6.2.2 for the stress test rig dimensions. Fracture surfaces were examined under SEM (Hitachi TM3030).

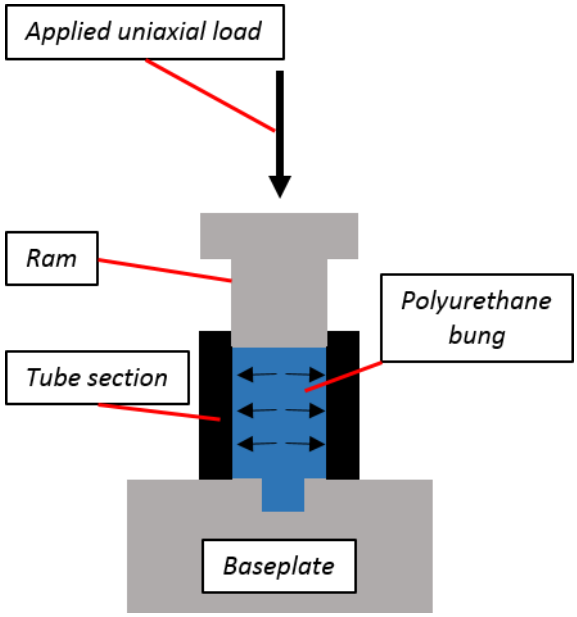

Fig.6.2.1 – Schematic of the test rig showing uniaxial force conversion to radial force.

The hoop stress rig is a simplified version based on the literature [3] [4] [5]. According to Mosley [6], when testing a tube to failure, the fracture force F can be determined from the following:

$$F = \left(1 + \frac{s}{S}\right)(F_T - F_R) \quad (6.2.1)$$

Where: F = actual load on tube at fracture (N); s = uniaxial stiffness of bung (N/m); S = uniaxial stiffness of testing rig and load cell (N/m); F_T = total load applied by load cell at fracture (N, measured) and F_R = residual load on bung after fracture (N, measured), assuming a negligible contribution from friction. By subtracting the load value post-fracture from the pre-fracture value and applying the correction for machine stiffness, we can find the value for the load on the tube. As the bung was designed for a snug fit in the bore, and polyurethane is taken to be incompressible (Poisson's ratio≈0.5) [3], we can assume a hydrostatic state. The internal pressure is then given by:

$$p = \frac{F}{\pi r_i^2} \quad (6.2.2)$$

Where: p = internal pressure at fracture (Pa) and r_i = radius of internal tube bore or the bung radius (m).

Typically a thin walled assumption can be made when testing cladding tubes, if the wall thickness is < one tenth of the tube radius. However, the tubes tested here do not fulfil that condition and so stresses vary throughout the wall thickness as a function of radius. To calculate the hoop stress σ_θ at the point of fracture as a function of r, one of Lamé's equations must be used:

$$\sigma_\theta = \frac{r_i^2 P_i - r_o^2 P_o}{(r_o^2 - r_i^2)} + \frac{(P_i - P_o) r_i^2 r_o^2}{(r_o^2 - r_i^2) r^2} \quad (6.2.3)$$

Where P_i = internal pressure (Pa); P_o = external pressure, in this case atmospheric (Pa); r_i = bore radius (m) and r_o = tube radius (m). Tubes tested had wall thicknesses of 1.8–2.7mm.

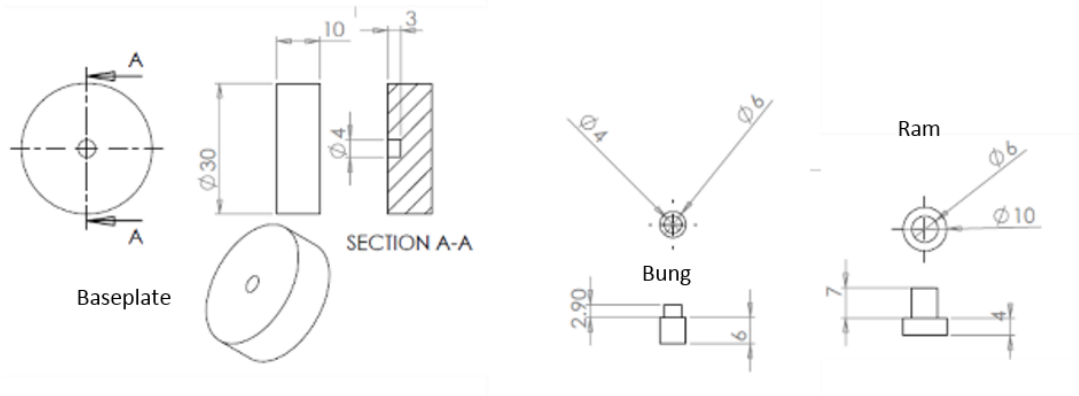

Fig. 6.2.2 – Three part hoop stress rig, with dimensions in mm.

6.2.2 – Results

Some photographs were taken post-sintering and after polishing, Fig. 6.2.3 and Fig. 6.2.4 respectively. Several tubes cracked in one or more places during removal, but the longest single piece was ~12cm. Unfortunately the tube warped and sagged during the sintering process, so was cut into two sections for drilling. Several tubes have non-centre holes running through them straight from the mould. During drilling some tubes failed, despite utmost care being taken during clamping and drilling. However several short sections of tube survived the process and were subsequently fine ground. During grinding, it was important to keep as uniform wall thickness as possible, for the hoop stress tests. This led to preferential use of P1800 grinding paper as material removal was slower, allowing for any errors to be corrected without ending up with very thin walls.

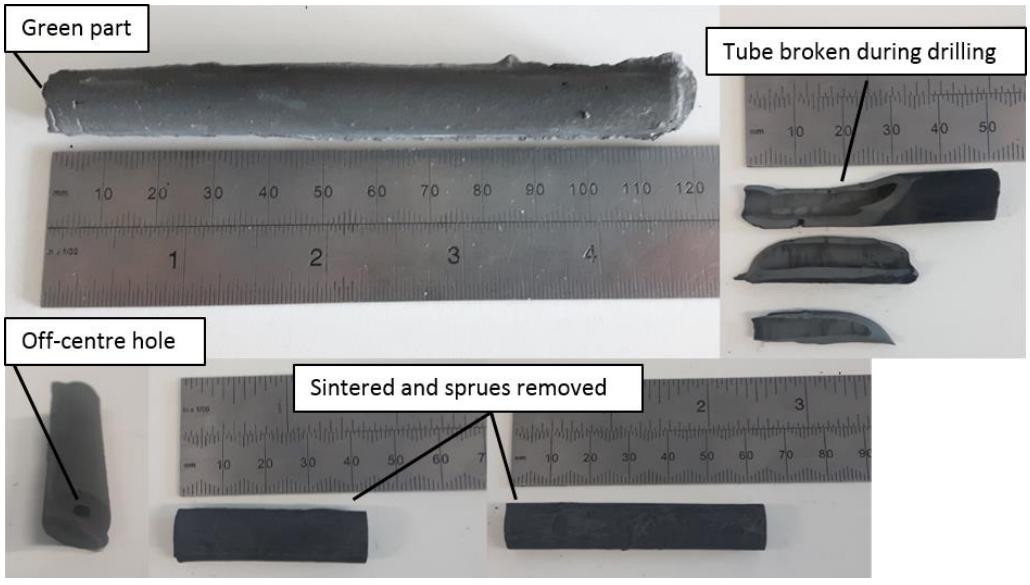

Fig.6.2.3 – Examples of cast tubes.

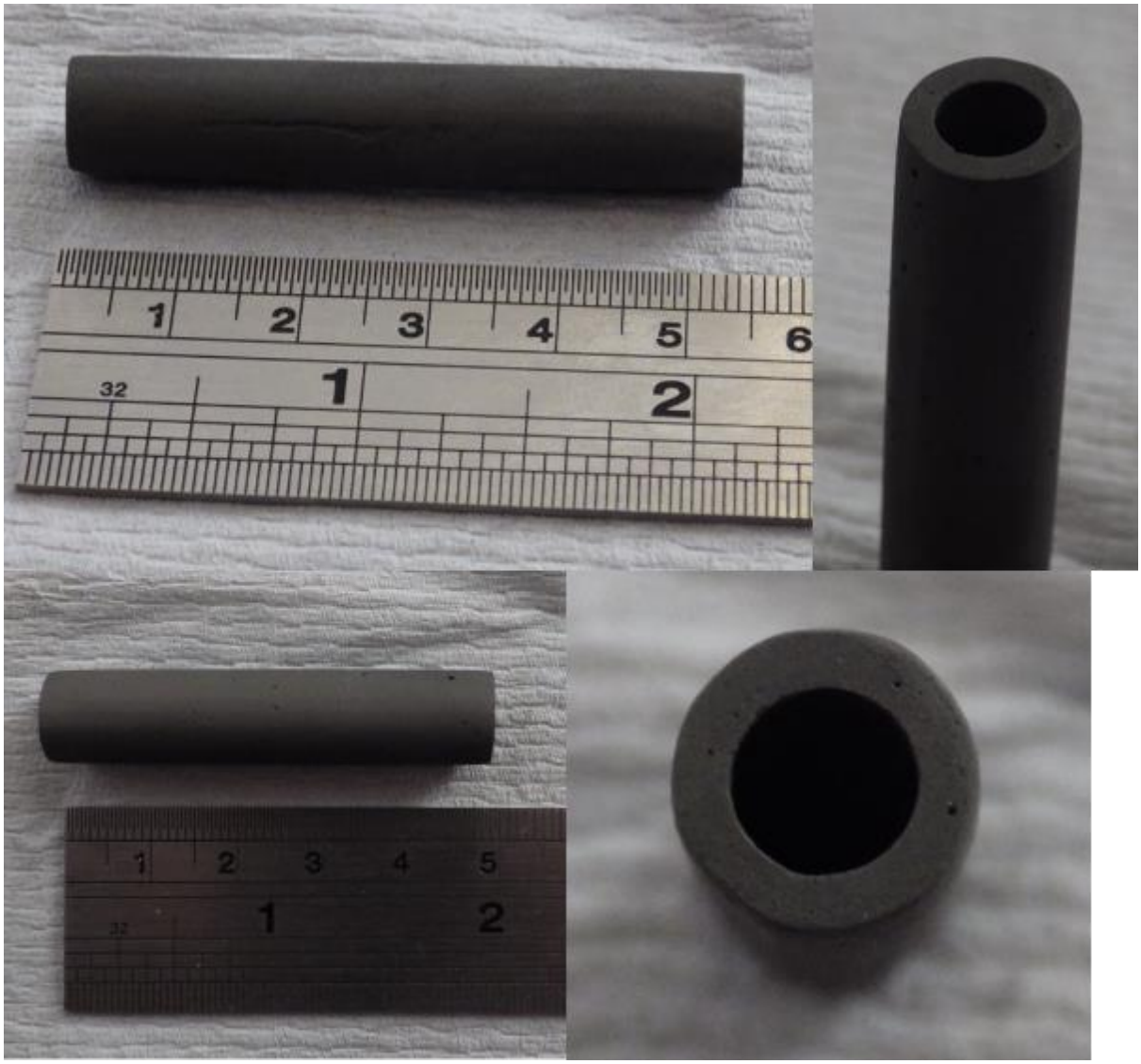

Fig.6.2.4 – Examples of two fine ground sections of tube, both approximately 5 cm long. Note that some bubble inclusions are still visible on the top and side surfaces.

Maximum calculated pressures at fracture for successful tube tests (see Discussion Section) are shown in Fig. 6.2.5 as a function of wall thickness. Results have been labelled 1–6 for comparison with subsequent Figures. There is a general upward trend of increasing wall thickness increasing maximum pressure withstood, however the significant variation suggests the quality of the tubes was inconsistent. Fig. 6.2.6 shows the variation of hoop stress with radius for the tested tubes. Because the Lamé equation has the form $Y=A+B/x^2$ the general curve shapes are identical. However there is again a great deal of variation on tested tubes, with maximum calculated hoop stresses at the internal surface varying between 2.54–20.95 MPa. Fig. 6.2.7 shows maximum hoop stresses (at the internal radius) for the tubes against wall thickness.

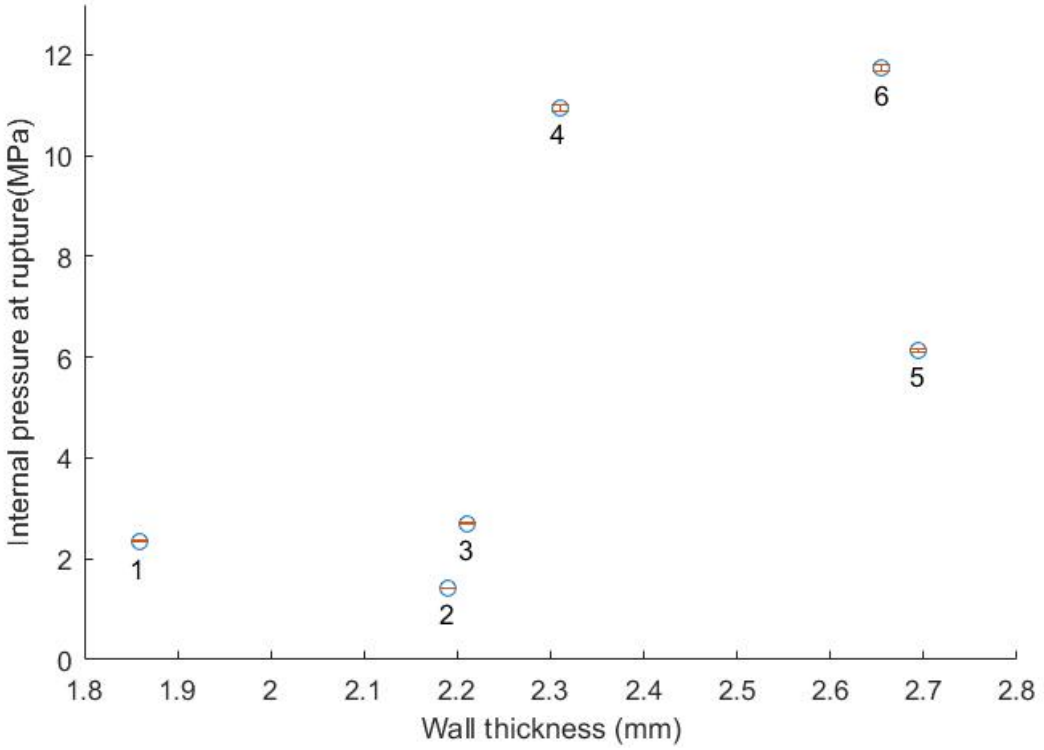

Fig. 6.2.5– Calculated maximum pressures for Ti_3SiC_2 slip cast tubes, shown against wall thickness.

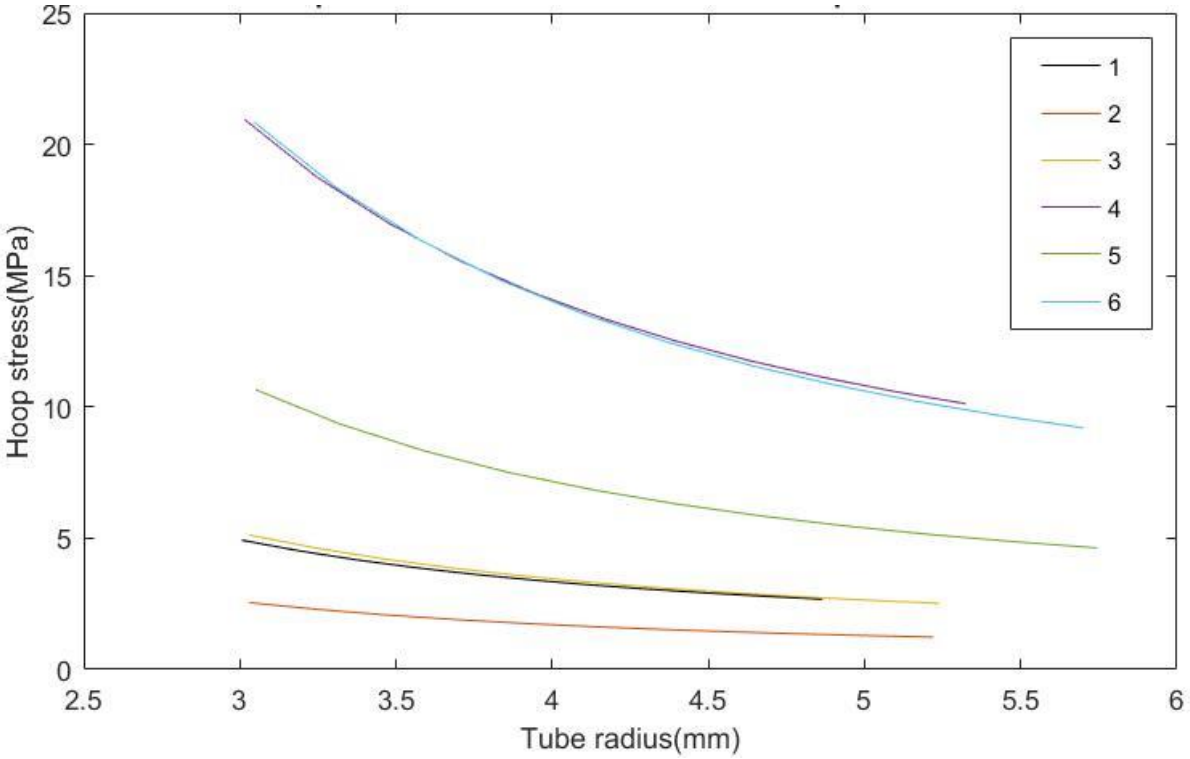

Fig. 6.2.6 – Hoop stresses through the tube walls at point of fracture.

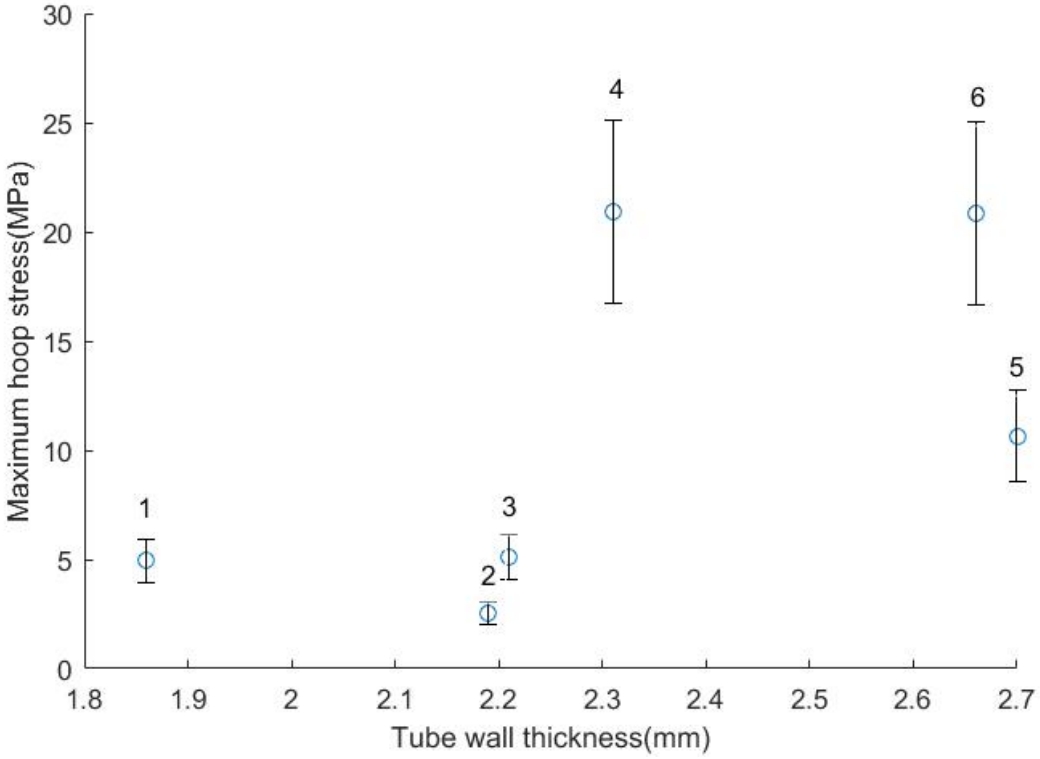

Fig.6.2.7- Maximum recorded hoop stresses as a function of wall thickness.

The fracture surfaces under SEM are shown in Fig.6.2.8. Based on a visual inspection, several fracture surfaces revealed voids and bubbles (although far less than the original cast piece), which were likely weak points for fracture. Grain pullouts are visible, and Tube 4 had an open fissure or crack on the fracture surface. Individual MAX phase grains can be clearly differentiated, indicating that overall densification was not entirely successful.

6.2.3 – Discussion

Hand grinding the tubes was far from ideal, as it was difficult to retain a cylindrical profile on the outside. There was also some bevelling towards the tube faces, but these sections were removed and excluded from testing, as were samples that had non-central bores. Of the samples tested, two exhibited unexpected force-deformation curves. These can be attributed to cases where a section of the tube failed, but a large arc section of the tube remained around the compressed bung, which subsequently failed after further compression. However these were discounted as the system was no longer radially symmetric. Table 6.2.1 displays a summary of the tubes tested.

Mould used	Slip used	Comments on green tubes	Sintering	Sintering comments	Machining	Suitable for hoop stress testing?	Tube number	Wall thickness (mm)	Maximum hoop stress (MPa)	Hoop stress/thickness (MPa/mm)
30mm diameter, 1 part	40:20:1 MAX:H_2O:PEI	**Cracked upon removal & contained several bubble inclusions**	500°C, Ar, 1h	Binder burnout (stage also part of subsequent runs)	**Not drilled as dimensions not representative of clad**	No			N/A	
			1300°C, Ar, 2h	Not densified						
		Small sections used for densification experiments	1400°C, Vac, 2h	Sample densified	**Some sintered cross section pieces polished for characterisation**					
			As above	87.6% of max.						
11.5mm diameter, 1 part		Unable to remove from mould due to narrow diameter	N/A			No			N/A	
11.5mm diameter, 2 part	Slip B (see Table 6.1.1) (Degassed)	Cracked, lower portion retrieved, had off centre hole	1450°C, Vac, 2h	None	Failed while trying to drill out centre	No			N/A	
		~120mm section removed intact		Tube sagged while sintering, sectioned into 2 straight pieces	1 surviving section after grinding Sub-sectioned into 2 pieces for testing	2 sections tested, 1 invalid (tube didn't break fully)	1	1.86±0.27	4.93±0.99	2.65±0.77 (Rank 4)
		Cracked, 2 sections retrieved		None	Drilled and hand ground	4 sections tested, 2 invalid (1 broke immediately, 1 didn't break fully)	2	2.19±0.27	2.55±0.51	1.16±0.30 (Rank 6)
							3	2.21±0.23	5.12±1.02	2.32±0.58 (Rank 5)
		Cracked, 2 sections retrieved		88.6% of max. density	Failure on 1 section failed during drilling	1 section tested	4	2.31±0.22	20.95±4.19	9.07±2.16 (Rank 1)
		Partial cracking during removal		None	Failed during drilling, 2 sections survived and were ground	2 sections tested	5	2.7±0.19	10.66±2.13	3.96±0.83 (Rank 3)
							6	2.66±0.19	20.85±4.17	7.85±1.66 (Rank 2)

Table 6.2.1 – Summary of tubes produced in this project.

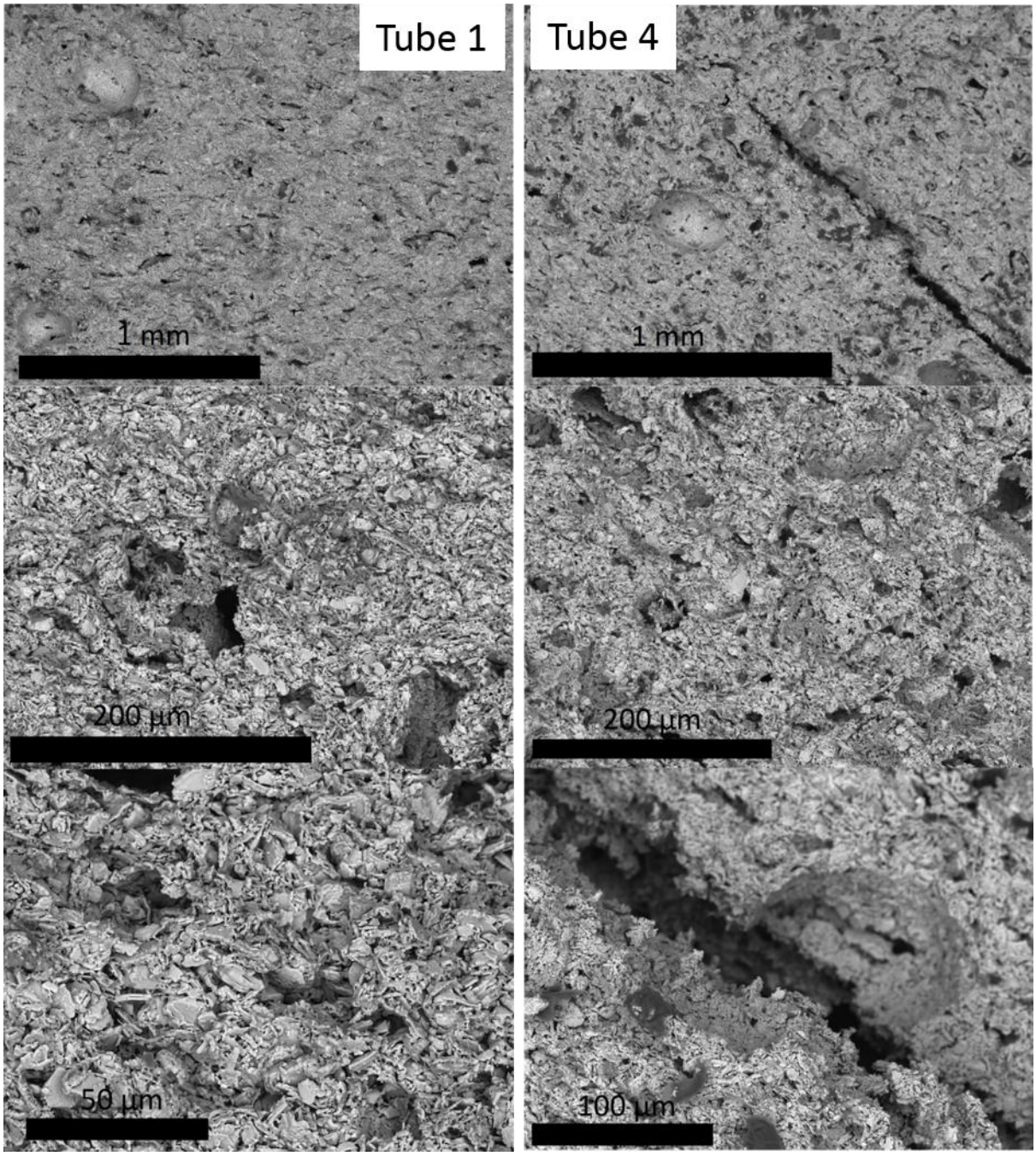

Fig.6.2.8 – SEM images of fracture surfaces of tubes. Images oriented so tube length is horizontal and radius is vertical.

The porosity and general faults in the tubes contributed to a wide range of failure pressures, and therefore hoop stresses. Hairline fractures may have been present in some tubes, resulting in premature failure, and as previously mentioned, internal voids also would have presented a problem. Repeated issues with the vacuum furnace led to operating pressures of 10^{-2} mbar. This was less than ideal and likely contributed to the poor densification. Ti_3SiC_2 has been synthesised at temperatures up to 1600°C [7] (via hot pressing), and so a higher temperature tube furnace may also have led to

improved results. A higher temperature would likely have volatilised more silicon (or 'A' element in general) but as the loss is constrained to the surface region this could be removed by grinding. Overall a better de-gassing step coupled with high vacuum sintering is required, along with the use of a lathe to polish/finish the tubes more accurately.

Considering the 'best' tube tested here (in terms of highest hoop stress for a given wall thickness), Tube 4 reached a hoop stress to wall thickness ratio of 9.07±2.16 MPa/mm and had a maximum hoop stress at the internal surface of 20.95±4.19MPa with a wall thickness of 2.66mm. However, the required hoop strengths are far larger in current zirconium alloy clads.

For comparison, the internal pressure of a rod in a Westinghouse 15x15 fuel assembly with a standard fill of helium at beginning of life (BOL) is 2.48MPa, and has a calculated end of life (EOL) pressure of 10.36MPa [8]. Although this falls below the failure pressure recorded in the experiment for Tube 4, it does not give much safety margin for the further increased pressures during a LOCA, and also does not take into account the external operating pressure inside the core (~15.5 MPa). Tests performed in this experiment were conducted at room temperature and ambient pressure due to equipment constraints.

Yield strength of zirconium alloys is potentially a more valid comparison against the MAX phase ultimate strength measurements made in the this work, as the point at which plastic deformation starts to occur is effectively the start of failure for zirconium alloys. As Ti_3SiC_2 MAX phases do not undergo significant plastic deformation, the yield and ultimate strengths will be almost identical in value and almost unchanged up to operational temperature of ~350°C [9].Therefore the ultimate strength measurements made in this work can also be considered representative of the yield at 350°C for comparison against the yield strength of zirconium alloys.

E110 zirconium alloy (used in Russian VVERs: equivalent to PWRs) has been shown to have a room temperature ultimate hoop strength of ~350MPa [10]. However, E110 is one of the least strong of the commercial zirconium alloys with its tensile yield being only ~40% of that of ZIRLO (potentially accommodated through thicker clad and/or reduced safety margin achieved through the clad, noting that VVERs use hollow pellets as alternate means of improving safety margins through the fuel [11]). Biaxial liquid pressure burst tests on un-irradiated Zr (1%Nb) alloy cladding tubes gave hoop stress at rupture values of ~950 MPa (~1350 MPa/mm) at ambient temperature, ~650 MPa (~950 MPa/mm) at operational temperatures and ~200 MPa (~300 MPa/mm) at ~700°C, although the value is almost nothing at ~1000°C (not taking into account oxidation and hydrogen embrittlement) [12]. It should however be noted that significantly variability has been shown between the maximum hoop stress values for zirconium cladding alloys recorded by different testing techniques, including between liquid

pressure burst tests and expansion due to compression (EDC) tests [13] such as used in the present work. Nevertheless, it is still apparent that the tubes made in this project are significantly weaker. Furthermore, the thickness of the tube must also be considered; a wall thickness of 2.66mm is likely not feasible for current PWRs (cladding thickness ~0.6mm [14]), and the porosity of the tested tubes would most likely render them unsuitable to hold gas pressure.

It must be emphasised, in spite of these factors that this work is a proof of concept experiment, and if denser MAX phase tubes were produced in the future, the failure pressure might be much higher. MAX phases are also expected to perform better at high temperature [2],[15] in LOCAs as zirconium alloys lose strength and balloon above 600°C [16]. A more fundamental issue arises when considering the literature fracture toughness values of MAX phases (4-20 MPa.m$^{1/2}$ [2]); even optimally created tubes might be too brittle to safely transport without risking breaches. Centrifugal slip casting has been shown to produce textured tubes [17], and this might provide a method for improving fracture toughness values over unoriented polycrystalline samples.

Ideally any future test MAX phase cladding tubes produced could be made thin enough to give a feasible comparison to existing Zr cladding. However, after some tube losses, it was decided to test thicker samples rather than risk breaking them by further grinding.

6.2.4 – Conclusion

The tubes were polished, removing this outer layer, and subjected to hoop stress tests. The highest pressure before rupture was 11.7MPa for a 6mm bore tube with walls 2.66mm thick. The highest hoop stress per wall thickness value was found to be 9.07 MPa/mm. Large variations across tests suggest overall tube quality was poor, mainly due to stress concentrating flaws (pores) in the cylinder wall. Nonetheless, the work reported in this chapter demonstrates clear proof of concept that MAX phases can be slip cast to form tubes which is encouraging for the use of this simple technology for the fabrication of fuel rods. However, significant more work is required to optimise the slip process and improve the mechanical properties. If high quality rods of 4m in length cannot be made, joining of lengths to make a complete rod could be considered as it is in some organisations for silicon carbide fibre composites (SiC_f/SiC) [18], though this would not be particularly attractive to industry (see Section 7 discussion). Ultimately, it is unlikely that, even with optimum casting and sintering conditions, a purely MAX phase cladding manufactured via slipcasting would be robust enough to safely replace Zr alloys entirely. A more realistic approach would be to consider a Zr/MAX phase combination, or a more textured solution akin to previously mentioned SiC fibre composites (see section 7 Discussion).

6.3 References

[1] H. A. Barnes, *The Handbook of Elementary Rheology*, 1st ed. The University of Wales Institute of Non-Newtonian Fluid Mechanics, 2000.

[2] M. W. Barsoum, “MAX Phases: Properties of Machinable Ternary Carbides and Nitrides,” in *Wiley-VCH*, vol. 1, Wiley-, 2013.

[3] H. Jiang and J. A. J. Wang, *Methodology for mechanical property testing of fuel cladding using an expanding plug wedge test*, vol. 446, no. 1–3. 2014.

[4] W. R. Hendrich, W. J. McAfee, and C. R. Luttrell, “Expanded plug method for developing circumferential mechanical properties of tubular materials,” US 7140259 B2, 2006.

[5] M. G. Jenkins and J. A. Salem, “Test methods for hoop tensile strength of ceramic composite tubes for light water nuclear reactor applications,” *Ceram. Eng. Sci. Proc.*, vol. 34, no. 9, pp. 119–129, 2014.

[6] K. Mosley, “The Stressing for Test Purposes of Materials in Tubular Form Using Elastomeric Inserts—Experimental and Theoretical Development,” *Proc. Inst. Mech. Eng.*, vol. 196, no. 1, pp. 123–139, Jun. 1982.

[7] M. W. Barsoum and T. El-Raghy, “Synthesis and Characterization of a Remarkable Ceramic: Ti3SiC2,” *J. Am. Ceram. Soc.*, vol. 79, no. 7, pp. 1953–1956, 1996.

[8] C. Brown *et al.*, “Maximum Cladding Stresses for Bounding PWR Fuel Rods During Short Term Operations for Dry Cask Storage,” *Pacific Northwest Natl. Lab.*, no. January, pp. 459–466, 2004.

[9] M. Radovic, M. . Barsoum, T. El-Raghy, S. . Wiederhorn, and W. . Luecke, “Effect of temperature, strain rate and grain size on the mechanical response of Ti3SiC2 in tension,” *Acta Mater.*, vol. 50, no. 6, pp. 1297–1306, 2002.

[10] M. Király, D. M. Antók, L. Horváth, and Z. Hózer, “Evaluation of axial and tangential ultimate tensile strength of zirconium cladding tubes,” *Nucl. Eng. Technol.*, vol. 50, no. 3, pp. 425–431, 2018.

[11] T. Abe and K. Asakura, “Chapter 2.15 - Uranium Oxide and MOX Production,” in *Material Properties/Oxide Fuels for Light Water Reactors and Fast Neutron Reactors, Volume 2, Comprehensive Nuclear Materials*, Elsevier, 2012, pp. 393–422.

[12] E. Kaplar, L. Yegorova, K. Lioutov, and A. Konobeyev, *International Agreement Report "Mechanical Properties of Unirradiated and Irradiated Zr-1 % Nb Cladding" NUREG/IA-0199*. U.S Nuclear Regulatory Commision, 2001.

[13] Z. Zhao *et al.*, "Mechanical Properties of Zircaloy-4 Cladding Tube by Advanced Expansion due to Compression (A-EDC) Test," *Mater. Trans.*, vol. 58, no. 1, pp. 46–51, 2016.

[14] "Fuel design data," *Nucl. Eng. Int.*, no. September, pp. 26–35, 2004.

[15] T. Lapauw *et al.*, "(Nbx, Zr1-x)4AlC3 MAX Phase Solid Solutions: Processing, Mechanical Properties, and Density Functional Theory Calculations," *Inorg. Chem.*, vol. 55, no. 11, pp. 5445–5452, 2016.

[16] J. C. Brachet *et al.*, "Behavior under LOCA conditions of Enhanced Accident Tolerant Chromium Coated Zircaloy-4 Claddings," *Top Fuel 2016*, no. September, pp. 1173–1178, 2016.

[17] G. A. Steinlage, R. K. Roeder, K. P. Trumble, and K. J. Bowman, "Textured ceramic tubes via centrifugal slip casting," in *Textures of Materials*, 1996, pp. 1045–1050.

[18] A. Kohyama, "Advances in Ceramic Materials - SiC/SiC composite," in *Fission Energy Workshop: Oppurtunities for Fundamental Research and Breakthrough in Fission, Global Climate and Energy Project, MIT*, 2007.

7. General discussion

This project was envisaged as a series of 'proof of concept' experiments, providing a route from synthesis of new MAX phases through to shape forming technology for their implementation in current PWR reactors. Particular consideration was given to the use with this material of techniques established for ceramic production on a large scale, e.g. traditional slip casting, rather than solely focusing on some of the more exotic but less proven innovative techniques, e.g. SPS, that dominate attention in scientific literature, though some of these were also studied in this work. Each section is here further discussed with respect to the literature, and its application in the nuclear industry.

7.1 – Synthesis routes

Despite its prevalence in the literature, reactive SPS failed to yield high purity, high density syntheses during this project. Despite milling, large particles of unreacted graphite were visible in the polished surface of the pellet made with elemental powders, so further size reduction and dispersal is imperative. Gao *et al.* synthesised Ti_3SiC_2 using SPS at 1200–1400 °C from TiC, Ti and Si using uniaxial pressures of 20, 40 and 60MPa [1], and reported <10wt.% TiC in samples sintered at 1300–1350°C at 40MPa, which is closest to conditions used in this project (10kN load on 20mm diameter die is ~32MPa). Higher applied pressure resulted in higher density pellets, but also raised the temperature at which the synthesised Ti_3SiC_2 broke down; Gao *et al.* reported that samples synthesised under 20MPa increase in TiC fraction at temperatures >1200 °C, while those at under 60MPa start increasing in TiC fraction at 1400°C. Gao *et al.* used initial reactant powder sizes comparable to this project, but do not give great detail on their pre-SPS preparation, other than they were ball milled in ethanol for an unspecified time. Based on this, it is possible that Ti_3SiC_2 was formed and then broke down as the temperature increased (experiments were performed in the region of 1300–1400°C) due to insufficient uniaxial pressure, or that the reactants were not ball milled as intensely or for as long as in the work of Gao *et al.*.

Another option that may have helped to increase the purity of Ti_3SiC_2 synthesis was the inclusion of small amounts of aluminium to elemental powders, as reported by Liang *et al.* [2] (addition of ~0.68wt.%) and Zhu *et al.* [3] (addition of 20mol.% of the silicon). Liang also used a turbula ball milling step to mechanically alloy the powders prior to SPS. Liang *et al.* posit that the molten aluminium in the sample reduces any surface oxides on the reactant powders. Zhu *et al.* observed a spike in the pressure of the vacuum chamber at ~900°C which suggests a rapid gas generating reaction takes place.

In both cases high purity is achieved, with either no XRD peaks suggesting ancillary phases (Zhu *et al.*) or 99.3wt.% pure (Liang *et al.*). The poor synthesis results, combined with the need to crush and mill the pellet to a powder for application, and batch size being constrained by the die size meant the focus on synthesis shifted to the Molten Salt Method (MSS).

MSS presents several advantages over SPS and other synthesis methods. The pellet it produces is porous and impregnated with salt, meaning it can be ground easily without a high pressure mechanical crushing step. Once the salt is removed the fine powder can be further milled if necessary. The synthesis requires no bespoke or specialist equipment and can be easily scaled up. The limiting factor is the size of the furnace. In the scale-up experiment performed in this work, a 10g batch was split into two pellets, but on an industrial scale large pellets or bricks could easily be pressed and fired to maximise efficiency.

MSS often results in a synthesis temperature lower than other methods. Guo *et al.* reported Ti_3SiC_2 synthesis 150°C lower than other methods [4] and Tian *et al.* synthesised Cr_2AlC at 1000°C [5], 400°C lower than via SPS [6]. This was also the case with Ti_2AlC in this project, achieving 89% pure Ti_2AlC at 1000°C, 100°C lower than by SPS [7], albeit held at temperature for much longer. Providing an energy-efficient method of industrial synthesis is important to keep overall costs down. This lower temperature is possible because the corrosive nature of the molten salt, can dissolve one or more of the reactants, and lead to MAX phase production by either templating (as determined to be the case with Ti_2AlC synthesis in this project) or a dissolution-precipitation reaction [8] [9].

However, MSS did present some problems during this project. Often the salt would vaporise in the furnace and crystallise on the inside of the tube and the gas exit fittings. This was particularly noticeable after running the 1300°C Ti_3AlC_2 samples but it occurred to some degree in the other furnace runs, so samples were covered with alumina crucibles. Guo *et al.* also performed their synthesis under argon, but did not specify if it is flowing or static [4], while Tian *et al.* specify that the sample was heated in a vacuum quartz tube [5]. This problem is minimal and is more based on the equipment used rather than a flaw inherent in the process. Sealed tubes filled with argon or evacuated as seen by Tian *et al*. would remove the problem of any line blockages, and reduce any cleaning needed.

Ti_3SiC_2 samples did not yield high purity, despite following the literature procedure. In the Ti_2AlC experiments, the reaction pathway involved the formation of TiAl and TiC, which then further reacted to form the product phase. If a similar reaction pathway is assumed for the initial formation of Ti-Si compounds and TiC, as determined by Li *et al.* [10] (although for a different synthesis route), then it can be deduced that it was the formation of Ti-Si compounds that was problematic, given that TiC

formed successfully as a precursor for Ti_2AlC. This is likely due to silicon melting at a much higher temperature than the aluminium in the successful experiments, but also could be due to the initial silicon powder being used in this project being a different size grade than that used by Guo *et al*: >44μm and 74μm respectively. Based on the information from the supplier, the silicon powder used only has a lower bound (retained by a sieve with 44μm openings), and so may contain particles larger than 74μm.

The hybrid syntheses also failed to produce any stable new phases, although several 'simple' MAX phases were present in the products. Removing the substitution element would likely have yielded some higher purity samples of existing MAX phases. For a nuclear application, the ideal phase would likely contain aluminium and or chromium for oxidation resistance, although untreated Cr_2AlC has been shown by Lee *et al.* to have poor tolerance to long term oxidation in air at 1300°C [11] and has been found to have poor radiation tolerance [12]. An option is some form of anodising or pre-oxidative treatment to form an alumina/chromia scale on the surface of the finished part before being put into operation, and some form of hybridisation to improve irradiation resistance.

The most relevant study into neutron transparency of MAX phases was performed by Grove *et al.* at NNL [13], and is based on simulations of thermal and fast neutron capture cross sections of select elements, identified from the literature as MAX phase components. However, while this work highlights good candidate elements for reactor suitable MAX phases to contain, it doesn't take into account the densities, which are difficult to predict theoretically for MAX phases [14] and therefore, it is difficult to predict the transparency of reactor suitable MAX phase until some are successfully synthesised. Both Zr_2AlC and Zr_3AlC_2 were successfully synthesised by Lapauw *et al.* [15] [16] via hot pressing, which represents a positive first step. More recently a number of zirconium-containing other hybrid phases with reactor potential have also been synthesised by hot pressing (see Literature Review), most notable of which are phase pure $(Zr_{0.8}, Nb_{0.2})_2(Al_{0.5}, Sn_{0.5})C$ also by Lapauw *et al.* [17] and $(Cr_{2/3}Zr_{1/3})_2AlC$ of relatively high purity by Chen *et al.* [18]. The significance of the former is the high percentage of Zr in the M sublattice which will act to minimise neutron absorption, but there is also the commercial-political factor that the nuclear industry is currently the only major user of Zr alloys and thus a number of nuclear fuel and reactor vendors are also zirconium producers, which means there is a disincentive to move away from Zr entirely to SiC_f/SiC for example. The latter is noteworthy because it contains a high percentage of chromium to potentially confer corrosion resistance but has greater structural ordering which may help to resist the amorphisation under irradiation that has been observed in non-hybridised Cr_2AlC. New zirconium-containing and chromium-coating hybrid phases continue to be discovered and once the properties of these have been thoroughly tested, a potential candidate incorporating these desirable elements may emerge.

The samples were hot pressed under 30MPa with a 60 minute dwell time, at temperatures of 1250–1600°C and show no ancillary phases. The addition of Nb and Sn were shown to reduce distortion that occurs in Zr_2AlC leading to a more complete synthesis. This research is particularly promising for MAX phases in the nuclear industry, not only because is high in zirconium (and so may be appropriate for a cladding material) but also as a potential method for stabilising and synthesising new potential cladding candidates.

As for the 'ideal' MAX phase, several show good oxidation resistance, sufficient neutron transparency and good radiation damage tolerance, although none currently exhibit all of these, which is why work into hybrid phases is being conducted. Some exhibit dynamic recovery from radiation damage, but only at temperatures above normal PWR operating conditions [19] [20].

7.2 – EPD and laser sintering of MAX phases

EPD provides a relatively simple and industrially cost-effective method for green coating fuel rod casings with MAX phases. The process has been shown to evenly coat cylindrical geometries, and a large bath or column could be constructed to coat all 4 m of a most likely but not necessarily empty fuel rod (capped at the ends to prevent suspension ingress). Using water also greatly reduces environmental risks posed by other organic solvents. However, separation due to gravity would likely be more noticeable in such a long column, so a better suspension composition is necessary. PEI is reported to be successful in the literature [21], although this project found little success with it. If the correct molecular weight and dose of PEI was used, it may effectively reduce flocculation in a 4m columnar bath, but it is also highly toxic to marine life, which would present a challenge for disposal. The waste suspensions and slips used in this project that contained PEI were collected in an open waste bottle and the water allowed to evaporate in a fume hood, greatly reducing the volume, although his may not be applicable on an industrial scale.

Although successful in densifying regions of coating and adhering them to the surface, more work needs to be done on the laser parameters to achieve a better coating. A different source of laser light would be far more useful, especially one which is more easily parametrised in terms of actual energy fluences on the surface. A laser beam welder or an engraving/cutting head could perhaps provide the fluences and the programmable mobility without requiring bespoke engineering.

Although the use of laser sintering of MAX phases is absent from the literature, some work has been done on other EPD ceramic coatings. Wang *et al.* used a High Powered Diode Laser (HPDL) module affixed to a CNC controlled XY table to densify yttria stabilised zirconia and alumina coatings onto

FeCrAl alloy substrates [22]. The laser had a wavelength of 808nm and 940nm (infrared) and a maximum power output of 1.5kW, and the substrate was placed on a 'cooling box' to reduce overheating. The laser spot was a 1x3mm rectangle, and was pulsed on the surface while the XY table moved the substrate. Wang *et al.* found that similar to this project, too low an energy fluence results in damage and delamination of the coating, while above a certain threshold (>67.5J/mm^2) the coating blistered and the substrate was damaged. Wang *et al.* give an ideal fluence value of 57J/mm^2 for their experiments.

Deckers *et al.*, similar to this work, used a SLM 3D printer (DTM Sinterstation 2000) as their laser source to densify EPD alumina layers, however their intention was to build up a thick freestanding pellet of alumina, analogous with what a SLM printer might produce under normal operation [23]. EPD was used to coat an electrode, which was then rubbed on the previously densified layer, liberating the coating and providing feedstock for the laser to densify. The whole procedure was also performed inside a custom built furnace within the SLM printer, keeping the environment at 800°C during the procedures, followed by further sintering at 1600°C. Although this is not directly relevant to work done in this project, it is noteworthy that Deckers *et al.* also observed globular surface deposits of alumina after the laser sintering, similar to the morphologies seen in this project. Laser power used was much lower (2W), but the influence of the bespoke furnace unit provided additional energy and post-laser sintering likely densified any particles that remained lightly adhered after laser sintering. Deckers *et al.* do not give energy density fluence values either which could be considered an issue with using SLM printers; a quantitative and comparable value for energy input per area would allow for better prediction of parameters, and allow for settings from a SLM printer to be more easily replicated in another setup.

Another option is the use of electron beam 3D printers/welders, as evidenced by De Riccardis *et al.*, who densified EPD alumina and alumina-zirconia coatings onto stainless steel [24]. Using an electron beam welder (Lara 52 TECHMETA) coatings were densified using 5.5–17.5J/mm^2 fluence (much lower energy density than Wang *et al.,* see above) and subjected the coatings to post-sinter heat treatments at 550–900°C. It was found that the porosity was reduced after electron beam densification, and the coatings were also adhered. This is likely partially due to the sub-micron particle size, which would aid densification by having a higher green packing fraction.

Although it is critical that the zirconium alloy substrate does not overheat, the increased penetration depth of electrons compared to an optical laser may improve adhesion between coating and substrate by not just heating the coating. Another method to improve adhesion between MAX phase and the titanium substrate would be the application of a TiC (or ZrC in the case of actual fuel rods) interlayer.

Such a layer could be applied via EPD or other techniques such as cold spraying or chemical vapour deposition (CVD), and either densified before the coating application, or left green and consolidated during the laser sintering.

In terms of industrial application, the rapid laser sintering presents a challenge with regards to scaling. Namely that a bespoke machine would be needed, with a movable laser gantry and a lathe to rotate the fuel rod, encased in an argon or vacuum chamber. This may be affordable as part of the capital cost of an ATF fuel plant, if such fuel can attract a price premium that is acceptable to utilities as result of allowing other economic benefits such as rendering some reactor back-up safety systems redundant. The lathe would require fine balancing or internal bracing of the fuel rods to reduce drooping or balance issues, but such a system could feasibly be constructed. Coating and densifying a flat surfaced geometry for items such as spacer grids could also potentially be achieved in a manner similar to that used in this project

Other coating methods of course exist in the literature, and result in MAX phase layers adhered to substrates, but they are often performed at high temperatures [25][26] (see Literature Review) above the limit for zirconium, which undergoes a phase change from α-Zr (hcp) to β-Zr (bcc) at 863°C [27], which can reduce the integrity of the cladding [28]. However, cold spraying of Ti_2AlC on Zr-based substrates has been performed using 600°C process gas by Maier *et al.* specifically targeting an ATF solution [29]. Layers of Ti_2AlC up to 100µm thick have been deposited onto flat and tubular Zr-containing substrates, and subsequent oxidation tests have shown coated samples have superior resistance compared to uncoated samples [30], [31].

The enthalpy for this transformation is 4.103 kJ/mol for elemental zirconium [32] which is a good starting point for an estimated maximum acceptable value of laser energy that can be imparted into zirconium alloys. If laser fluences are accurately known it could be determined whether or not this change could be minimised. By using a high speed laser, the time each region of the sample is exposed to high temperatures is greatly reduced, which should minimise the phase change. However, a better idea of acceptable fluences is required in future work.

From work done in this project, the best adhered coating samples were intermittent densified bands. These bands are likely due to issues with the hatching pattern used by the 3D printer laser, and further work with another laser source needs to be done to confirm this. However, a fuel rod striped with bands of densified max phases could still provide protection. As mentioned before, a pre-operational oxidation step will likely be needed to give an initial protective oxide layer, and close bands of a scale-forming MAX phase could provide complete coverage of the oxide but the increased surface area may make any protective gains negligible. In terms of overall surface roughness, the laser sintered coating

is particularly globular, and has TiC_{1-x} present, so a final finishing polish would be required. Coating thicknesses achieved here were between 10–30 µm so polishing would have to be precise, or thicker green layers required; an overly thick coating would be easier to bring down to a consistent thickness without wearing through it. However, as a proof of concept this experiment has been largely successful for Ti, and warrants further exploration and refinement for Zr in a more suitable sintering set-up (see 9. Future work).

7.3 – Slip casting MAX phase tubes

Slip casting is certainly an industrially scalable procedure as it is used to make a wide range of commercial products, from plates to bathroom ceramics. Several factors contributed to the varying quality of slips and pieces cast during this project. First of all, slip composition could be improved. Compared (qualitatively) to a typical alumina/mullite slip used to create in-house crucibles, the rate of water uptake is dramatically faster in the MAX phase slips used during this project. Particle size is a definite issue; the finer the particles the better their suspension and traditional ceramic slips have a particle size on the order of ~10^2 nm [33]. By slowing the water uptake considerably, and with very fine particles, the layer build-up on the mould inside is considerably denser, and provides time for any trapped bubbles to rise to the surface.

In terms of MAX phase slip casting, the literature is relatively scarce. A patent held by El-Raghy and Barsoum covers the slip casting of MAX phases specifically for glove and condom formers [34] but give vague descriptions of the slip constituents, even for the MAX phase used. However this demonstrates it could be a viable method for producing dense pieces more complex than tubes [35]. Sun *et al.* cast dense pieces using 2.5µm average size Ti_3AlC_2 from slips using Polyacrylic acid, (PAA) a different branch chain polymer as a dispersant. Sun *et al.* had success using flowing argon at 1420°C for 90 minutes to densify their pieces to 96% of theoretical maximum, likely due to the smaller particle size and fewer bubbles and voids.

Another industrially feasible option would be to use centrifugal slip casting as mentioned in the literature review. Reported on and patented by Steinlage *et al.*, it is used to create furnace tubes by spinning the moulds along their axis to create high density textured green bodies [36][37] . This also would remove voids and bubbles which are displaced inwards by the movement of the denser particles to the outer edges. This combined with a professionally made mould offer the best chance for slip casting such a long piece. As mentioned in the chapter discussion (Section 6.2.3), higher sintering temperature and lower sintering pressure would have yielded a denser finished product, but

this is an issue of the available equipment rather than an industrial hurdle. A high temperature 4m vacuum tube furnace could be constructed without too many bespoke parts.

The use of a lathe to finish the surface would yield more even tubes with perfectly central bores, and due to the machinability of MAX phases, a compressed air lubricated tungsten carbide composite cutting tool could be used effectively with only slightly more wear than usual [38]. However, as with the sintering of a coating on fuel rods (see above: Section 7.2), it would be difficult but potentially not completely unfeasible to keep a thin 4m tube centred on a lathe while applying cutting force.

A potential workaround for this is to cast smaller sections and connect them. This removes the difficulty in working with such long brittle pieces before they are sintered. Shen et al. reported on a method of joining MAX phase bulk samples via pulsed electric current, in a manner similar to SPS or spot welding [39]. This method is quick (processing time ~6 minutes in the experiment), produced strong joints (reported shear stresses of 50–60MPa). However, research on the joint strength both before and after irradiation would be needed to determine if this is appropriate, as potential weaknesses (mechanical or radiation) would be a serious problem.

A big issue standing in the way of MAX phase only cladding is their potential permeability by fission products. Jiang et al. have shown that ions implanted into Ti_3SiC_2 tend to migrate to the surface at reactor operating temperatures [40]. Although Ti_3SiC_2 is an unlikely candidate for a reactor MAX phase, it is a concerning result, and work needs to be done to see if this is characteristic of other MAX phases.

As mentioned previously, literature values of MAX phase fracture toughness are similar to SiC, but much lower than zirconium alloy cladding. Therefore, it is unlikely that, unless a reinforcing method can be developed for MAX phases similar to SiC fibre composites, a pure MAX phase slipcast tube could safely function as a cladding without radically increasing the thickness.

The use of a thin liner inside fuel rods may help diffusion and the mechanical property issues; a kind of ‘half and half’ cladding with a thinner than usual zirconium alloy insert surrounded by a thin MAX phase tube might give the best of both worlds, but at the expense of cladding thickness and ultimately the neutronics of the reactor. The tubes tested in this project were much thicker (1.88–2.66±0.005 mm) than existing fuel rod cladding (thickness 0.58 mm [41]) and it is unlikely that a perfectly dense MAX phase tube could be made that thin without compromising its strength, so thickness would have to be increased.

7.4 – References

[1] N. F. Gao, J. T. Li, D. Zhang, and Y. Miyamoto, “Rapid synthesis of dense Ti3SiC2 by spark plasma sintering,” *J. Eur. Ceram. Soc.*, vol. 22, no. 13, pp. 2365–2370, 2002.

[2] B. Y. Liang, S. Z. Jin, and M. Z. Wang, “Low-temperature fabrication of high purity Ti3SiC2,” *J. Alloys Compd.*, vol. 460, no. 1–2, pp. 440–443, 2008.

[3] J. Zhu and B. Mei, “Fabrication of high-purity Ti 3 SiC 2 by spark plasma sintering (SPS) of elemental powders,” *Most*, no. c, pp. 889–890, 2003.

[4] X. Guo, J. Wang, S. Yang, L. Gao, and B. Qian, “Preparation of Ti3SiC2 powders by the molten salt method,” *Mater. Lett.*, vol. 111, pp. 211–213, 2013.

[5] W. B. Tian, P. L. Wang, Y. M. Kan, and G. J. Zhang, “Cr2AlC powders prepared by molten salt method,” *J. Alloys Compd.*, vol. 461, no. 1–2, pp. 6–11, 2008.

[6] W. Tian, K. Vanmeensel, P. Wang, G. Zhang, Y. Li, J. Vleugels, and O. Van der Biest, “Synthesis and characterization of Cr2AlC ceramics prepared by spark plasma sintering,” *Mater. Lett.*, vol. 61, no. 22, pp. 4442–4445, 2007.

[7] W. B. Zhou, B. C. Mei, J. Q. Zhu, and X. L. Hong, “Rapid synthesis of Ti2AlC by spark plasma sintering technique,” *Mater. Lett.*, vol. 59, no. 1, pp. 131–134, 2005.

[8] M. L. Hand, M. C. Stennett, and N. C. Hyatt, “Rapid low temperature synthesis of a titanate pyrochlore by molten salt mediated reaction,” *J. Eur. Ceram. Soc.*, vol. 32, no. 12, pp. 3211–3219, 2012.

[9] T. Kimura, “Molten Salt Synthesis of Ceramic Powders,” *Adv. Ceram. - Synth. Charact. Process. Specif. Appl.*, pp. 75–100, 2011.

[10] S. B. Li and H. X. Zhai, “Synthesis and reaction mechanism of Ti3SiC2 by mechanical alloying of elemental Ti, Si, and C powders,” *J. Am. Ceram. Soc.*, vol. 88, no. 8, pp. 2092–2098, 2005.

[11] D. B. Lee, T. D. Nguyen, J. H. Han, and S. W. Park, “Oxidation of Cr2AlC at 1300°C in air,” *Corros. Sci.*, vol. 49, no. 10, pp. 3926–3934, Oct. 2007.

[12] C. Wang, T. Yang, J. Xiao, S. Liu, and J. Xue, “Structural Transitions Induced by Ion Irradiation in V2AlC and Cr2AlC,” *J. Eur. Ceram. Soc.*, vol. 99, no. 5, pp. 1769–1777, 2016.

[13] C. Grove, D. Shepherd, M. Thomas, and P. Little, “Neutronics of MAX phase materials,” *Struct. Mater. Innov. Nucl. Syst. (SMINS-4), Univ. Manchester*, 2016.

[14] P. Eklund, M. Beckers, U. Jansson, H. Högberg, and L. Hultman, “The M n + 1 AX n phases : Materials science and thin-film processing,” *Thin Solid Films*, vol. 8, no. 518, pp. 1851–1878, 2010.

[15] T. Lapauw, K. Lambrinou, T. Cabioc’h, J. Halim, J. Lu, A. Pesach, O. Rivin, O. Ozeri, E. N. Caspi, L. Hultman, P. Eklund, J. Rosén, M. W. Barsoum, and J. Vleugels, “Synthesis of the new MAX phase Zr2AlC,” *J. Eur. Ceram. Soc.*, vol. 36, no. 8, pp. 1847–1853, 2016.

[16] T. Lapauw, J. Halim, J. Lu, T. Cabioc’h, L. Hultman, M. W. Barsoum, K. Lambrinou, and J. Vleugels, “Synthesis of the novel Zr3AlC2 MAX phase,” *J. Eur. Ceram. Soc.*, vol. 36, no. 3, pp. 943–947, 2016.

[17] T. Lapauw, B. Tunca, D. Potashnikov, A. Pesach, O. Ozeri, J. Vleugels, and K. Lambrinou, “The double solid solution (Zr , Nb) 2 (Al , Sn) C MAX phase : a steric stability approach,” *Sci. Rep.*, vol. 2, pp. 1–13, 2018.

[18] L. Chen, M. Dahlqvist, T. Lapauw, B. Tunca, F. Wang, J. Lu, R. Meshkian, K. Lambrinou, B. Blanpain, J. Vleugels, and J. Rosen, “Theoretical Prediction and Synthesis of (Cr 2/3 Zr 1/3) 2 AlC i -MAX Phase,” *Inorg. Chem.*, vol. 57, no. 11, pp. 6237–6244, Jun. 2018.

[19] A. T. Motta, A. Couet, and R. J. Comstock, “Corrosion of Zirconium Alloys Used for Nuclear Fuel Cladding,” *Annu. Rev. Mater. Res.*, vol. 45, no. 1, pp. 311–343, 2015.

[20] M. W. Barsoum, “Neutron Damage and MAX Phase Ternary Compounds,” *U. S. Dep. Energy, Nucl. Energy Univ. Programs*, no. 09, p. No. 09-790, 2014.

[21] M. Mishra, Y. Sakka, C. Hu, T. S. Suzuki, T. Uchikoshi, and L. Besra, “Electrophoretic deposition of Ti 3 SiC 2 and texture development in a strong magnetic field,” *J. Am. Ceram. Soc.*, vol. 95, no. 9, pp. 2857–2862, 2012.

[22] X. Wang, P. Xiao, M. Schmidt, and L. Li, “Laser processing of yttria stabilised zirconia/alumina coatings on Fecralloy substrates,” *Surf. Coatings Technol.*, vol. 187, no. 2–3, pp. 370–376, 2004.

[23] J. Deckers, S. Meyers, J. P. Kruth, and J. Vleugels, “Direct selective laser sintering/melting of high density alumina powder layers at elevated temperatures,” *Phys. Procedia*, vol. 56, no. C, pp. 117–124, 2014.

[24] M. F. De Riccardis, D. Carbone, E. Piscopiello, and M. V. Antisari, “Electron beam treatments of electrophoretic ceramic coatings,” *Appl. Surf. Sci.*, vol. 254, no. 6, pp. 1830–1836, 2008.

[25] H. Gutzmann, F. Gärtner, D. Höche, C. Blawert, and T. Klassen, “Cold spraying of Ti2AlC MAX-phase coatings,” *J. Therm. Spray Technol.*, vol. 22, no. 2–3, pp. 406–412, 2013.

[26] J. Frodelius, M. Sonestedt, S. Björklund, J. P. Palmquist, K. Stiller, H. Högberg, and L. Hultman, “Ti2AlC coatings deposited by High Velocity Oxy-Fuel spraying,” *Surf. Coatings Technol.*, vol. 202, no. 24, pp. 5976–5981, 2008.

[27] I. Schnell and R. C. Albers, “Zirconium under pressure: Phase transitions and thermodynamics,” *J. Phys. Condens. Matter*, vol. 18, no. 5, pp. 1483–1494, 2006.

[28] P. Ashcheulov, R. Škoda, J. Škarohlíd, A. Taylor, F. Fendrych, and I. Kratochvílová, “Layer Protecting the Surface of Zirconium Used in Nuclear Reactors,” *Recent Pat. Nanotechnol.*, vol. 10, pp. 59–65, 2016.

[29] B. R. Maier, B. L. Garcia-Diaz, B. Hauch, L. C. Olson, R. L. Sindelar, and K. Sridharan, “Cold spray deposition of Ti2AlC coatings for improved nuclear fuel cladding,” *J. Nucl. Mater.*, vol. 466, no. June, pp. 1–6, 2015.

[30] H. Yeom, B. R. Maier, and G. Johnson, “Cold Spray Coatings for Accident Tolerant Zr-Alloy Cladding in Light Water Reactors,” *Adv. Mater. Manuf.*, no. June, 2018.

[31] B. Maier, H. Yeom, G. Johnson, T. Dabney, J. Walters, J. Romero, H. Shah, P. Xu, and K. Sridharan, “Development of Cold Spray Coatings for Accident-Tolerant Fuel Cladding in Light Water Reactors,” *JOM*, vol. 70, no. 2, pp. 198–202, Feb. 2018.

[32] S. Banerjee and P. Mukhopadhyay, *Phase Transformations: Examples from Titanium and Zirconium Alloys*. Elsevier, 2010.

[33] C. Tallon, M. Limacher, and G. V Franks, “Effect of particle size on the shaping of ceramics by slip casting,” *J. Eur. Ceram. Soc.*, vol. 30, no. 14, pp. 2819–2826, 2010.

[34] T. El-Raghy and M. W. Barsoum, “Max Phase glove and condom formers,” US 2004/0250334 A1, 2004.

[35] M. W. Barsoum, “MAX Phases: Properties of Machinable Ternary Carbides and Nitrides,” in *Wiley-VCH*, vol. 1, Wiley-, 2013.

[36] G. A. Steinlage, R. K. Roeder, K. P. Trumble, and K. J. Bowman, “Textured ceramic tubes via centrifugal slip casting,” in *Textures of Materials*, 1996, pp. 1045–1050.

[37] G. A. Steinlage, K. P. Trumble, and K. J. Bowman, “Process for slip casting textured tubular structures,” US 6,335,065 B1, 2002.

[38] S. Hwang, S. C. Lee, J. Han, D. Lee, and S. Park, “Machinability of Ti3SiC2 with layered structure synthesized by hot pressing mixture of TiCx and Si powder,” *J. Eur. Ceram. Soc.*, vol. 32, no. 12, pp. 3493–3500, Sep. 2012.

[39] L. Shen, J. Xue, M. W. Barsoum, and Q. Huang, “Rapid bonding of Ti3SiC2 and Ti3AlC2 by pulsed electrical current heating,” *J. Am. Ceram. Soc.*, vol. 97, no. 12, pp. 3721–3724, 2014.

[40] W. Jiang, C. H. Henager, T. Varga, H. J. Jung, N. R. Overman, C. Zhang, and J. Gou, “Diffusion of Ag, Au and Cs implants in MAX phase Ti 3 SiC 2,” *J. Nucl. Mater.*, vol. 462, pp. 310–320, Jul. 2015.

[41] K. Kim, Y. Jang, and J. Kim, “In-Reactor Performance of an Advanced PWR Fuel , PLUS7 , for OPR1000s in Korea for OPR1000s in Korea,” *J. Nucl. Sci. Technol.*, vol. 45, no. 8, pp. 836–849, 2008.

8. Conclusions

This project set out to address some crucial considerations in practically applying MAX phases for the purpose of coating or replacing fuel rods for existing LWRs.

Initially SPS was considered as a synthesis route, and the reactive SPS of Ti_3SiC_2 was undertaken from both elemental reactants and from mixtures of TiC, Ti and Si. Between the dwell temperatures of 1300–1400°C for 10 or 15 minutes, the samples made from elemental powders displayed ancillary $TiSi_2$, TiC as well as unreacted graphite, which was confirmed in surface SEM images of the pellets. Using fine TiC (2µm) as a carbon source resulted in better conversion to the product, although still displayed graphite peaks, which were thought to originate from graphite foil inclusions from the process. SEM showed the presence of silicon around unreacted titanium particles at 1300 °C, which were absent from the higher temperature samples.

The MSS technique was also investigated as a scalable synthesis route; Ti_3SiC_2 synthesis was explored based on the literature from elemental powders and from a novel reactant composition: Ti, SiC and C mixtures. The samples made from SiC were unsuccessful at producing Ti_3SiC_2, while those from elemental powders held at 1200°C for 2 hours resulted in the MAX phase alongside titanium silicides and TiC_{1-x}. The different salts used (NaCl, KCl and a eutectic mix of the two) had little bearing on the outcome.

MSS was further utilised to synthesise Ti_2AlC and Ti_3AlC_2 for the first time via this method. 89% pure Ti_2AlC (by weight, determined via Rietveld refinement) was synthesised at 1000°C, with the remainder of the sample being $Ti_{0.9}Al_{1.1}$ and very weak peaks of an unknown phase. Examination of the powders under SEM and EDX revealed the reaction pathway consisted of the formation of TiAl and TiC, with TiC templating onto the graphite particles. These then combine to form the product phase Ti_2AlC. Ti_3AlC_2 was also synthesised but at the higher dwell temperature of 1300°C, and resulted in 61% Ti_3AlC_2, 21% Ti_2AlC and 18% TiC. For both experiments the salt had little effect on the composition. This work was published in the Journal of the European Ceramic Society [1].

An experiment to try and create hybrid MAX phases with element substitution on the ‘M’ site was carried out using MSS at 1100 °C and via SPS at 1300°C. Binary combinations of Zr, Cr and Nb were used alongside Al and C to try and synthesise MAX phases in the form of $(A_xB_{1-x})_2AlC$ where A and B are two of the previously listed elements. Although the synthesis did result in some stable ‘simple’ MAX phases, no substitution was observed using MSS or SPS. However, MSS still represents a potential viable, scalable low temperature synthesis route and potentially some of the newly reported pure hybrid Zr-based MAX phases produced by hot pressing [2] [3] [4]could be trialled for MSS production.

Using commercially available Ti_3SiC_2 powder as a placeholder, experiments were undertaken to create a dense coating of MAX phase. The route to apply a green coating was chosen to be EPD for its prevalence in industry and due to lack of any specialist equipment needed. PSA revealed the as-received MAX phase was too coarse, and so it was ball milled down to a median diameter of 4.79µm. Based on zeta potential measurements, a 1vol.% suspension of Ti_3SiC_2 in water at pH 9 was found to exhibit the maximum absolute surface charge and was used for subsequent deposition experiments. Suspensions were made with PEI as a dispersant, but were found to be less effective.

Deposition was undertaken on a variety of substrates, namely copper foil, titanium sheet, graphite rods and ZIRLO sheets. Using 10V as a deposition voltage for 10 minutes provided thin even depositions without significant electrolysis, and samples could be removed, dried and further deposition undertaken to improve the thickness. After 10 minutes, a coating surface density of 1.89±0.26mg/cm^2 was achieved, and SEM revealed an even green coating on the substrates.

Densification via traditional means presented a problem with adhesion, and due to temperature constraints of zirconium, a novel approach for MAX phases via laser sintering was trialled. By simple modifications to a SLM 3D printer, coatings on titanium sheet were rapidly scanned by the pulsed IR laser, with varying beam focus and overall laser power. Narrow focus was shown to ablate the coating under the beam, but densify the adjacent coating. As the beam spot was widened the ablation was reduced and overall coverage improved. Dense coating approximately 30µm thick was produced.

Low power (>10W) and a narrow beam focus (5mm) gave densified bands that were well adhered when the sample cross sections were examined under SEM. There was a nodular surface phase, determined to be $TiC_{1-x.}$ This surface phase can easily be removed with polishing and does not present a problem. Widening the focus (10mm) did improve the coverage at the expense of adhesion. Very high power and wide focus (50W and 10mm focus) gave wider densified bands that were adhered but exhibited some cracking, as well as a large amount of the TiC_{1-x} surface phase. Raman of the coating confirmed the sample had not amorphised. Attempts to densify the coating on a ZIRLO substrate failed; this was possibly due to the unavoidable use of different equipment (which also did not result in densification onto Ti substrate), or that an interlayer is needed to bond Ti_3SiC_2 to a Zr-based substrate.

As an alternative to coated zirconium alloy cladding, the possibility of cladding made entirely from MAX phase was explored, once again using Ti_3SiC_2 as a placeholder. The rheology of various slip compositions were tested, and a suitable candidate was found (46%DWB water, 4%DWB PEI and 0.5%DWB methylcellulose). Tubes were cast in custom made moulds, and sintered under argon and vacuum at 1300–1450°C, with a prior 500°C burnout to remove the polymer additives. Under vacuum

at 1400 and 1450°C resulted in a ~89% dense tube after degassing the slip prior to casting. The surfaces of the cast pieces were found to be deficient in silicon indicating some of the MAX phase had decomposed, however EDX shows this is constrained to approximately 100 µm depth and could be removed by machining.

Samples of the cast tubes were drilled out and hand polished down to wall thicknesses of 1.88–2.66mm and tested to failure on a custom designed hoop stress rig. Results varied due to the presence of bubbles and voids at the failure sites, but the best tube failed at an internal pressure of 20.85MPa when tested in atmospheric pressure, and had a maximum hoop stress at the inside surface of 11.75MPa.

This project has explored potential routes to MAX phase use in ATF cladding, through a series of proof-of-concept experiments encompassing both novel and well documented techniques, that provide a starting point for further experimentation.

References

[1] T. Galvin, N. C. Hyatt, W. M. Rainforth, I. M. Reaney, and D. Shepherd, “Molten salt synthesis of MAX phases in the Ti-Al-C system,” *J. Eur. Ceram. Soc.*, vol. 38, no. 14, pp. 4585–4589, 2018.

[2] T. Lapauw, B. Tunca, D. Potashnikov, A. Pesach, O. Ozeri, J. Vleugels, and K. Lambrinou, “The double solid solution (Zr , Nb) 2 (Al , Sn) C MAX phase : a steric stability approach,” *Sci. Rep.*, vol. 2, pp. 1–13, 2018.

[3] B. Tunca, T. Lapauw, O. M. Karakulina, M. Batuk, T. Cabioc’h, J. Hadermann, R. Delville, K. Lambrinou, and J. Vleugels, “Synthesis of MAX Phases in the Zr-Ti-Al-C System,” *Inorg. Chem.*, vol. 56, no. 6, pp. 3489–3498, 2017.

[4] L. Chen, M. Dahlqvist, T. Lapauw, B. Tunca, F. Wang, J. Lu, R. Meshkian, K. Lambrinou, B. Blanpain, J. Vleugels, and J. Rosen, “Theoretical Prediction and Synthesis of (Cr 2/3 Zr 1/3) 2 AlC i -MAX Phase,” *Inorg. Chem.*, vol. 57, no. 11, pp. 6237–6244, Jun. 2018.

9. Future Work

Arguably the most important step in future work in this area is the development of either new or hybrid MAX phases with a combination of oxidation resistance, radiation damage resistance and neutron transparency, all within an acceptable limit. Once suitable candidates have been synthesised and identified, more accurate work can be done in determining optimum thickness for a coating or a full cladding without affecting reactor efficiency. Further to this, candidate MAX phases require studying in terms of the migration of fission products within them, as this determines whether a ceramic only cladding could be viable. As previously mentioned in Section 7.1, a pre-oxidation step will likely be necessary to provide protection, so the thickness and constituent oxides of this scale will also need testing; if it spalls off it will not provide adequate protection. Further work into neutron damage resistance of MAX phases is needed, as currently the literature largely comprises studies performed with helium or heavy metal nuclei.

Laser sintering provides a viable method for rapid densification of MAX phase coatings, but using a laser from a welding or engraving machine needs exploring, as well as the possibility of using electron beams. Once a more accurate understanding is obtained of the surface fluences used to densify the coating, along with accurate temperature measurement of the substrate, it can be determined whether a zirconium alloy would be overly heated during the procedure. Further to this, mechanical properties of the fully adhered coating would be needed to make sure it isn't easily scratched off during fuel rod assembly insertion/removal.

Finally, a smoother mould is needed for slip casting, along with a better slip composition with finer powder. Information from a professional slip casting firm could greatly improve the green body and post-sintering strength, as has been shown to be possible with MAX phases. The joining of short sections of tube could be considered and the strength investigated of the joined region, both before and after irradiation to ensure no leaks.

For both coated zirconium alloy and full MAX phase cladding, if they reach a stage where viable prototypes are constructed, a method of *in-situ* testing would be needed, to try and simulate LOCA conditions: properties of the bulk may differ in a thin film and increased internal pressure of the fuel rods at high temperature is likely to cause cracking in a coating. The permeability of hydrogen into and through MAX phases is also important to provide adequate protection of fuel rods.

10. Treatment of errors

In this section, potential sources of error for certain experiments are discussed. Measurement uncertainty is dealt with mathematically by the propagation of errors method, while the uncertainty from systematic errors (such as an offset error or scale error in case the of instrument calibration imperfection) are estimated. Random errors are addressed in some cases by measurement repetition and by calculating an average, typically the mean or median in the case of PSA.

Rietveld refinement

When performing Rietveld refinement, there are several potential methods of assessing how accurate the fitted simulation is to the experimentally gathered data [1]. Those used in this project are known as χ^2 and weighted profile R-factor (wRp or weighted Rp factor). Errors can arise in Rietveld from an unusual background profile, height errors, incorrect identification of the phase composition, and any crystal orientation in the powder sample. These can all be partially mitigated by following correct procedure when loading powder samples, collecting spectra and subsequent analysis using the characterising software. χ^2 and wRp values of the studied MAX phases are given in Table 10.1.

Target phase. Figure no. in parentheses.	**X^2**	**Weighted-profile R factors**
Ti_3SiC_2 (4.2.1)	3.362	0.1070
Ti_2AlC (4.4.2)	4.919	0.1337
Ti_3AlC_2 (4.4.3)	2.603	0.0997

Table 10.1 – Rietveld refinement and associated errors.

Vickers hardness

The largest source of error when performing Vickers hardness tests is from measuring the length of the diagonals of the indent, more specifically the correct lining up of the markers with the diamond corners. The American Society for Testing Materials (ASTM) suggest 5 indents in a known hardness test block should not differ by more than 2% [2]. However a larger error of 10% has been assumed to compensate for any operator error. 5 indents were made on each sample and a mean average calculated. Standard deviation was presented as spread bars on the mean values.

Particle Size Analysis

Errors in PSA can occur from the non-sphericity of particles and agglomerations of small particles. To try and mitigate these, Mie scattering settings were used (for non-spherical particles) as MAX phases tend to form longer platelets, which was confirmed by SEM (See Section 4.1). During the pre-measurement circulation, the suspended particles were ultrasonically agitated to try and breakup any agglomerations. Further to this an error of 5% was assumed for Mass Median Diameter (D_{50}) measurements.

Zeta-potential

The Malvern Zetasizer was set to record ζ-potential measurements 5 times for a given pH value and a mean average value was calculated. Standard deviation is displayed as spread bars. This process is automated, as is the measurement of the sample pH, so user error is minimised. However as it uses a similar technique to PSA, errors can arise from agglomerates and non-spherical particles. Mie scattering settings were once again used, but the electrode cell doesn't have an ultrasonic agitator. Therefore an error of 10% was assumed for ζ-potential measurements.

Time deposition graph

For the experiment displayed in Fig 5.2.3, (to calculate surface density of EPD deposits using Equation 5.2.1) measurements of the 'length' of the deposit (measured perpendicular to the longer side of the substrates) were assumed to be more inaccurate, due to the lack of hard edges on which to close the jaws of the callipers. Moreover the top edge of the deposit appears visually thinner than the bulk (likely due to interruption by the water meniscus or decreased field strength at the water/air interface) so an estimate had to be made as to where the coating ended. For these reasons, the error in the y measurement was taken to be 2mm.

Calliper (length) uncertainty: 0.05mm

Balance (mass) uncertainty: 0.005g

The error in the coating area A is calculated to be:

$$\frac{\delta A}{A} = \sqrt{\left(\frac{\delta x}{x}\right)^2 + \left(\frac{\delta y}{y}\right)^2} \quad (10.1)$$

The error in mass change M:

$$\frac{\delta M}{M} = \frac{1}{M}\sqrt{\delta {m_1}^2 + d{m_2}^2} \quad (10.2)$$

Finally by applying Equation 5.2.1, the error in ρ, the coating surface density has been given by:

$$\delta\rho = \rho\sqrt{\left(\frac{\delta A}{A}\right)^2 + \left(\frac{\delta M}{M}\right)^2} \quad (10.3)$$

Values and there error are presented in Table 10.2.

Time (minutes)	**Calculated value (mg/cm^2)**
2	0.87±0.25
4	0.96±0.25
6	1.31±0.28
8	1.68±0.26
10	1.89±0.26

Table 10.2 – Values and errors for the deposition-time experiment displayed in Fig.5.2.3

Hoop stress/pressure tests

Measurement error of the tube wall thickness was taken to be ±0.5mm to accommodate any minor variation occurring from hand grinding. Likewise the error was increased for values pertaining to bore/tube diameter.

Calliper (length) uncertainty for bung diameter measurement: 0.5mm

Uncertainty for bore diameter/tube diameter (length) measurements: 0.05mm

Compression rig (force) uncertainty: 0.0005N

The hoop stress at the point of fracture on the inside radius can be calculated using Lamé's Equation (Equation 6.2.3).

Considering Equation 6.2.1, the error on the force has been calculated by:

$$\frac{\delta F}{F} = \frac{1}{F}\sqrt{\delta {F_T}^2 + d{F_R}^2} \quad (10.4)$$

The error in the two stiffness values were deemed to be negligible due to its minimal effect and the high degree of precision in the data from the Zwick-Roell testing machine. The error in the pressure with reference to Equation 6.2.2 is then given by:

$$\frac{\delta P_o}{P_o} = \sqrt{\left(\frac{\delta F}{F}\right)^2 + \left(\frac{\delta(r_i{}^2)}{(r_i{}^2)}\right)^2} \quad (10.5)$$

Where the error in r_i^2 (δr_i^2) is given by:

$$\delta r_i{}^2 = \sqrt{\delta r_i{}^2 + \delta r_i{}^2} = \sqrt{2}\delta r_i \quad (10.6)$$

Error values for the tube/bore radii were taken to be half the uncertainty for the measured diameters. The uncertainty values here were then propagated through Lame's equations (6.2.3), and calculated values and their associated errors are displayed in the Table 10.3. This gives an error of ~10% for hoop stress values. However due to the small sample size, and because in most cases only 1 sample per tube was able to be tested, 20% error is quoted in Table 6.2.1 and Fig. 6.2.7 to address the potential for random error.

References

[1] B. H. Toby, "R factors in Rietveld analysis: How good is good enough?," *Powder Diffr.*, vol. 21, no. 01, pp. 67–70, 2006.

[2] ASTM, "ASTM E92 Standard test methods for Vickers hardness of metallic materials," vol. 82, no. Reapproved, p. 10, 1997.

Appendix

Papers published:

- T. Galvin *et al.* "Molten salt synthesis of MAX phases in the Ti-Al-C system" Journal of the European Ceramic Society, 38 (2018) 4585-4589
- T. Galvin *et al. "*Laser sintering of electrophoretically deposited (EPD) Ti_3SiC_2 MAX phase coatings on titanium" Submitted to Surface and Coatings Technology (awaiting response at time of writing).